The Impact of Mergers on Relaxed X-ray Clusters

by
Gregory B. Poole
B.Sc. University of Waterloo 1997
M.Sc. University of Toronto 1999

A Thesis Submitted in Partial Fulfillment of the
Requirements for the Degree of

DOCTOR OF PHILOSOPHY

in the Department of Physics and Astronomy

© Gregory B. Poole, 2006,
University of Victoria.

All rights reserved. Thesis may not be reproduced in whole or in part, by mimeograph or other means, without the permission of the author.

The Impact of Mergers on Relaxed X-ray Clusters

by
Gregory B. Poole
B.Sc. University of Waterloo 1997
M.Sc. University of Toronto 1999

Supervisory Committee:

Dr. A. Babul, Supervisor (Department of Physics & Astronomy)

Supervisor

Dr. F. D. A. Hartwick, Departmental Member (Department of Physics & Astronomy)

Departmental Member

Dr. C. J. Pritchet, Departmental Member (Department of Physics & Astronomy)

Departmental Member

Dr. R. Chapman, Outside Member (School of Earth and Ocean Sciences)

Outside Member

Dr. N. Katz, External Examiner (University of Massachusetts)

Additional Member

Supervisory Committee:

Dr. A. Babul, Supervisor (Department of Physics & Astronomy)

Supervisor

Dr. F. D. A. Hartwick, Departmental Member (Department of Physics & Astronomy)

Departmental Member

Dr. C. J. Pritchet, Departmental Member (Department of Physics & Astronomy)

Departmental Member

Dr. R. Chapman, Outside Member (School of Earth and Ocean Sciences)

Outside Member

Dr. N. Katz, External Examiner (University of Massachusetts)

Additional Member

Abstract

We generate a suite of idealized two-body X-ray cluster merger simulations with which we study the impact of mergers on the properties of relaxed X-ray clusters. We identify a common dynamical progression which typical merger events proceed through and use simulated *Chandra* observations to identify observable transient structures in surface brightness, temperature and entropy which emerge in the process. These simulated observations are also used to determine when the systems would appear relaxed under reasonable observational circumstances. This time is compared to other, more quantitative measures of a system's apparent dynamical state, all of which are compared to the time when the system formally relaxes to a virialized or hydrostatic state. The effects of mergers on observable X-ray and Sunyaev-Zel'dovich (SZ) observables are then explored and the contribution of merger events on scaling relations generated from these quantities examined. We conclude that mergers are

likely not capable of accounting for the observed scatter in these relations. We then examine the effects of mergers on the morphology and structure of compact cool cores (CCCs) observed to be present in the majority of X-ray clusters. We find that mergers can warm CCC systems, potentially transforming them (either transiently or for extended periods) into two additional morphologies: extended warm core (EWC) and compact warm core (CWC) systems. These morphologies segregate in all scaling relation planes in a way which is qualitatively consistent with what is observed. Lastly, we find that mergers do not efficiently mix the intracluster medium (ICM). Mergers between systems which initially possess central metalicity gradients (as CCC systems generally do) produce remnants with metalicity gradients very similar to those of the parent systems. Together, these results pose a significant challenge to a popular hypothesis in X-ray cluster studies: that mergers are responsible for producing extended core systems.

Contents

List of Tables

List of Figures

Preface

The work described in this thesis was undertaken between June 2004 and October 2006 while the author was a Ph.D. candidate under the supervision of Prof. Arif Babul in the Department of Physics and Astronomy at the University of Victoria.

Chapters 2 and 3 have been accepted by Monthly Notices of the Royal Astronomical Society and Chapters 4 and 5 will soon be submitted to Monthly Notices of the Royal Astronomical Society.

The simulations presented in this thesis were performed with the N-body/hydrodynamical code `GASOLINE` written by James Wadsley, Joachim Stadel, and Thomas Quinn. They were designed collaboratively with Mark Fardal, who generated them.

Contributions from Arif Babul, Ian McCarthy, Chris Bildfell, Tom Quinn and James Wadsley have greatly added to the success of this work. Mike Balogh and Richard Bower have also contributed through insightful comments and conversations.

Acknowledgements

This work is dedicated to all those who have inspired and nurtured my spirit – not only through my sunny days – but my long dark nights as well. You have never given up on me and I am blessed to have you standing with me now, at a bright new dawn.

To all the great friends I was blessed to meet in those Brown House years (and since; in order of your appearance) – April, Emily, Jon Brown, Mike Anderson, Graeme, Kelly, Jim, "the Matts", Colleen, Aaron, Ben, Jen and the huge list of supporting characters:

> *You lived life daily and welcomed me on your ride. I don't know what I would have done without your companionship. Thank-you.*

To Corey:

> *You breathed fire back into me when my light had gone out.*
> *I owe you my life.*

To my Patupaiarehe:

> *Kia Kaha! You represent it well and inspire me always. I know you'll always be there to remind me, and I hope you know that I'll always be there for you. Thanks for your patience, and for not throwing eggs at me. Your friendship has been so nourishing. I Love you dearly.*

To my family – Frank, Nancy, David, Lisa, Michael, Gwen and Lois:

> *You made me who I am and accept me for what I have become.*
> *A greater gift a person has never had.*

To all these people I say this: your support has taken so many forms and been so consistent that I once took it for granted as easy and to be expected from all. I have seen a lot of the world with you and I understand now how much of yourselves you've given to me and the kind of beautiful souls you all are for it.

Everything that comes after this is dedicated to you as well.

We shall not cease from exploration

And the end of all our exploring

Will be to arrive where we started

And know the place for the first time.

– T. S. Eliot

Chapter 1

Introduction

Human beings are blessed with an exceptional capacity to imagine that which is not immediately apparent to their senses. This ability to contemplate the "unseen" enables us to ask questions which range beyond the satisfaction of our immediate needs for food and shelter. It enables us to wonder what is beyond the next hill, beyond the horizon or beyond vast uncharted oceans — even beyond the air of our atmosphere.

Perhaps out of instincts of self preservation, this ability has evolved to expresses itself spontaneously when we are challenged by the unknown. This gives rise to curiosity; a state in which we compulsively seek to resolve confusions which arise from these challenges. In so doing, we ultimately transform uncomfortable ignorance into notions which we can confidently understand and use to manipulate our circumstances. We are also social creatures and seek ways to express our understandings within structures of language and to find commonality in the similar expressions of others. The resulting discourse and process of discovery leads to more refined and penetrating questions, with our persistent curiosity pulling us forever along into realms of the unknown.

Ancient humans were born, lived and died under the rising and setting Sun,

the rotating heavens and the changing seasons. Such rhythms set the timetable by which harvests had to be performed and signalled the arrival of hostile weather. As a result, a visceral and intimate cultural relationship to the night sky emerged early in our development. From this relationship and the understanding generated from the curiosity it inspired, the science we now know as astronomy emerged.

With such a long and central role in the world's cultures, astronomy has rapidly grown to encompass a vast body of knowledge. Originally merely the study of the Sun-Earth-Moon system, visible planets and stars, a dizzying and ever expanding zoology of physical phenomena are now the subject of its study: stars of many varieties (*e.g.* white dwarfs, red giants, blue super giants and variable stars), accompanying solar systems of planets and rocky debris, clusters of stars (*e.g.* young open clusters and old globular clusters), luminous clouds produced from the birth or death of stars, and giant clouds of cold molecular gas from which they all ultimately originated. It has also spawned a field of scientific study which attempts to account for the large scale structure, dynamics and history of the universe as a whole – physical cosmology.

In 1922, the last paper refining the dominant cosmological model at the turn of the 20^{th} century – the "Kapteyn Universe" – was published (Kapteyn, 1922, see Fig. 1.1). In this model, the universe was static and consisted of an oblate spheroid of stars $\sim 4 \times 10^4$ light years in size, with the Sun and it's solar system sitting a mere 2×10^3 light years from the preferred location of its centre. However, a radical alteration of this picture was forced in 1923 when Edwin Hubble discovered that the mysterious nebulae that we now call galaxies, are actually distant "island universes" of many billions of stars, existing unto themselves and outside of this distribution. Furthermore, he also discovered that (with few exceptions) galaxies are rapidly receding from us at a rate proportional to their distance from the Milky Way. This was the first solid evidence that the universe is expanding and ended our belief in a static universe.

We now know that galaxies are themselves arranged in even larger structures:

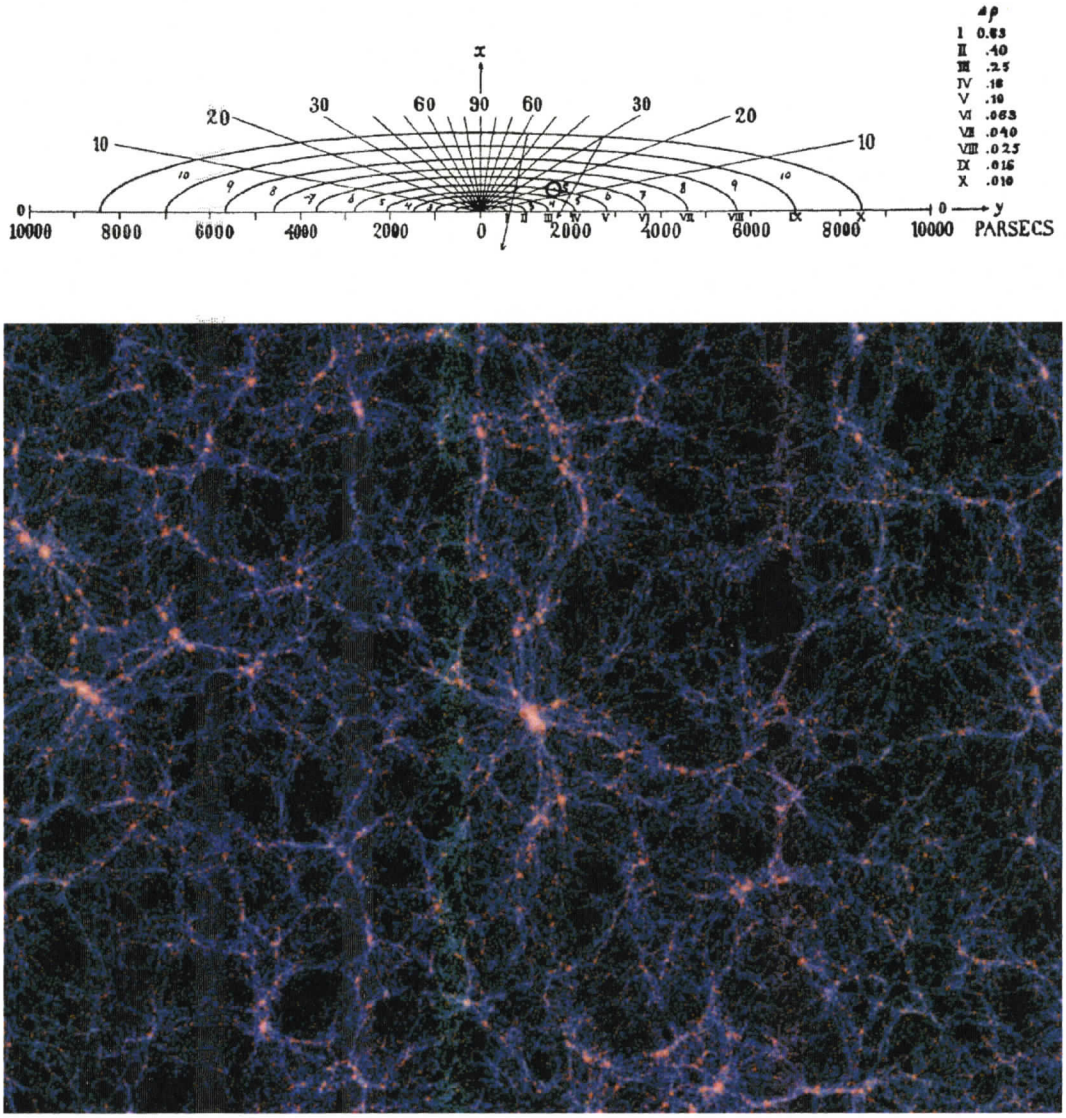

Figure 1.1: Two images comparing leading cosmological models from the turn of the 20^{th} century and from the turn of the 21^{st} century. The top panel, illustrating "Kapteyn's universe" (Kapteyn, 1922), is a map of stellar isodensity contours (the scale in pc is provided along the bottom; the figure spans roughly 20 kpc) of the largest structure then known. The bottom panel illustrates the largest structures now known. It presents the projected distribution of galaxies produced in the Millennium simulation (Springel et al., 2005) for a box spanning $\sim 4 \times 10^5$ kpc ($\sim 20000\times$ larger than Kapteyn's universe – although this simulation is intended to represent only a patch of a spatially unbounded universe). In the center is a rich galaxy cluster, sitting at the convergence of several filaments which thread between large voids in the distribution.

filaments, walls, voids and the largest bound objects in the universe – clusters of galaxies (see Fig. 1.1). Continuous progress has been made since Hubble's discovery of the large and distant nature of galaxies and we can now study their distribution out to distances reaching nearly the limit of the observable universe[1]. The tools for measuring the large scale structure and dynamics of the universe (*e.g.* large scale galaxy surveys, precision observations of the cosmic microwave background) have become so powerful that we are said to be living in the "era of precision cosmology". Present indications are that the universe becomes homogeneous and isotropic at very large scales ($\gg 100\,\mathrm{Mpc}$). In addition, the universe is spatially unbounded (*i.e.* extends infinitely in all directions) and its expansion is presently accelerating. To explain these and many other observations (*e.g.* elemental abundances, the cosmic microwave background), a highly successful cosmological model has emerged.

Fig. 1.1 depicts the dramatic change which has taken place in our understanding of the universe since 1922. Whereas the Kapteyn Universe placed us at the center of a finite, relatively small and static spheroid of stars, contemporary cosmological models position us in no preferred place or time in a spatially infinite and evolving universe. In a span of time covering merely one healthy human's life, our perspective on nature (and our relationship to it) has been radically, permanently and profoundly changed.

How has this transformation come about? The story is often told as a series of giant conceptual leaps involving recognizable names such as Nicolaus Copernicus, Galileo Galilei, Tycho Brahe, Johannes Kepler, Issac Newton and Albert Einstein. In reality, these individuals (brilliant and remarkable though they may be) stand-out merely as beacons of progress upon a sea of many minds, whose persistent efforts provided the context for timely insights. The road that has permitted the dramatic

[1]Due to the finite speed of light and the finite time since the Big Bang, there is a fundamental limit to the distances we can observe. Everything within this limit is said to lie within the "observable universe".

leaps in our knowledge has been paved by the efforts of many unacknowledged people through the careful consideration of seemingly innocuous inconsistencies in the dogma of their time.

The difficulties involved in making confident statements about complicated phenomena operating beyond the immediate access of our senses force us to work predominantly in this mode. In the words of Issac Newton (from *Opticks*):

> *To explain all nature is too difficult a task for any one man or even for any one age. 'Tis much better to do a little with certainty and leave the rest for others that come after, than to explain all things by conjecture without making sure of any thing.*

Due in part to the pace by which our understanding has grown, we have hardly even begun to appreciate the consequences of our changed perspective. Despite this and the broad and detailed success of modern cosmology, astronomers are compelled to continue refining their models of the universe. Unexplored or unexplained phenomena often go unnoticed within broadly successful fields of study and even a cursory examination of the history of scientific pursuit reveals the regularity with which new insights emerge from unanticipated directions.

This thesis is an attempt to contribute to this tradition of scientific discovery. It is a careful examination of the consequences of mergers on galaxy clusters using a more simplified approach than typically implemented for such studies. Although our model will prohibit us from addressing many interesting aspects of X-ray cluster mergers, we shall gain a great deal of experimental control and confidence that our initial conditions faithfully reflect the observed properties of the specific systems we wish to study. In short, we shall "do a little with certainty and leave the rest for others that come after".

First however, what are galaxy clusters and why are they merging?

1.1 Hierarchical structure formation

The cosmic microwave background (CMB) is a radiation field which permeates the universe and consists of the photons which were present when the universe suddenly became transparent at the "epoch of recombination"[2]. Ever since the first analysis of data from the *Cosmic Background Explorer* (*COBE*, Smoot et al., 1992) it has been known that this field is extremely uniform with temperature fluctuations (which roughly correspond to density fluctuations) on the order of only $\Delta T/T \sim 10^{-6}$. This indicates that the universe was extremely homogeneous roughly 3×10^5 years after the Big Bang. However, when we observe the present-day universe there is considerably more structure than this. How did the transformation occur?

Because gravity is a purely attractive force, small perturbations in a density field sufficiently large to resist the restorative forces of acoustic oscillations can only be amplified by its influence. This leads to a "gravitational instability" (first identified by Jeans , 1902) whereby small positive fluctuations in the field grow to form bound objects. Modern models of large-scale structure formation apply this mechanism to an early spectrum of primordial density fluctuations, reproducing observations of the present-day universe with remarkable success.

However, such a model is not complete without accounting for the initial conditions of the system in a sensible way. Presently, the most successful account of the origin of primordial density fluctuations is provided by the inflationary model, first proposed by Guth (1981). In this model, the universe experienced an early ($t < 10^{-33}$s) non-adiabatic phase transition which drove an exponential expansion of space. During this epoch, quantum fluctuations are believed to have generated density inhomogeneities which become diluted and stretched to enormous scales by rapid

[2]In the universe's early history, the baryonic material of the universe existed as a hot ionized plasma. Once the universe had expanded sufficiently for this plasma to cool to $\sim 2.5 \times 10^4$K, its electrons abruptly recombined with protons and alpha particles to yield an unionized (and transparent) gas of hydrogen and helium.

expansion. This scenario accounts for several problems in the standard Big Bang model (*e.g.* the flatness problem, the horizon problem, and the observed absence of magnetic monopoles). Furthermore, because fluctuations which happened earliest should have become stretched and diluted the most, it predicts an initial density field with more power on small scales and a power law spectrum of the form $\Delta\rho/\rho \propto r^{-n}$ with $n \sim 1$.

Following inflation, the universe continued to expand. Under these circumstances, the onset of gravitational instability is delayed to a degree inversely proportional to the density contrast of the perturbation. Starting with the spectrum of density perturbations predicted by inflation, small systems (like galaxies and groups of galaxies) overcome expansion and collapse first, with ever larger systems collapsing at ever later stages of the universe's evolution.

Such a scenario manifestly involves, at all times and on all scales, the assembly of objects through the repeated accretion of smaller systems. This process is called "hierarchical structure formation" and it is the paradigm within which the most successful modern theories of cosmological structure formation operate. Within this picture, galaxies formed early in the history of the universe ($\sim 0.5\,\mathrm{Gyr}$ after the Big Bang) and have since collected into larger structures – galaxy groups and clusters. The largest of these are expected to have been assembled recently through several merger events of smaller clusters.

1.2 Galaxy clusters and the discovery of the intracluster medium (ICM)

When viewed at optical wavelengths, galaxy clusters appear to be collections of hundreds or thousands of galaxies (see Fig. 1.2) orbiting around their mutual centre of mass (for good reviews of the study of galaxy clusters, see Sarazin, 1988; Mulchaey

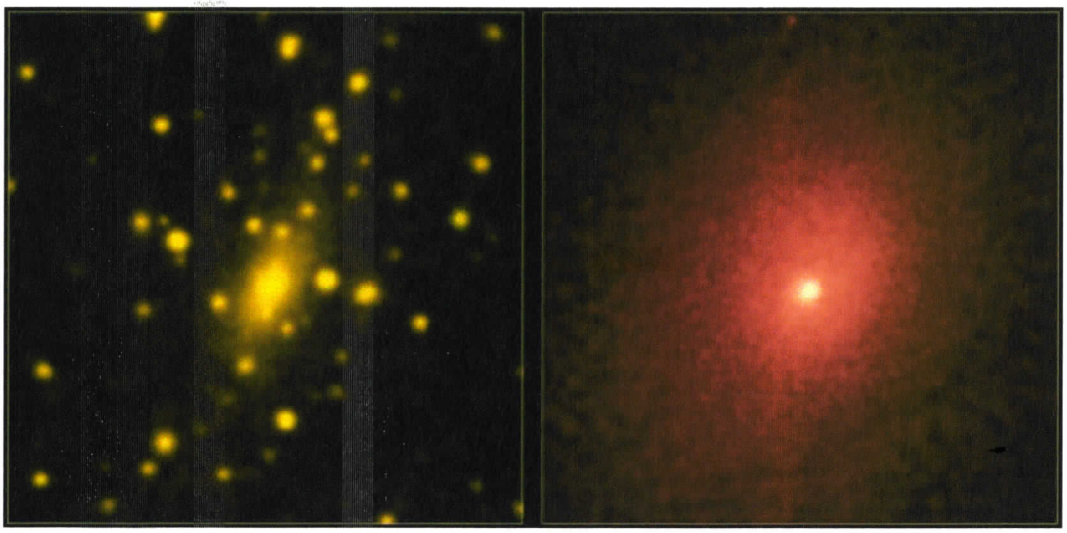

Figure 1.2: The galaxy cluster A2029 as seen at optical wavelengths (on the left, from the Digital Sky Survey) and at X-ray wavelengths (on the right, from *Chandra*).

et al., 2004). However, several discoveries have revealed that a great deal of a galaxy cluster goes undetected in such observations.

The first of these was made by Zwicky (1933) who found, through velocity dispersion studies, that galaxy clusters must consist of considerably more mass than what is implied by the light from their galaxies. Now known as dark matter (and generally believed to consist of an as yet unidentified particle which does not couple to the electromagnetic force), this unseen mass constitutes $\sim 90\%$ of a galaxy cluster's mass. We now know that most of this material exists as a great halo within which the galaxies of the cluster are embedded.

Another undetected component of galaxy clusters revealed itself to us between the years of 1966 and 1971 when engineers were able to place primitive X-ray detectors into orbit[3] and detect emission from the Virgo, Coma and Perseus clusters (Byram et al., 1966; Fritz et al., 1971; Meekins et al., 1971; Gursky et al., 1971a,b). In

[3]The atmosphere is opaque to X-rays making it necessary to study astrophysical X-ray sources using space born instruments.

1971, Cavaliere et al. (1971) suggested that all galaxy clusters may be sources of X-ray emission and subsequently, the first all-sky X-ray survey (conducted by the *Uhuru* satellite) found this to be true.

What is giving rise to the X-ray emission from galaxy clusters? Initially, several processes were explored, the three most popular being: thermal bremsstrahlung from a hot diffuse plasma, inverse Compton scattering of CMB photons by relativistic electrons, and a hypothetical population of X-ray luminous stellar sources. As the available observational resources and techniques improved, it soon became apparent from the spatial extent and spectral properties of the emission (most notably, the ubiquitous presence of a 7 keV FeXXV emission line), that thermal bremsstrahlung is the mechanism responsible. We now understand that the X-ray emission from galaxy clusters (referred to as X-ray clusters when discussing their X-ray properties) is due to a hot, diffuse and enriched intracluster medium (ICM; $T_x \sim 10^8$K, $n \sim 10^{-3}$cm^{-1} and $Z \sim 0.3Z_{\odot}$), which fills the system, constitutes $\sim$ 90% of its baryons and is bound by its dark matter halo. For a comparison of a galaxy cluster's appearance in optical and X-ray bandpasses, see Fig. 1.2.

1.3 The ICM – modern observational perspective

Early progress in our understanding of the ICM was driven by improvements in observational resources and this trend has continued to the present date. Following *Uhuru*, several satellites were placed in orbit with ever expanding and improving capabilities. The *Einstein* satellite (operating from 1978 to 1981) for instance was the first true X-ray imaging platform and the first instrument to offer a guest observer program to the general community. This lead, among other things, to the first detections of galaxy clusters at cosmological distances (z = 0.1 to 0.75; Henry et al., 1979).

The 1990s were dominated by three observatories. Launched in 1990, *ROSAT* had

an effective collecting area 3× larger, and detectors 6× more sensitive, than *Einstein* and was the first imaging X-ray telescope to perform an all-sky survey. The Japanese Advanced Satellite for Cosmology and Astrophysics (*ASCA*), with energy resolution 10× better than all predecessors and a wide bandpass ($0.1 - 10\,\mathrm{keV}$) made significant contributions towards measuring the spatially varying temperature structure of clusters. Lastly, *BeppoSAX* had a very wide spectral coverage ($0.1 - 300\,\mathrm{keV}$) and made important contributions to the study of non-thermal X-ray emission from clusters.

We are now in an era driven by the discoveries of two new advanced X-ray observatories: *Chandra* and XMM. Deployed by the Space Shuttle Columbia in 1999, the *Chandra X-ray Observatory* provides arc second spatial resolution (comparable to the capabilities of many great optical observatories), a large collecting area and a wide bandpass ($0.1 - 10\,\mathrm{keV}$). Launched the same year, the X-ray Multiple Mirror (XMM-Newton) observatory provides 6× the collecting area of *Chandra* and greater high energy sensitivity at a wider band-pass ($0.1 - 15\,\mathrm{keV}$), although with poorer spatial resolution (15").

The capabilities of these instruments are complimentary, and the result has been the detection of many new phenomena at work in X-ray clusters (*e.g.* bubbles being inflated in the cores by AGN jets, shocks and "cold fronts" from the disruption of merging systems, surface brightness edges due to bulk motions in cluster cores; see Fig. 1.3). High resolution spectroscopic imaging from these observatories has provided dramatic evidence of ongoing mergers in several systems. As a result, we now know that the intracluster medium of merging clusters can express a variety of complicated transient features including cold fronts (Markevitch et al., 2000), shock fronts (Markevitch & Vikhlinin, 2001) and the "sloshing" of cool cores in their dark matter potentials (Markevitch, Vikhlinin, & Mazzotta, 2001; Dupke & White, 2003). Significant progress in our understanding of the global structure of the ICM has also resulted, due primarily to accurate measurements of deprojected temperature profiles

for many systems.

1.4 The ICM – modern theoretical perspective

The utility of galaxy clusters as tools for studying cosmology and the history of structure formation is well established. Furthermore, sizable samples of clusters extending to high redshift will soon be available from wide field X-ray and Sunyaev-Zel'dovich (SZ) surveys, greatly expanding their importance and ensuring that they will feature prominently in these pursuits throughout the foreseeable future.

Often implicit in such studies is the assumption that clusters are in equilibrium. However, recent *Chandra* and XMM observations routinely reveal evidence of recent merger activity in clusters. Such observations have stimulated several theoretical and computational studies devoted to understanding the impact of mergers on clusters. Bialek et al. (2002), for instance, have shown that cold fronts can be produced through the disruption of cold cores during mergers while Motl *et. al.* (2004) have shown that a significant fraction of a merging cold core can avoid shock heating, contributing to the assembly of the remnant's cold core. Furthermore, Rowley et al. (2004) have shown that smooth accretion and mergers lead to different evolutions in a system's X-ray luminosity and temperature. Combined with the results of O'Hara et al. (2006) who suggest that all clusters may exhibit departures from equilibrium due to the lingering effects of their past merger activity, it becomes clear that we must understand the impact of merging in accounting for the observed properties of clusters; even the seemingly relaxed ones.

Most studies of cosmological structure formation are conducted with the use of sophisticated smoothed particle hydrodynamics (SPH) or adaptive mesh refinement (AMR) simulation codes. These algorithms are capable of solving for the gravitational and hydrodynamical evolution of arbitrary distributions of gas and/or dark matter. To simulate clusters in a way which accurately includes the effects of sub-

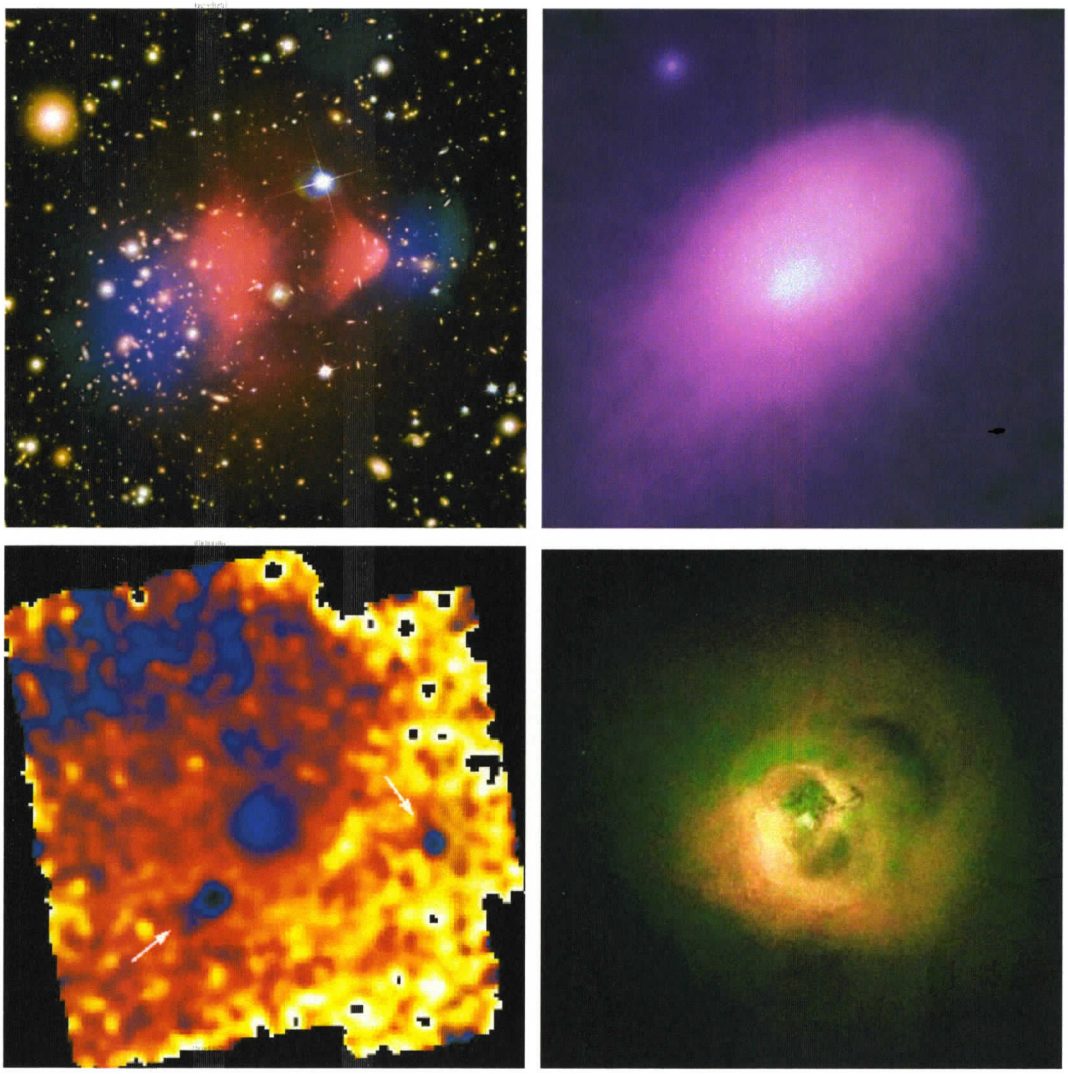

Figure 1.3: New phenomena being discovered and studied by *Chandra* and XMM. Top left panel: a comparison of the X-ray surface brightness (in red) to a projected mass map (in blue) of the near-axis X-ray cluster merger known as the "Bullet Cluster". Top right: *Chandra* X-ray surface brightness map of A2142 illustrating a surface brightness edge due to an on-going merger. Bottom left: an X-ray temperature map (temperature increases from blue, to red, to yellow) of A754 as measured by *Chandra*. The two white arrows mark merging galaxies. The distributed cold region towards the top is referred to as a "cold front". Bottom right: the active core of the Perseus cluster as seen by *Chandra*. Jets from an active galactic nucleus are inflating the dark cavities and driving acoustic ripples into the ICM.

structure and large-scale tidal effects, large-scale "cosmological simulations" are often performed with relatively low-resolution. Bound structures within such a simulation are identified and used to set initial conditions for smaller-volume/higher-resolution simulations of the cluster environment.

Because cluster evolution is mediated by so many processes acting over extremely large ranges of density and size, many approaches have been followed to optimally perform this task. For instance, because gas dynamical calculations are so computationally expensive, simulations concerned primarily with the dynamics of substructure often include only the effects of dark matter in their calculations. This permits larger volumes and density contrasts to be accurately modelled, with gas dynamical physics sometimes included in post processing using semi-analytic models. For studies of the ICM, cosmological simulations generally include a gaseous component to properly account for complicated shock heating processes which are of central importance to shaping its structure. The results of such a simulation are illustrated in Fig. 1.4.

Cosmological simulations such as these have the advantage of being capable of self-consistently rendering many aspects of cluster formation: the effects of shock heating as gas collapses from large distances onto a complex network of dense structures, dynamical heating due to a diversity of orbiting substructure, rotation induced by torques from large scale structure, *etc.* . However, the successes of this approach have been so dramatic that its disadvantages have been marginalized. For instance, it is a well hidden fact that they predict the conversion of far too much gas into stars ($\sim$ 20% versus the observed value of$\sim$ 5%). This is known as the "over-cooling" problem and likely has important consequences for the accurate modeling of cluster cores. Furthermore, their predictions for scaling relations formed from X-ray properties such as luminosity and temperature (L_x and T_x) do not exhbit as much scatter as observations (Kay et al., 2006). One possible avenue by which such discrepancies with observations arise is through processes which are active on scales smaller than the resolution reached by the simulation. Such "sub-grid" processes are often omitted

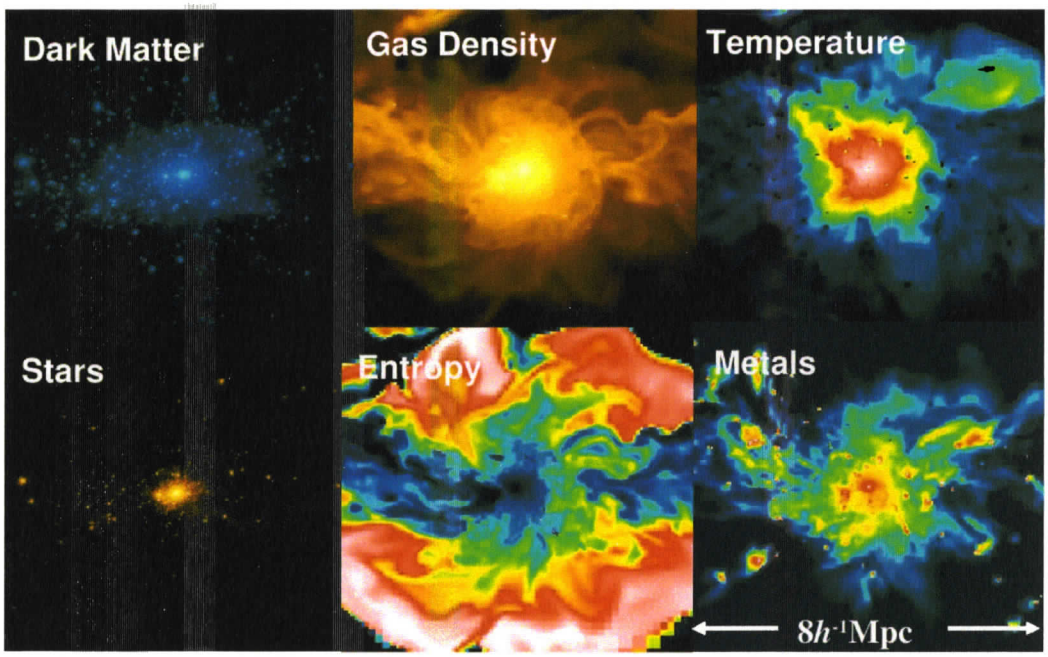

Figure 1.4: The distribution of various components (dark matter, stars and gas) or ICM properties (temperature, entropy and metallicity) for a simulated galaxy cluster.

(*e.g.* AGN) or included through crude and highly uncertain semi-analytic recipees (*e.g.* feed back from star formation).

1.5 Aims of this study

Determining the detailed effects of a single merger on a cluster evolving in a cosmological environment can be greatly complicated by the presence of extant substructure, subsequent mergers and smooth accretion. Simulations of idealized two-body cluster mergers provide an alternative approach and, given the fact that most clusters obtain much of their mass through significant mergers (Cohn & White, 2005), are not a significant departure from cosmological simulations. They allow control of the initial structure and orbits of the interacting systems and facilitate the investigation of not only the obvious short-term effects of the event, but more subtle long-term effects as well. They also simplify the interpretation of specific merger observations which typically involve only two dominant components.

Several authors have explored cluster mergers in this way (see Roettiger et al., 1993; Schindler & Mueller, 1993; Pearce et al., 1994; Roettiger et al., 1997, for pioneering studies). Among recent studies, Gomez et al. (2002) have constructed a suite of idealized merging systems of 4:1 and 16:1 mass ratios to study the effects of mergers on the stability of central cool cores. The initial conditions for their clusters were chosen to have gas core radii of $r_c \sim 250\,\mathrm{kpc}$ and the dark matter in their simulations was distributed according to a King model. Ricker & Sarazin (2001, RS01 hereafter) have studied mergers between idealized systems with cuspy dark matter profiles. Since the focus of their study was on the luminosity and temperature "boosts" which a merger system experiences upon impact of the cluster cores, they did not include the effects of cooling in their simulations. Lastly, Ritchie & Thomas (2002) have analyzed a set of simulations incorporating cooling and star formation for idealized merging systems constructed with cuspy dark matter profiles. Their initial conditions primarily exam-

ine systems with long cooling times and core radii of $r_c \sim 100\,\mathrm{kpc}$, although three cases represent systems with short cooling times and small core radii ($r_c \sim 50\,\mathrm{kpc}$).

However, it is now known that clusters have cuspy dark matter profiles and that the majority of observed systems possess compact cores ($r_c \sim 50\,\mathrm{kpc}$, Peres *et. al.* , 1998; Edge et al., 1992) with cooling times short enough to be of significant importance to their structure. Hence, a comprehensive study of cluster mergers utilizing initial conditions faithful to our contemporary understanding of a typical cluster's structure while including the important effects of cooling has not been performed. Given the wide ranging applications of cluster studies, the importance of mergers to understanding the structure of the ICM and the wealth of detailed cluster merger observations requiring interpretation, a thorough revisit of the issues introduced by cluster mergers would be of great utility.

In this thesis, we will present an analysis of a suite of SPH simulations of isolated two-body mergers between idealized clusters constructed to possess realistic compact cool cores. With this study we seek to provide a conceptual foundation for subsequent studies to be conducted in a full cosmological context. Our approach utilizes insights provided by recent high resolution observations of clusters to motivate the initial conditions for a set of nine hydrodynamic simulations (incorporating the effects of cooling and star formation) involving a representative range of mass ratios and impact parameters. Such an approach is not capable of addressing many issues involved with the formation and evolution of galaxy clusters, but is particularly well suited to the questions we will focus on.

Through this study, we shall see the power which appropriately simplified yet highly focused numerical experiments can provide, even when applied to phenomena extensively studied with more elaborate methods. We shall demonstrate how simplified approaches can uncover hidden problems in the conventional wisdom of mature fields of study, generating possibilities for new discoveries to follow.

In Chapter 2 we will present the details by which we have constructed our merger

simulations. In Chapter 3 we will examine the dynamical evolution of our systems and the transient structures formed from their ICM during the interaction. In Chapter 4 we study the evolution in the global properties of our systems and draw conclusions regarding the influence of mergers on the scatter in scaling relations formed from these properties. In Chapter 5 we will examine the effects of mergers on the structure and morphology of X-ray cluster cores. Lastly, in Chapter 6 we will discuss the conclusions of our study, its consequences for our models of structure formation and briefly discuss directions for future examination.

In all cases we will assume a cosmological model defined by a Hubble constant of H_0=75 km/s/Mpc, matter density of $\Omega_M = 0.3$, dark energy density of $\Omega_\Lambda = 0.7$, and baryon density of $\Omega_b = 0.02$ (all densities are in units of the critical density, $\rho_c = 3H_0^2/8\pi G$ where G is Newton's gravitational constant).

Chapter 2

Simulating mergers between relaxed X-ray clusters

Abstract

We describe our method of constructing idealized clusters and placing them on realistic orbits. Our initial conditions are chosen so that our clusters resemble relaxed clusters with cool compact cores observed by *Chandra* and XMM. We use the results of published dark matter simulations to ensure that our simulations sample the most interesting, theoretically plausible, range of impact parameters and progenitor mass ratios. In future chapters we will be interested in when our simulated mergers would appear relaxed under reasonable observational circumstances. We briefly describe in this chapter our method of generating simulated *Chandra* observations for this purpose.

We run our simulations with GASOLINE (Wadsley, Stadel, & Quinn, 2004), a versatile parallel SPH tree code with multi-stepping. We include the effects of radiative cooling, star formation and minimal feedback from supernovae in our simulations but the effects of feedback from active galactic nuclei (AGN) are omitted. It is important to note that we do not include the effects of magnetic fields, pressure generated from cosmic rays or conduction and that our choice of algorithm is not well suited to modelling the effects of turbulence. The relevance of each of these processes is not well established (theoretically or observationally) and we can only provide the

caveat that some of our results are susceptible to change once we have the resources to properly model them (although, see Markevitch et al., 2003; Fabian et al., 2003, for references suggesting that neither conduction nor turbulence are relevant in cluster cores).

In this section we describe how our clusters are initialized, how we set up pairs of clusters to form a merging system and the numerical methods and code parameters of our runs.

2.1 Cluster initial conditions

The structure of a merger remnant is likely to depend sensitively on the initial structure of the interacting systems (Gomez et al., 2002) making it important to implement realistic initial conditions for the gas and dark matter properties of our clusters. We follow the analytic prescription of Babul *et. al.* (2003) and McCarthy *et. al.* (2004) to produce systems which conform with recent theoretical and observational insights into cluster structure.

The dark matter density profiles of our systems follow an NFW-like form (Navarro, Frenk, & White, 1996; Moore et al., 1998) given by

$$\rho_{DM}(r) = \frac{\rho_s}{(r/r_s)^{\beta}\left(1+(r/r_s)\right)^{3-\beta}} \tag{2.1}$$

with a normalization given by ρ_s, a central asymptotic logarithmic slope chosen to be $\beta = 1.4$ and scale radius r_s selected to yield a concentration $c = R_{200}/r_s = 2.6$ (we will use R_{Δ} throughout to indicate the radius within which the mean density of the system is Δ times the critical density, $\rho_c = 3H_0^2/8\pi G$; $R_{200} = 1785\,\mathrm{kpc}$, $R_{500} = 1166\,\mathrm{kpc}$ and $R_{cool} = 180\,\mathrm{kpc}$ initially for our primary systems). This dark matter distribution would yield $c = 4.5$ if fit by Eqn. 2.1 with $\beta = 1$ and is consistent with results from

cosmological N-body simulations (Eke et al., 2001).

The initial density and temperature profiles of the clusters are set by requiring that (1) the gas be in hydrostatic equilibrium within the halo, (2) the ratio of gas mass to dark matter mass within the virial radius be $\Omega_b/(\Omega_m - \Omega_b)$, and (3) the initial gas entropy[4] scale as $S(r) \propto r^{1.1}$ over the bulk of the cluster body.

Our choice for the initial gas distribution is motivated by the fact that we are interested in studying "typical" systems which correspond to the most likely pre-interaction configuration for merging clusters. Estimates in the literature suggest that the majority of observed clusters (70–90%) possess dense, cool, compact cores with short cooling times (Peres *et. al.* , 1998). Recent *Chandra* observations reveal that these systems exhibit power-law entropy profiles of the form $S(r) \propto r^{1.0-1.3}$, beyond the central 10 kpc, over a wide range of mass scales (Donahue et al., 2005). We note that our choice for the form of the initial density profile conforms not only with these observations but also with the results of high resolution cluster simulations (Lewis et al., 2000; Voit et al., 2003).

We normalize the entropy profiles such that the temperature of the ICM at R_{vir} is half the virial temperature. This also approximately matches cosmological simulations (Lewis et al., 2000; Loken et al., 2002) and observations (De Grandi & Molendi, 2002). Finally, for practical purposes, we start our systems with small, constant, low-entropy (10 keVcm^2) cores. The cores, however, evolve to equilibrium power-law distributions quickly (~ 0.5 Gyr) and well before the clusters begin interacting significantly.

Particle realizations are initialized using the ZENO package of J. Barnes. Gas particles are distributed spherically and assigned temperatures according to the model described above. The dark matter velocity distribution is taken to be isotropic and the distribution function of particle energies calculated by solving the Abel integral equation (Binney & Tremaine, 1987; Kazantzidis, Magorrian, & Moore, 2004). Previous

[4]We use the standard proxy for entropy given by $S \equiv kT/n_e^{2/3}$ with n_e and T representing the electron density and temperature of the gas.

cluster merger studies have been initialized with Gaussian distributions resulting in systems which subsequently evolve significantly from their initial conditions (RS01). Our approach initializes the system very close to equilibrium, ensuring that our interacting systems accurately maintain our desired initial conditions until they collide. To illustrate the results of this proceedure, we present the initial conditions of our primary systems 2 Gyr after the beginning of our simulations in Fig. 2.1.

Negative values for the dark matter energy distribution function are avoided by truncating our clusters (dark matter and gas) smoothly beyond the virial radius (R_{vir}) with the function $\rho(r) \propto (r/R_{vir})^{\gamma} \exp(-[(r-R_{vir})/R_{sm}]^3)$, where γ is set to ensure a continuous first derivative for $\rho(r)$. Beyond the point where the gas pressure reaches that of the intergalactic medium (IGM) (we choose $P_{IGM} = (\Omega_b \rho_c \, kT_{IGM})/(\mu m_H)$ with $T_{IGM} = 3 \times 10^5$ K), we surround our systems with a dynamically negligible uniform gaseous medium of pressure P_{IGM}. This is done mainly to confine small numbers of high-velocity gas particles occasionally produced during our simulations. Without this external medium, these particles would adiabatically expand to unrealistically low densities and temperatures and pose numerical difficulties for the code.

In this study we examine mergers between systems set to have mass ratios of 1:1, 3:1 and 10:1. In what follows we shall distinguish the two interacting clusters by identifying the most massive $10^{15} M_{\odot}$ system as the primary system (with mass M_p) and the smaller incident system (with mass M_s) as the secondary. For our equal mass mergers, we arbitrarily choose one system as the primary with no effect on our results due to the symmetry in such cases. All positions and velocities are measured relative to the centre of mass of the primary system.

The virial mass of the primary system is set to $10^{15} M_{\odot}$ in all cases and the secondary systems have virial masses of $10^{15} \, M_{\odot}$, $10^{14.5} \, M_{\odot}$, and $10^{14} \, M_{\odot}$. These values are larger than M_{200}, which takes the values $7.5 \times 10^{14} \, M_{\odot}$, $2.4 \times 10^{14} \, M_{\odot}$, and $7.8 \times 10^{13} \, M_{\odot}$for the three systems. We shall, however, refer to the systems by their virial mass rather than M_{200}. The circular velocities of the halos at R_{200} (V_{200}) are

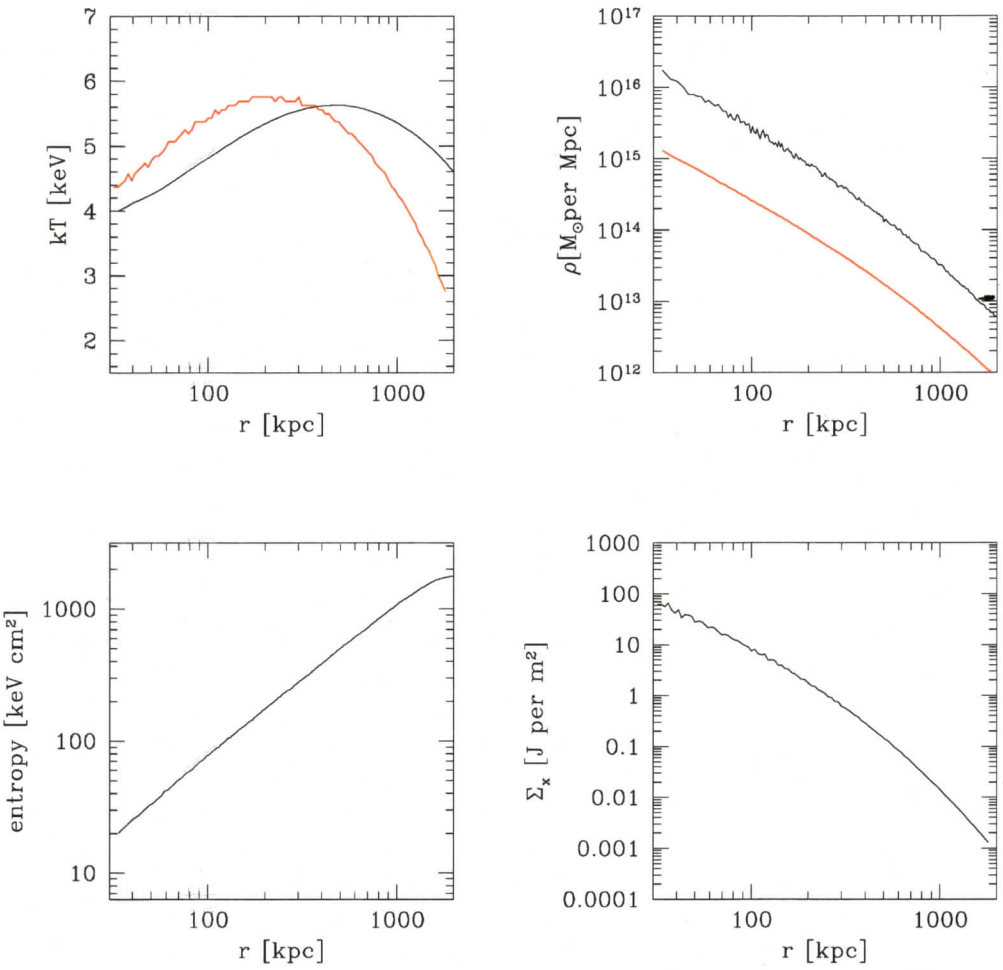

Figure 2.1: Initial conditions of our primary systems after 2 Gyr of evolution and relaxation (*i.e.* shortly before the systems begin significantly interacting) in our equal-mass head-on merger. Clockwise from the top left, each panel illustrates the temperature (black is the radial mass-weighted temperature and red is the projected spectrally-fit temperature), density (black is the dark matter density and red is the gas density), bolometric surface brightness and entropy of the system.

1340 km s^{-1}, 920 km s^{-1}, and 630 km s^{-1} respectively.

2.2 Initial kinematics

The problem of initializing the kinematics of idealized merging clusters has been faced by several authors (*e.g.* Ritchie & Thomas , 2002, RS01). Whereas previous studies have initialized orbits based on analytic arguments, our initial conditions are motivated by analysis of the orbital properties of substructure in high-resolution cosmological dark matter simulations.

We construct orbits for our systems which produce specified radial and tangential velocities for the secondary system (v_r and v_t respectively) when its centre of mass reaches the virial radius of the primary (R_{vir}). For each of the three mass ratios we study, we examine three orbits selected to produce a typical value of $v_r(R_{vir})$ and to cover a significant range of the transverse velocity $v_t(R_{vir})$ giving rise to mergers found in cosmological dark matter simulations.

In an N-body study of halos merging onto rich clusters, Tormen (1997) find that the average velocity of an accreting secondary system is $v(R_{vir}) = (1.1 \pm 0.1)V_c(R_{vir})$, where V_c is the primary system's circular velocity. In another study, Vitvitska et al. (2002) (see also Benson, 2005) examine the distribution of secondary subhalo velocities moving within the virial radius of massive halos. They find that the total velocities of accreting systems (*i.e.* those with negative radial velocities in the range $r = 0.8$–$1.2R_{vir}$) relative to the primary are distributed normally. They report mean infall velocities of $\langle v \rangle \approx V_c$ (independent of mass), consistent with Tormen (1997). They also find that tangential 2-dimensional rms velocities ($\sigma_\perp$) decrease with the secondary mass, ranging from $\sigma_\perp \approx 0.4V_c$ for 1:1 mergers to $\sigma_\perp \approx 0.67V_c$ for 10:1 mergers. It is important to note that these statistics likely include systems making secondary or tertiary encounters with their primary. The orbits of such systems have likely been rendered more isotropic, making these tangential dispersions upper limits

for substructure accreting for the first time. To produce systems which will merge fully within a reasonable amount of time, we have chosen to examine three values of v_t/V_c which roughly span the lower half of the Vitvitska et al. (2002) distribution. Specifically, we construct orbits to produce $v_r(R_{vir}) = 1.2V_c(R_{vir})$ (slightly higher but consistent with the mean velocities cited above) and $v_t/V_c = 0$, 0.15, and 0.4. Unlike in the rest of this study, we define the virial radius here by an overdensity $\Delta = 100$, corresponding to the threshold used by Vitvitska et al. (2002). Doing this for mass ratios of 1:1, 3:1 and 10:1 produces nine simulations which constitute the basis of this thesis.

Throughout our analysis we shall refer to three coordinate axes; x and y will denote directions in the plane of the initial orbit and z the direction orthogonal to this plane. To properly capture the initial effects of the encounter as the outermost envelopes of the systems make contact and the interaction shocks begin to form, we initialize our clusters separated along the x axis so that their smoothly truncated envelopes barely touch (*i.e.* separated by slightly more than the sum of their virial radii). As a result, the initial conditions we have outlined above must be imposed at a time part way through the run when the centre of mass of the secondary system crosses the virial radius of the primary. To determine the initial velocities which yield these conditions, we first approximate the systems as point masses and analytically determine the initial conditions which yield the desired constraints. To account for the extended, tidally deforming mass distributions, we then iteratively refine these orbits with low-resolution dark-matter-only simulations.

Table 2.1 lists the parameters relevant to the initial conditions of our runs including the centre-of-mass separation of the secondary from the primary (r), initial tangential and radial centre-of-mass velocities of the secondary relative to the primary (v_t and v_r), the time of virial crossing (t_o, using the virial radius R_{200}), and the centre-of-mass distances of closest approach (r_{min}). As a test of the validity of our orbits we have compiled the spin parameter and dark matter triaxial shapes for our final

combined systems. We compute the spin parameter from $\lambda = J|E|^{1/2}/GM^{5/2}$ with J being the total angular momentum, E the total energy and M the total mass of the remnant, all integrated within R_{200}. We compute the triaxial axes ratios at R_{200} (denoted q_{200} and s_{200}) following the approach of Dubinski & Carlberg (1991). All are in reasonable agreement with accepted distributions from cosmological simulations (Barnes & Efstathiou, 1987; Jing & Suto, 2002).

2.3 Numerical methods

To compute the hydrodynamic forces between gas particles, we use GASOLINE in its default configuration (Wadsley, Stadel, & Quinn, 2004): we use the Benz arithmetic-asymmetric implementation of the SPH momentum and energy equations. The gas quantities are smoothed over 32 particles, the Courant time step parameter is set to $\eta_c = 0.4$, and the viscosity uses the standard Monaghan formulation of viscosity with $\alpha = 1$ and $\beta = 2$.

The gravitational forces are calculated with a tree that uses an opening angle $\theta = 0.8$. Each particle trajectory is integrated on its own time step Δt_i, which is related to the particle's acceleration a_i by the criterion $\Delta t_i < \eta(\epsilon/a_i)^{1/2}$ with tolerance parameter $\eta = 0.2$. The gravitational softening uses spline kernel interpolation, and the spline softening length is set to a constant value of $\epsilon = 10\,\mathrm{kpc}$ for all cluster particles. This ensures that gravitational forces in the core are well resolved.

Radiative cooling allows for the formation of resilient dense gaseous cores. In some cases it can also dissipate significant amounts of the thermal energy deposited in the centres of merger remnants, further stabilizing them. Since we are acutely interested in the evolution of these regions in this thesis, the inclusion of cooling in our simulations is necessary.

We focus our analysis on radii $r > 40\,\mathrm{kpc} \sim 0.03R_{500}$ and have sought to ensure that we accurately model the behaviour of the system in that range. This is because

the precise nature of very central regions of the observed compact cool cores is still not well understood. The temperature floors observed in their centres (Peterson *et. al.* , 2003) indicate the presence of a source of heating whose nature is still highly uncertain with several candidate mechanisms presently being considered (*e.g.* heating from AGN, conduction and turbulent mixing to name only a few). There is also evidence of other complex phenomena occurring in the central 40 kpc, such as multiphase cooling and ongoing star formation (Jaffe et al., 2005; Egami et al., 2006). These processes cannot be realistically captured with SPH simulations such as ours. In light of these issues, we shall compute "central" quantities at 40 kpc and shall exclude the central 30 kpc $\sim 0.025 R_{500}$ of the system from integrated quantities such as globally averaged temperatures.

For our simulations we use a cooling function appropriate to a primordial gas. However, typical clusters have metallicities of $Z \sim 0.3 Z_{\odot}$ (where $Z_{\odot}$ is the solar value) and by omitting heavy element line emission, we are underestimating the cooling rate of material with temperatures $T = 10^5$–10^7 K. A very small fraction ($< 1\%$) of the gas mass in our systems exists at these temperatures; most of the mass has $T = 10^7$–10^8 K. Additionally, this discrepancy has a negligible effect on the dynamics of our simulations. All subsequent analyses (*e.g.* producing X-ray surface brightness maps) are computed assuming a more realistic Raymond and Smith model (Raymond & Smith, 1977) compiled for a metallicity of $Z \sim 0.3 Z_{\odot}$.

We include star formation in our simulations using an algorithm which turns cold and dense gas into collisionless star particles, using a recipe similar to that of Katz et al. (1996) and Stinson et al. (2006). We first select gas particles which are capable of forming stars on the basis of four eligibility criteria: the gas must be dense ($n_H > 0.1\,\mathrm{cm}^{-3}$); it must be either cool ($T < 3 \times 10^4$ K) or cooling ($dT/dt < 0$); its flow must be converging ($\nabla \cdot \vec{v} < 0$); and the particle must be Jeans unstable. Once selected, star formation produces star particles with a probability $p = 1.0 - \exp(-c_* \Delta T / t_{form})$ where the star-formation efficiency is taken to be $c_* = 0.1$. We set t_{form} to the

maximum of the cooling time and the dynamical time, unless the particle is already cool ($T < 3 \times 10^4\,\mathrm{K}$) in which case we always set it to the dynamical time. If the particle is chosen to form stars, a new star particle is created with 1/3 of the mass of a full-sized gas particle.

Star formation and supernova explosions go hand in hand. The energy released by the supernovae is injected into the surrounding intracluster medium as follows. At every timestep, we consider each star particle in the simulation and based on its age, determine the associated supernovae rate. The total energy released by the supernovae over the course of the timestep is then injected at a steady rate to the surrounding gas particles over the timestep. The star formation and feedback recipe we use is similar to that described in Stinson et al. (2006), except that we do not disable radiative cooling during feedback, and stellar winds which release mass from intermediate-mass stars are not included. This is a "minimal" feedback scheme, since the energy is quickly radiated away and the feedback does not impact the evolution of the ICM in any meaningful fashion.

Finally, we note that our chosen mass resolution models the initial conditions of a $10^{15} M_\odot$ system with 217441 dark matter and 211914 gas particles, where about 70% of the particles in each species are within R_{200}. The dark matter particle mass is $4.4 \times 10^9 M_\odot$ and the initial gas particle mass is $5.9 \times 10^8 M_\odot$. In test runs, we have found that the cooling rates of isolated clusters are not robust until there are ~ 100 particles within the "cooling radius" (*i.e.* the radius within which $t_{cool} < t_{Hubble}$; $R_c \sim 150\,\mathrm{kpc}$ for our simulations). With our initial conditions, the central core ($r_c \sim 50\,\mathrm{kpc}$) of a $10^{15} M_\odot$ system is initially resolved by ~ 240 particles, and its cooling radius by ~ 6300 particles.

2.4 Simulated observations

In the following chapters we will wish to know when our systems would look relaxed under reasonable observational circumstances. For this reason as well as to determine the observability of features in the projected mass, temperature and entropy maps presented in Figs. 3.1 to 3.9, we have created mock *Chandra* observations of our simulations. To create these we generate 325 projected X-ray maps ranging from 0.5 keV to 7.0 keV in 20 eV intervals using the Theoretical Image Processing System (TIPSY). This package takes the SPH outputs from our GASOLINE simulations and produces smoothed projected X-ray surface brightness maps with the appropriate variable SPH kernel applied individually to the flux represented by each particle. To these we add a three component X-ray background (following the prescription of the Quicksim XMM simulation package) consisting of an extragalactic power-law component (Chen et al., 1997) and two thermal components of 10^6 K and $10^{6.6}$ K modelled with a Raymond and Smith plasma (Raymond & Smith, 1977). Generally, each image would then be multiplied by a energy-dependent radially varying effective area. However, we are interested in the detectability of extended features at $z = 0.1$ and our merging systems rarely fit within the *Chandra* field of view (FOV) at such a redshift. For this reason, we simulate a "mosaic" mode for our simulated observations using constant but energy dependent effective areas, area averaged over the *Chandra* FOV. An unvignetted and spectrally flat particle background is then added with normalisation 3.5×10^{-2} cts arcmin^{-2}s^{-1} keV^{-1}. The resulting images are convolved with an azimuthally symmetric energy dependent PSF taken from the on-axis PSFs specified by version 2.23 of the *Chandra* CALDB. The result is converted to a photon flux at a redshift of $z = 0.1$, quantized with a Poisson distribution, and co-added. We use an integration time of 50 ks.

Table 2.1: Initial separations (r), radial and transverse velocities (v_r and v_t respectively) for our simulation orbits and measures of the final remnant's global structure (the spin parameter λ_{200} and triaxial ratios q_{200} and s_{200}, all measured within R_{200}). At the start of our simulations, $t = 0$; when the secondary's centre of mass passes the virial radii R_{100} or R_{200} of the primary, $t = t'_o$ or $t = t_o$ respectively.

M_p:M_s	$v_t(t'_o)/v_c(t'_o)$	$t_o[Gyrs]$	$r(0)[Mpc]$	$v_t(0)[km/s]$	$v_r(0)[km/s]$	$r_{min}[kpc]$	λ_{200}	q_{200}	s_{200}
1:1	0.00	3.4	6.54	0	-721	5	0.0	0.67	0.62
1:1	0.15	3.4	6.54	-111	-708	110	0.021	0.70	0.65
1:1	0.40	3.2	6.54	-315	-925	390	0.059	0.68	0.65
3:1	0.00	3.4	5.53	0	-574	12	0.0	0.76	0.73
3:1	0.15	3.4	5.53	-87	-587	103	0.014	0.80	0.75
3:1	0.40	2.6	5.53	-271	-908	360	0.042	0.78	0.76
10:1	0.00	2.2	4.81	0	-905	10	0.0	0.96	0.94
10:1	0.15	2.4	4.81	-106	-872	130	0.007	0.96	0.92
10:1	0.40	2.2	4.81	-284	-950	419	0.018	0.97	0.93

Table 2.2: Times of important stages in the dynamical evolution of our simulations measured relative to t_o, the time when the secondary's centre of mass crosses the primary's R_{200} radius. These are as follows: $t_{closest}$ is the time of first pericentric passage; t_{apo} is the time of the first apocentric passage; $t_{accrete}$ is the time of the second pericentric passage typically during which the secondary's gas core merges with that of the primary and it also marks the beginning of stream accretion; t_{relax} is the time at which the total system visually appears relaxed in simulated 50 ks *Chandra* observations at $z = 0.1$; t_{virial} is time at which the system's dark matter is assessed to be virialized within R_{500}; and t_{hydro} is the time at which the system returns to hydrostatic equilibrium (to within 10%) at R_{500}. Quantities in brackets indicate the redshift at which the secondary core would have to cross R_{200} of the primary for the system to be observed in the given state at $z = 0.1$ and $z = 0.5$ respectively. Additional parameters in the table are: the mass ratio of the primary to the secondary (column 1) and the secondary's transverse velocity at when its centre of mass crosses the virial radius of the primary, in units of the primary's circular velocity (column 2).

M_p:M_s	v_t/v_c	$t_{closest}$	t_{apo}	$t_{accrete}$	t_{relax}	t_{virial}	t_{hydro}
1:1	0.00	0.5 (0.14, 0.58)	1.2 (0.21, 0.70)	2.2 (0.33, 0.92)	4.4 (0.65, 1.73)	4.4 (0.65,1.73)	7.9 (1.73,>10)
1:1	0.15	0.6 (0.15, 0.60)	1.5 (0.25, 0.77)	2.3 (0.34, 0.95)	4.4 (0.65, 1.73)	4.4 (0.65,1.73)	–
1:1	0.40	0.5 (0.14, 0.58)	1.4 (0.24, 0.75)	2.7 (0.39, 1.06)	5.4 (0.85, 2.44)	3.8 (0.55,1.44)	3.3 (0.47,1.25)
3:1	0.00	0.5 (0.14, 0.58)	1.4 (0.24, 0.75)	2.3 (0.34, 0.95)	5.0 (0.77, 2.10)	3.4 (0.49,1.28)	4.3 (0.63,1.67)
3:1	0.15	0.5 (0.14, 0.58)	1.5 (0.25, 0.77)	2.5 (0.26, 1.00)	4.6 (0.69, 1.84)	3.4 (0.49,1.28)	4.3 (0.63,1.67)
3:1	0.40	0.8 (0.18, 0.63)	1.9 (0.29, 0.85)	3.5 (0.50, 1.32)	5.7 (0.92, 2.75)	4.3 (0.63,1.67)	3.6 (0.52,1.36)
10:1	0.00	0.8 (0.18, 0.63)	2.2 (0.33, 0.92)	3.5 (0.50, 1.32)	4.8 (0.73, 1.96)	4.6 (0.69,1.84)	5.2 (0.81,2.26)
10:1	0.15	0.6 (0.15, 0.60)	2.1 (0.32, 0.90)	3.8 (0.55, 1.44)	5.6 (0.90, 2.65)	4.5 (0.67,1.78)	5.1 (0.79,2.18)
10:1	0.40	0.8 (0.18, 0.63)	2.5 (0.26, 1.00)	4.8 (0.73, 1.96)	7.8 (1.68,>10)	5.6 (0.90,2.65)	5.8 (0.95,2.88)

2.5 Chapter summary

We have presented the details by which we have constructed a suite of 9 idealized two-body X-ray cluster mergers which incorporate the effects of radiative cooling, star formation and associated SNe feedback. Our approach confidently ensures that we have initialized our systems to accurately reflect the observed structure of relaxed clusters with compact cool cores. We have used the results of published cosmological dark matter simulations to ensure that the orbits we construct for our systems cover the most interesting and plausible range of impact parameters and mass ratios.

We would like to reiterate that our simulations do not incorporate the physical processes associated with magnetic fields, pressure from cosmic rays or thermal conduction nor do we adequately model the effects of turbulence. The influence of these processes on clusters remain contentious issues and we can not make any confident predictions at this point regarding their effects on our results.

In the following chapter we shall use these simulations to examine the morphological and dynamical evolution of X-ray cluster mergers.

Chapter 3

Dynamical evolution and emergent transient structures

Abstract

We find that all mergers evolve via a common progression. We illustrate this progression in the projected gas density, X-ray surface brightness, SZ, temperature, and gas entropy maps of our simulations. Several different classes of transient "cold front"-like features can arise over the course of a merger. Each class is distinguished by a distinct morphological signature and physical cause. We find that all of these classes are present in *Chandra* and XMM observations of merging systems and propose a naming scheme for them: "comet-like" tails, bridges, plumes, streams and edges. In none of the cases considered do the initial cool compact cores of the primary and the secondary get destroyed during the course of the mergers. Instead, the two remnant cores eventually combine to form a new core that, depending on the final mass of the remnant, can have a greater cooling efficiency than either of its progenitors. We quantify the evolving morphology of our mergers using centroid variance, power ratios and offset between the X-ray and the projected mass maps. We find that the centroid variance best captures the dynamical state of the cluster. It also provides an excellent indicator of how far the system is from virial and hydrostatic equilibrium. Placing the system at $z = 0.1$, we find that all easily identified observable traces of the secondary disappear from a simulated 50 ks *Chandra* image following the second pericentric passage. The system, however, takes an additional ~ 2 Gyr to relax and virialize. Observationally, the only reliable indicator of a system in this state is the smoothness of its the X-ray surface brightness isophotes, not temperature fluctuations. Temperature fluctuations at the level of $\Delta T/T \sim 20\%$, can persist in the final systems well past the point of virialization, suggesting that that the existence of tem-

perature fluctuations, in and of themselves, do not necessarily indicate a disturbed or unrelaxed system.

In this chapter we present the general dynamical progression and eventual relaxation of an X-ray cluster merger and describe the transient phenomena which manifest in the process. Since many of the phenomena we study have low surface brightnesses, we utilize synthetic observations to delineate realistically observable phenomena from those which are not.

In Section 3.1 we qualitatively describe the evolution of our cluster mergers through a generic sequence of states and introduce the transient structures formed in the process. In Section 3.2 we examine the evolution of several measures of our mergers' apparent degree of disruption to determine when our systems would appear undisturbed under reasonable observational circumstances. In Section 3.3 we assess the degree to which our apparently relaxed merger remnants are formally so. In Section 3.4 we examine in further detail the different transient structures which form during a merger, describing their properties and the processes which drive their creation. Finally we summarize the chapter in Section 3.5.

3.1 Qualitative evolution

In what follows we present a qualitative account of common elements in the dynamical evolution of typical cluster mergers. A series of stages which mergers generically progress through will be identified and the evolution of the system's physical and observable properties described. In the process, several classes of transient structures will be introduced. This discussion is kept brief and is intended to provide a context for the discussion of the observability of substructure and relaxation which follows

in Sections 3.2 and 3.3[‡]. For those seeking a more detailed description, a specific discussion of each class of transient structure can be found afterwards in Section 3.4. All quoted times are measured from t_o, the moment at which the secondary system traverses R_{200} of the primary.

3.1.1 Evolutionary stages

All of the simulations we have studied proceed through a similar evolutionary sequence involving five distinct stages: a pre-interaction phase, first core-core interaction, apocentric passage, secondary core accretion, and relaxation. Several important times during this progression which we shall refer to throughout our analysis are listed in Table 2.2.

Initially, our systems are constructed to possess small core radii ($r_c \sim 50\,\mathrm{kpc}$, measured from β-model fits), low central entropies ($S = 10\,\mathrm{keVcm}^2$ at 10 kpc) and strong central positive temperature gradients. The low-density outer atmosphere of each system becomes distorted during pre-interaction through tidal forces and compression, adiabatically raising the temperature of material between and producing a short-lived bridge in surface brightness joining them. As the cores continue to accelerate upon approach, a pair of shock fronts materialize and are driven towards each core, heating and compressing them briefly. The effects of this interaction reaches its maximum strength at $t_{closest} = 0.5 - 0.8\,\mathrm{Gyr}$ when the cores reach their closest approach. The system's temperature and luminosity increase sharply for $\sim 400\,\mathrm{Myr}$ at this point. Cooling of gas to a cold ($T < 2.5\times10^4\,\mathrm{K}$) state or to stars is subsequently quenched for $2 - 3\,\mathrm{Gyr}$ in most cases but is merely suppressed in the off-axis 10:1 interactions. Meanwhile, the primary system's projected central positive temperature gradient is strongly reduced and its core radius increased. A detailed analysis of these

[‡]Readers are invited to peruse relevant digital movies detailing the evolution of various system properties over the course of the simulations at http://astro.phys.uvic.ca/~babul/Merger_PaperI

phenomena is presented in following Chapters of this thesis.

In every case (including the head-on collisions) some part of the secondary's cool core survives its first encounter with the primary core, forming a single clump and large cool stream of stripped material in off-axis cases and strings of one or more clumps in head-on cases.

At $t_{apo} = 1.2 - 2.5\,\mathrm{Gyr}$ the disturbed secondary core reaches a maximum separation of 1.2-1.7 Mpc from the primary core. The surviving portion then returns for another encounter with the primary, reaching a second pericenter at $t_{accrete}$= $2.2 - 4.8\,\mathrm{Gyr}$. In Table 2.2 we see that the time elapsed until either of these stages generally correlates with the mass ratio and impact parameter of the interaction, presumably due to the declining efficiency of dynamical friction. Second pericentric passage marks the beginning of an extended period of several Gyr during which material dispersed from the secondary core accumulates onto the core of the primary system. Although a small portion of the secondary core can survive the resulting disruption and experience tertiary encounters with the primary, there are no realistically observable traces of it following $t_{accrete}$ in any of the cases we have studied[5]. For this reason, our systems are considered to be evolving as a single merger remnant from $t_{accrete}$ onwards.

In a study of the orbital parameters of cluster substructure in a cosmological context (including gas but not cooling), Tormen et al. (2004) similarly find that the gaseous component of secondary systems becomes disrupted shortly after second pericentric passage. They also present simple analytic models for predicting the time and distance of first pericentric and apocentric passages. Our simulations compare well to their model predictions, supporting the consistency of our initial conditions with the orbital properties of substructure in cosmological simulations.

Following the accretion of the secondary core, the resulting remnant proceeds

[5]Higher impact parameters than probed by our simulations, although atypical, could result in longer lived distinct secondary cores.

through a period of relaxation. It appears undisturbed under reasonable observational circumstances in simulated *Chandra* observations by $t_{relax}= 4.4 - 7.8\,\mathrm{Gyr}$ but past this time, continues to evolve until the end of our simulations: recovery of the core's central temperature decrement is still proceeding (see Chapter 5for more details) as well as accretion of both dark matter and gas dispersed beyond the R_{200} radius during the merger. The system sustains a virialized state within R_{500} after t_{virial} and hydrostatic equilibrium at R_{500} after t_{hydro} (see Section 3.3).

Following $t_{closest}$, short-lived structures in the system's distribution of X-ray surface brightness, SZ signature, temperature and entropy arise. In Figs. 3.1 to 3.9 we present projected gas surface density/X-ray brightness, temperature/SZ and entropy maps of each of our simulations near several of the times discussed above. In what follows we shall use these figures to present the progression of these structures (both physical and observable) as they arise and dissolve.

Readers may find it useful to refer to movies of our simulations[‡] while reading the following subsections.

3.1.2 Evolution of head-on mergers

Our head-on mergers evolve in a distinctly different way from our off-axis mergers, with even their qualitative evolutions exhibiting strong dependences on the mass ratio of the systems. We thus isolate the account of their evolution from that of the off-axis cases.

Physical state

In our equal mass head-on merger, two near-planar shocks are produced shortly before $t_{closest}$ and are driven into and through each core (in good agreement with RS01). They subsequently exit the system as two symmetric hemispherical fronts. Due to the confining geometry of this situation, material initially in the cores of

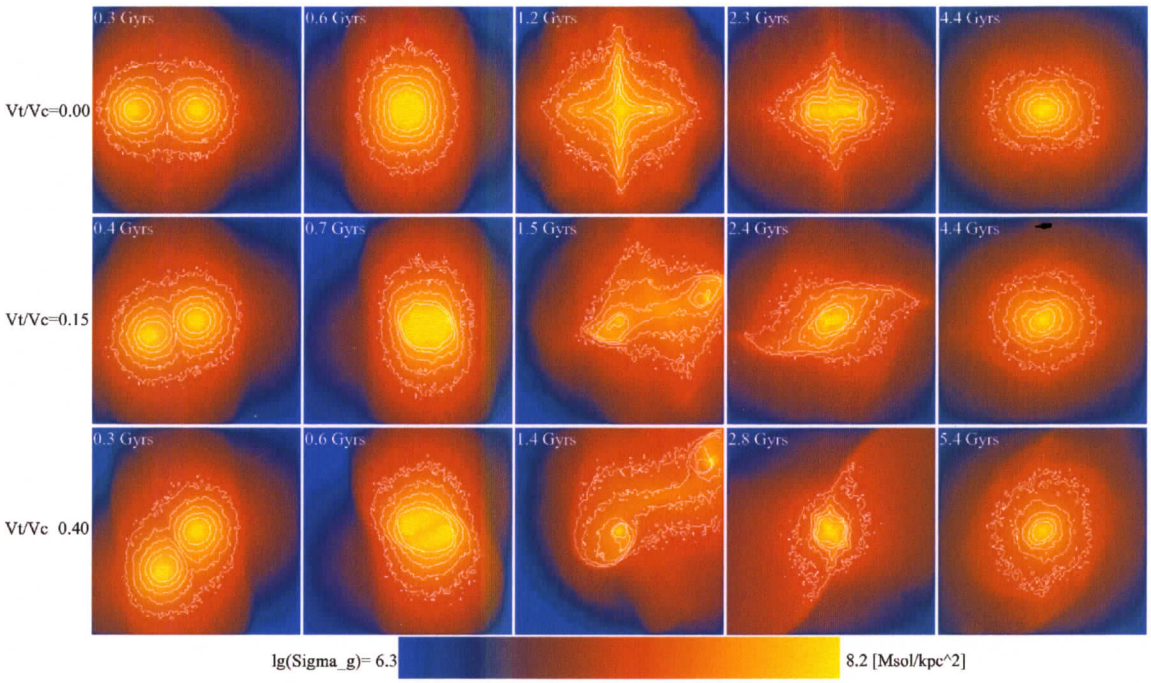

Figure 3.1: Maps of the gas surface density for our 1:1 simulations, projected along an axis normal to the plane of the orbit (3 Mpc on a side). White contours are X-ray surface brightness isophots from simulated 50 ks $z = 0.1$ *Chandra* observations ($3\times$ to $48\times$ the background stepping by factors of 2). Times depicted are $t_{closest}-200$ Myr (where $t_{closest}$is the time of first pericentric passage), $t_{closest}+100$ Myr, t_{apo}(where $t_{apo}$is the time of first apocentric passage), $t_{accrete}+100$ Myr (where $t_{accrete}$is the time of the second and usually the final pericentric passage) and t_{relax}, the time when system appears relaxed. All times are measured relative to t_o (the time when the secondary's centre of mass first crosses R_{200} of the primary)[†].

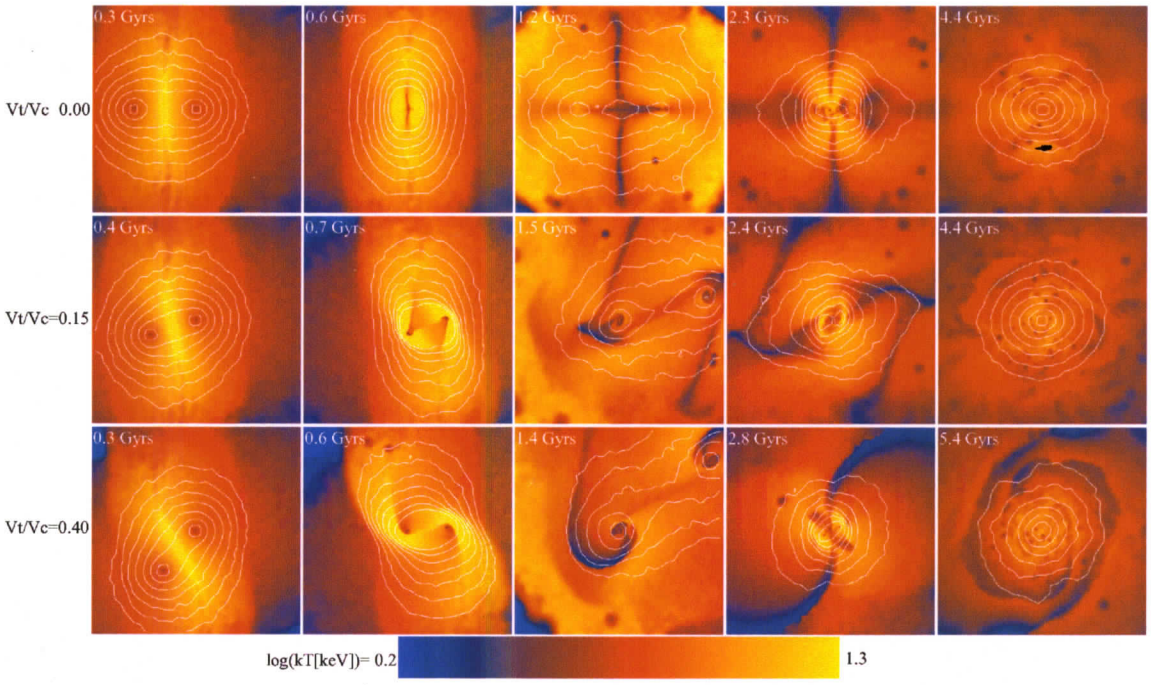

Figure 3.2: Maps of the projected "spectroscopic-like" temperature (Mazzotta et al., 2004) maps for a 0.5 Mpc thick slice (3 Mpc on a side) passing through the centre of our 1 : 1 simulations. Contours depict the SZ effect (for the entire simulation volume along the line of sight) and represent $log(y) = -5.5$ to -4 in increments of $0.25^{\dagger}$. The times represented are the same as Fig. 3.1.

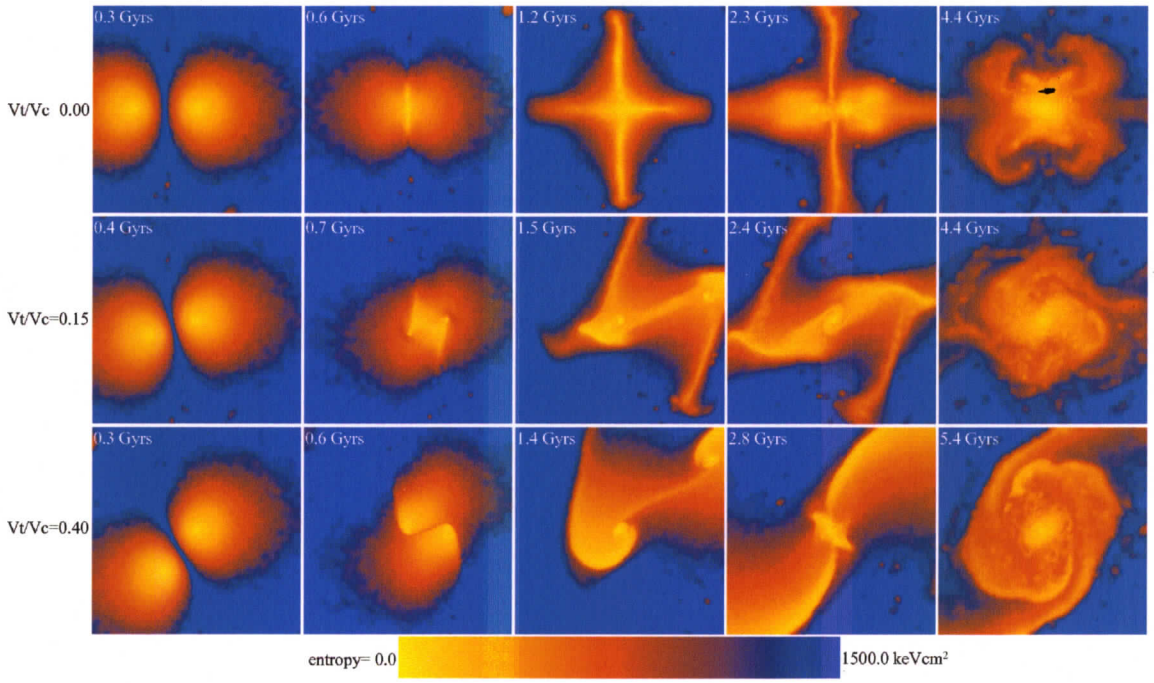

Figure 3.3: Entropy maps for a 0.5 Mpc thick slice (3 Mpc on a side) through the centres of our 1 : 1 simulations†. The times represented are the same as Fig. 3.1.

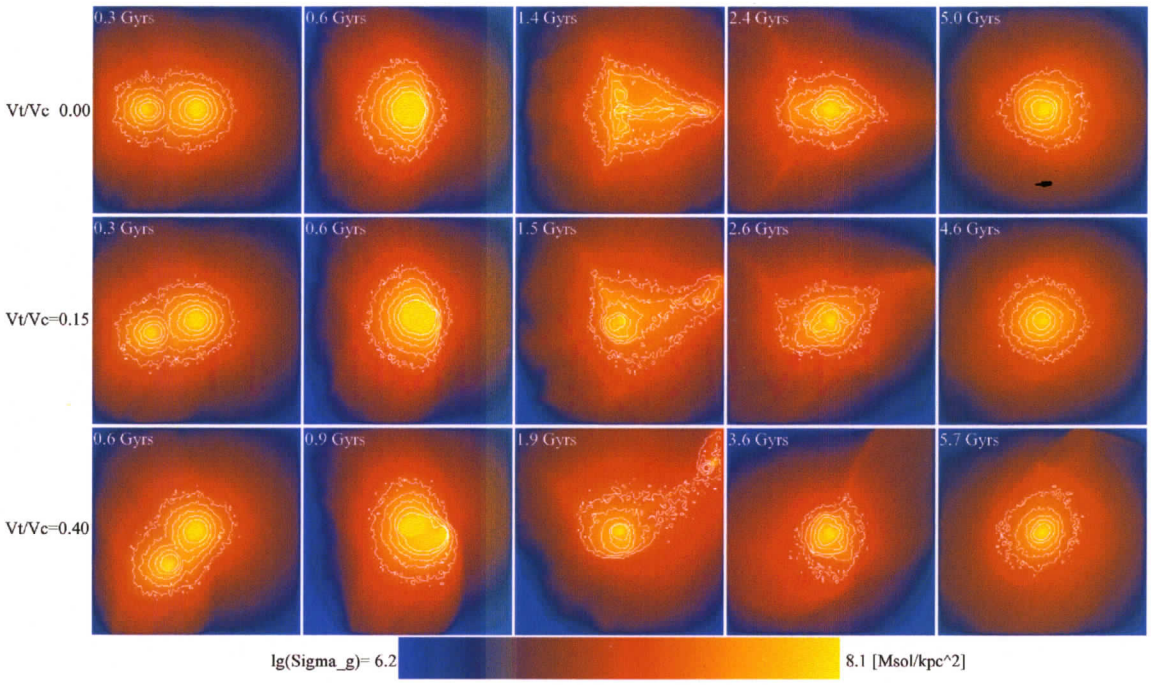

Figure 3.4: Maps of the gas surface density for our 3:1 simulations, projected along an axis normal to the plane of the orbit (3 Mpc on a side). White contours are X-ray surface brightness isophots from simulated 50 ks $z = 0.1$ *Chandra* observations (3× to 48× the background stepping by factors of 2). Times depicted are $t_{closest}$−200 Myr, $t_{closest}$+100 Myr, t_{apo}, $t_{accrete}$+100 Myr and t_{relax}. See Figure 1 caption or Table 2 for a brief definition of the timescales. All times are measured relative to the t_o when the secondary's centre of mass crosses the virial radius of the primary for the first time†.

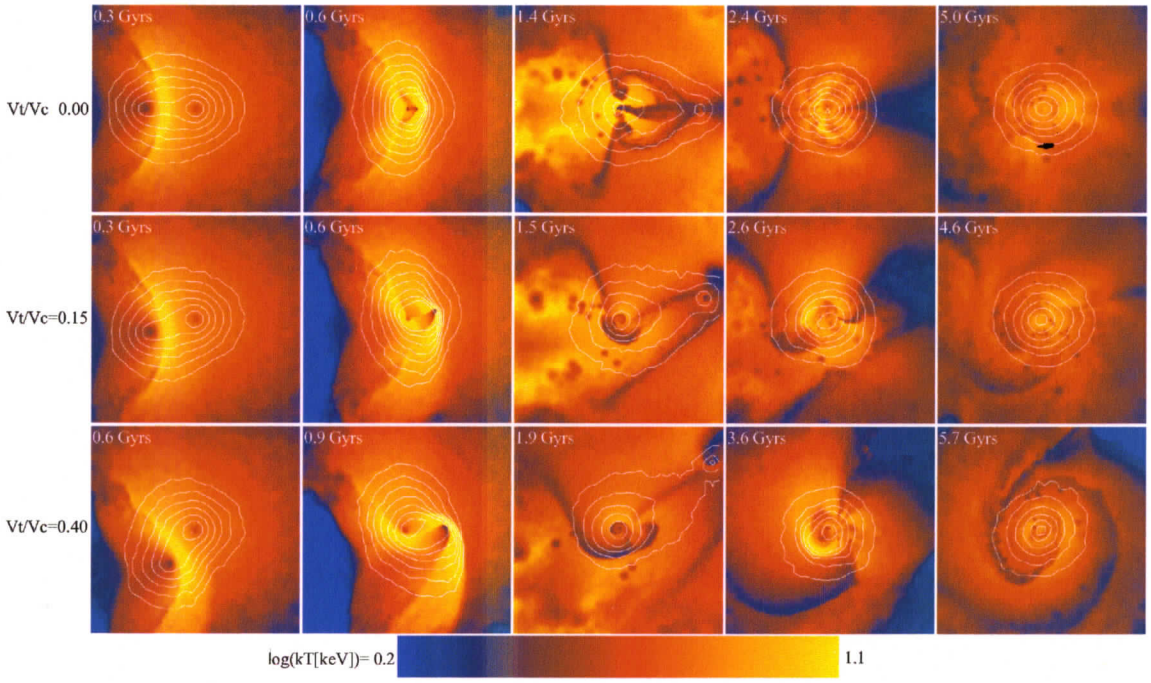

Figure 3.5: Maps of the projected "spectroscopic-like" temperature (Mazzotta et al., 2004) maps for a 0.5 Mpc thick slice (3 Mpc on a side) passing through the centre of our 3 : 1 simulations. Contours depict the SZ effect (for the entire simulation volume along the line of sight) and represent $log(y) = -5.5$ to -4 in increments of $0.25^{\dagger}$. The times represented are the same as Fig. 3.4.

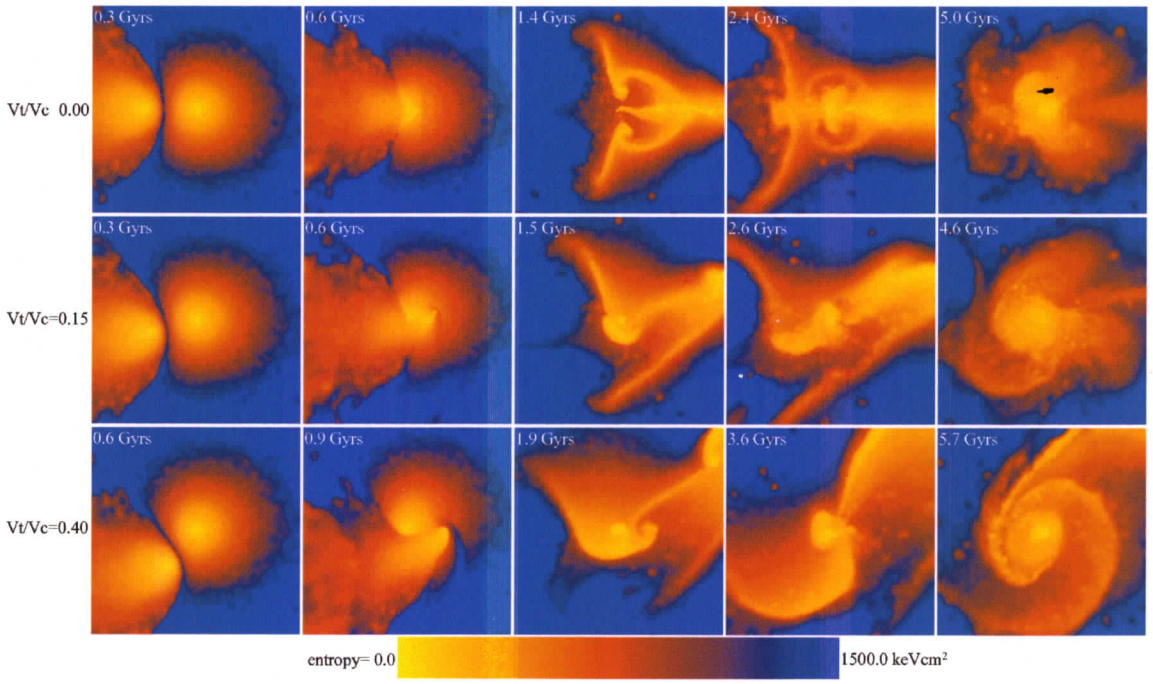

Figure 3.6: Entropy maps for a 0.5 Mpc thick slice (3 Mpc on a side) through the centres of our 3 : 1 simulations†. The times represented are the same as Fig. 3.4.

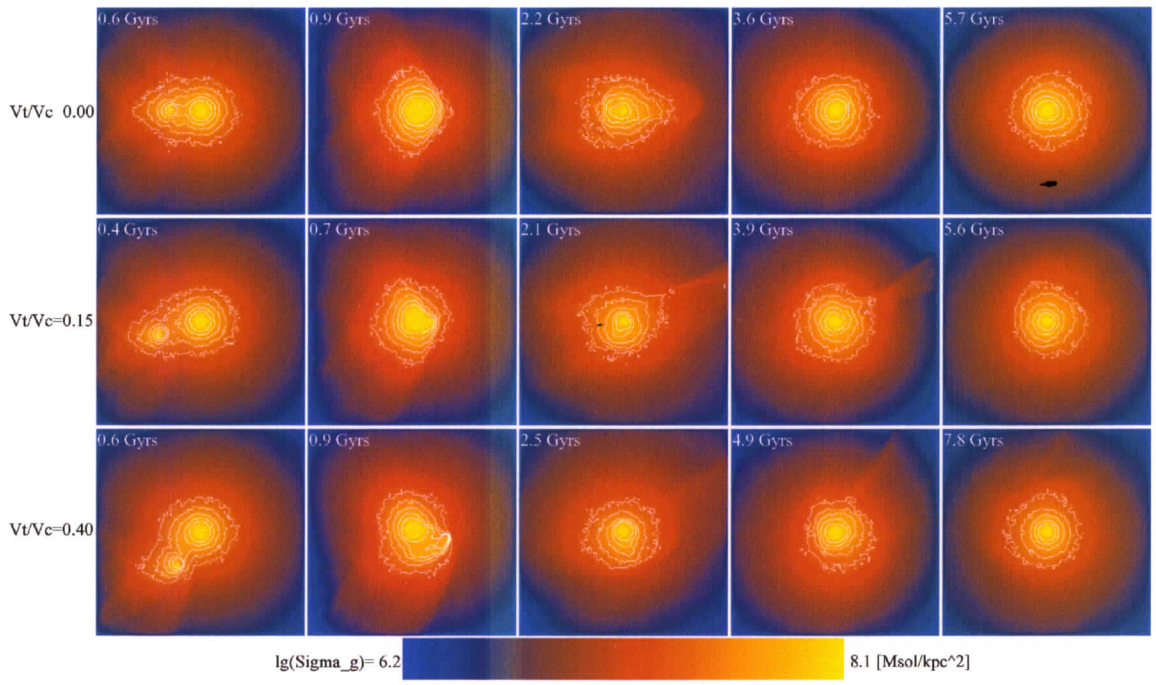

Figure 3.7: Maps of the gas surface density for our 10:1 simulations, projected along an axis normal to the plane of the orbit (3 Mpc on a side). White contours are X-ray surface brightness isophots from simulated 50 ks $z = 0.1$ *Chandra* observations (3× to 48× the background stepping by factors of 2). Times depicted are $t_{closest}$−200 Myr, $t_{closest}$+100 Myr, t_{apo}, $t_{accrete}$+100 Myr and t_{relax}. See Figure 1 caption or Table 2 for a brief definition of the timescales. All times are measured relative to the t_o when the secondary's centre of mass crosses the R_{200} radius of the primary for the first time†.

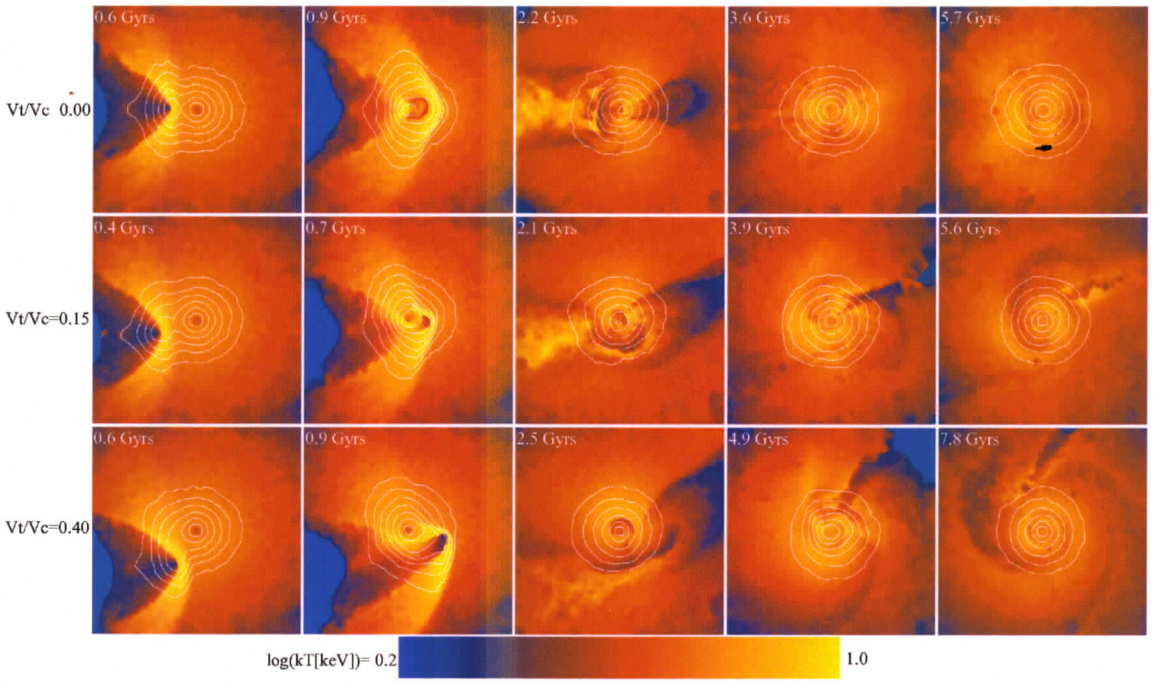

Figure 3.8: Maps of the projected "spectroscopic-like" temperature (Mazzotta et al., 2004) maps for a 0.5 Mpc thick slice (3 Mpc on a side) passing through the centre of our 10 : 1 simulations. Contours depict the SZ effect (for the entire simulation volume along the line of sight) and represent $log(y) = -5.5$ to -4 in increments of 0.25†. The times represented are the same as Fig. 3.7.

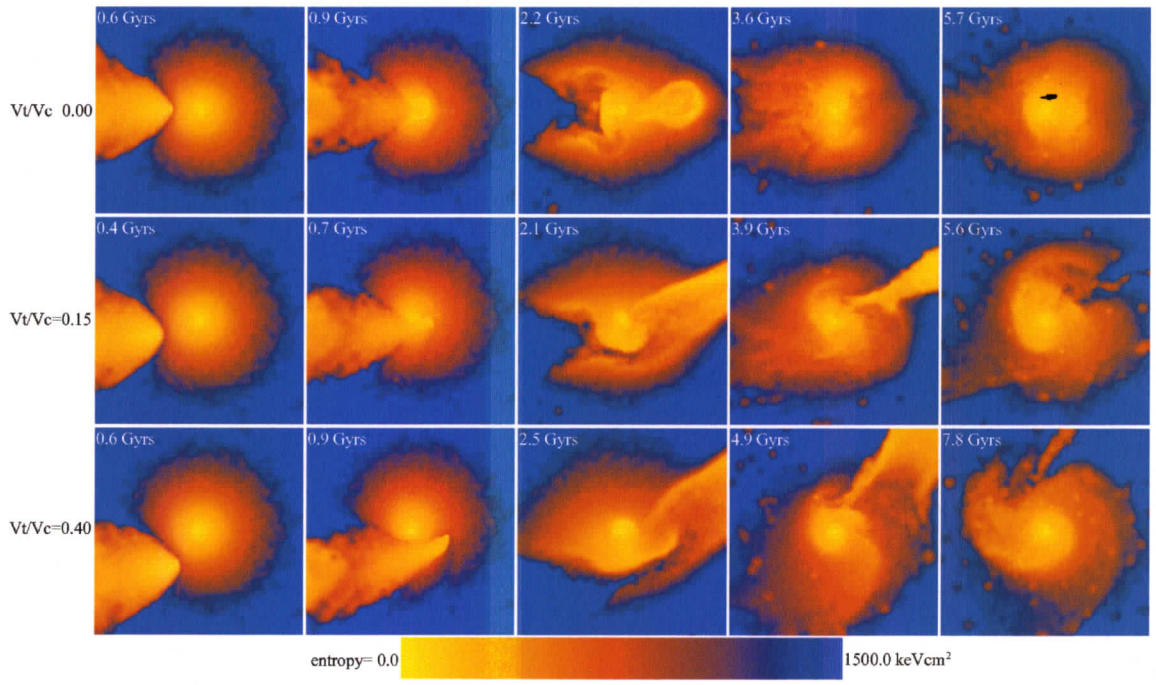

Figure 3.9: Entropy maps for a 0.5 Mpc thick slice (3 Mpc on a side) through the centres of our 10 : 1 simulations†. The times represented are the same as Fig. 3.7.

the merging systems remains in relatively high density structures during the impact. From $t_{closest}$ to approximately t_{apo}, much of this material occupies an expanding disk oriented normal to the axis of the merging systems' motion and a filament of dense clumps strung between the remnants of the two cores, both of which are clearly visible in Fig. 3.1. In Figs. 3.2 and 3.3 we see that this material is cold ($T \sim 1.0\,\mathrm{keV}$) and has low entropy ($S \sim 10\,\mathrm{keVcm}^2$). At approximately $t_{accrete}$ it reaccretes to the remnant core having radiated most of the thermal energy generated by the impact. As a result, the system's core returns to a state of cooling twice as efficient at converting the hot ICM into stars and condensed gas ($T < 2.5 \times 10^5\mathrm{K}$) as the primary prior to the merger. Although equal mass head-on mergers are predicted to be rare in CDM models of structure formation[6], this supports the findings of Motl *et. al.* (2004) who find that mergers can act as a means of constructing actively cooling cores. We will study this in more detail in Chapter 5.

Comparing Fig. 3.1 to Fig. 3.4 we can see that reducing the mass of the secondary to a third of the primary's dramatically changes even the qualitative behaviour of a head-on collision. Although two shocks are still produced, the one leading the secondary's motion is much more significant to the system's evolution. As Figs. 3.5 and 3.6 show, the bow-shaped geometry of this shock (again, in good agreement with RS01) displaces the material of the primary core forward and laterally. The result is a conical shell of cool ($T \sim 3\,\mathrm{keV}$) moderate-entropy ($S \sim 150\,\mathrm{keVcm}^2$) gas, entrained by the remainder of the secondary core at its apex. This structure surrounds a bubble of hot ($T \sim 10\,\mathrm{keV}$) high-entropy ($S \sim 550\,\mathrm{keVcm}^2$) gas. These figures also illustrate how the low pressure region created in the wake of the secondary's motion is quickly and convectively filled by this displaced material. Material displaced most laterally reaccretes first, flowing in through the back of the secondary's wake. Material initially

[6]However, they are not without observational precedence; RXCJ0532.9-3701 (Finoguenov et al., 2005) has boxy isophots and a cloverleaf morphology in entropy, much like our relaxing equal mass head-on merger

displaced more forwardly is dragged in behind afterwards. Upon returning to the core, this material experiences additional shocking, resulting for example in the high temperature ($T \sim 9.5\,\mathrm{keV}$) region seen to the left of the core shortly after $t_{accrete}$ in Fig. 3.5.

In the 10:1 case, the secondary core penetrates the primary core and deposits nearly all the kinetic energy of its gaseous component into the core of the primary. The result is a large ($\sim 500\,\mathrm{kpc}$) bubble with an expanding shell of cool ($T \sim 3.5\,\mathrm{keV}$) low-entropy ($S \sim 70\,\mathrm{keVcm}^2$) material filled with hot ($T \sim 7\,\mathrm{keV}$) moderate-entropy ($S \sim 180\,\mathrm{keVcm}^2$) gas. In Fig. 3.8 the initial formation of the bubble after $t_{closest}$ is illustrated. This bubble lasts for $\sim 1.5\,\mathrm{Gyr}$ and is carried forward to a radius of $\sim 750\,\mathrm{kpc}$ by the momentum of the collision. Its final extent can be seen in Figs. 3.8 and 3.9. Shortly before t_{apo} it stops moving and expanding, collapses into a low entropy stream and accretes back to the core by $t_{accrete}$.

Observable state

Following the procedure detailed in Section 2.4 we have produced simulated *Chandra* observations and overlaid their contours onto the projected gas surface density maps presented in Figs. 3.1, 3.4 and 3.7. This allows us to determine which distributed features have sufficiently high surface brightnesses to be detected under reasonable observational circumstances. We have also generated SZ maps and overlaid their contours on the temperature maps presented in Figs. 3.2, 3.5 and 3.8. Since these maps do not include the effects of instrumentation, we cannot comment in detail on the detectability of low surface brightness features through SZ observations. We place our faintest contours at a level of $\log y = -5.5$ ($\delta T = -17\mu K$ at 30GHz, McCarthy et al., 2003) to approximate the depth to which the next generation of SZ imaging instruments will reach (*e.g.* $-10\mu K$ for SZA at 30GHz, Knox et al., 2004). The resulting SZ limit is a good match to the system extent realistically observable

by *Chandra*.

In the 1:1 case, we can see in Figs. 3.1 and 3.2 that both the expanding disk and filament of disturbed core material created in the impact and discussed above are reasonably observable through X-ray observations. Comparing these figures we can see that the remnant's X-ray isophotes are extremely boxy while the SZ contours are significantly more regular and much less elliptical (this is a trend that we observe in all of our simulations). Complicated temperature and entropy variations are seen throughout the duration of the merger, with small $\sim 100\,\mathrm{kpc}$ scale variations ($\Delta T/T \sim 15\%$) remaining at t_{relax}.

In the 3:1 head-on case, Figs. 3.4 and 3.5 illustrate that the extended features generated in this merger following $t_{closest}$ are similarly observable as in the 1:1 case. However, we can see that at $t_{accrete}$ there are large extended low surface brightness features that escape detection by *Chandra*. Complicated temperature and entropy variations, distinctly different from those observed in the 1:1 case, emerge after $t_{accrete}$ and persist until the end of the simulation. The temperature fluctuations present at t_{relax} are more significant ($\Delta T/T \sim 20\%$) and spatially irregular than in the 1:1 case.

Lastly, Figs. 3.7 and 3.8 illustrate the observability of extended structures formed in our 10:1 head-on merger. We can see from these that the large expanding bubble formed from the collision is not detectable when it reaches its largest extent at t_{apo}. Furthermore, the system looks quite regular in both X-ray and SZ at $t_{accrete}$, although small but significant irregularities in the central X-ray isophotes persist for $\sim 2\,\mathrm{Gyr}$ afterwards. Temperature and entropy fluctuations are present throughout the merger with the bubble formed from the core material dominating the temperature and entropy distributions after $t_{closest}$. Significant fluctuations in temperature ($\Delta T/T \sim 20\%$) are present at t_{relax}, with little change occurring between $t_{accrete}$ and t_{relax}.

3.1.3 Evolution of off-axis mergers

In all of the off-axis simulations we have studied, several distinct classes of transient structure are formed when the secondary (and sometimes primary) system's core becomes disturbed. Interestingly, the qualitative evolution of these structures is remarkably independent of impact parameter and mass ratio over the ranges we have studied. Furthermore, their properties are consistent with those of "cold fronts" observed in many *Chandra* and XMM observations (Markevitch et al., 2000). Cold fronts are contact discontinuities between regions of bright, dense, cold gas and faint, hot, rarefied gas. These regions are observed to be in near pressure equilibrium with the surrounding ICM and the jumps in temperature across their interface imply mildly sonic or sub-sonic velocities.

Several authors have studied simulations of merging clusters illustrating that the ram pressure disruption of cold low entropy cores during mergers can account for these features (Bialek et al., 2002; Heinz et al., 2003; Mathis et al., 2005). Once removed from the dark matter potential confining it, stripped gas lags behind its dark matter and galactic components, adiabatically expanding and cooling until it establishes pressure equilibrium within the resulting merger remnant.

Our simulations confirm these results. In what follows we will give a qualitative account of our off-axis mergers' evolution through a series of transient structures and discuss their observable properties. We shall find that there are many points when several classes of structure resembling cold fronts can be created. Additional details can be found in Section 3.4 where each of these classes will be studied in detail and new mechanisms involved in the production and evolution of cold fronts will be presented.

Physical state

In all of our 1:1 and 3:1 off-axis mergers, ram pressure stripping causes both the primary and secondary cores to develop "comet-like" head/tail morphologies in gas surface density, X-ray surface brightness, temperature and entropy during their first pericentric passage. In the 10:1 cases, this is true only for the secondary core. In all cases, this morphology starts $\sim 100\,\mathrm{Myr}$ before $t_{closest}$ and ends shortly before t_{apo} with a typical duration of $\sim 0.5\,\mathrm{Gyr}$.

Upon reaching apocentric passage, several extended structures in the system's distribution of temperature, entropy and gas density have evolved. In Figs. 3.1 and 3.4 we see that a bridge connecting the surviving portions of the primary and secondary cores has formed in the 1:1 and 3:1 cases (see Section 3.4.1). Several long and roughly radial outwardly moving plumes of cool ($T \sim 3\,\mathrm{keV}$) low-entropy ($S \sim 60\,\mathrm{keVcm}^2$) material have also formed (see Section 3.4.2). These features are not obvious in the system's gas density or surface brightness maps, but are evident in the temperature and entropy maps presented in Figs. 3.2, 3.3, 3.5 and 3.6. All of these structures are essentially absent in our off-axis 10:1 mergers.

Following t_{apo}, material displaced as plumes from the primary and secondary cores stops expanding away from the system and begins returning towards the remnant core. At $t_{accrete}$, the secondary core returns for its second (and last) pericentric passage of the system. After this, plume material begins accreting to the remnant core as collimated high velocity ($\sim 1000\ \mathrm{km\,s^{-1}}$) streams of material (see Section 3.4.4). At this point, evidence of a secondary core has been destroyed and these features are not associated with an apparent merging system. Stream material is generally shock heated as it accretes to the remnant core. These streams occur even in our 10:1 cases and are visible in the temperature and entropy maps presented in Figs. 3.2, 3.3, 3.5, 3.6, 3.8 and 3.9 as narrow and radially oriented cold low entropy structures following $t_{accrete}$. When they accrete directly to the remnant core, these streams lead to multiple

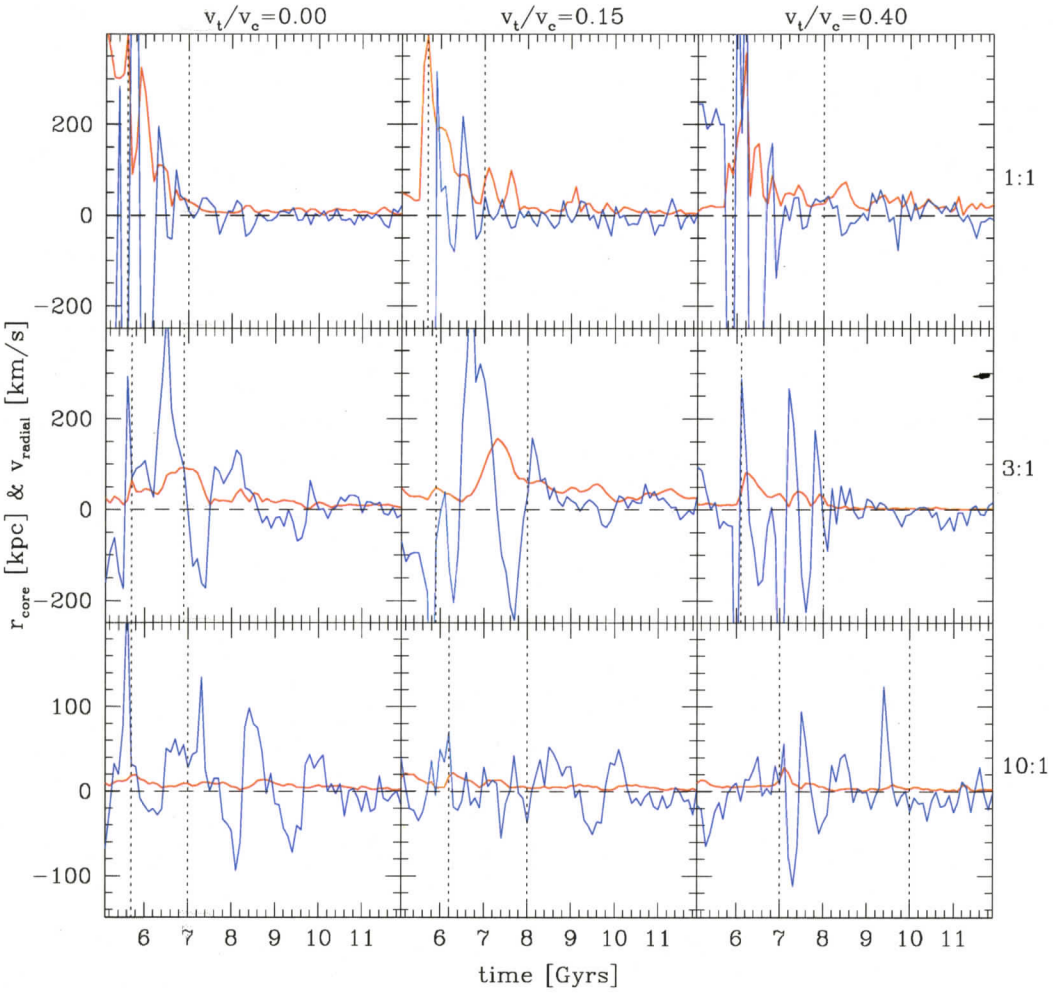

Figure 3.10: Displacement of the centre of mass of gas within the central 150 kpc from its dark matter centre of mass (smoother, lower-amplitude red curve) and the mass-averaged velocity of the same material in the direction of that displacement (the more erratic blue curve) for the late stages of each of our simulations. Vertical dashed lines correspond to $t_{accrete}$ and t_{relax}. The increased activity between these two timescales is primarily the result of the gas core being disturbed by the secondary's gas core during the second and typical the final pericentric passage, and by the ensuing cold stream. Values across the top indicate the transverse velocity at t_o depicted by each column while text on the right indicates the mass ratio depicted by each row.

discontinuities, or "edges" in the system's central surface brightness distribution (see Section 3.4.5).

Observable state

Elongated and curved disturbed cores have been observed in several systems (*e.g.* A85, A1758, and A2256) and are frequently attributed to the disruption of accreting systems due to ram pressure stripping. We observe this for only a short duration ($\lesssim 0.5\,\mathrm{Gyr}$) following $t_{closest}$ in all of our off-axis mergers. Prior to $t_{closest}$, this morphology does not manifest. At t_{apo}, longer lived elongated tails are created but the ejection mechanism is not ram pressure stripping (see Section 3.4.2).

In Fig. 3.1 we see that the bridge formed after $t_{closest}$ in our off-axis 1:1 mergers remains visible in our simulated *Chandra* observations until destroyed at $t_{accrete}$. The material forming this structure is not stripped from the central core but from the region just outside the initial cooling radius. Hence, it is of intermediate entropy ($300 - 500\,\mathrm{keVcm^2}$) and temperature ($\sim 6.5\,\mathrm{keV}$). No strong pressure gradients arise across it, as shown in the SZ maps in Fig. 3.2.

The bridges formed in our off-axis 3:1 mergers remain detectable for only 1.0 Gyr following $t_{closest}$, or roughly until t_{apo}. As in the 1:1 cases, the entropy of the bridge material is of intermediate entropy ($200 - 400\,\mathrm{keVcm^2}$) and temperature ($\sim 4.5\,\mathrm{keV}$) and exhibits no strong pressure gradients.

In Figs. 3.1 and 3.4 we also see that the plumes generated from the disturbance of the primary and secondary cores are observable in the 1:1 cases but only marginally so in the 3:1 cases. Figure 3.7 shows that in the 10:1 cases, although the system appears disturbed after $t_{closest}$, no extended features exist with sufficient surface brightness to be detected.

At $t_{accrete}$, very significant temperature fluctuations ($\Delta T/T \sim 20\%$) are present in all cases and persist until well after t_{relax}. Because the accreting streams retain

angular momentum from the merger and do not readily mix with the remnant, they produce spiral structures in the remnant's temperature and entropy distribution which are visible in our temperature and entropy maps at t_{relax}.

Because the SZ signature is proportional to gas density (ρ_g) rather than the ρ_g^2 dependence of the X-ray surface brightness, extended low density features tend to be washed-out in the SZ maps. Despite this, we can see that our SZ maps indicate that the bridges formed in the 1:1 and 3:1 mergers remain above our nominal SZ threshold. At t_{relax} , when accreting streams leave the X-ray surface brightness elongated in these cases, the SZ maps look significantly more regular with only the 1:1 $v_t/V_c = 0.15$ case looking comparably disturbed to its X-ray surface brightness.

3.1.4 Core oscillations

In several of the cases we have studied, we find that the central ($r \lesssim 0.5R_{500}$) ICM of our merger remnants oscillate with respect to their dark matter distributions. In the discussion of the evolution of disturbed morphology and relaxation which follows, there will be several instances when these oscillations will be relevant. Such oscillations have been discussed by several authors in attempts to account for "edges" observed in the central surface brightness of some clusters (see Section 3.4.5 for more details and references).

In Fig. 3.10 we present the displacement of the centre of mass of the densest central 150 kpc of our remnant gaseous cores relative to the centre of mass of the densest central 150 kpc of dark matter. To differentiate oscillating modes from the influence of substructure passing through the core in this calculation, we also present the mass averaged velocity of the gas in the direction of this displacement's vector. Displacement due to coherent oscillations will be accompanied by positive velocities until peak displacement when the velocity turns around and becomes negative, returning to zero when the displacement does. The displacement of the core due to the

arrival of substructure is revealed by increases in the displacement at times of small or negative radial velocity. There are several instances of significant core oscillations following $t_{accrete}$ stimulated by the second pericentric passage of the secondary core. They generally last until t_{relax}.

We have performed this calculation for material within 50 kpc as well. On these scales we observe no oscillations larger than the softening length (10 kpc) at times when oscillations are present on 150 kpc scales. Hence, gas in the central regions of our remnant cores (where cooling is most rapidly taking place) remains tightly coupled to the dark matter potential with the surrounding material constituting the oscillation seen on 150 kpc scales. It has been hypothesized that energy from bulk oscillations in the potential of the core due to displacements of the gas from the dark matter could act as a source of heating for compact cool cores (Markevitch, Vikhlinin, & Mazzotta, 2001). Our analysis suggests that although oscillations may occur on 150 kpc scales, the actively cooling gas on 50 kpc scales can remain strongly coupled to the dark matter. In such cases, oscillations in the potential may not be affecting cooling. Further study is required to determine if this is the case for oscillations stimulated through close encounters by secondary systems with mass ratios of only a few percent, such as those studied by Tittley & Henriksen (2005).

All of these calculations determine the motion of the gaseous core relative to the dark matter core. We have checked to see how the dark matter core is itself moving within its halo. For our 1:1 cases, we find that on both 150 and 50 kpc scales the dark matter cores remain stationary relative to the centre of mass of the system following $t_{accrete}$. However, the dark matter cores of our 3:1 and 10:1 mergers experience significant motions about the system's centre of mass until well after t_{relax}. The oscillations we observe between the gas and dark matter on 150 kpc scales are thus a result of the dark matter core orbiting the centre of mass of the system. As the gravitationally dominant dark matter core moves, the gaseous component is dragged behind it but with a lag due to the extra pressure it experiences. The result is an

oscillation between the two components as the dark matter core moves in its orbit. On 50 kpc scales, baryonic material dominates the potential of most of the gas and the dark matter can follow it since it is not subject to pressure. As a result, oscillations between the gas and dark matter do not occur on these scales.

Following $t_{accrete}$, the gaseous and dark matter cores of our 1:1 merger remnants rapidly become concentric by t_{relax}. A few displacements of the core position with respect to the dark matter are apparent but these are generally accompanied by negative radial velocities indicating that they are a product of the accretion of substructure onto the core.

The cores of our 3:1 merger remnants all experience bulk oscillations between their gaseous and dark matter components following $t_{accrete}$. In the head-on and $v_t/V_c = 0.15$ cases, the amplitude of these motions are 100 kpc and 150 kpc respectively with velocities reaching 400 $\mathrm{km\,s^{-1}}$. These motions last for ~ 1 Gyr and end immediately before t_{relax}. In the $v_t/V_c = 0.4$ case, a series of 4 core oscillations occur beginning at $t_{accrete}$ with amplitudes as large as 50 kpc and velocities of $175 - 250$ $\mathrm{km\,s^{-1}}$. They are of much shorter duration (~ 0.5 Gyr) and are finished by t_{relax}.

Some part of the dark matter cores of the secondary systems in our 10:1 mergers remain intact in near circular orbits within 50 kpc of the remnant's centre until the end of our simulations. This is not surprising since the sinking timescale due to dynamical friction is the longest. As a result, we measure small amplitude (< 20 kpc) oscillations in our 10:1 merger remnants. These motions are most coherent in the head-on case and involve bulk velocities of < 100 $\mathrm{km\,s^{-1}}$.

3.2 Evolution of disturbed morphology

With the general evolution of merging systems accounted for, we now discuss the timescales by which evidence of the merger event disappears. Determination of the degree to which a cluster is disturbed has generally taken three approaches in

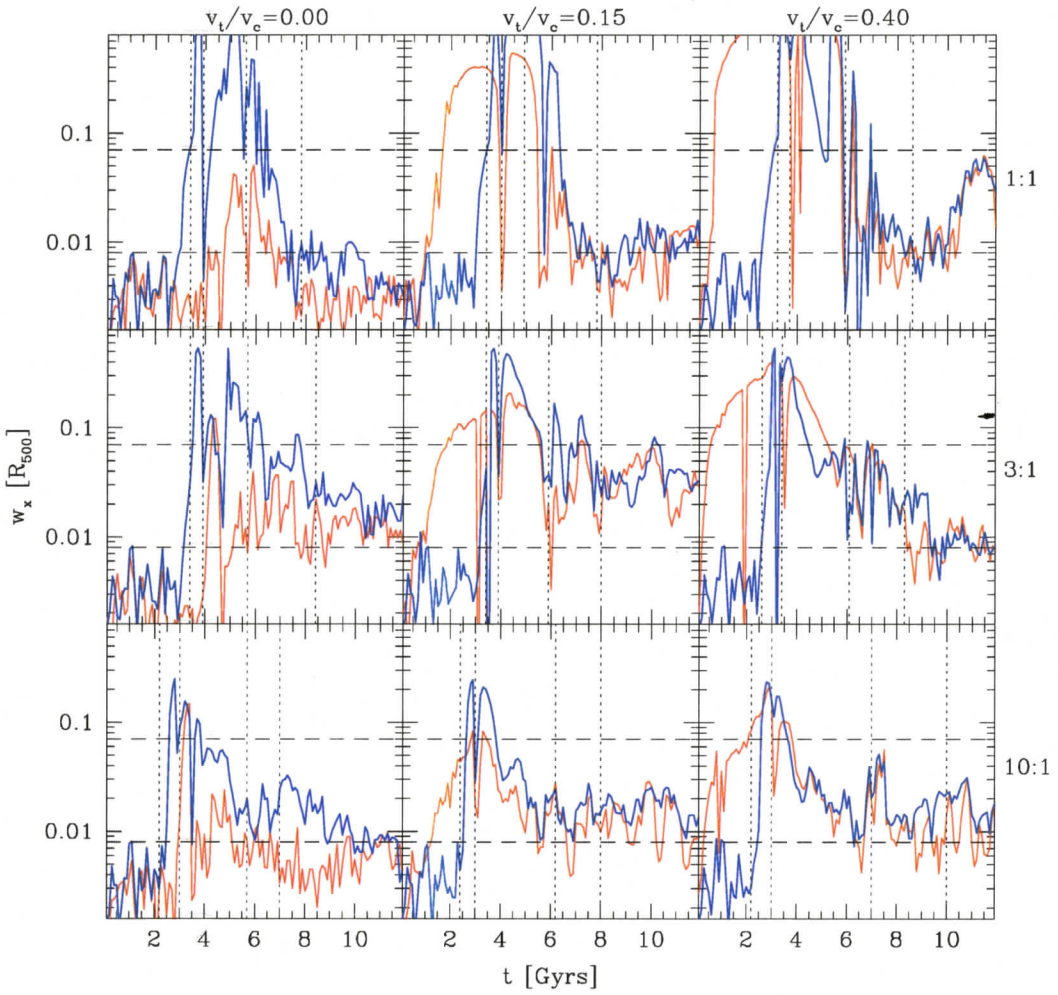

Figure 3.11: Evolution of the centroid variance computed from the X-ray surface brightness maps in the x (line of sight) and z (orthogonal) projections (thin red lines and thick blue lines respectively). Horizontal dashed lines indicate the range of centroid shifts observed by O'Hara et al. (2006) while vertical dotted lines indicate (from left to right) t_o, $t_{closest}$, $t_{accrete}$ and t_{relax}. Centroids are computed within 1.2 Mpc (roughly the initial R_{500} of the primary). The centroid statistic traces the qualitative evolution of the merging system very well. The statistic takes on its maximum values when the system is in its most disturbed state and typically, it falls off between $t_{accrete}$ and t_{relax} as the system recovers. Over the course of the merger, the statistic spans the entire range of values found by O'Hara et al. (2006) in an analysis of 45 clusters.

observational studies: visual inspection, measurement of displacements of the X-ray peak from the X-ray or mass centroid of the system, and power-ratio analyses of the system's X-ray surface brightness. In this section we shall apply each of these approaches in turn to establish when our simulated merger remnants would return to apparently undisturbed states. In the section which follows, we shall compare these timescales to more formal and physical measures of the system's dynamical state.

3.2.1 Simulated observations

In evaluating the effectiveness of quantitative measures of our remnants' dynamical state, we shall use as a fiducial the time when our systems appear relaxed under reasonable observational circumstances. We determine this time by visual judgement of our simulated *Chandra* observations and of the uniformity of their isophotes; a process we facilitate by generating unsharp masked images with smoothing kernel sizes of 1.5" and 15" (Chatzikos et al., 2006). This is all done in projections normal to the plane of the orbit. Substructure is likely most identifiable in this projection and thus, this measure represents a conservative upper limit on the time when the system would look disturbed. We have studied how our results change if evaluation is performed in x-projections and find that the systems tend to look undisturbed as much as 2 Gyr earlier.

Generally speaking, evidence of substructure disappears first from the simulated images, then from the unsharp masked images and finally in the structure of the X-ray isophotes. The delay between the dissolving of substructure in the images and the regularization of their isophotes can take several Gyr and varies significantly from case to case. Since the isophotes are the most sensitive measure, the system will be said to appear relaxed at t_{relax} when all isophotes brighter than $6\times$ the background level (*i.e.* all but the faintest in Fig. 3.1, 3.4 and 3.7) appear regular by visual inspection. These times are tabulated in Table 2.2.

In one case (1:1 head-on), minor complications arose during this procedure. Although the simulated observations appear regular and relaxed by $t \sim 3.8\,\mathrm{Gyr}$, their isophotes remain significantly boxy until $t \sim 4.4\,\mathrm{Gyr}$. Some evidence of this boxy morphology lingers until the end of the simulation making a clear determination of t_{relax} difficult.

3.2.2 Centroid shifts

The apparent displacement of a system's core from the centre of the system has been used as a measure of dynamical disequilibrium by several authors and has been implemented in several different ways. For instance, Mohr et al. (1993) quantify X-ray centroid shifts (w_x) using the offset of a system's X-ray surface brightness peak from its surface brightness centroid (integrated within a projected radius r_p). They argue that systems for which w_x is dependent on r_p are dynamically young. For a sample of 46 *Einstein* observed clusters, they obtain an average value $\langle w_x \rangle = 62\,\mathrm{kpc}$ with 71% of systems having $w_x > 0$ at a 3σ or greater significance. These results generally conform with more recent results of Kolokotronis et al. (2001) who find $\langle w_x \rangle = 83\,\mathrm{kpc}$ for a sample of 22 ROSAT observed systems.

We have chosen to quantify the centroid variance of our systems using the method employed by O'Hara et al. (2006). This approach determines the offset between the X-ray peak and centroid as a function of $r_p \lesssim R_{500}$ and assigns to w_x the RMS of the resulting profile. We determine this profile by computing the centroid within a circular aperture of size $r_p = R_{500}$ and then reducing its size by 5% until it reaches $r_p \leq 0.05 R_{500}$. We have experimented with various details of this procedure and find that it is essential to exclude the bright central core if the statistic is to detect subtle distortions. Hence, we excise the central $r_p = 30\,\mathrm{kpc}$ when computing centroids (but retain it when we compute the position of the peak).

In Fig. 3.11 we plot the time dependence of w_x measured in this way for each of

our simulations in x and z-projections. The evolution of this quantity in y-projections is very similar to its evolution in the z-projection and is omitted to clarify the plot. We also indicate the range of typical values observed by O'Hara et al. (2006) in their study of 45 ROSAT observed clusters ($w_x = 0.008R_{500}$ to $0.07R_{500}$, with 5 extreme points excluded) as well as the times of several important stages in each system's evolution.

As a product of our idealized initial conditions, all of our systems start with values of w_x less than the lower bound of the observations. In off-axis cases, it immediately begins to increase in x-projections as the cores slowly move apart in projection. This effect grows more significant with increasing v_t/V_c as we would expect. In z-projections, no increase occurs until $\sim t_o$ when the body of the secondary enters the $R_{500} \sim 1.2\,\mathrm{Mpc}$ aperture used for our calculations. In the off-axis cases, the statistic for the x and z-projections are virtually indistinguishable following $t_{closest}$. In the head-on cases, the signal is much lower when the merger proceeds along the line of sight. Typically, the statistic drops sharply when the primary and the secondary are close together, as in the line-of-sight/head-on case and more generally at $t_{closest}$ and $t_{accrete}$. This is due to the fact that the centroid shift in all the apertures is nearly the same. In detecting disturbances, the centroid variance method depends on the displacement varying as the aperture is reduced and successively more distant surface brightness fluctuations are excluded from consideration.

Our 1:1 mergers evolve to values of w_x much larger than those observed for a duration of $\sim 4\,\mathrm{Gyr}$. During this time, the system is a distinct binary and is not representative of any of the systems present in the O'Hara et al. (2006) catalogue. Following $t_{accrete}$, w_x declines rapidly and reaches a roughly constant level near the minimum observed value $\sim 1\,\mathrm{Gyr}$ before t_{relax}. In our $v_t/V_c = 0.4$ case, there is a subsequent rise at late times due to a late accretion of material. It is likely that the strength of this rise would not be as significant in a system hosting realistic substructure where the effect of late accreting material from multiple mergers would

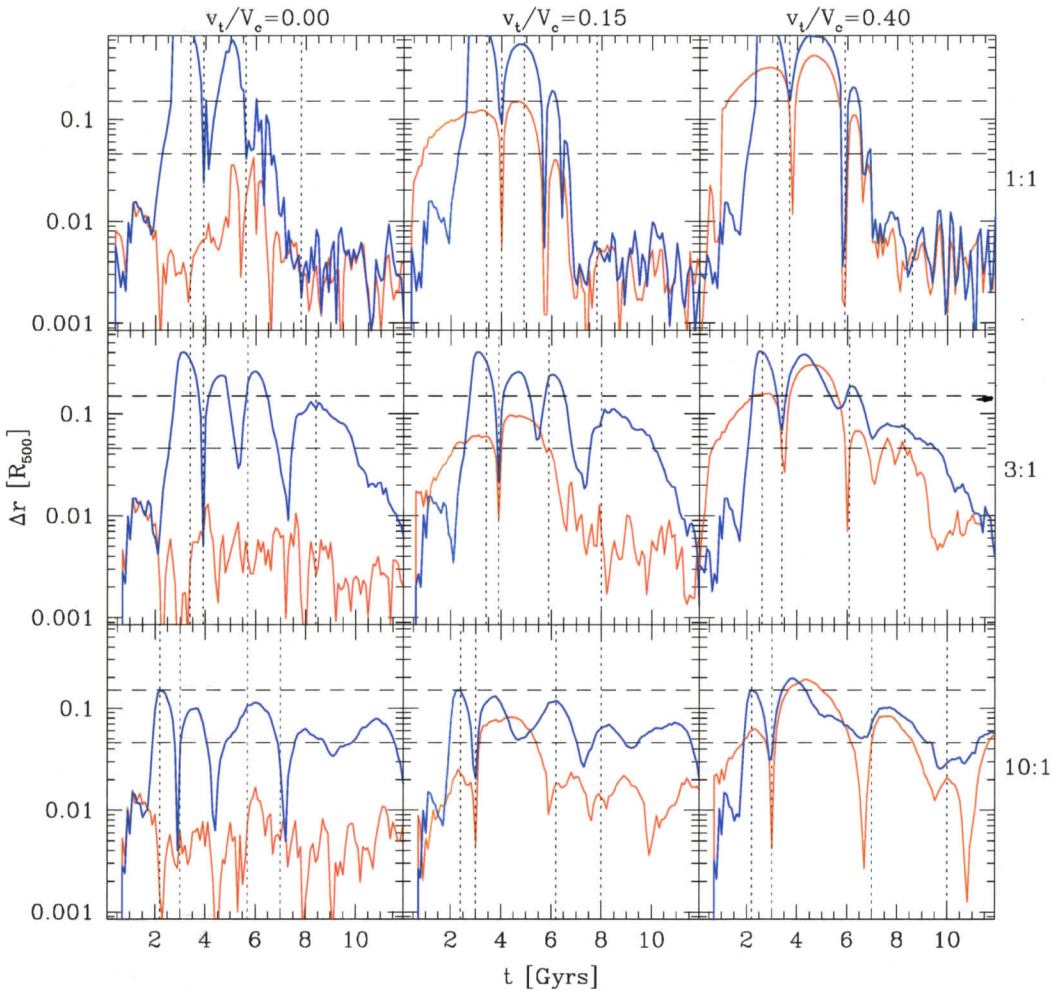

Figure 3.12: Time evolution of the displacement between the X-ray peak and the centroid of the projected mass maps in the x (line of sight) and z (orthogonal) projections (thin red lines and thick blue lines respectively). Horizontal dashed lines indicate the mean and maximum centroid shifts measured by Smith et al. (2005) (normalised by R_{500} of our system) while vertical dotted lines indicate (from left to right) t_o, $t_{closest}$, $t_{accrete}$ and t_{relax}. In the case of massive (1:1) mergers, the statistic behaves like w_x and tracks the morphological evolution of the system over the course of the merger. For moderate and minor mergers, the statistic remains high well past t_{relax} although the system is close to being virialized for $t > t_{relax}$. This signal is entirely due to low-mass remnant dark matter substructure that keeps jiggling the mass centroid.

tend to cancel their individual effects. For this reason, we will consider the system to have relaxed according to this measure $\sim 1\,\mathrm{Gyr}$ prior to t_{relax} in this case but acknowledge that more study is required to understand clearly the role long lasting substructure has on w_x in realistic environments.

In the 3:1 cases we see a similar rise after t_o to values greater than the maximum observed but lasting for a much shorter duration ($\sim 2\,\mathrm{Gyr}$). Following $t_{accrete}$, w_x oscillates erratically amongst the highest values observed by O'Hara et al. (2006). It slowly declines to the minimum observed value by the end of the simulations in the head-on and $v_t/V_c = 0.4$ cases but remains high in the $v_t/V_c = 0.15$ case. The cause of this slowed or absent decline in w_x following $t_{accrete}$ is a sustained shift of the centroid in the central $0.5R_{500}$. This is due to oscillations in the remnant's central dark matter distribution.

Lastly, our 10:1 cases are disturbed to high levels of w_x for $\sim 4\,\mathrm{Gyr}$ following t_o and for $\sim 1\,\mathrm{Gyr}$ following $t_{accrete}$ in the $v_t/V_c = 0.4$ case (due to the reduced disruption of the core). They oscillate just above the minimum observed value otherwise.

Thus, our systems appear exceptionally disturbed to our centroid variance measure for $\sim 4\,\mathrm{Gyr}$ between $t_{closest}$ and $t_{accrete}$ when they generally appear as two distinct clusters. Immediately following $t_{accrete}$ for our major/moderate (1:1 and 3:1) mergers and $\sim 2\,\mathrm{Gyr}$ after $t_{closest}$ for our 10:1 mergers (when the systems appear as single remnants), our simulations all exhibit values of w_x similar to the maximum observed by O'Hara et al. (2006) (with the natural exception of the head-on cases in x-projections). In 3:1 cases, w_x remains high until well past t_{relax}. Our equal mass and 10:1 mergers quickly relax to levels comparable to the minimum values observed by O'Hara et al. (2006). Referring to Table 2.2 we can see that for a cluster observed at $z = 0.1$, most 10:1 mergers occurring before $z \sim 0.5$ will have evolved past $t_{accrete}$ and will thus yield $w_x \sim 0.01R_{500}$. This fact combined with the expectation that most clusters should have experienced such an event naturally explains the observed minimum of this statistic.

We have also computed this statistic for SZ maps (w_{SZ}) of our systems. We find that the evolution of w_{SZ} is nearly identical to that of w_x, with both producing very similar maximum shifts and periods during which w_x is significantly higher than $0.1R_{500}$.

Another approach to measuring centroid shifts has been implemented by Smith et al. (2005) who measure the shift between the peak in the X-ray surface brightness and the centre of projected mass of the system (Δr), as determined from weak lensing maps. For a sample of 10 clusters, they find $\langle \Delta r \rangle = 55\,\mathrm{kpc}$ ($\sim 0.045R_{500}$ for our systems) with 70% of their systems having $\Delta r > 0$ at a 3σ or greater significance. In Fig. 3.12 we present the evolution of this statistic for our simulations. Again, we plot only x and z-projections due to the similarity of results in y and z-projections.

Examining Fig. 3.12 we see that for the 1:1 mergers, this statistic drops precipitously after $t_{accrete}$ (similarly to w_x) and sustains similar values after t_{relax}. For the 3:1 mergers however, there is a long lived late time shift in z-projections which does not reach maximum amplitude until t_{relax} and does not reduce to $\Delta r \sim 0.01R_{500}$ until shortly before the end of our simulations. A similar but even longer lived shift persists in our 10:1 mergers which fail to sustain $\Delta r \lesssim 0.01R_{500}$ for more than 0.5 Gyr in any projection for any case. These sustained shifts are due to central dark matter oscillations (see Section 3.1.4).

Given the relatively high frequency of 10:1 mergers and the long duration of their impact on Δr, we expect that few systems should exhibit $\Delta r < 0.045R_{500}$ (the mean value for our 10:1 $v_t/V_c = 0.15$ merger after t_{relax}) and therefore, it is surprising that Smith et al. (2005) find any systems consistent with $\Delta r = 0$. However, if projection effects are considered, it may be that some or all of the 3 systems to which they assign relaxed morphologies using this statistic are being seen with their X-ray peak merely in projection against their centre of mass. Alternatively, long lived substructure from multiple past minor mergers may compete against each other in their influence on the centre of mass, reducing its overall offset from the X-ray peak. Further study of this

statistic and its efficacy as an indicator of disturbed systems in a full cosmological context is clearly necessary.

3.2.3 Power ratio morphology

The use of surface brightness moment decomposition for quantifying the degree to which systems appear relaxed was first introduced by Buote & Tsai (1995) and has since been utilised in several observational (Buote & Tsai, 1996; Jeltema et al., 2005) and theoretical studies (Thomas et al., 1998; O'Hara et al., 2006). This method uses power ratios (P_m/P_0) computed from moments of the system's surface brightness distribution; $\Sigma(x)$, where $x' = (R, \phi)$ is in polar coordinates. Following the procedure of Jeltema et al. (2005, J05 hereafter), we have applied this procedure to our simulations computing power ratios from

$$P_0(R) = [a_o \ln(R)]^2 \tag{3.1}$$

$$P_m(R) = \frac{1}{2m^2 R^{2m}} \left(a_m^2 + b_m^2\right) \tag{3.2}$$

where a_m and b_m are moments of the distribution given by

$$a_m(R) = \int_{R' \leq R} \Sigma(x')(R')^m \cos m\phi' \, d^2x' \tag{3.3}$$

$$b_m(R) = \int_{R' \leq R} \Sigma(x')(R')^m \sin m\phi' \, d^2x' \tag{3.4}$$

These statistics are usually normalised by P_0 (*i.e.* expressed as P_m/P_0), a measure of the total luminosity of the system.

We have studied the effects of removing the central cores of our simulated clusters when computing these statistics. We find this to be particularly necessary when the

system is only subtly disturbed. At such times, the contribution of any persisting structure in $\Sigma(x)$ to Eqns. 4 and 5 becomes overwhelmed by the bright and centrally concentrated cores of the merging systems. When we exclude the central cores from our calculations of P_m we find a significant increase in amplitude and scatter. For the discussion which follows, we have computed power ratios with the central 30 kpc $\sim 0.025R_{500}$ excised. We have confirmed that there is little effect on our conclusions if this radius is reduced to 15 kpc or increased to 50 kpc.

In Fig. 3.13 we plot the time evolution of P_2/P_0, P_3/P_0 and P_4/P_0 in a 0.5 Mpc z-projected aperture for each of our mergers. Buote & Tsai (1995) find that model systems with power ratios identically equal to zero can be assigned significant values (a few times 10^{-7} for P_3/P_0 for instance) when realistic noise is added to simulated X-ray images. Based on their analysis of an observed sample of clusters, J05 found that median noise contributions resulted in values for P_2/P_0, P_3/P_0 and P_4/P_0 of 7.5×10^{-8}, 1.9×10^{-8}, and 9.4×10^{-9} respectively. We indicate these levels in the plot. The plot illustrates that in the absence of noise, the values of the power ratios for the mergers are typically well below the median noise levels, except when the systems are in their most disturbed state. In practise, the values assigned to a relatively relaxed-looking cluster will be highly dependent on the quality of the individual observation. In fact, the lowest values of P_N/P_0 quoted by J05 are a factor of $\sim$ 10 below the median noise levels. In what follows we shall loosely refer to the median noise levels reported by J05 as the "observable levels" of each statistic. We will treat these levels as a reasonable fiducial when determining the point at which our systems would be judged as undisturbed by this approach.

The evolution of P_3/P_0 and P_4/P_0 is very similar; the latter behaves more or less like a scaled version of the former. In the approach to the first pericentric passage at $t_{closest}$, both power ratios experience a brief sharp spike which exceeds observable levels in all cases, though just barely in the 3:1 and 10:1 mergers. This is followed by a climb to a plateau or a broad peak, during which time the signal remains at or

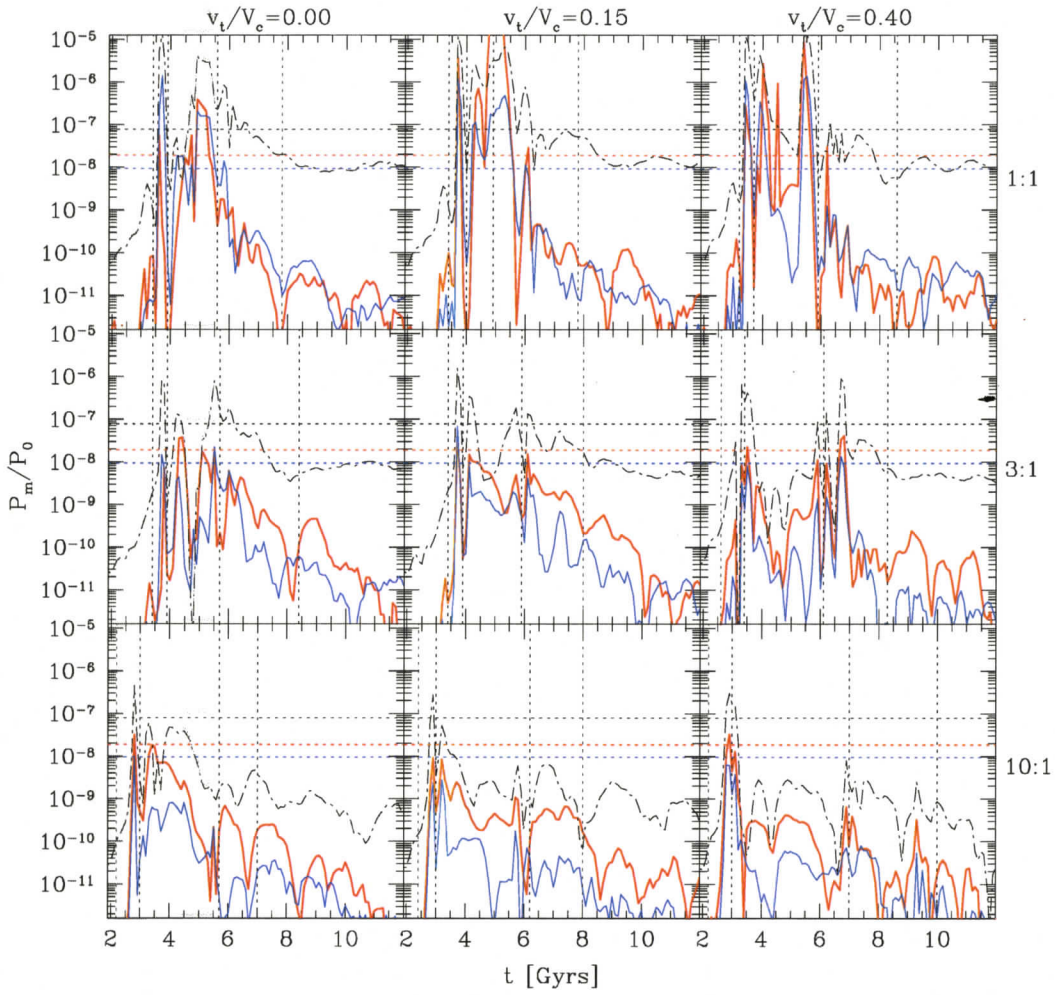

Figure 3.13: The time evolution of the X-ray surface brightness power ratios computed within a 0.5 Mpc aperture in the z-projection, the projection in which the merger-induced disturbances are the most apparent. Dotted horizontal lines depict the median noise levels for the observational sample analysed by Jeltema et al. (2005) for (in descending order) P_2/P_0, P_3/P_0 and P_4/P_0. Dash-dotted black, thick red and blue lines correspond to P_2/P_0, P_3/P_0 and P_4/P_0 respectively. Vertical dotted lines represent (from left to right) t_o, $t_{closest}$, $t_{accrete}$ and t_{relax}. The power ratios can easily pick out the very short-duration highly disturbed states but for the most part the amplitudes tend to be comparable to or less than the median noise levels for the J05 sample of clusters. See also Fig. 3.14.

below the observable levels except in the 1:1 case, and a fall-off at $\sim t_{accrete} \pm 1\,\mathrm{Gyr}$. The amplitudes of the initial spike and of the plateau/broad peak are correlated with the secondary's mass, with the most massive merger generating the greatest signal. There does not appear to be any clearly discernible correlations with impact parameter. Once the signal falls below observable levels after the second drop, it remains so for the duration of the simulation under all conditions.

The evolution of P_2/P_0 is different from that of P_3/P_0 and P_4/P_0. Like the latter two, the signal briefly spikes above the noise level at $t_{closest}$ but rapidly drops below. It exceeds the noise level again at $t_{accrete}$ for $\lesssim 2\,\mathrm{Gyr}$ and then generally only for the mergers with mass ratios greater than 3:1. (At 3:1, the second spike just exceeds the observable level). Afterwards, it stabilises at values far below observable levels, changing very little after t_{relax}. For the major/moderate (1:1 and 3:1) mergers, P_2/P_0 settles at $\sim 10^{-8}$ while our 10:1 mergers, the power ratio hovers at values of about $\sim 10^{-9}$.

In their study of the redshift evolution of power-ratios, J05 find that between $z = 0.5 - 0.9$ (their high-z sample) and $z < 0.5$ (their low-z sample), the P_3/P_0 and P_4/P_0 ratios show statistically significant declines while the P_2/P_0 ratio shows no significant change. Furthermore, observed values of P_2/P_0 are confined to a range more narrow than P_3/P_0 or P_4/P_0. Our simulations reproduce these trends but with a much lower normalisation. Further study is required to understand if this discrepancy is a product of noise effects or our idealized initial conditions and lack of cosmological substructure. Since P_2/P_0 is the power ratio most sensitive to the large scale ellipticity of the system, it would be interesting to determine if more realistic triaxial initial conditions would produce a similar narrow range of near constant final P_2/P_0 but with a higher normalisation comparable to that observed. As it stands, our results suggest that the power ratios are most sensitive to gross disturbances such as those that arise early in the merging process.

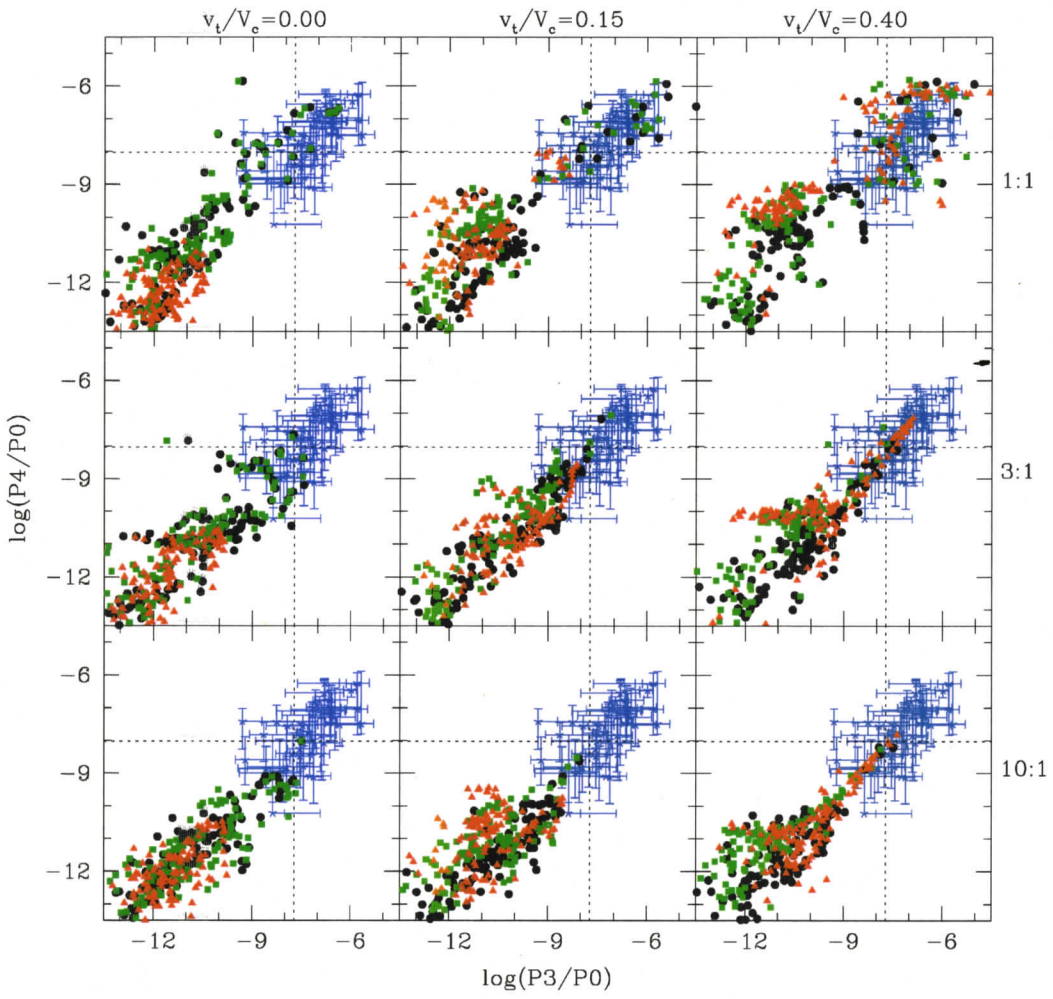

Figure 3.14: Plot of P_4/P_0 vs. P_3/P_0 for our simulations measured at different time snapshots over the course of the merger, within an aperture of 0.5 Mpc. The data of Jeltema et al. (2005) is plotted in blue with our simulations plotted as red triangles, green squares and black circles for x, y and z projections respectively. This combination of power ratios yields a signal above the median noise level of J05 sample (shown as horizontal and vertical lines) only when system is caught in the short-lived highly disturbed state. It is most sensitive to disturbances induced by highly off-axis mergers and least sensitive to line-of-sight mergers.

Correlations between different power ratios have generally been used to identify disturbed systems and to study the evolution of cluster substructure. Here, we focus our attention on the P_4/P_0-P_3/P_0 plane. In Fig. 3.14, we present a comparison in this plane between the observations of J05 and our simulations computed within apertures of 0.5 Mpc. Results computed in x, y and z-projections are presented with red triangles, green squares and black circles respectively. In Fig. 3.14, we can see that the observed trends in normalisation, maximum amplitude and scatter are well reproduced, though our measurements cluster at values of P_3/P_0 and P_4/P_0 well below the observations. These two power ratios return values above the observable levels only during the highly disturbed phases of the merger, and during the initial stages of the off-axis mergers.

We have also examined the distribution of points in the P_4/P_0-P_3/P_0 plane, where the power ratios are computed within a larger aperture of radius $R_{500} \sim 1.2$ Mpc. With the exception of some reduction in the scatter, the results are very similar to those presented in Fig. 3.14

Finally, we also applied the power ratio analysis to total projected mass and SZ maps to examine the efficacy of this approach to measuring substructure through weak lensing and microwave observations. The results were indistinguishable from the X-ray results, with amplitudes of the P_3/P_0 and P_4/P_0 for the projected mass maps being lower.

3.2.4 Comparison of disturbed morphology measures

We have examined several methods of determining the dynamical state of galaxy clusters. In Figs. 3.11, 3.12 and 3.13 we present the time evolution of w_x, Δr and P_m/P_0. In each case we indicate the moment when the isophotes of our simulated 50 ks $z = 0.1$ *Chandra* observations appear undisturbed as a fiducial reference for the sensitivity of each approach.

We find that while the centroid shift and power ratio approaches are both capable of identifying highly disturbed systems or systems with significant, well-defined substructures, the w_x is more sensitive to subtler disturbances and its time evolution tracks the visual appearance as well as the dynamical state of the merging system quite well. The amplitude of the power ratios is relatively low when the system is not highly perturbed (for example, the analysis barely registers 10:1 mergers) and appears to be highly susceptible to noise in the X-ray images. More study is required to understand in exactly what way realistic noise affects the sensitivity of the P_m/P_0 statistics.

Our experiments with the Δr statistic introduced by Smith et al. (2005) suggest that it is very sensitive to long lived substructures and oscillating modes in the dark matter haloes of merger remnants. The statistic yields a signal even when dynamically the system is within 2% of being relaxed as defined by our virial indicator (see Section 3.3 and Fig. 3.15). However, it is likely that our idealized mergers are exaggerating this sensitivity. More study with cosmological simulations which include a proper account of halo substructure should be conducted to determine exactly how effective Δr is relative to centroid shift and power ratio measures.

In summary, for clusters at $z = 0.1$, the eye is remarkably adept at identifying disturbed morphologies in deep *Chandra* images but quantitatively, we find that the centroid variance, w_x, is the most effective measure of a system's dynamical state.

3.3 Relaxation

Is a system which appears undisturbed actually in a relaxed state? This is commonly assumed to be the case in studies which have selected compact cool core systems with regular and symmetric isophotes to represent equilibrium systems. However, all clusters are a product of mergers and even though their dynamical timescales are short ($\sim 1.5\,\mathrm{Gyr}$ at R_{200}), the timescales by which bound substructures become dis-

rupted and dissolve into the accreting halo can be much longer, as illustrated in the preceding sections. As a result, a merger remnant can take significant lengths of time to reach a proper equilibrium state, perhaps even longer than the typical interval separating merger events.

In practical terms, the point at which a system appears undisturbed depends on the state of the system's baryonic component whose signatures of disturbance can be diluted by observational limitations. Furthermore, the gaseous component is subject to disruptive gas dynamical forces which do not act on the dynamically dominant dark matter component, perhaps erasing evidence of substructure faster than it loses dynamical relevance. Hence, it is natural to suspect a discrepancy between when a system appears relaxed and when it is formally so.

In this section we will quantify the relaxation of our merger remnants by studying their recovery towards a virialized and hydrostatic state of equilibrium. We shall compare the timescales by which they do this to the point at which the system would look relaxed under typical observational circumstances. We shall find that our systems typically achieve a virialized state approximately when they appear relaxed but continue to exhibit deviations from hydrostatic equilibrium at the level of $10-20\%$ until the end of our simulations.

3.3.1 Virialisation

To study the virialisation of our systems we employ the scalar virial theorem (see Collins, 1978; Spitzer, 1978; Binney & Tremaine, 1987, for good reviews) which states that

$$\frac{1}{2}\frac{d^2 I}{dt^2} = 2T + W + S \tag{3.5}$$

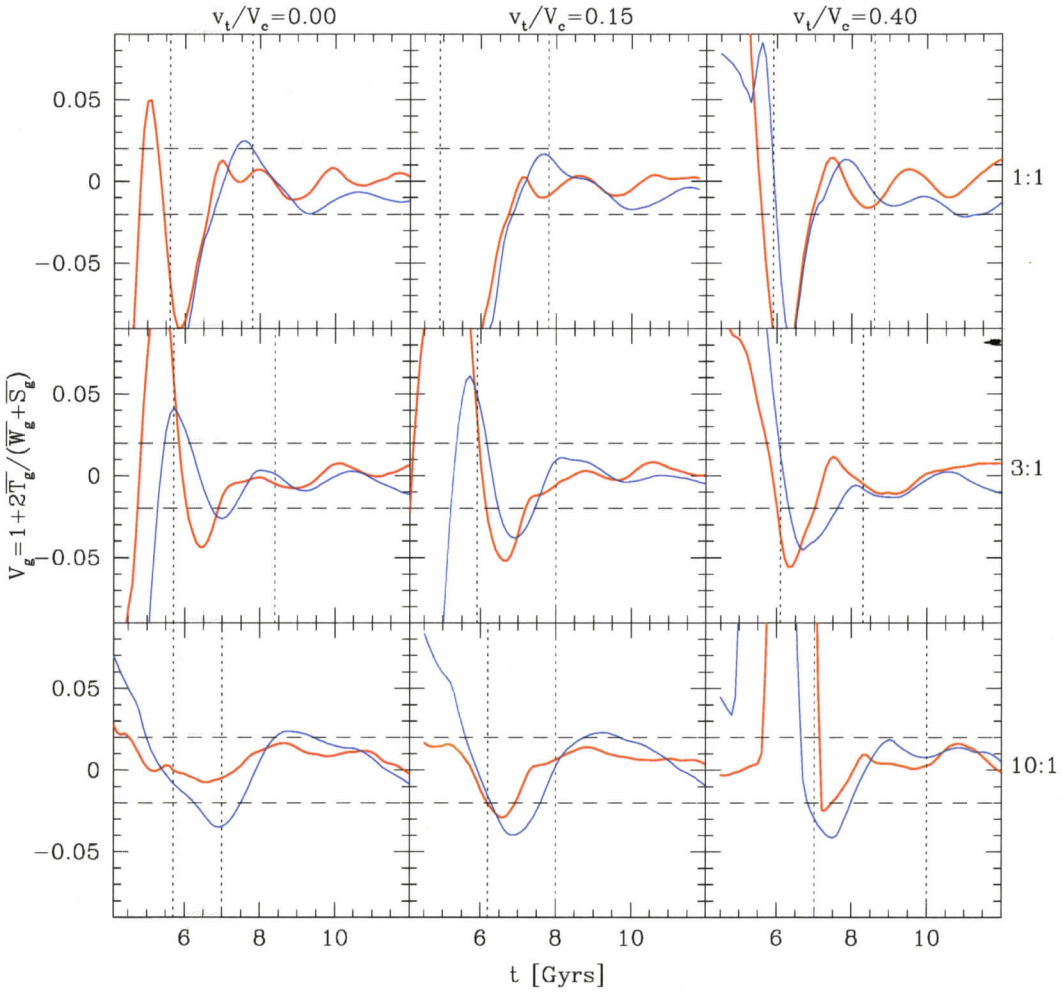

Figure 3.15: Time evolution of the virial parameter computed over a volume of radius R_{500} (thick red) and R_{200} (blue) for the gaseous component of our simulations. The evolution of the *gas* virial parameters for these two volumes is very similar. The horizontal dashed lines indicate our 2% virialisation criteria. The vertical dotted lines indicate $t_{accrete}$ and t_{relax} for each case. If we define the system to be relaxed when the virial parameter drops to and remains at $|V| < 0.02$, then the gas component typically relaxes halfway between $t_{accrete}$and t_{relax}.

where $T = K + U$ is the sum of the system's kinetic (K) and thermal (U) energies, $W = \sum_{i=1}^{N} \vec{F}_i \cdot \vec{r}_i$ is the 'virial', and I is the system's moment of inertia, all computed within a specified volume. The term denoted by $S = S_g + S_d$ is a surface pressure term integrated over the bounding surface of the volume, with contributions S_g and S_d due to the gaseous and collisionless (dark matter and stellar) components given by

$$S_g = -\oint Pr\, dA \tag{3.6}$$

$$S_d = -\oint \rho_d \sigma_d^2\, dA \tag{3.7}$$

where $P = nkT$ is the pressure of the gas with a number density n and temperature T and σ_d and ρ_d denote the velocity dispersion normal to the surface and mass density of the collisionless component.

Averaged over an interval in which the system is periodic (or instantaneously for a steady state system), the left side of Eqn. 3.5 vanishes. Furthermore, when integrated over the entirety of an isolated system, S becomes zero and Eqn. 3.5 takes its popular form

$$2T + W = 0. \tag{3.8}$$

It is commonly taken for granted that W represents the gravitational binding energy of the system but it must be emphasised that this is strictly true only when computed over the totality of an isolated system. In general, W is not equivalent to the gravitational binding energy within r.

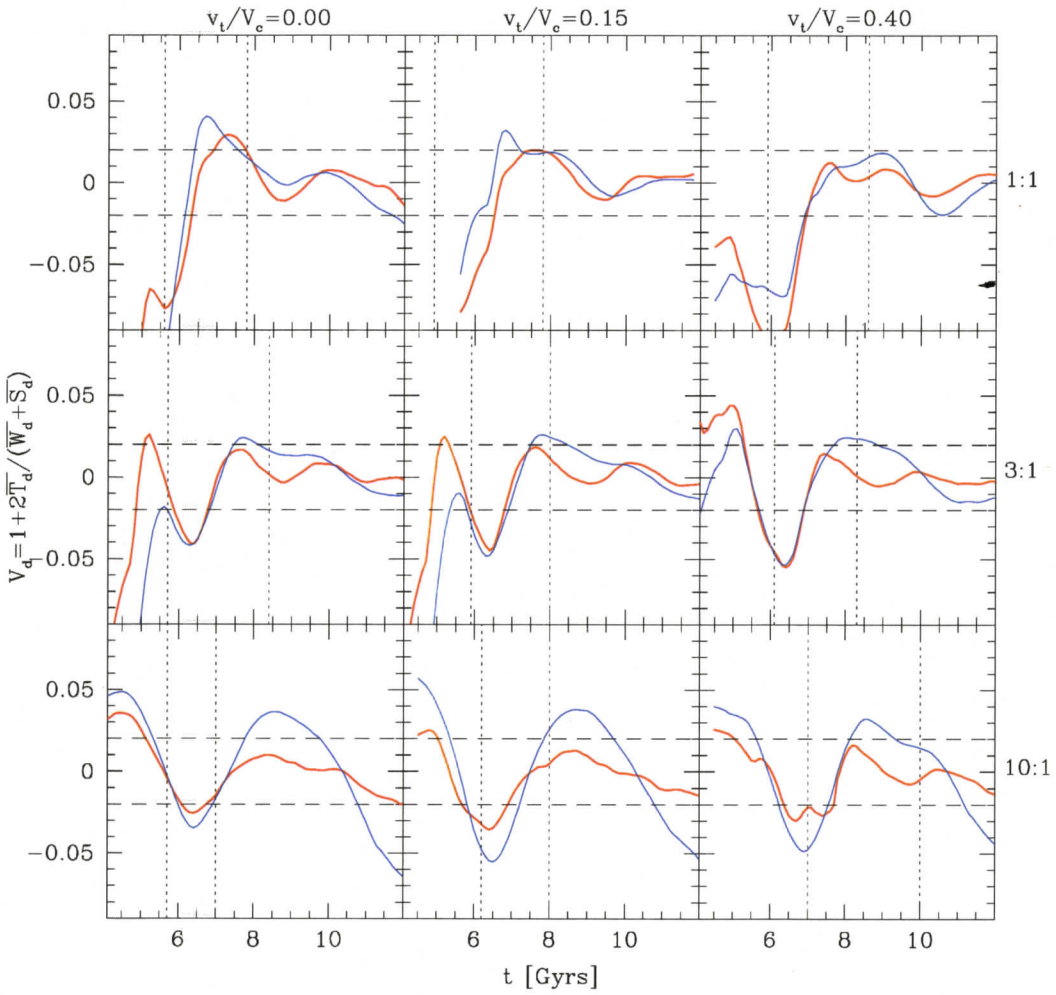

Figure 3.16: Same as Fig. 3.15 but depicting the virialisation of the dark matter component of our simulations. The dark matter component typically relaxes slightly later than the gas component and the oscillations in V damp out more slowly. Also, the central regions of the systems relax faster than the full cluster.

In Figs. 3.15 and 3.16 we present the temporal dependence of the virial disequilibrium parameter (Ricker, 1998) for the gaseous and dark matter components of our evolving merger remnants following $t_{accrete}$ (when the system can be considered to be a single remnant). (Although the baryonic component's contribution to the virial parameter of the total system is negligible, it is interesting to see if the observable gaseous component virialises on the same timescales as the dark matter component.) This virial parameter is defined as follows:

$$V = 1 + \frac{2\bar{T}}{\bar{W} + \bar{S}} \tag{3.9}$$

where $\bar{T}$, $\bar{W}$ and $\bar{S}$ are time averages computed to account for the fact that the canonical form of the virial theorem presented in Eqn. 3.8 holds only when the quantities in Eqn. 3.5 are averaged over an interval in which the system is periodic. This is done using a dynamical time $t_{dyn} = \sqrt{3\pi/16G\Delta\rho_c}$ (where Δ is the over density being considered) for quantities involving the collisionless component and the local isothermal sound crossing time $t_{sc} = r\sqrt{\mu m_p/kT}$ for quantities involving the gaseous component. Although the system may not be strictly periodic over these timescales, we have confirmed that the term involving I in Eqn. 3.5 contributes negligibly during the period we present in figures 3.15 and 3.16. Following RS01, we select the moment of virialisation to be when the system sustains a value of $|V| < 0.02$.

Overall, we find that the virial parameters for the gas and the dark matter track each other's general trends although the oscillations in the gas virial parameter tend to be of slightly lower amplitude and damp more quickly. As a result, the gas component typically relaxes (*i.e.* the gas virial parameter drops to and remains at $|V| < 0.02$) earlier than the dark matter component. There is not much difference in the relaxation time of gas within R_{500} and R_{200}. On the other hand, the dark matter distribution within R_{500} relaxes earlier than the full cluster.

In more detail, our 1:1 mergers all virialise by t_{relax}. The gaseous component generally virialises $\sim$ 0.5 Gyr before the dark matter component which virialises almost exactly at t_{relax} in all cases. Thus, the system is virialized approximately 4.5-5.5 Gyr (or 3-4 dynamical times) after the secondary initially crosses R_{200} of the primary (in good agreement the findings of previous studies, *e.g.* Roettiger et al., 1997). The virialisation of our 3:1 mergers proceeds similarly to our 1:1 mergers for the dark matter. In the 10:1 case, the gaseous component within R_{500} achieve virialisation at or well before our 1:1 and 3:1 mergers: immediately after $t_{accrete}$ in the off-axis cases and well before in the head-on case. Within R_{200}, however, our 10:1 gaseous components reach virialisation much later ($\sim$ 2 Gyr) than our 1:1 and 3:1 cases. The dark matter behaves similarly. Within R_{500} the system is virialized at or before t_{relax} while within R_{200}, the system never reaches our virialisation criteria. In these cases, the system sustains a state where V_d oscillates with an amplitude of $\sim$ 5% until the end of our simulations. The retarded onset or absence of virialisation within R_{200} for our 10:1 mergers is a result of late infall of material dispersed beyond R_{200} during the merger.

3.3.2 Hydrostatic equilibrium

Another independent measure of the equilibrium status of our merger remnants is the dynamical criterion of hydrostatic equilibrium. For a pressure supported medium in a gravitational potential, hydrostatic equilibrium implies

$$\rho^{-1}\frac{dP}{dr} = -\frac{GM(<r)}{r^2} \tag{3.10}$$

Given that X-ray derived mass determinations of clusters assume that this condition holds, its validity following mergers is of significant importance. Recent studies

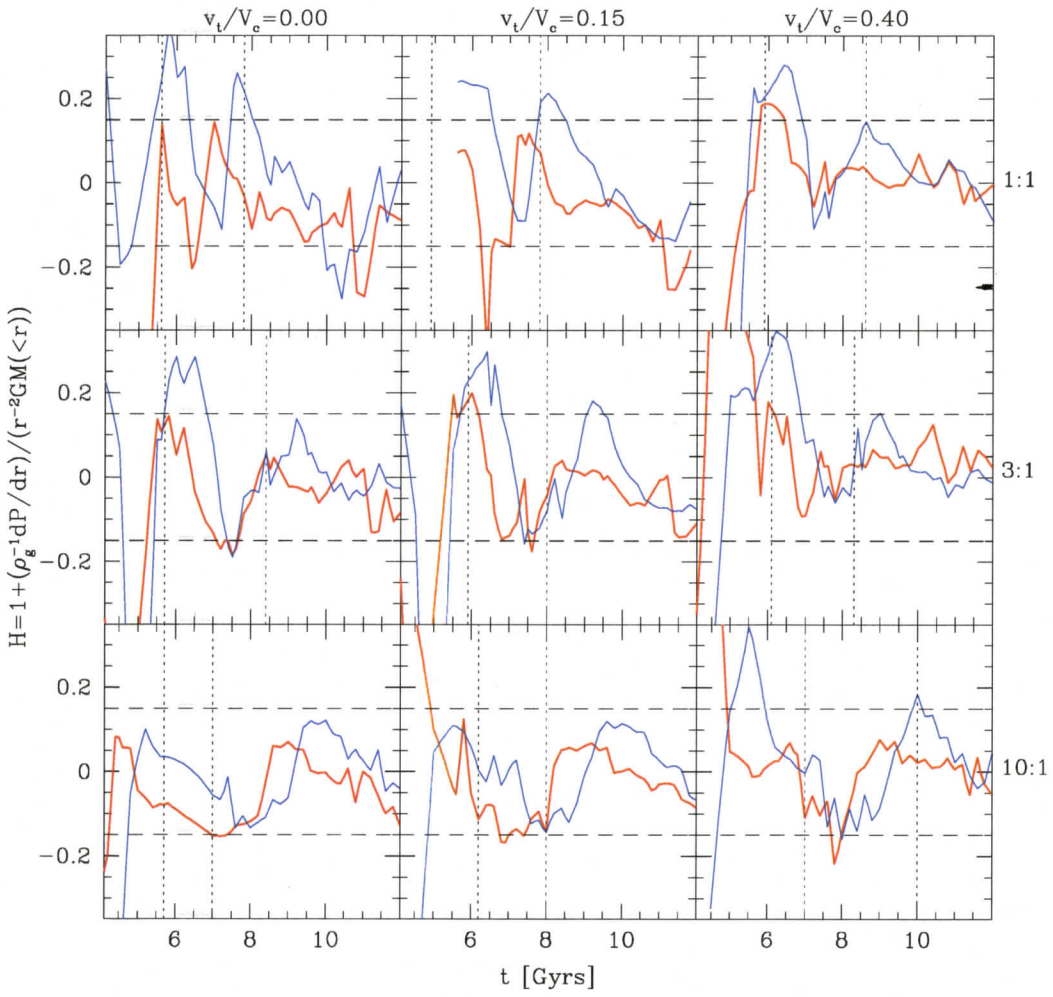

Figure 3.17: Hydrostatic disequilibrium parameter measured at R_{500} (thick red) and R_{200} (blue). The horizontal dashed lines indicate 15% equilibrium (the criteria used for t_{hydro} in Table 2.2). The vertical dotted lines indicate $t_{accrete}$ and t_{relax} for each case.

have found evidence suggesting that clusters for which hydrostatic equilibrium can be accurately assumed are rare but no consideration has yet been given to whether systems can fail to be in hydrostatic equilibrium while appearing undisturbed. In Fig. 3.17 we plot the evolving hydrostatic disequilibrium parameter of our merger remnants following $t_{accrete}$ given by

$$H = 1 + \frac{\rho^{-1}\frac{dP}{dr}}{r^{-2}GM(<r)} \tag{3.11}$$

The evolution of hydrostatic disequilibrium for our systems all follow the same qualitative pattern. Shortly before $t_{accrete}$, at both R_{500} and R_{200}, they experience significant positive excursions in H as the secondary core accretes to the remnant core. Following this, H is seen to oscillate with damped amplitude in each case with the oscillations at R_{200} lagging in phase behind those at R_{500} by $\sim 0.5\,\mathrm{Gyr}$. The phase of these oscillations is generally such that at R_{200}, a period of positive H lasting $\sim 2\,\mathrm{Gyr}$ with an amplitude of $10-20\%$, occurs at or shortly after $t_{accrete}$. At R_{500}, slightly lower amplitude (typically $\sim 10-20\%$) and less coherent oscillations persist until the end of our simulations.

Regular disruptions of hydrostatic equilibrium such as those depicted in Fig. 3.17 could translate into discrepancies in X-ray mass measurements obtained from methods which assume the validity of Eqn. 3.10. We shall examine this issue in more detail in Chapter 4 where we will discuss the effects of mergers on global cluster observables and scaling relations.

3.3.3 Comparison of apparent and formal states of relaxation

In Section 3.2 we found that our merger remnants generally appear relaxed through centroid (our preferred method) and power ratio measures once the isophotes

of our simulated $z = 0.1$ *Chandra* observations appear undisturbed at t_{relax}.

In Table 2.2 we list the times at which our systems are formally virialized (t_{virial}; measured for the dark matter) or in hydrostatic equilibrium (t_{hydro}; taken to be when the system sustains $|H| < 0.15$) at R_{500}. Our systems are generally virialized (both the gas and dark matter) within R_{500} at or near t_{relax} while late accretion of material renders the system somewhat less virialized (5% versus our 2% virialisation criterion) at R_{200} in our 10:1 mergers at t_{relax}. We also list the redshifts at which the secondary would have to cross R_{200} of the primary in order to be seen in each phase at redshifts of $z = 0.1$ and $z = 0.5$. We can see from this how unlikely virialised or hydrostatic clusters should be at $z = 0.5$.

We thus find that our merger remnants are generally virialized at or shortly ($\lesssim 2\,\mathrm{Gyr}$) after appearing relaxed to visual inspection. However, even at this time merger remnants are adiabatically oscillating, exchanging energy between thermal and kinetic components. They are in hydrostatic equilibrium only at the 10-20% level at this time and sustain this level of hydrostatic disequilibrium with little change after appearing relaxed.

3.4 Transient Structures

Our simulations reveal that the phenomena generally referred to as "cold fronts" consist of several classes of transient structure formed by the disruption of compact cool cores in off-axis mergers. Previous theoretical studies of cold-front production have focused primarily on the disruption of the secondary's core but our analysis reveals that both cores can be involved. Several other transient phenomena such as core surface brightness discontinuities and oscillations are naturally formed in the process as well. In this section we shall discuss in more detail the processes driving the formation of these structures, noting where possible the occurrence of each in presently published observations of cluster mergers.

3.4.1 Bridges

At two points during a cluster merger, luminous bridges connecting the interacting systems can be formed. In the first, the outer atmospheres of the merging clusters become compressed on the incident side of the collision during preinteraction. The resulting increase in gas density and temperature between the systems leads to enhanced surface brightness between the two systems and the formation of a luminous bridge. This effect is short-lived ($\sim 0.5\,\mathrm{Gyr}$ in the 1:1 cases, less in others) but has been observed in several systems including A399/401 (Sakelliou & Ponman, 2004) and A1750 (Belsole et al., 2005).

As discussed in Section 3.1.3, material stripped by ram pressure from the interacting clusters becomes dispersed, forming comet-like tails which trail their surviving cores following $t_{closest}$. Due to the density gradients of the systems they are passing through and the scaling of ram pressure with the density of the flowing material, this process is more efficient on the side of each core incident to the collision. As a result, overlapping enhancements of stripped material form behind each core, producing a luminous bridge which joins the two systems.

Following $t_{closest}$, material from these regions moving in the plane of the orbit is driven together. It becomes particularly concentrated in a curved planar feature oriented normal to the plane of the orbit. As a result, the surface brightness of this bridge is most bright and concentrated in z-projections. In x-projections it is not discernible and in y-projections it is significantly wider and more diffuse. The cores of both clusters appear disturbed at these times, distinguishing this process from the one acting during preinteraction.

The dependence of the brightness and shape of the bridge could be used as a useful cue when interpreting the orientations of observed merging systems. In A1758 (David & Kempner, 2004) for instance we see an excellent example of a system apparently exhibiting a post-interaction bridge. The two merging systems in this case (A1758N

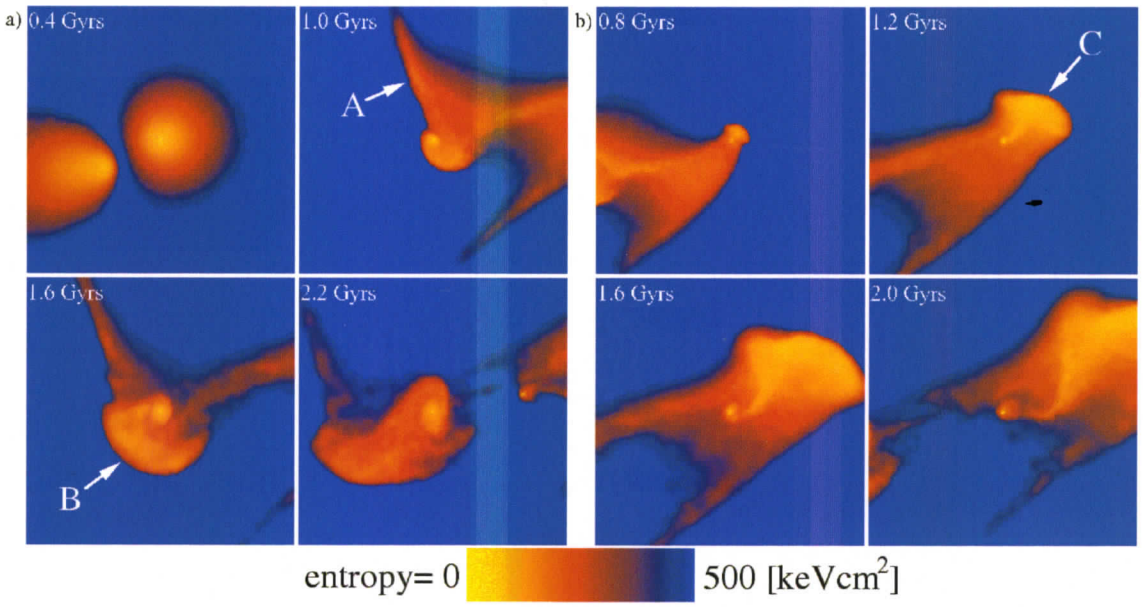

Figure 3.18: The left panel of four plots shows entropy maps for our 3:1 $v_t/V_c = 0.15$ simulation illustrating the ejection of two distinct "plumes" (labelled A and B) of low entropy material from the primary core in response to the pericentric passage of the secondary. The first is triggered by the shocks that precede the secondary, and the second by negative pressure gradients in the wake behind the secondary. The right panel of plots illustrates the ejection of a plume (labelled C) from the secondary at apocentre in the same simulation. The plumes eventually evolve into streams and most of the ejected low entropy material flows along the streams into the primary core. Each frame above is 1.5 Mpc on a side and is a z-projection of a 0.5 Mpc thick slice.

and A1758S) both have disturbed cores and there is an obvious bridge connecting them. The width of the bridge is more than 1.2 Mpc suggesting that the system may be significantly inclined to the plane of the sky. Other systems exhibiting similar morphologies include A1644 (Reiprich et al., 2004), A754 (Henry et al., 2004) and A115 (Gutierrez & Krawczynski, 2005).

3.4.2 Plumes

In Section 3.1.3 we noted that in all of the off-axis cases we have studied, outwardly propagating collimated plumes of primary and secondary core material are produced between $t_{closest}$ and t_{apo}. Several mechanisms are involved in the production of these structures, a few of which have been discussed previously in the literature. Mathis et al. (2005) provide a good summary of theoretical research involving the disruption of cold cores. Their work supports the claims of Heinz et al. (2003) who illustrate the important influence of ram pressure stripping during the disruption of merging cluster cores. However, they emphasise that other processes are likely essential to the formation of cold fronts.

Our study confirms and expands upon this claim. Although ram pressure is certainly important for the disruption of both clusters, it is primarily only responsible for the stripping of material roughly beyond $R_{2500} \sim 500$ kpc (moderately high entropy material). It does not lead to the prominent low entropy radial plumes produced in our simulations. In our simulated *Chandra* images, the period during which ram pressure stripped material is bright enough to produce an observable "comet-like" surface brightness feature is brief (~ 0.5 Gyr) and occurs only at or shortly after $t_{closest}$. A disturbed merging system spends most of its time at or near apocentric passage. In our simulations, material stripped by ram pressure has dispersed and is no longer apparent in surface brightness by that point. Bright features of displaced core material are produced primarily by other mechanisms during this longer lived

phase.

In Fig. 3.18 we illustrate the production of three low entropy plumes generated from the cores of the primary (Fig. 3.18a) and secondary (Fig. 3.18b) with a series of entropy maps covering the evolution of our 3:1 $v_t/V_c = 0.15$ simulation during first pericentric passage (Fig. 3.18a) and apocentric passage (Fig. 3.18b). In these figures, the secondary enters from the bottom left and passes underneath and near to the core of the primary.

In Fig. 3.18a we see that two plume-like structures (labelled "A" and "B") are produced from the primary core. The one labelled "A" is produced on the side roughly opposite from the point of closest contact with the secondary core at $t_{closest}$. This feature is generated from material which has become confined in a narrow structure by the convergence of the shock as it passes the primary core. This behaviour is produced by refraction of the shock due to the decline in the primary core's sound speed into the centre.

The other two plumes ("B" and 'C' in Fig. 3.18) are produced through distinctly different means. In the off-axis simulations we have studied, short-lived but strong negative radial pressure gradients can be generated near the cores of the interacting clusters, leading to the ejection of low entropy material into the outer regions of the merger remnant. Since these gradients are often very localised, the ejection tends to be highly directional leading to the formation of large outwardly flowing collimated plumes. Since the process is adiabatic, the ejected material retains its low entropy and eventually reaccretes to the core of the remnant. This occurs as low entropy streams of high velocity material over an extended period lasting well after $t_{accrete}$ (see Section 3.4.4).

Two mechanisms generally conspire to make this happen: the sudden release of compressive forces due to changes in the relative radial motion of the systems and the presence of low pressure regions in the direction toward which material is dispersed as a result. After pericentric passage, the primary's core is rapidly compressed and the

wake of the secondary's motion creates a large low pressure region on the incident side of the collision. Low entropy material from the primary's core becomes ejected back along the secondary's path as a result, forming plume "B"' which reaches a radius of $\sim 800\,\mathrm{kpc}$ in this case.

The secondary core is subject to these mechanisms at t_{apo} when it turns around and returns to the primary core. The decline of ram pressure at that time results in the release of compressive forces and the strong negative pressure gradient of the primary at such radii provides a low pressure region for the secondary core's material to disperse towards. These mechanisms are assisted by a gravitational "sling-shot" effect resulting from the lag of the secondary's gas core behind its dark matter halo, as noted by Bialek et al. (2002). This lag is due to the additional pressure experienced by the gas but not the dark matter. The net result of these processes is the displacement of a significant portion of the surviving secondary core's material outwards to its tidal radius. This material is then efficiently stripped away by tidal effects forming plume 'C' depicted in Fig. 3.18b. As a result, the plume formed from the secondary after apocentric passage assumes the morphology of a trailing tidal tail (Toomre & Toomre, 1972). More specifically, it has a shape which is curved in the same sense (from tail to core) as the orbit (see Fig. 3.18b). As the system passes apocentre, this structure precesses until it is oriented radially with the primary core. Plumes ejected from primary cores at $t_{closest}$ are confined by the pressure gradients of the secondary's wake and do not share this shape nor evolution.

The symmetry of our 1:1 off-axis mergers means that all of the processes discussed above act on both cores equally to create a pair of symmetric plumes. They connect at $t_{accrete}$ forming an "integral" shaped structure. Its curvature is much more pronounced in the $v_t/V_c = 0.4$ case. Comparing Figs. 3.3 to 3.6, we can see that the plumes formed from the secondary cores are quite similar between the 1:1 and 3:1 cases. However, in the 3:1 cases the plumes formed from the primary core reach much smaller radii.

The compressive forces generated in our 10:1 simulations are far less significant

than in the 1:1 or 3:1 cases resulting in a much less significant plume of primary core material following $t_{closest}$. Furthermore, the resulting pressure gradients are far less localised and result in a broader and less collimated displacement of material. By t_{apo}, all of the material of the secondary beyond 300 kpc has been completely stripped and dispersed into the outer regions of the system. Part of the core survives until $t_{accrete}$ though, generating a small but undetectable plume after t_{apo}.

Several examples of observed systems exhibiting these morphologies exist including A1758 (David & Kempner, 2004) and A2744 (Kempner & David, 2004). These systems possess disturbed accreting cores with curved shapes. In both cases, the authors suggest that they are products of ram pressure stripping but this interpretation is not consistent with our simulations in either case: their large projected separations from their primary cores and their shape suggest they have ejected plumes similar to plume 'C'. A1758N appears to have passed in front of A1758S from east to west, transited apocentric passage and is ejecting a plume of material as it returns back toward A1758S. The A1758N plume is curved in the sense expected from such an orbit. A plume from the core of A1758S is apparent but lacks the same curved appearance. This may mean that A1758S is the more massive of the systems and has a plume such as plume "B" depicted in Fig. 3.18a, or that projection effects are distorting its appearance.

A more secure example of a plume being ejected from a massive primary system such as plume "B" can be seen in A1644 (Reiprich et al., 2004). As noted above, this system has a significant bridge joining the interacting systems. It appears to be at or near apocentric passage and the bridge's lack of curvature, the absence of curved plumes and the thickness of the bridge suggest that the system's orbit is highly inclined. Although the temperature map is cut-off near the main system to the south west, there is a strong suggestion of an elongated cold region similar to plume "B" seen in a y-projection. As we would expect from such an orientation, this feature is nearly collinear with the bridge.

Another good example of a system which appears to have had a plume of primary core material ejected by a merger is A2744. Kempner & David (2004) suggest that this system is a 4:1 merger and should compare well to our 3:1 off-axis cases. We conclude from the structure of the bridge joining the interacting systems and the shape of the secondary's plume that this system is near apocentric passage and significantly inclined. The left-handed orientation of the secondary plume's curvature suggests that it has passed behind the primary in a north western direction and is now travelling towards us near apocentric passage. Consistent with this interpretation we find a cold region to the south east of the primary, where the secondary would have entered the system, ejecting a plume from the primary's core.

3.4.3 Induced core rotation

Due to the initial gas density gradients of the systems, the ram pressure acting on the cores as they pass each other is differential in off-axis cases. This induces torques on the gaseous components of each system causing them to rotate. Generally, the result is two co-rotating cores lasting from $t_{closest}$ to the second pericentric passage at $t_{accrete}$ when the coherence of this motion is disturbed. Remarkably, the release of the pressure gradients which lead to plume "B" in Fig. 3.18a applies enough torque on the primary core in our 3:1 $v_t/V_c = 0.15$ case to cause the core to counter-rotate. This is the only instance in which we witness such counter rotation and more exploration of orbital and mass ratio parameter space is needed to understand how often this occurs.

As a result of its induced rotation prior to apocentric passage, our secondary cores have prograde rotations when they eject the material which form the tidal tail plumes discussed above. This enhances the efficiency of the process.

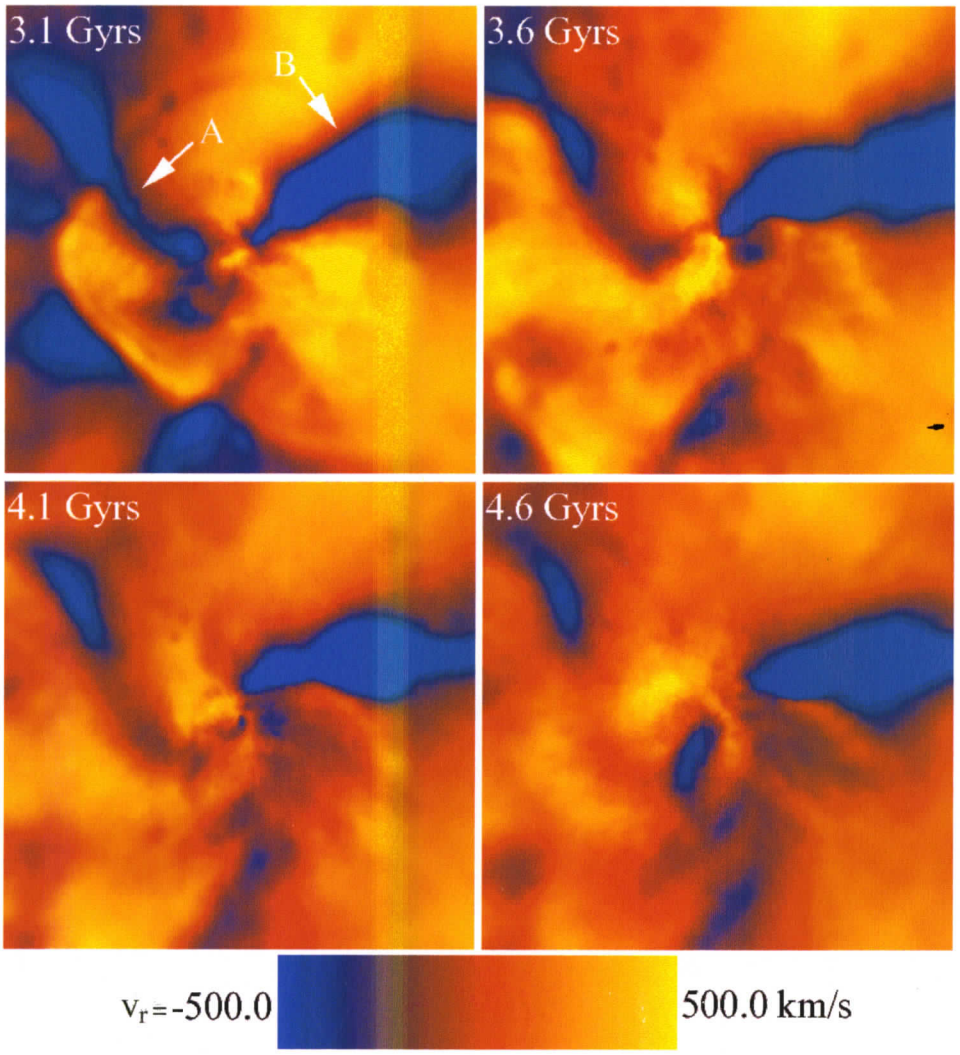

Figure 3.19: Different time snapshots of the radial velocity maps (mass weighted) for the gaseous component in the 3:1 $v_t/V_c = 0.15$ simulation showing the collision of a high velocity stream (labelled B) with the remnant core. In this specific case, the primary and the secondary cores merged at $t_{accrete}$= 2.5 Gyr. Stream B consists of low entropy material that was originally part of the secondary core but shorn off during the course of the merger. Also shown is a stream feature (labelled A) that is not readily apparent in the surface brightness map but which corresponds to a stream associated with returning material originally ejected from the primary core during the creation of plume 'A' (see Fig. 3.18a). Each frame here is 3.0 Mpc on a side and is a z-projection of a 0.5 Mpc thick slice.

3.4.4 Streams

The plumes of material removed from the cores of merging clusters discussed in Section 3.4.2 collect into large collimated structures. Because of the reduced entropy of this material, its buoyancy is low and it ultimately accretes onto the remnant core after the remainder of the secondary core does so at $t_{accrete}$. As a result, long lived ($\sim 2\,\mathrm{Gyr}$) high velocity ($v \sim 1000\ \mathrm{km\,s^{-1}}$) structures form in the cores of the remnant before the system relaxes. We distinguish these structures from plumes because they are inwardly propagating high velocity structures of low (generally undetectable) surface brightness and are not associated with an apparent merging core (the secondary having been accreted and its observable presence destroyed at $t_{accrete}$).

In Fig. 3.19 we present a series of radial velocity maps for our 3:1 $v_t/V_c = 0.15$ simulation illustrating the interaction of two low entropy streams (labelled "A" and "B") with the remnant core. The secondary core accretes from the top right at $t_{accrete}$= 2.5 Gyr in this case and the stream formed from its disruption (labelled "B") follows it from the same direction. Another inwardly radial (but unapparent in surface brightness) feature (labelled "A") can be seen on the opposite side of the system in these frames. It is a long lasting stream formed from plume "A" identified in Fig. 3.18a.

Large scale bulk motions with velocities similar to these streams were observed in the cores of merger remnants in the cosmological AMR simulations of Motl *et. al.* (2004). These authors raise concerns that such motions preclude the existence of actively cooling cores. In our simulations, high velocity structures in the core remain highly collimated and completely disrupt cooling of the core in only one case (3:1 $v_t/V_c = 0.15$). Even in this extreme case, cooling resumes on rapid ($\sim 300\,\mathrm{Myr}$) timescales once the stream finishes its accretion. This takes $\sim 2\,\mathrm{Gyr}$. In all other 1:1 and 3:1 off-axis cases we have studied, the high velocity streams possess enough angular momentum when they accrete to miss the region of active cooling. In the 10:1 cases, the stream

does not significantly disrupt cooling even when it does interact directly with the remnant core. In Chapter 5 we will examine in more detail the effect these streams can have on the final structure of a merger remnant.

The low entropy streams formed in the 1:1 off-axis cases are highly collimated and accrete quickly soon after $t_{accrete}$. In all cases, some portion of the streams are visible until $t_{accrete}$ when their appearance becomes disrupted by the second interaction of the cores. In the $v_t/V_c = 0.4$ case, the accreting streams form a large low entropy spiral which evolves into a ring roughly 1 Mpc in diameter by t_{relax} (see Fig. 3.2). This structure then slowly dissolves, disappearing ~ 2 Gyr after forming.

The secondary cores in our 3:1 mergers become more significantly disrupted after $t_{closest}$ than in the 1:1 cases. As a result, material stripped from the secondary core becomes dispersed over a larger volume. Furthermore, it accretes slightly later than $t_{accrete}$ and over a longer period. The streams are barely observable in our simulated *Chandra* observations for only a ~ 300 Myr following $t_{accrete}$.

Streams such as these have low surface brightness and are best observed in the temperature structure of clusters. They should manifest as cold fronts oriented radially to the primary core with no obvious secondary core being present. There are several examples of observed systems like this. In A576 for instance, Kempner & David (2004) note a "finger" of cool gas which extends to the northwest of the system from its core. In A2255 (Sakelliou & Ponman, 2006) there is a distinct cool region to the southeast of the cluster core which is not associated with an obvious peak in X-ray brightness. Finally, in A2034 (Kempner et al., 2003) there is a large diffuse tail of relatively cool gas extending towards the south of the cluster centre with no obvious X-ray peak associated with it.

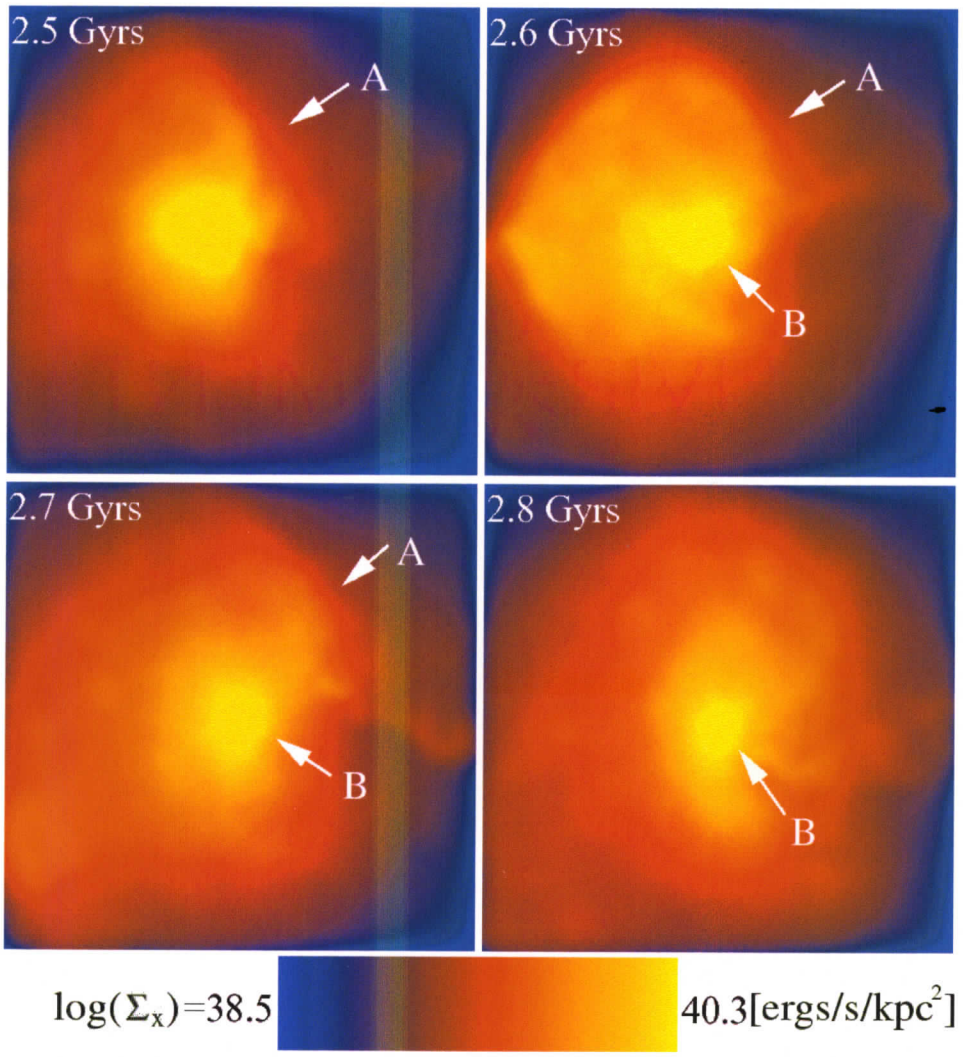

Figure 3.20: Surface brightness maps of our 3:1 $v_t/V_c = 0.15$ simulation showing the formation of 2 "edges" associated with the accretion of the secondary (labelled A) and the stream of low entropy material that follows the secondary (labelled B). The first "edge" is weak feature that moves outward in radius and disappears soon after $t_{accrete}$. The second "edge" is more well-defined and remains stationary during the accretion of the stream material, a process that can last for ~ 0.5 Gyr. We do not see any examples of "edges" produced by core oscillations, nor do we find evidence for significant core oscillations in our simulations. Each frame shown is a z-projection 0.5 Mpc on a side.

3.4.5 Edges

The enhanced spatial resolution of *Chandra* has revealed that the central regions of several clusters exhibit "edges" in their surface brightness as a result of large and localised gas density gradients. Among these are RXJ1720.1+2638 (Mazzotta et al., 2001), A496 (Dupke & White, 2003) and A1795 (Markevitch, Vikhlinin, & Mazzotta, 2001). Systems with several of these features have also been found including A576 (?) which has at least 2 within 50 kpc and ZW3146 (Forman et al., 2002) which has 3 at $r \sim 20$, 45 & 170 kpc. Attempts to account for these features have generally invoked bulk motions of cold core material with respect to its surrounding ICM. Explored mechanisms capable of driving such motions include the activity of jets from central AGN (Fabian et al., 2005) or gravitationally induced motions due to small passing substructure (Markevitch, Vikhlinin, & Mazzotta, 2001; Tittley & Henriksen, 2005).

Occasionally when the streams discussed in Section 3.4.4 accrete to the centre of the remnant, an interface forms between it and the stationary core. Significant and abrupt jumps in density, temperature and pressure can result accompanied by a jump in surface brightness reminiscent of observed edges.

In Fig. 3.20 we show the evolution of two such edges following $t_{accrete}$ for our 3:1 $v_t/V_c = 0.15$ simulation. As the secondary core accretes to the primary core in this case, it does so on the top right side. This leads to an expanding edge (labelled "A") which starts at a radius of 120 kpc and disappears 0.3 Gyr later at a radius of 210 kpc. The stream which follows the accreting secondary core gets deflected towards the bottom of the core by this structure, forming a more significant edge (labelled "B") at a radius of 40 kpc which lasts for 0.5 Gyr.

In Section 3.4.4 we noted several systems which show evidence of streams of radially collimated material. In two of these, A576 and A2034, there are obvious edge features present. In the case of A576, these edges are aligned properly with the orientation of the stream to be a produced by it. In the case of A2034, the edges are

apparently on the opposite side from the stream. In our simulations, multiple streams are typically produced by a single merger. It may be that an unseen stream (possibly produced by the same event which generated the observed stream) is responsible for the observed edge in this case. It may also be that the observed stream is passing in front of or behind the core before making contact with it.

No obvious edges are produced in our simulations by core oscillations. Edges produced through the accretion of streams are distinct, long lived ($\sim 500\,\mathrm{Myr}$) and can yield multiple edges (such as those seen in A576) simultaneously. The last of these properties is difficult to account for through core oscillations but naturally explained as a product of accreting streams.

3.5 Chapter summary

Using the simulations presented in Chapter 2, we have studied the dynamical evolution of typical X-ray cluster mergers. The findings of this chapter are:

- Following a detailed qualitative analysis, we have identified a generic progression for typical cluster mergers. The stages of this progression are: (i) pre-interaction, (ii) initial closest approach, (iii) apocentric passage, (iv) accretion and disruption of the secondary core and (v) relaxation. To facilitate comparison and interpretation of observations, we describe in detail the interactions associated with the gas components of the two merging systems during each of the stages and quantify the times at which these stages arise relative to the beginning of the merger. We also show gas density, X-ray surface brightness, gas temperature, SZ and gas entropy maps at different points during the mergers.

- Moderate and massive mergers tend to run for 4.5–5.5 Gyr, while minor mergers last for up to $\sim 2\,\mathrm{Gyr}$ longer (in good agreement with the trend identified by Tormen et al., 2004). This duration is the elapsed time from the point when

the secondary's centre of mass crosses R_{200} of the primary (the beginning) to the time when the gas distribution in the final system has relaxed and nearly returned to virial/hydrostatic equilibrium (the end). Typically, off-axis mergers run longer than head-on mergers.

- In simulated 50 ks *Chandra* observations (assuming $z = 0.1$), all easily identifiable substructure generated by our merger events disappear during the secondary's second pericentric passage of the primary core. However, the system takes an additional ~ 2 Gyr for its isophots to appear relaxed. Temperature fluctuations are not necessarily a reliable indicator of the system's dynamical state.

- We find that following the merger, the resultant system settles into virial equilibrium sooner than into hydrostatic equilibrium. In many cases, the final cluster exhibits oscillations that result in instantaneous deviations from hydrostatic equilibrium by as much as 15% for as long as 7 Gyrs after the beginning of the merger. We also find that generically complex patterns of entropy and temperature fluctuations, at the level of $\Delta T/T \sim 20\%$, can persist in the final systems well past the point when the systems appears relaxed. Based on our findings, we suggest that temperature fluctuations of this order, without any other corroborating signatures of ongoing merger, should not be interpreted as evidence of a highly disturbed system.

- We find that in none of the cases considered are the initial cool compact cores of the primary and the secondary destroyed during the course of the mergers. Instead, the two remnant cores eventually combine to form a new core that, depending on the final mass of the remnant, can have a greater cooling efficiency than either of its progenitors. We will discuss this behaviour in more detail in Chapter 5.

- While the large scale coherent displacements between the dark matter and gas components in the merging system are not uncommon, they do not trigger any obvious surface brightness discontinuities. Within the central 50 kpc, the gas and the dark matter remain tightly coupled to each other. We do not see any evidence of core oscillations or of any associated heating.

- We investigated the efficacy of three measures used to quantify the degree to which observed clusters are disturbed. These are (i) centroid variance, (ii) power ratios, and (iii) X-ray surface brightness/projected mass displacement. We find that the centroid variance is the best of the three. It best reflects the state of the cluster as determined by visual examination. It also provides an excellent indicator of how far the system is from virial and hydrostatic equilibrium. The power ratios are very sensitive to noise and once this is factored in, they provide an unambiguous signal only when the system is highly disturbed. The X-ray/mass displacement are extremely sensitive to weak but long-lived perturbations in the dark matter distribution caused by low mass mergers.

- During the course of the merger, we find a variety of transient features arising and disappearing in the projected temperature, entropy and surface brightness maps, most of which resemble "cold fronts" observed in recent *Chandra* and XMM observations. While "cold fronts" are generally associated with the disruption of the secondary's core, we find that they can be caused by several different mechanisms. The resulting features can potentially be distinguished based on their morphological properties. Interested readers are referred to Section 3.4 for examples of clusters whose recently published X-ray images show examples of the different types of transient structures. We propose the following classification scheme based on their origin and appearance:

  - *"Comet-like" tails*: Ram pressure strips the outer atmospheres of sec-

ondary systems forming very brief (~ 0.5 Gyr) comet-like morphologies for both cluster cores (except the primary in 10:1 mergers). This morphology is observable only between first pericentric and apocentric passages.

- *Bridges*: Ram pressure disperses core material from both cluster cores in 1:1 and 3:1 cases. A luminous moderate-entropy bridge resulting from the convergence of the two resulting regions of dispersed material is produced. This structure remains observable in 50 ks *Chandra* exposures at $z = 0.1$ until secondary core accretion in our 1:1 mergers and until apocentric passage in our 3:1 mergers. The morphology of this structure could be useful as a cue for determining the inclination of observed merger systems.

- *Plumes*: Pressure gradients produced by the secondary's motion at $t_{closest}$ and t_{apo} can lead to the ejection of significant amounts of the primary and secondary cores' gas. This material forms large collimated plumes of low-entropy material. At apocentric passage, material ejected in this way from the secondary's core becomes tidally stripped and adopts the morphology of a trailing tidal tail. The majority of observed disturbed merging cores likely owe their appearance to this process, rather than ram pressure stripping.

- *Streams*: Low entropy streams form from these plumes and accrete to the centre of the remnant following the second pericentric passage and disruption of the secondary core at $t_{accrete}$. This material remains collimated and typically has enough angular momentum to avoid a direct impact with the remnant core. This mitigates the concerns of Motl *et. al.* (2004) who suggest that high velocity structures formed in mergers may prevent the formation of compact cool cores. These streams may also play an important role in fuelling the activity of central AGN in clusters.

- *Induced core rotation*: Off-axis mergers subject the gaseous cores of both

merging clusters to torques which induce rotation. In one simulation (our 3:1 $v_t/V_c = 0.15$ case), the resulting rotation of the primary's core is retrograde to the secondary's orbit. In all cases, the coherence of this rotation is completely disrupted by the disruption of the cores during second pericentric passage.

– *Edges*: Streams can accrete directly onto the core of the remnant, generating strong "edges" in surface brightness and gradients in temperature and density. The resulting features are similar to several cold front systems whose morphology had previously been attributed to AGN activity or motion of the gaseous core within its dark matter potential.

In the following chapter we will use this understanding of the dynamical progression of mergers to interpret the evolution of a merging system's observable global X-ray and SZ properties.

Chapter 4

Effects on X-ray and SZ scaling relations

Abstract

We use the suite of simulations presented in Chapter 2 to examine global X-ray and Sunyuev-Zeldovich (SZ) observables for systems of merging relaxed X-ray clusters. The time evolution of our merging systems' X-ray luminosities, temperatures, total mass measures, SZ central Compton parameters and integrated SZ fluxes are presented and the resulting impact on scaling relations examined. In all cases, and for all parameters, we observe a common time evolution: two rapid transient increases during first and second pericentric passage, with interceding values below their initial levels. This is in good qualitative agreement with previous idealized merger simulations (*e.g.* Ricker & Sarazin, 2001), although we find several important differences related to the inclusion of radiative cooling in our simulations. These trends translate into a generic evolution in the scaling relations as well: a rapid transient roughly along the mass scaling relations, a subsequent slow drift across the scatter until virialization, followed by a slow evolution along and up the mass scaling relations as cooling recovers in the cluster cores. In none of the scaling relations we have examined with observations sufficient for comparison (the $L_x - T_x$, $M_t - T_x$, and $M_t - L_x$) is this drift sufficient during typical events to account for the observed scatter. In addition, the scatter in the limited available observations of the $y_o - L_x$ plane is too large to be accounted for by our mergers. Lastly, we examine the X-ray SZ proxy proposed by Kravtsov et al. (2006) and find that the tight mass scaling relation they predict remains secure through the entire duration of a merger event, independent of projection effects.

It has been known for some time that clusters obey simple and relatively well defined power-law scalings between many of their globally integrated or averaged properties (*e.g.* temperature, X-ray luminosity and mass). Due to their proven utility in cosmological studies (see Voit, 2005, for an excellent review), their use as constraints on theoretical models of galaxy formation (Babul *et. al.* , 2003) and the significant discrepancy between observations and simple early theoretical expectations (*e.g.* Kaiser, 1986; Markevitch, 1998), these relations have received a great deal of scrutiny in recent years.

Significant progress has recently been made towards reconciling theoretical expectations for these relations with observations (*e.g.* Voit et al., 2005). As a result, attention is now being diverted towards accounting for their observed scatter. One significant early step towards this goal was made by McCarthy *et. al.* (2004, M04 hereafter) who illustrated that the position of systems relative to the mean observed $L_x - T_x$ and $M_t - L_x$ relations correlates with the system's central entropy, and hence the morphology of a system's core. Specifically, they found that systems with compact cool cores (CCCs; classically identified as "cooling flow" systems) and low central entropies tend to lie on the high-luminosity/low-temperature sides of observed distributions while systems lacking compact cool cores (NCCs; classically identified as "non-cooling flow" systems) and possessing elevated central entropies lie on the low-luminosity/low-mass sides. Recently, O'Hara et al. (2006) have demonstrated that these two populations exhibit similar scatter in these planes when their cores are removed during analysis. This suggests that variations in core properties are primarily responsible for the scatter in observed scaling relations and that clusters of all morphologies exhibit similar deviations from equilibrium due to past merger activity (this is supported by the results of Chapter 3).

These results are corroborated by Balogh et al. (2006) who find that variations in dark matter structure and uncertainties in cosmological models can not account for the scatter in $L_x - T_x$ or $M_t - L_x$ scaling relations, suggesting that variations in the minimum level of core entropy due to differences in heating and/or cooling efficiencies of core material are responsible. Little speculation is made regarding the physical origins of such efficiency variations but they suggest that mergers are not likely the source, sighting qualitative observations made by authors of previous theoretical merger studies that mergers generally drive systems to evolve parallel to observed scaling relations. This lies in stark contrast to the work of Smith et al. (2005) however, who use strong lensing measurements and high resolution *Chandra* observations to illustrate a correlation between the degree to which local cluster cores are disturbed and their variance from the mean $M_t - L_x$, $M_t - T_x$, and $L_x - T_x$ scaling relations.

Hence, several unresolved issues regarding the role of mergers in shaping the scatter in observed cluster scaling relations persist. Furthermore, scaling relations involving the integrated Sunyuev-Zeldovich (SZ) properties of clusters, although previously considered (McCarthy et al., 2003), have received significantly less attention than those involving mass, X-ray luminosity and temperature. With the impending availability of large and statistically significant datasets of SZ observations, a careful examination of the effects of mergers on SZ scaling relations is warranted.

In this chapter we will use the set of simulations presented in Chapter 2 to examine the effects of mergers on cluster scaling relations (see RS01 for a particularly good study of some of the issues addressed in this chapter).

In Section 4.2 we present the temporal evolution and scaling relation of our systems' X-ray luminosity and temperature, examining the effects of various temperature measures and of core excision on the behaviour of these quantities. In Section 4.3 we examine the effectiveness of hydrostatic mass estimates, its isothermal β-model implementation and the $M_t - T_x$ and $M_t - L_x$ scaling relations which are obtained

from them. In Section 4.4 we study the evolution of our systems' SZ properties (both central Compton parameters and integrated SZ fluxes), examining the effectiveness of the β-model approximation often implemented by observers as well as the most relevant scaling relations which can be constructed from them. In Section 4.5 we examine the effects of mergers on the X-ray SZ proxy recently proposed by Kravtsov et al. (2006). Finally, we summarize the most notable results of the chapter in Section 4.6.

4.1 Some comments regarding the frequency of mergers

In this chapter we seek to understand the role which mergers are likely playing in shaping the statistical properties of clusters as studied through observed scaling relations. It is important to note however that our simulations certainly are not uniformly represented in these statistics.

Table 4.1: Percentage difference of the global properties of our systems from the values required to preserve their mass scaling relations at the end of our simulations and at t_{relax} (in parenthesis). In the case of y_o and $S_\nu(R_{2500})$, our fiducial theoretical model is used (see Section 4.2.3) to determine the expected mass scaling. For temperature we use the mass temperature relation of Sanderson et al. (2003) and for luminoisty we use the mass-luminosity scaling relation of Reiprich & Böhringer (2002) Corrected results are for analysis conducted with the central $0.1R_{200}$ excised and uncorrected values are performed without excising the central regions.

M_p:M_s	v_t/v_c	L_x (uncorrected)	L_x (corrected)	T_x (uncorrected)	T_x (corrected)	y_o	S_ν
1:1	0.00	21.1 (-13.1)	-13.0 (-2.0)	10.3 (5.5)	2.9 (-1.5)	28.8 (-3.3)	3.4 (0.6)
1:1	0.15	-25.6 (-38.3)	-13.3 (-0.6)	8.2 (13.1)	-1.3 (-0.4)	-8.7 (-27.6)	-8.2 (1.0)
1:1	0.40	-49.6 (-52.9)	-27.6 (-26.1)	7.5 (9.2)	-3.1 (-4.9)	-24.2 (-39.3)	-22.0 (-20.9)
3:1	0.00	-13.3 (-27.1)	3.3 (14.6)	10.9 (14.7)	2.1 (2.2)	-17.2 (-37.7)	0.1 (3.9)
3:1	0.15	-38.6 (-40.4)	-3.2 (5.7)	14.6 (13.7)	0.9 (0.3)	-29.8 (-47.6)	-4.9 (-1.9)
3:1	0.40	-31.7 (-35.2)	-24.9 (-16.0)	5.3 (9.6)	-1.7 (0.0)	-15.0 (-33.6)	-25.9 (-18.5)
10:1	0.00	5.7 (12.3)	-10.7 (19.1)	3.7 (13.1)	-1.0 (4.4)	-6.2 (-11.4)	-10.0 (4.8)
10:1	0.15	-16.0 (-18.4)	-13.5 (7.7)	6.5 (12.7)	0.6 (3.9)	-18.0 (-23.8)	-15.8 (-1.9)
10:1	0.40	-17.5 (1.4)	-23.3 (-7.7)	5.8 (11.8)	-0.2 (4.4)	-21.6 (-7.6)	-28.0 (-16.0)

In current theories of hierarchical cluster formation, the likelihood of merger events is expected to have a strong dependence on the mass ratio of the interacting systems. Equal mass mergers are expected to be exceptionally rare, 3:1 mergers common and 10:1 mergers ubiquitous (Cohn & White, 2005). Although there is evidence that equal mass mergers have occurred (*e.g.* the Cloverleaf cluster studied by Finoguenov et al., 2005), they are exceptionally rare and we include them in this study primarily for completeness. All clusters should have experienced mergers similar to our 10:1 mergers. For these reasons, when considering the effects of mergers on scaling relations, we will primarily be concerned about the effects of 3:1 and 10:1 events.

4.2 Luminosity and Temperature

In this section we present the details of how we compute global luminosities and temperatures for our simulations. We shall find that the temperatures of our merger remnants scale in accord with observed mass scaling relations, but that the luminosity does not. Excising the cores of our clusters improves this discrepancy. We will then illustrate the consequences of this for the $L_x - T_x$ scaling relation.

4.2.1 Luminosity

A cluster merger leads to transient increases in both X-ray luminosity (L_x) and temperature (T_x) which can pose significant problems for cosmological studies (Randall et al., 2002). In their study, RS01 found that after an initial transient increase at the time of first pericentric passage, the luminosity of the system drops to a fraction of its initial value with a second smaller peak $\sim 2\,\mathrm{Gyr}$ later when the secondary core returns from apocentric passage. These sharp transient increases in L_x can translate into a skewing of the high-mass end of mass functions derived from observed X-ray

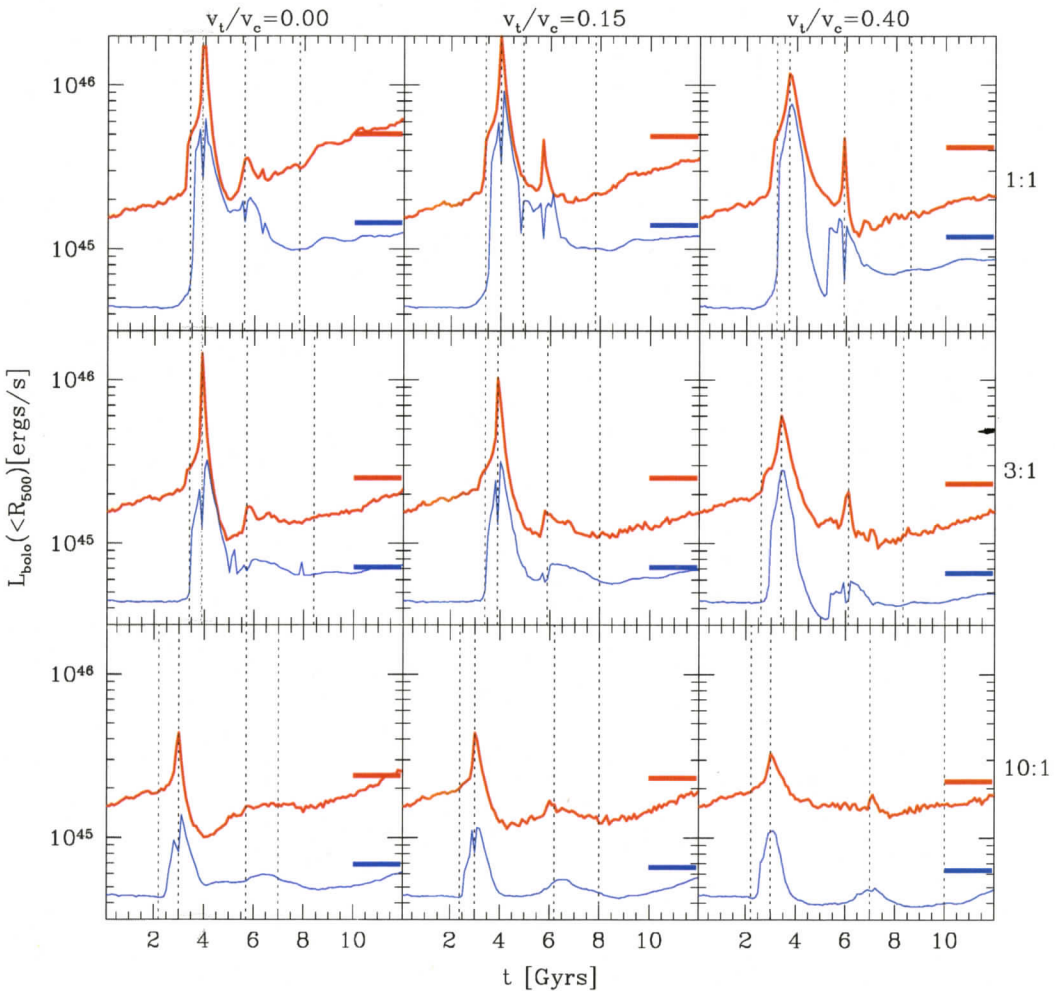

Figure 4.1: Bolometric X-ray luminosities (L_x) measured within $R_{500}(t)$. The thin blue curve traces the evolution of the system with the central $0.1R_{200}$ excised from consideration (*i.e.* "core corrected" luminosities) while the thick red curve traces the evolution with this region included (*i.e.* "uncorrected" luminosities). Thick horizontal dashes indicate the initial bolometric luminosities scaled by the change in total mass within R_{500} from initial to final states using the observed $M_t - L_x$ scaling relation of Reiprich & Böhringer (2002). Vertical dotted lines indicate (from left to right) the times t_o (virial crossing), $t_{closest}$ (first pericenter), $t_{accrete}$ (second pericenter) and t_{relax} (the moment our remnants would appear relaxed to a 50 ks *Chandra* exposure at $z = 0.1$). Black text around the boundary indicates the mass ratio and v_t/V_c depicted by each panel.

luminosity functions and mass luminosity scaling relations. This can translate into a upward bias in σ_8 of as much as 20% and a downward bias in Ω_M of comperable extent.

In Fig. 4.1 we present in red the temporal evolution of the bolometric X-ray luminosities of our simulations integrated within the varying radius $R_{500}(t)$. Although detailed comparisons to RS01 are complicated by the fact that we are not integrating over the entire simulation volume, we see a similar double peaked evolution in luminosity to what is noted in their work. Furthermore, we find a similar trend in the reduction of the final remnant's luminosity with impact parameter.

There is however one notable and generic feature of our simulations not present in RS01: a persistent increase in luminosity after t_{relax}. This increase follows the relation $L_x(t) = L_x(t_{relax}) \exp(\alpha t)$ where $\alpha = 0.08 - 0.14$. We also plot, in blue on this figure, the evolution of each system's luminosity with the central $0.1R_{200}$ excised. These curves (and an examination of the evolving surface brightness profiles of our simulations) reveal that most of this change is arising from increases in the surface brightness of the system within this excised region. This is a result of increasing central gas densities arising primarily from cooling and (to a lesser extent) the accretion of material, dispersed to large radii during the interaction, reaccreting to the center of the system.

Also plotted on Fig. 4.1 are horizontal dashes indicating the bolometric luminosities that we would expect if our remnant systems evolved to states which preserve the observed $M_t - L_x$ scaling determined by Reiprich & Böhringer (2002). We use the total mass integrated within R_{500} for this purpose. For the total luminosity (in red) we see that our remnant systems generally manage to recover their expected values by the end of the simulation in head-on cases. However, the luminosities of our off-axis merger remnants are systematically lower (by $16 - 50\%$; see table 4.1) than expected from the observed mass scaling relation. This discrepancy generally increases with impact parameter.

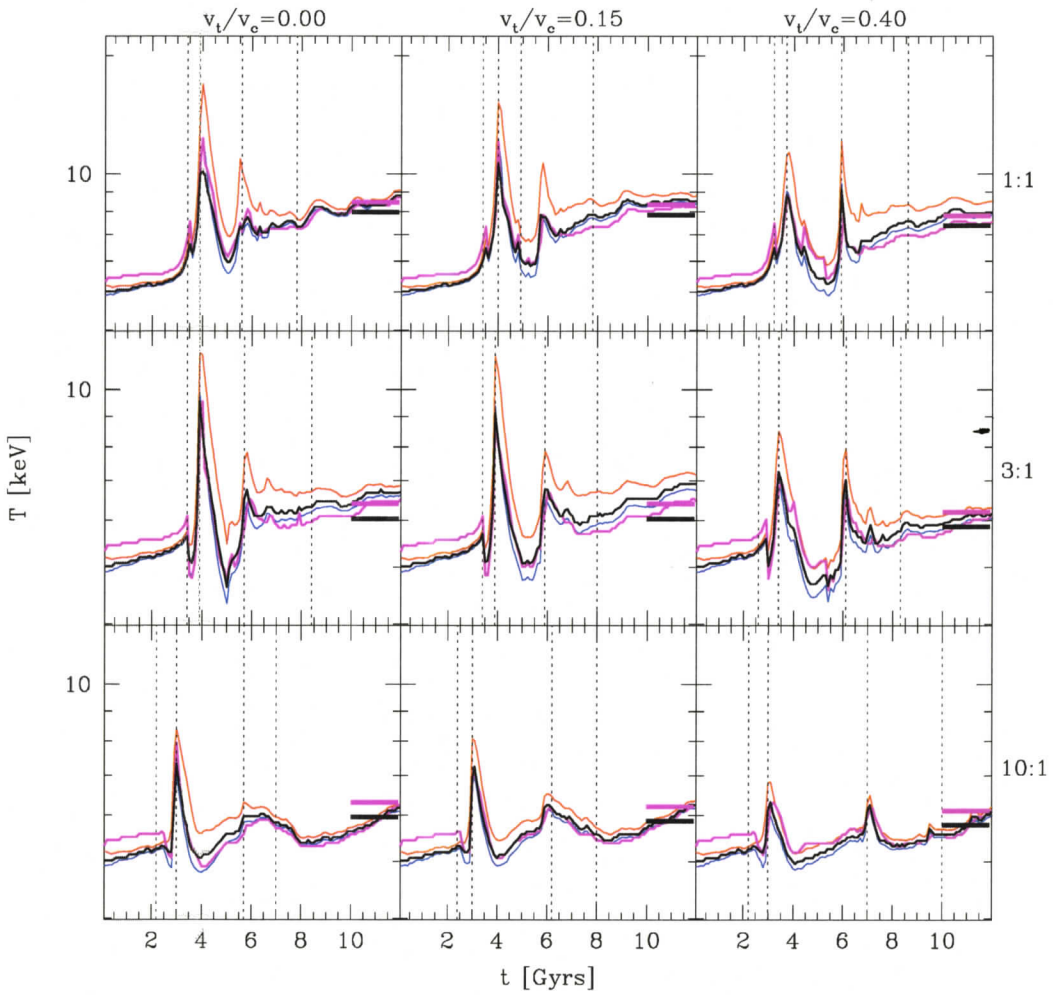

Figure 4.2: Temperatures (T_x) measured within $R_{500}(t)$ using several techniques discussed in the text. Emission weighted temperatures (T_{ew}) are illustrated with red curves, spectrally fit temperatures (T_{spec}) with black curves, and "spectroscopic-like" (T_{sl}, computed according to Mazzotta et al., 2004) temperatures with blue curves. The thick magenta lines are spectrally fit temperatures with the cool cores ($r < 0.1R_{200}$) excised. Horizontal dashes indicate spectral temperatures scaled from their initial values using the observed $M_t - T_x$ scaling relation of Sanderson et al. (2003). Vertical dotted lines indicate (from left to right) the times t_o (virial crossing), $t_{closest}$ (first pericenter), $t_{accrete}$ (second pericenter) and t_{relax} (the moment our remnants would appear relaxed to a 50 ks *Chandra* exposure at $z = 0.1$). Black text around the boundary indicates the mass ratio and v_t/V_c depicted by each panel. Note that the vertical scale changes for each mass ratio.

Luminosities computed with the central $0.1R_{200}$ excised (in blue) are more successful at preserving the observed mass scaling relation. The discrepancies of the final luminosities from these scalings are only $3 - 28\%$ (see table 4.1) in these cases.

4.2.2 Temperature

Recently several authors have raised concerns that traditional methods of computing ICM temperatures in theoretical studies may be introducing systematic biases during comparisons to observations (Mathiesen & Evrard, 2001; Gardini et al., 2004; Mazzotta et al., 2004; Vikhlinin, 2006). This bias is introduced because the ICM of both theoretical and observed systems is not isothermal and the methods used to compute representative temperatures have been fundamentally different.

Most theoretical measures of temperature are computed through one of a variety of possible weighted averages while observational temperatures are obtained from fits of plasma models to observed spectra. The most widely used theoretical measure has been the emission weighted temperature computed from

$$T_{ew} \equiv \frac{\int \Lambda(T) n_e^2 T \, dV}{\int \Lambda(T) n_e^2 \, dV} \tag{4.1}$$

where $\Lambda(T)$ is the emissivity of the ICM and n_e its electron density. More accurate but similarly convenient and computationally inexpensive "spectroscopic-like" weightings have recently been proposed by Mazzotta et al. (2004) and Vikhlinin (2006). From comparisons to hydrodynamic simulations, Mazzotta et al. (2004) find that the weighting

$$T_{sl} \equiv \frac{\int n_e^2 T^{1-\alpha} \, dV}{\int n_e^2 T^{-\alpha} \, dV} \tag{4.2}$$

with $\alpha = 0.75$ gives results in much better agreement to temperatures obtained from simulated *Chandra* observations. In their analysis, they typically find T_{sl} to be lower than T_{ew} by $20-30\%$. This relation is calibrated from mixtures of isothermal plasmas of two temperatures, with variations of T_{sl} from spectral fits being less than 10%.

The weighting of Vikhlinin (2006) is somewhat more complicated but more accurately takes into account effects on T_x introduced by instrumental variations and metallicity dependent line emission. They find a very similar power law scaling ($\alpha = 0.79$ for *Chandra*) as Mazzotta et al. (2004) for continuum contributions but significant spatial variations may exist between the two measures, particularly in cluster cores which are dominated by low temperature line-emitting gas. However, we are only interested in globally averaged temperatures in this work, which are dominated by continuum emission from hot gas. Under these circumstances, very little difference is expected between these measures and so we shall presently focus our attention on the simpler method of Mazzotta et al. (2004).

Our systems constitute mixtures of gas covering an extremely wide range of densities and temperatures, naturally raising concerns that the weightings determined for T_{sl} by Mazzotta et al. (2004) and Vikhlinin (2006) may breakdown occasionally during the interaction. To check this we have also computed spectrally fit temperatures (T_{spec}). To produce this measure we compute integrated spectra over the *Chandra* bandpass (0.7-7 keV with 20 eV resolution) and fit isothermal plasmas to them. This is done via χ^2 minimization weighted by the photon flux of each spectral bin. The instrumental response of *Chandra* is included in this analysis as well as galactic absorption at a level of $N_H = 2 \times 10^{20} cm^{-2}$.

In the analysis of RS01, the emission weighted temperature of the system remains relatively constant, interrupted only by a pair of transient increases commensurate with the increases in luminosity discussed above. These transient increases occur during first and second pericentric passages, when the cluster cores are shock heated and compressed. As their systems relax, they recover to slightly higher emission weighted

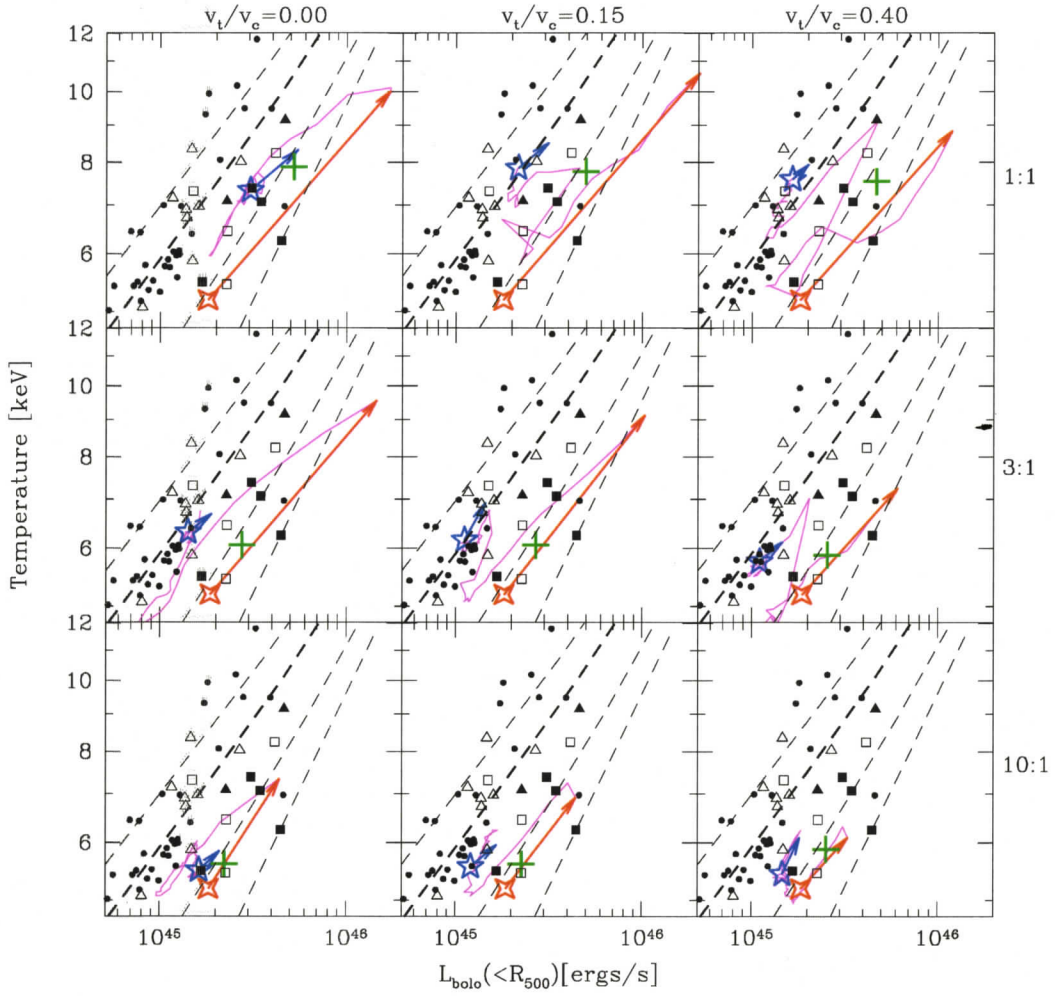

Figure 4.3: X-ray temperatures (spectrally weighted) plotted against bolometric luminosities for our simulations (both integrated within R_{500}) and compared against observations. Red four and blue five point stars indicate the states of the system at t_o and t_{relax} respectively. The red vector indicates the evolution from t_o to $t_{closest}$ while the blue vector illustrates 3 Gyr of evolution following t_{relax}. The magenta line tracks the evolution from $t_{closest}$ to t_{relax} (generally 4-5 Gyr) during which the system is visibly disturbed. Green crosses indicate the remnant state necessary to preserve the observed mass-scaling relations. Black points are the observed catalogue of Horner (2001) with squares and triangles denoting compact cool core and non-compact core systems and open and filled points indicating apparently disturbed and relaxed systems respectively, following the approach of McCarthy *et. al.* (2004). Dashed lines are our fiducial analytic entropy injection models (S_o = 10,100,300, and 500 keVcm^2, increasing with decreasing luminosity). Black text around the boundary indicates the mass ratio and v_t/V_c depicted by each panel.

temperatures in equal mass events and to approximately the initial temperature in 3:1 cases.

In Fig. 4.2 we present the temporal evolution of the three temperature measures discussed above, integrated within $R_{500}(t)$ for our simulations. In all cases we witness the familiar double peaked behaviour noted by RS01. We additionally observe the trend noted by RS01 that the amplitude of the initial peak decreases with impact parameter while the relative strength of the two peaks becomes more similar.

The amplitude of these peaks is significantly higher for the emission weighted approach than for all of the other measures, suggesting that the transient increases determined by RS01 (who present emission weighted temperatures) are significantly overestimated. This further suggests that the influence of transient temperature increases on measures of σ_8 determined by Randall et al. (2002) are overestimated.

As expected, T_{sl} and T_{spec} are systematically lower than T_{ew} at all times. Initially, this difference is small ($\sim 3\%$) but at late times it can be as much as $\sim 10\%$. Given that T_{sl} produces results in very good agreement (less than 5% difference at all times, in all cases except 500 Myr during first pericenter in the 1:1 near-axis cases where we see a 20% difference) with T_{spec} throughout our merger interactions, we conclude that the methods of spectrally weighted temperature averages developed by Mazzotta et al. (2004) and Vikhlinin (2006) are indeed very robust during the complicated evolution of a cluster merger. We shall use our spectrally fit temperatures for the remainder of our analysis however, unless otherwise stated.

Given that there is such a persistent offset between the emission weighted temperatures and the spectrally fit temperatures, the normalization of theoretical temperature scaling relations generated with this approach are likely too high. This has important implications for cosmological studies utilizing emission weighted temperature functions as well.

In Fig. 4.2 we place thick horizontal dashes to indicate the spectral temperature the final remnant would have if it were scaled from the initial temperature by the

observed $M_t - T_X$ relation of Sanderson et al. (2003). We see that immediately following t_{relax}, the system is significantly cooler than this scaled value. Late increases evolve according to $T_x(t) = T_x(t_{relax}) \exp(\alpha t)$ (with $\alpha = 0.01 - 0.03$), taking the system in all cases to roughly the observed mass-scaled temperature by the ends of our simulations. Of the three temperature measures, T_{ew} produces results which most often and most significantly fail to yield the mass-scaled result, suggesting that previous theoretical studies of the $L_x - T_x$ and $M_t - T_x$ relations which have employed T_{ew} as a temperature measure, have exaggerated the scatter in this relation introduced by mergers. In Table 4.1, we list the discrepancies of our remnants' temperatures from the observed mass-scaling relation.

4.2.3 $L_x - T_x$ relation

In Fig. 4.3 we present the evolution of our systems in the $L_x - T_x$ plane. We illustrate the evolution from the initial state (red 4 point star) to $t_{closest}$ with a red arrow and the evolution for 3 Gyr following t_{relax} (blue five point star) with a blue arrow. In each case, the final L_x and T_x, scaled from their initial values by the observed mass scaling relations of Reiprich & Böhringer (2002) and Sanderson et al. (2003), are illustrated by a green cross. Magenta lines track the evolution of the system from $t_{closest}$ to t_{relax}, while the system appears significantly disturbed (an interval of $4 - 5$ Gyr, except for the 10:1 $v_t/V_c = 0.4$ case which takes 7 Gyr to appear relaxed). This format will be used for all the scaling relations we subsequently present.

It has been known for some time that variations in the structure of the central regions of clusters contribute significantly to the scatter in both luminosity and temperature mass scaling relations. For this reason, and out of a desire to obtain the tightest relations possible (usually for the purposes of obtaining mass functions for cosmological studies), authors (*e.g.* cite) have typically presented "core-corrected"

observations for studying the $L_x - T_x$ relation. It has been shown by M04 however that there is very interesting structure in the $L_x - T_x$ plane which correlates with the morphology of the cores when the central regions are retained for analysis. To explore the consequences (and possible contributions of) mergers to this structure, we use the "uncorrected" catalogue presented by Horner (2001) for comparison of our results to observations (presented in black on Fig. 4.3).

On Fig. 4.3 (and most subsequent scaling relation plots) we have also placed dashed lines depicting theoretical mass scaling relations for a set of fiducial analytic entropy injection models for systems with various minimum entropies. These models are computed following the procedure of McCarthy et al. (2003) with the following exceptions: we use the mass-concentration relation from the Millennium Simulation, the baseline entropy profile of Voit et al. (2005), and assume a bias $M_g(< R_{200})/M_t(< R_{200}) = 0.9\Omega_b/\Omega_m$. Four lines (of decreasing luminosity at constant temperature respectively) are plotted for core entropies of 10, 100, 300 and 500 keVcm^2. In Babul *et. al.* (2003) it was found that the 300 keVcm^2 model best fits the mean relation of the data. This model is thus indicated with a thicker line type and we shall consider it to represent the mean relation of the data in all discussions which follow.

Fig. 4.3 illustrates an evolutionary progression which we will generically find (with occasional important differences) in all the scaling relations we present in this paper. Initially, the red vector illustrating the evolution from initial conditions to the maximum disturbance at $t_{closest}$ runs roughly parallel to our fiducial models, supporting similar findings in previous merger studies. The magenta line (tracing $4-5$ Gyr of evolution while the system is significantly disturbed) then illustrates the second transient increase in these quantities during second pericenter. It also illustrates the increase in the significance of this event with increasing impact parameter. Also during this time, the system migrates slightly across the dispersion in the scaling relations. Once second pericentric passage has passed and obvious substructure dissolved, the blue vector illustrates that the systems once again evolve parallel to the

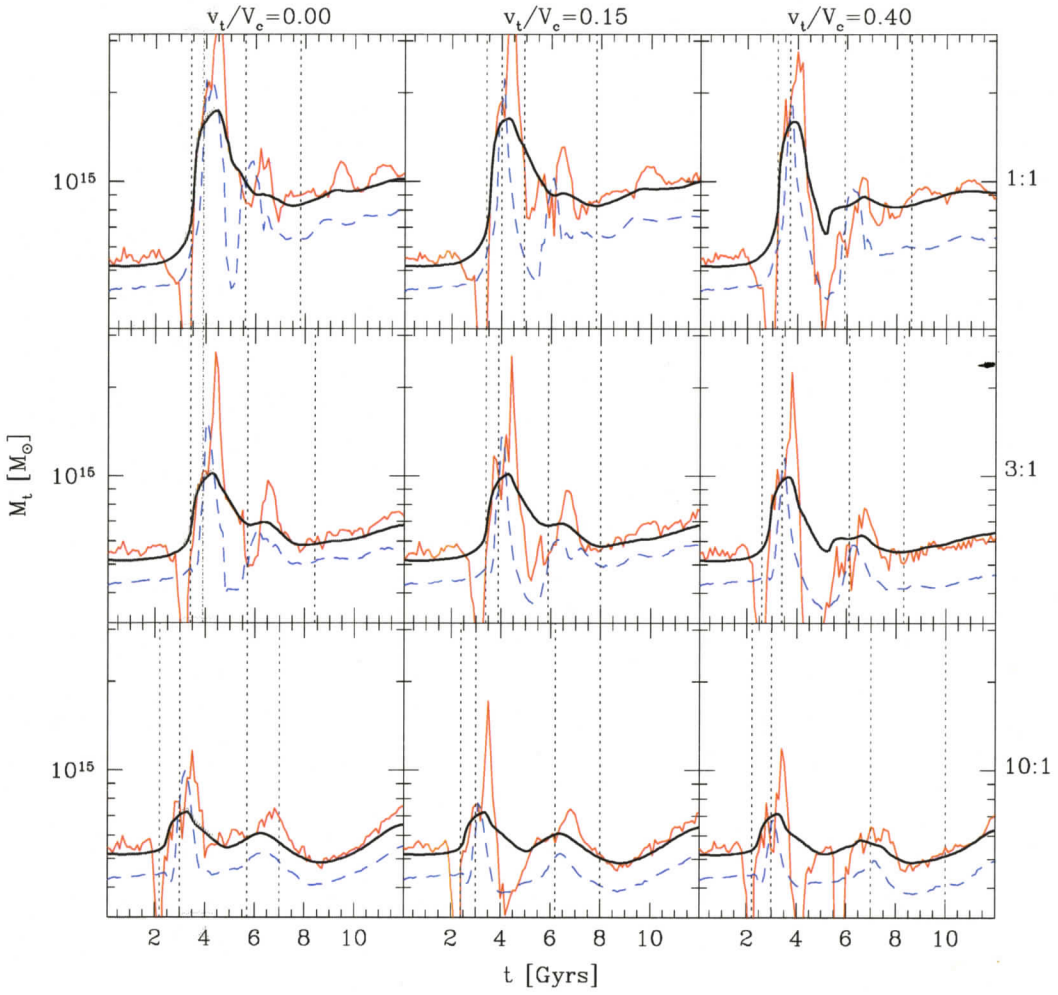

Figure 4.4: Total masses within $R_{500}(t)$ computed from our simulations. The total mass is plotted as a thick black curve, the hydrostatic equilibrium mass (computed from Eqn.4.4) is plotted as a red curve and the isothermal β-model mass (computed from Eqn.4.8) is plotted as a dashed blue curve. Vertical dotted lines indicate (from left to right) t_o (the time of virial crossing), $t_{closest}$ (first pericenter), $t_{accrete}$ (second pericenter) and t_{relax} (the moment our remnants would appear relaxed to a 50 ks *Chandra* exposure at $z = 0.1$). Black text around the boundary indicates the mass ratio and v_t/V_c depicted by each panel.

mass scaling relations. This occurs as cooling leads to denser, more luminous cores and material dispersed by the interactions reaccretes to the system centres, deepening their gravitational potentials and increasing their temperatures.

The initial conditions we have chosen place our primary systems on the high luminosity side of the scatter in the $L_x - T_x$ plane, where systems with compact cool cores are typically found (M04). In Section 4.2.2 we found that mergers tend to evolve to states which preserve the observed mass-temperature scaling relation but in Section 4.2.1 found that they create remnants which are under luminous with respect to the observed mass-luminosity scaling relation. In Fig. 4.3 we see the consequences of these trends: off-axis mergers tend to push typical compact cold core systems towards the low-luminosity side of the observed $L_x - T$ relation.

In our off-axis 1:1 cases (which we must emphasize, are rarely observed and expected to be exceptionally uncommon) our mergers are able to drive systems to states which cover the majority of the scatter in this plane. However, in the more common (yet still rare) situations represented by our 3:1 mergers, states represented by our fiducial entropy injection models with entropies higher than $S = 300\,\mathrm{keVcm}^2$ are not reached, not even transiently. Our 10:1 mergers fail to reach the mean relation of the data under any circumstance.

When this plot is generated utilizing emission weighted temperatures, the full dispersion of the observations is covered by both our 1:1 and 3:1 mergers. It is now well established that this temperature measure is not viable however, so this does not represent a means by which to account for the observed scatter. Instead, it further emphasizes the importance of computing proper spectral temperatures when comparing theoretical models of X-ray clusters to observations. Furthermore, not only should the normalization of past temperature scaling relations generated with the emission weighted measure be viewed with some scepticism (as argued in Section 4.2.2), the scatter should be as well.

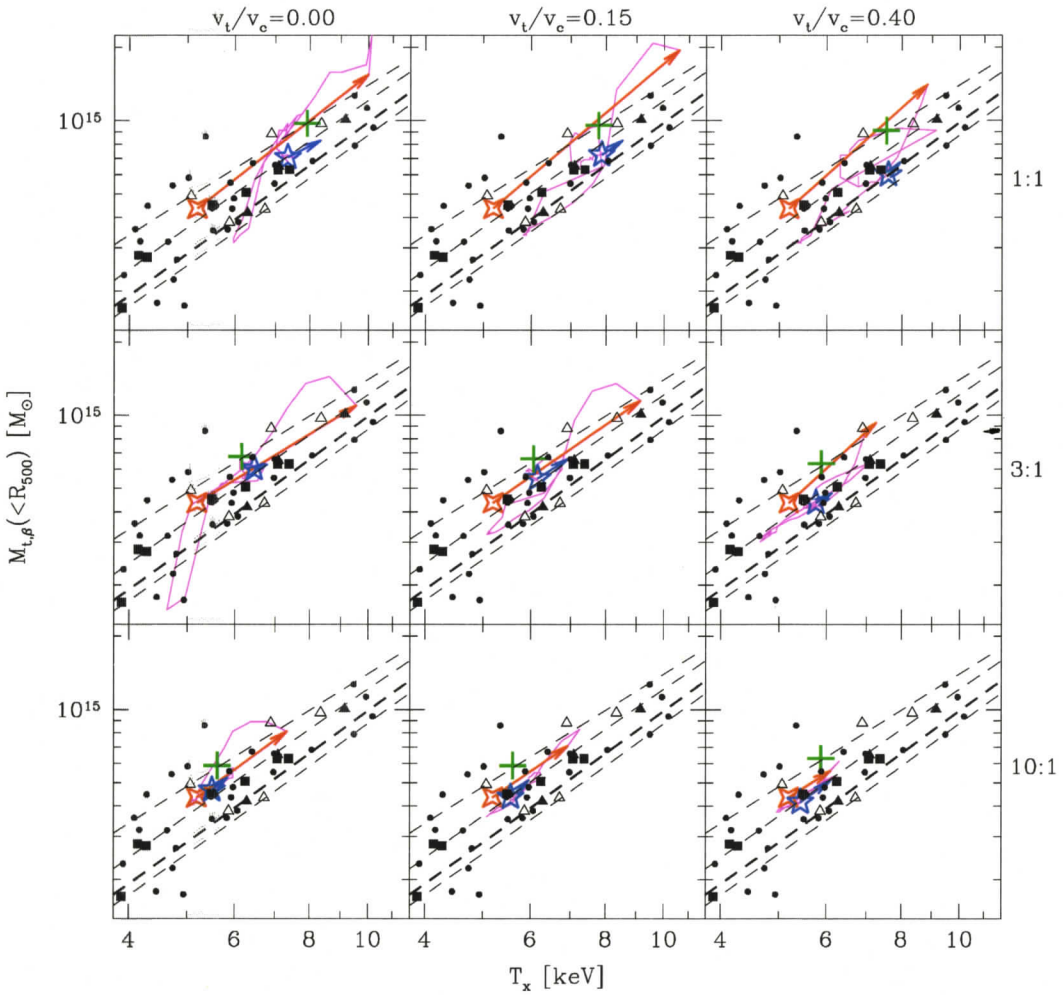

Figure 4.5: Isothermal β-model masses plotted against spectrally fit temperatures for our simulations (both integrated within R_{500}) and compared against observations. Red four and blue five point stars indicate the states of the system at t_o and t_{relax} respectively. The red vector indicates the evolution from t_o to $t_{closest}$ while the blue vector illustrates 3 Gyr of evolution following t_{relax}. The magenta line tracks the evolution from $t_{closest}$ to t_{relax} (generally 4-5 Gyr) during which the system is visibly disturbed. Green crosses indicate the remnant state necessary to preserve the observed mass-scaling relations. Black points are the observed catalogues of Horner (2001) and Reiprich & Böhringer (2002) with squares and triangles denoting compact cool core and non-compact core systems and open and filled points indicating apparently disturbed and relaxed systems respectively, following the approach of McCarthy *et. al.* (2004). Dashed lines are our fiducial analytic entropy injection models (S_o = 10,100,300, and 500 keVcm^2, increasing with decreasing luminosity) with the masses reduced by 30% to account for the bias in the isothermal β-model approach. Black text around the boundary indicates the mass ratio and v_t/V_c depicted by each panel.

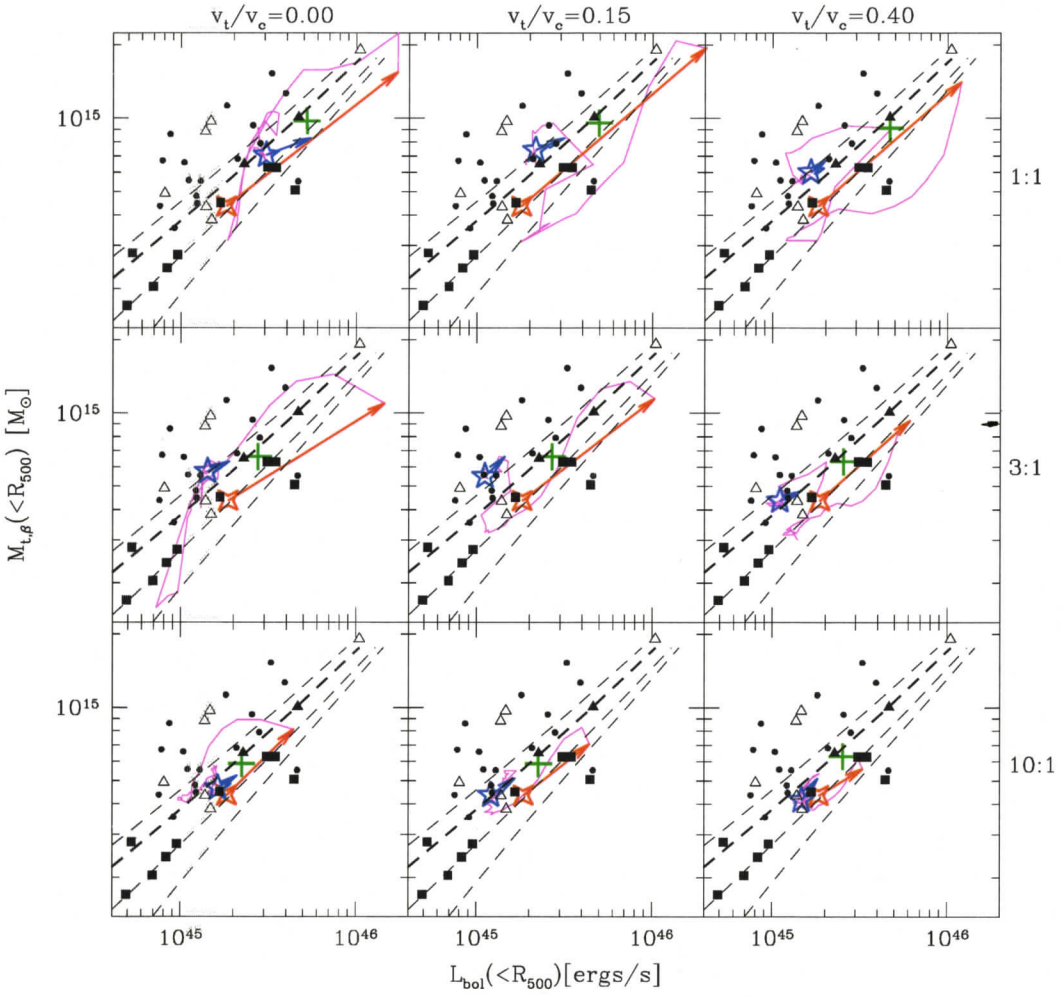

Figure 4.6: Isothermal β-model masses plotted against bolometric luminosities for our simulations (both integrated within R_{500}) and compared against observations. Red four and blue five point stars indicate the states of the system at t_o and t_{relax} respectively. The red vector indicates the evolution from t_o to $t_{closest}$ while the blue vector illustrates 3 Gyr of evolution following t_{relax}. The magenta line tracks the evolution from $t_{closest}$ to t_{relax} (generally 4-5 Gyr) during which the system is visibly disturbed. Green crosses indicate the remnant state necessary to preserve the observed mass-scaling relations. Black points are the observed catalogues of Horner (2001) and Reiprich & Böhringer (2002) with squares and triangles denoting compact cool core and non-compact core systems and open and filled points indicating apparently disturbed and relaxed systems respectively, following the approach of McCarthy *et. al.* (2004). Dashed lines are our fiducial analytic entropy injection models (S_o = 10,100,300, and 500 keVcm^2, increasing with decreasing luminosity) with the masses reduced by 30% to account for the bias in the isothermal β-model approach. Black text around the boundary indicates the mass ratio and v_t/V_c depicted by each panel.

4.3 Mass

To date, all catalogues of cluster masses involving significant sample sizes have been compiled from X-ray observations. The methods used are thus not direct (such as with lensing measures) but are inferred from temperature and surface brightness profiles using methods which may be highly susceptible to systematic biases, particularly during a merger. These approaches generally assume that the system can be described as being in a state of hydrostatic equilibrium; a condition given by

$$\rho_g^{-1}\frac{dP}{dr} = -\frac{GM_t(<r)}{r^2} \tag{4.3}$$

This yields a mass profile of the general form

$$M(r) = -\frac{kT(r)}{G\mu m_p}r\left[\frac{d\log\rho_g(r)}{d\log r} + \frac{d\log T(r)}{d\log r}\right] \tag{4.4}$$

where G and k are Newton's and Boltzmann's constants respectively, $T(r)$ is the temperature profile of the system, μ the mean molecular weight, m_p the mass of the proton and $\rho_g(r)$ the gas density profile. In Chapter 3 we examined the evolution of a hydrostatic disequilibrium parameter given by

$$H = 1 + \frac{\rho_g^{-1}\frac{dP}{dr}}{r^{-2}GM_t(<r)} \tag{4.5}$$

and illustrated that few clusters should satisfy the condition of hydrostatic equilibrium to better than $H = 15\%$. How does this affect masses obtained from Eqn. 4.4?

In Fig. 4.4 we present (in red) the evolution of the mass of our systems within $R_{500}(t)$ computed directly from our simulations using this relation. For comparison,

the actual total mass is presented as well (thick black). We can see from this plot that despite the limited validity of the hydrostatic equilibrium condition, masses computed from Eqn. 4.4 after t_{relax} (when the system appears as a single undisturbed remnant) successfully reproduce the system mass to within $\sim 5\%$, with a slight systematic bias towards higher values.

To implement Eqn. 4.4 to measure cluster masses without additional assumptions, accurate measurements of $\rho_g(r)$ and $T(r)$ must be made. The observational challenges of doing so have been considerable but with the increasing availability of high quality *Chandra* observations, significant progress has recently been made. Vikhlinin et al. (2006) for instance have presented a method of gas density and temperature deprojection which they have demonstrated to be accurate to a few percent (Nagai et al., 2006).

Presently however, statistically representative *Chandra* catalogues of sufficient size to study mass scaling relations are not available. For this reason, we shall use for comparison the catalogue of Reiprich & Böhringer (2002) who report masses within R_{500} measured from ROSAT and ASCA observations. These authors measure masses assuming that their observed systems are in hydrostatic equilibrium but make the further assumptions that the gas is isothermal and that it's density profile follows a parameterized form given by the β-model. For an X-ray surface brightness profile given by

$$S_x(r_p) = \frac{S_o}{(1 + (r_p/r_c)^2)^{3\beta - 1/2}} \tag{4.6}$$

the gas density profile of an isothermal gas is given by

$$\rho_g(r) = \frac{\rho_o}{(1 + (r/r_c)^2)^{3\beta/2}} \tag{4.7}$$

Under these assumptions, fitting Eqn. 4.6 to the surface brightness profile yields the logarithmic derivative of the density profile, producing the following relation for the total mass within R_{500}

$$M_\beta(R_{500}) = \frac{3\beta k T_x R_{500}}{G\mu m_p} \frac{(R_{500}/r_c)}{1 + (R_{500}/r_c)^2} \tag{4.8}$$

Temperature and β-model fits in the results presented by Reiprich & Böhringer (2002) are fit to the flux which extends to the observed radius of the system (with the central $0.1R_{200}$ excised for the temperature fits). The observed radius is generally comparable to R_{500} which is the radius we use to generate the isothermal β-model masses (computed from Eqn. 4.8) we present in Fig. 4.4 (in blue).

From this figure we can see that the isothermal β-model systematically underestimates the mass of our systems by $25 - 40\%$. This result is in good agreement with the findings of several other authors (*e.g.* Hallman et al., 2006; Rasia et al., 2006). The general trends in the scaling relations should not be affected much by this bias, but the normalization will be. This could have significant implications for cosmological studies conducted with isothermal β-model masses.

4.3.1 $M_t - T_x$ relation

In Fig. 4.5 we present the evolution of our isothermal β-model masses against temperature and compare them to the observed temperature catalogue of Horner (2001) and mass catalogue of Reiprich & Böhringer (2002). We follow the same format here as for Fig. 4.3. Red four and blue five point stars indicate the system's

state initially and when it appears relaxed at t_{relax}. The red vector indicates the evolution from t_o to $t_{closest}$ and the blue vector shows 3 Gyr of evolution following t_{relax}. The magenta line traces the evolution of the system between $t_{closest}$ and t_{relax}, when the system looks visibly disturbed. Green crosses indicate the β-model masses of our remnants scaled from their initial values by the actual change of mass within R_{500}, and their temperatures similarly scaled by the observed $M_t - T_x$ scaling relation of Sanderson et al. (2003). Dashed lines indicate our fiducial entropy injection models (with the entropy minimum increasing with temperature at a constant mass). For this plot, we have reduced the masses of these models by 30% to reflect the downward bias in isothermal β-model masses found in Section 4.3. When we do so, we find a good agreement between our fiducial models and the observed catalogue.

First, we see that there is a considerably smaller degree of scatter (in both the observations and our fiducial models) in this plane compared to what is seen in the $L_x - T_x$ plane. This is not a surprise given the strong correlation we expect between these quantities: it is the depth of the potential (which is set by the mass) which determines the virial temperature (and hence, X-ray temperature) of the system.

Next we see that the qualitative evolution of our mergers in this plane follows a very similar pattern to what is seen in the $L_x - T_x$ case: two transient increases in both quantities at $t_{closest}$ and $t_{accrete}$ which take the system roughly along our fiducial mass scaling relations, followed by a period of relaxation during which the system slowly evolves upward along the scaling relation but offset to some degree across its scatter. In both planes, the initial transient tends to pull the system towards the low temperature side of the scatter (away from the side preferentially occupied by NCC systems).

There are interesting differences between the evolution in the $L_x - T_x$ and $M_t - T_x$ planes however. Most notably, our mergers occasionally (in the head-on and $v_t/V_c = 0.15$ 1:1 and 3:1 cases) spend very brief ($t < 0.5$ Gyr) periods outside of the bounds of our fiducial models, at the very limits of the scatter in the observations. These

periods correspond to those in Fig. 4.4 during which we witness strong failures of the isothermal β-model at capturing the total mass of the system. We also see a couple of brief ($t < 0.5\,\mathrm{Gyr}$) excursions to the high temperature side of the observations after $t_{accrete}$ and before t_{relax} in the 1:1 off-axis and 3:1 $v_t/V_c = 0.15$ cases. These are not seen in the $L_x - T_x$ plane. This highlights the vulnerability of isothermal β-model mass estimates to the effects of mergers and the spurious contributions to scatter in the scaling relations likely being introduced by its use.

Such rare differences aside, our simulations suggest that mergers have a similar effect on the scatter of the $M_t - T_x$ plane as on the $L_x - T_x$ plane. Our (exceptionally rare) 1:1 off-axis mergers produce relaxed states which spread across the majority of the scatter in the observations while more common 3:1 and 10:1 mergers do not create states which reach the side of the observations preferentially inhabited by NCC systems.

Recently, Balogh et al. (2006) have studied the $M_t - L_x$ and $M_t - T_x$ scaling relations, paying attention to the scatter introduced by variations in dark matter halo concentrations and formation epochs. They find that, although reasonable variations in these properties can account for the observed scatter in the $M_t - T_x$ plane, they can not do so for the observations in the $M_t - L_x$ plane.

Variations in dark matter halo concentrations are a product of system-to-system variations in formation histories, which regularly consist of several merger events. The fact that our simulations generally remain well within the scatter of the $M_t - T_x$ plane lends support to the claims of Balogh et al. (2006) that mergers do not produce significant scatter beyond their effects in driving variations in formation time and concentration.

4.3.2 $M_t - L_x$ relation

In Fig. 4.6 we present the evolution of our isothermal β-model masses against luminosity, following the same format as Fig. 4.5. Once again we see the same qualitative evolution witnessed in the $L_x - T_x$ plane: two transients at $t_{closest}$ and $t_{accrete}$ followed by a period of relaxation during which the system evolves up the mass scaling relations. Furthermore, we see the same brief failures of the β-model mass estimates seen in the $M_t - T_x$ plane, which drive the system briefly ($< 0.5\,\mathrm{Gyr}$) outside our fiducial analytic models.

The scatter in this plane is much larger and it is immediately obvious that our simulations fail to produce states of sufficiently low luminosity to account for the observations in this plane. There is a hint that our systems evolve towards the low-luminosity side of the observed scaling relation, but only briefly ($< 0.5\,\mathrm{Gyr}$) and during the extreme disruptions generated during the head-on cases. In the more common off-axis cases, the system tends to evolve away from this side of the scatter when significantly disturbed.

4.4 Sunyaev-Zeldovich effect

Quite some time has passed since the original realization that the spectral signature of inverse Compton scattering of the cosmic microwave background (CMB) by the hot ICM of galaxy clusters could be detected as a temperature increment in the CMB and used as a probe of the ICM's structure (Sunyaev & Zeldovich, 1970, 1972). Known as the thermal Sunyaev-Zeldovich (SZ) effect, the observational challenges involved in its detection have been significant, making reliable data slow to emerge.

Several sensitive large-area SZ surveys will soon be available however and due to the near absence of redshift dependence on the mass-limit of the SZ effect's detectability, catalogues of tens of thousands of clusters will soon be available as an incredibly

powerful tool for studying cluster evolution and cosmology. The potential for mergers to introduce biases in these catalogues has a similar, but likely less severe potential to introduce systematic uncertainties into the analysis of these datasets (Majumdar & Mohr, 2003). Furthermore, because the SZ effect is dependent on a line of sight integral involving a single factor of density (rather than the ρ^2 dependence of emission studies), SZ observations of mergers will be useful as a complimentary tool to X-ray emission observations for determining the structure of the ICM.

The magnitude of a system's thermal SZ signature as a function of position on the sky (denoted by θ) is typically quantified by the Compton "y-parameter" given by

$$y(\theta) = \frac{\sigma_T}{m_e c^2} \int P_e(\vec{r})\, dl \tag{4.9}$$

where the integral is of the three dimensional pressure $P_e(\vec{r}) = n_e(\vec{r})kT(\vec{r})$ at position $\vec{r}$ and is performed along the line of sight through the system.

Compton parameters through the centre of the system ($\theta = 0$; denoted y_o) are commonly reported for systems. In Fig. 4.7 we plot the time evolution of y_o for each of our mergers, measured in the z-projection. Four lines are illustrated in each case: the red curves are y_o computed directly from our simulations and the blue curves are from an isothermal β-model fit to each output. This is done for comparison to observations which regularly assume this structure for observed systems when converting SZ decrements into values of y_o. Thick lines are for values generated from integrating through the entire system, while thin curves are generated with the central 30kpc of the system excised from the integration.

Whether the central core is excised or not, we can see from this plot that initially the β-model (blue curves) does an excellent job of capturing the value of y_o integrated directly from the simulations (red curves). However, when the core is included in

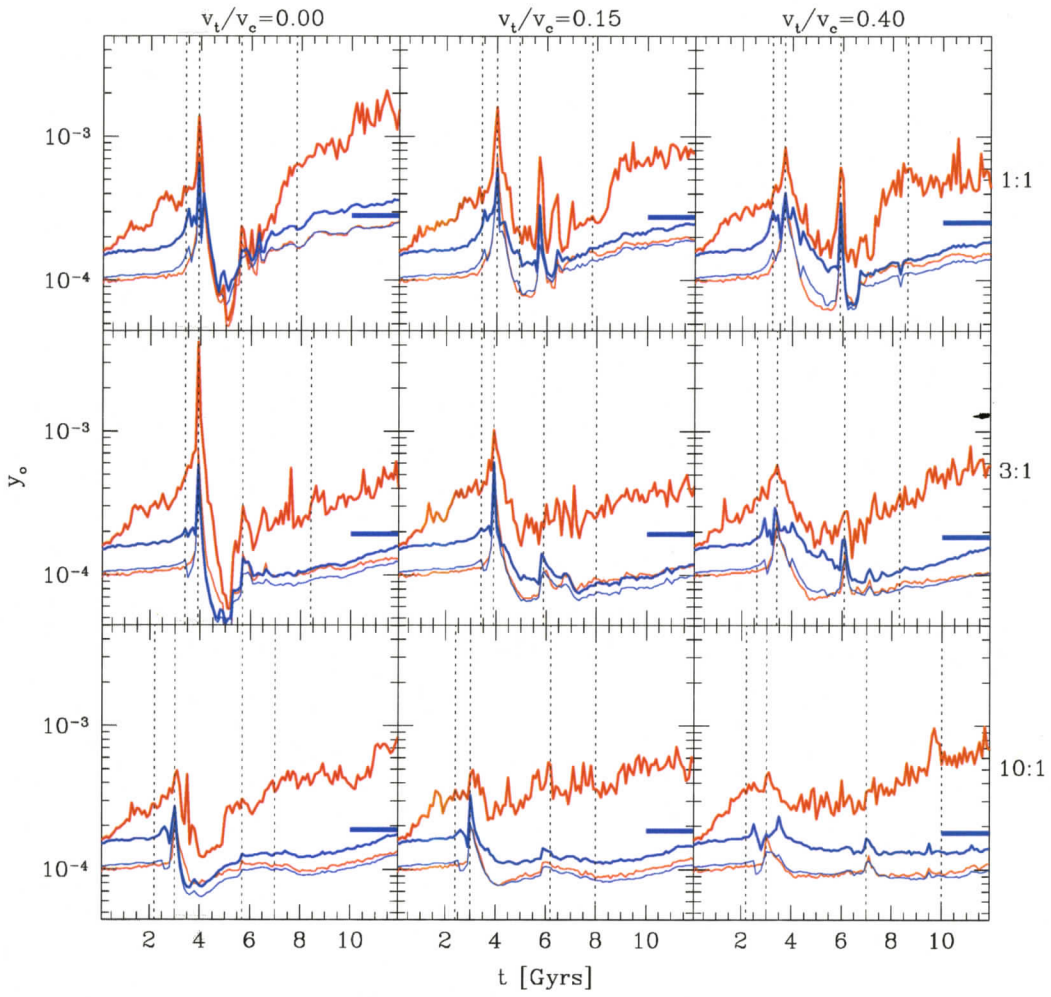

Figure 4.7: The evolution of central Compton parameter (y_o) as a function of time for our simulations. Results computed assuming an isothermal β-models are shown in blue while direct integrations of our simulations are in red. Thin lines are generated from integrations which excise the central 30 kpc of the system, while thick lines are from integrations through the entirety of the system. Horizontal dashes represent the final values expected from the mass scalings derived from our fiducial models (see Section 4.2.1). Vertical dotted lines indicate (from left to right) t_o (the time of virial crossing), $t_{closest}$ (first pericenter), $t_{accrete}$ (second pericenter) and t_{relax} (the moment our remnants would appear relaxed to a 50 ks *Chandra* exposure at $z = 0.1$). Black text around the boundary indicates the mass ratio and v_t/V_c depicted by each panel.

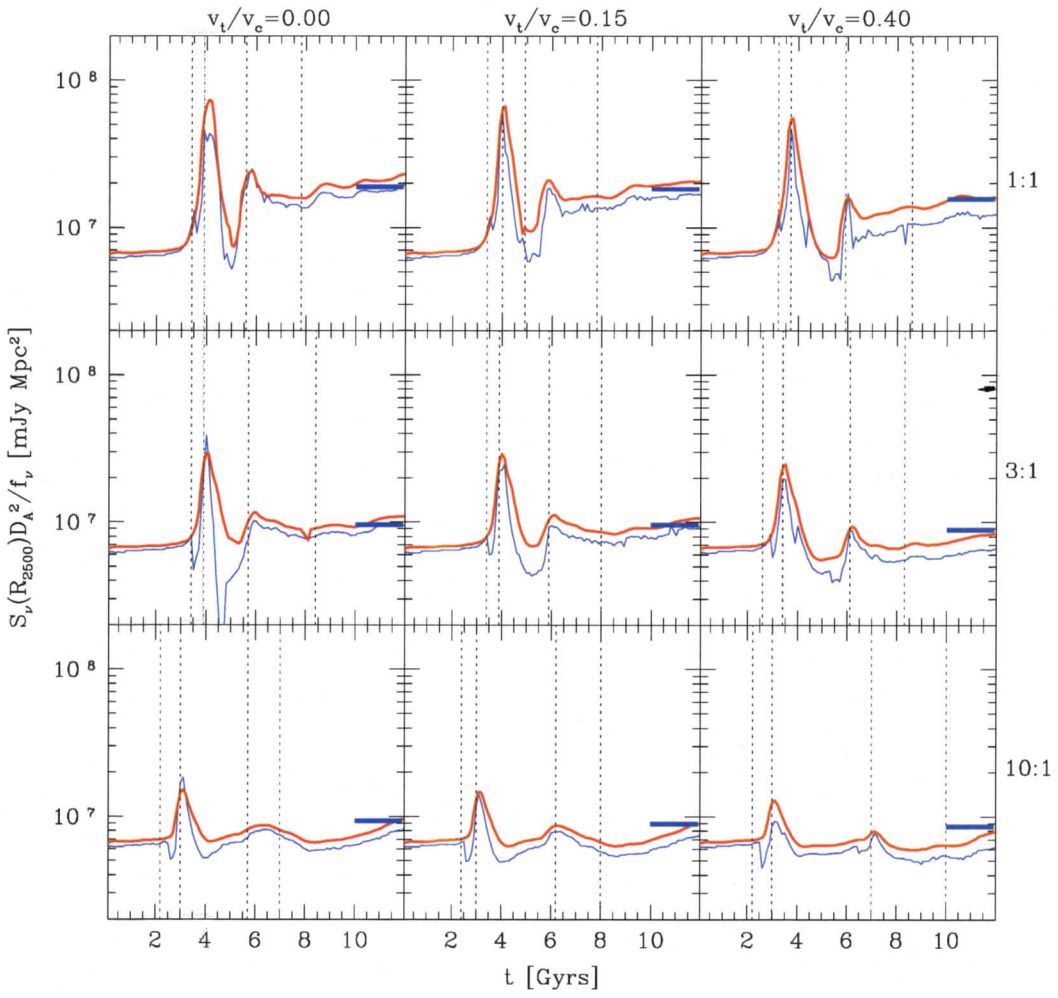

Figure 4.8: The evolution of integrated SZ fluxes ($S_\nu D_A^2/f_\nu$) computed within R_{2500} for our simulations as a function of time. Results computed assuming an isothermal β-model are shown in blue while direct integrations from our simulations are shown in red. Horizontal dashes represent the final values expected from the mass scalings derived from our fiducial models (see Section 4.2.1). Vertical dotted lines indicate (from left to right) t_o (the time of virial crossing), $t_{closest}$ (first pericenter), $t_{accrete}$ (second pericenter) and t_{relax} (the moment our remnants would appear relaxed to a 50 ks *Chandra* exposure at $z = 0.1$). Black text around the boundary indicates the mass ratio and v_t/V_c depicted by each panel.

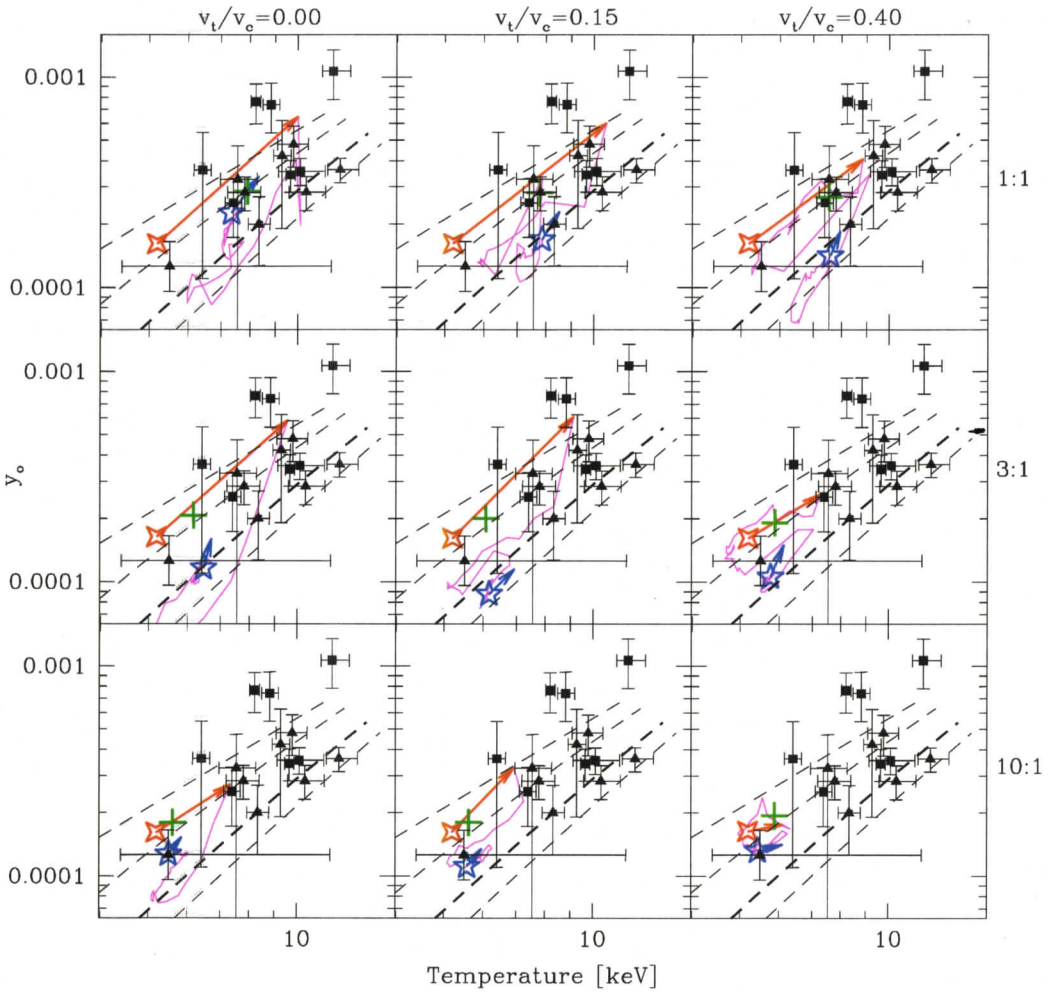

Figure 4.9: Evolution of the SZ Compton parameter (y_o) plotted against temperature for our simulations (both integrated within R_{500}) and compared against observations. Red four and blue five point stars indicate the states of the system at t_o and t_{relax} respectively. The red vector indicates the evolution from t_o to $t_{closest}$ while the blue vector illustrates 3 Gyr of evolution following t_{relax}. The magenta line tracks the evolution from $t_{closest}$ to t_{relax} (generally 4-5 Gyr) during which the system is visibly disturbed. Green crosses indicate the remnant state necessary to preserve the observed mass-scaling relations. Black points are the observed catalogue of Horner (2001) and Benson et al. (2004) with squares and triangles denoting compact cool core and non-compact core systems, following the approach of McCarthy *et. al.* (2004). Dashed lines are our fiducial analytic entropy injection models (S_o = 10,100,300, and 500 keVcm^2, increasing with decreasing luminosity). Black text around the boundary indicates the mass ratio and v_t/V_c depicted by each panel.

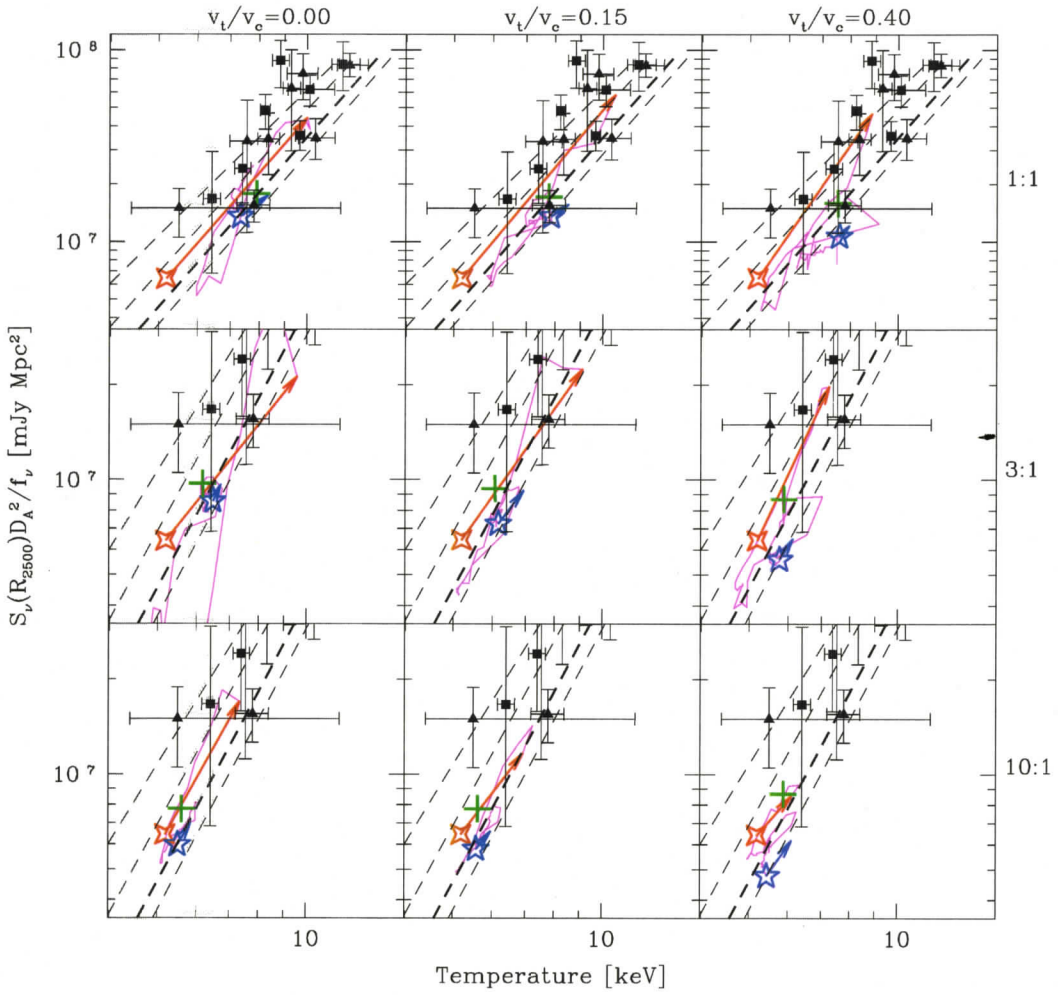

Figure 4.10: Evolution of the integrated SZ Compton parameter (S_ν, integrated within R_{2500}) plotted against temperature (integrated within R_{500}) for our simulations and compared against observations. Red four and blue five point stars indicate the states of the system at t_o and t_{relax} respectively. The red vector indicates the evolution from t_o to $t_{closest}$ while the blue vector illustrates 3 Gyr of evolution following t_{relax}. The magenta line tracks the evolution from $t_{closest}$ to t_{relax} (generally 4-5 Gyr) during which the system is visibly disturbed. Green crosses indicate the remnant state necessary to preserve the observed mass-scaling relations. Black points are the observed catalogue of Horner (2001) and Benson et al. (2004) with squares and triangles denoting compact cool core and non-compact core systems, following the approach of McCarthy *et. al.* (2004). Dashed lines are our fiducial analytic entropy injection models (S_o = 10,100,300, and 500 keVcm^2, increasing with decreasing luminosity). Black text around the boundary indicates the mass ratio and v_t/V_c depicted by each panel.

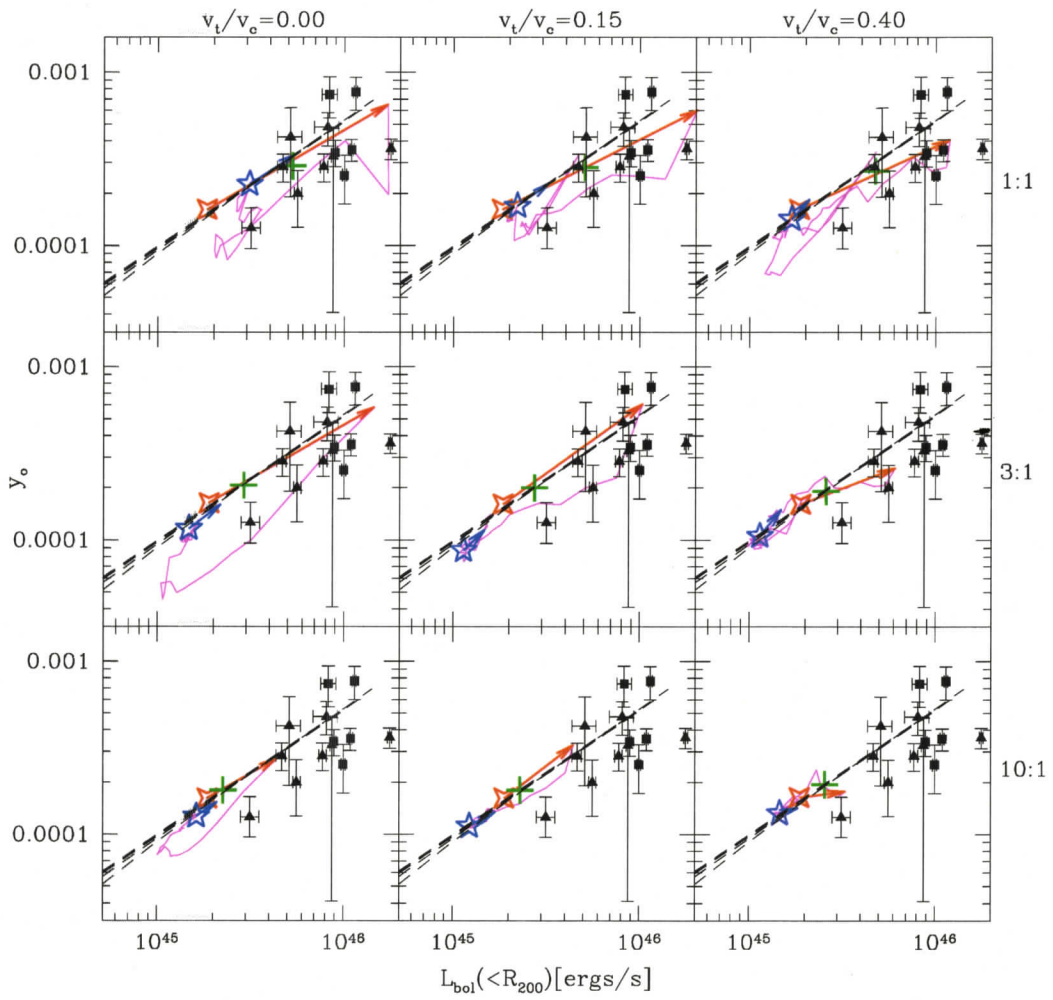

Figure 4.11: Evolution of the SZ Compton parameter (y_o) plotted against bolometric luminosity (integrated within R_{500}) for our simulations and compared against observations. Red four and blue five point stars indicate the states of the system at t_o and t_{relax} respectively. The red vector indicates the evolution from t_o to $t_{closest}$ while the blue vector illustrates 3 Gyr of evolution following t_{relax}. The magenta line tracks the evolution from $t_{closest}$ to t_{relax} (generally 4-5 Gyr) during which the system is visibly disturbed. Green crosses indicate the remnant state necessary to preserve the observed mass-scaling relations. Black points are the observed catalogue of Horner (2001) and Benson et al. (2004) with squares and triangles denoting compact cool core and non-compact core systems, following the approach of McCarthy *et. al.* (2004). Dashed lines are our fiducial analytic entropy injection models (S_o = 10,100,300, and 500 keVcm^2, increasing with decreasing luminosity). Black text around the boundary indicates the mass ratio and v_t/V_c depicted by each panel.

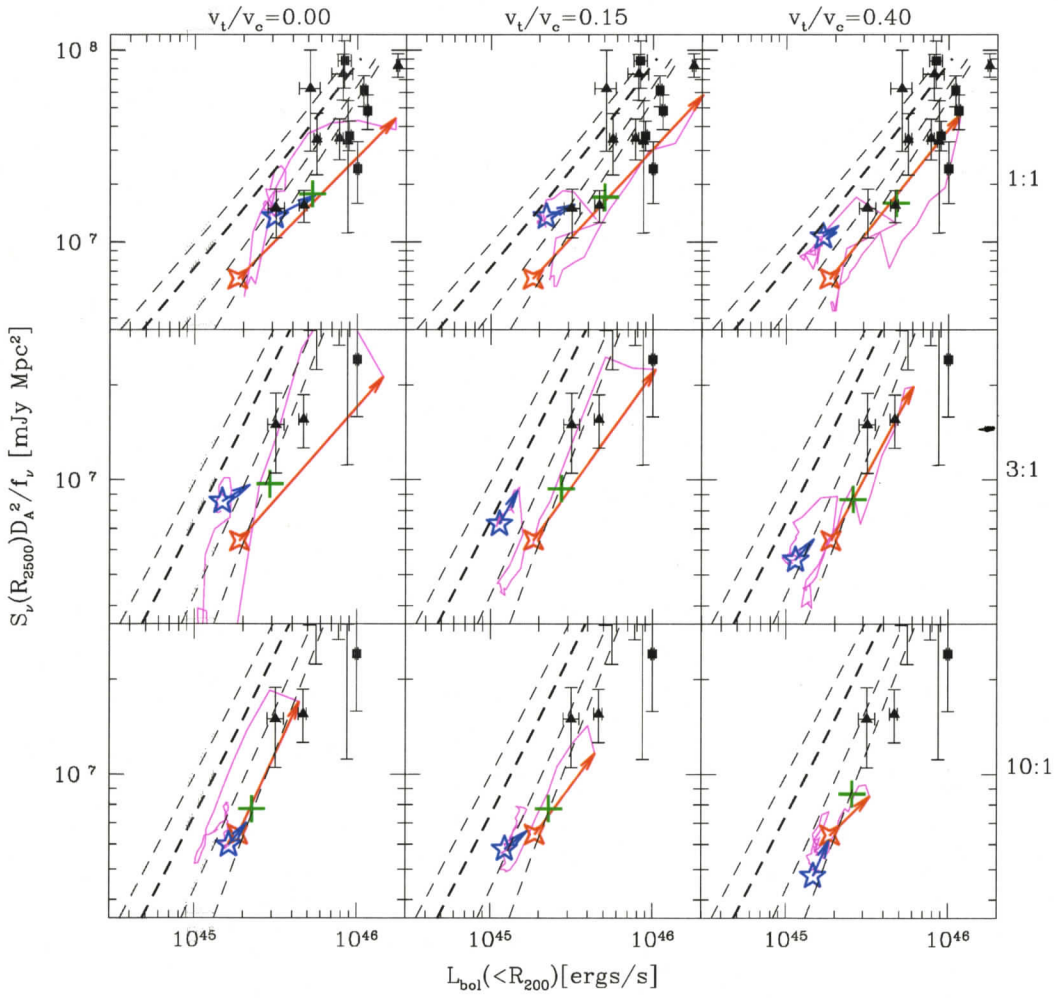

Figure 4.12: Evolution of the integrated SZ Compton parameter (S_ν, integrated within R_{2500}) plotted against bolometric luminosity (integrated within R_{500}) for our simulations and compared against observations. Red four and blue five point stars indicate the states of the system at t_o and t_{relax} respectively. The red vector indicates the evolution from t_o to $t_{closest}$ while the blue vector illustrates 3 Gyr of evolution following t_{relax}. The magenta line tracks the evolution from $t_{closest}$ to t_{relax} (generally 4-5 Gyr) during which the system is visibly disturbed. Green crosses indicate the remnant state necessary to preserve the observed mass-scaling relations. Black points are the observed catalogue of Horner (2001) and Benson et al. (2004) with squares and triangles denoting compact cool core and non-compact core systems, following the approach of McCarthy *et. al.* (2004). Dashed lines are our fiducial analytic entropy injection models (S_o = 10,100,300, and 500 keVcm^2, increasing with decreasing luminosity). Black text around the boundary indicates the mass ratio and v_t/V_c depicted by each panel.

the integration (thick curves), a rapid discrepancy grows between the direct and β-model results. The β-model remains nearly constant while the direct integration rises significantly until $t_{closest}$, when the primary core is disturbed. After $t_{accrete}$ (or continually since $t_{closest}$ in the off-axis 10:1 cases which do not significantly disturb the primary core), the values of y_o obtained directly from the simulations resume their rise relative to the β-model values.

Examining the evolution of y_o with the central 30 kpc excised, we see that the β-model does an excellent job of capturing the correct result through the entire duration of the event. This illustrates the extent to which the values of y_o computed directly from the simulations are sensitive to variations in the core's structure. Since 30 kpc is much smaller than r_c for almost all systems, and the β-model will treat regions within r_c as homogeneous, variations in this region will tend to be diminished by the β-model approach. This can be clearly seen in the β-model integrations which do not excise the core (think blue line): they trace the curves generated with the core excised (thin blue line) with a near constant offset of $\sim 75 - 95\%$, while the direct integration exhbits significant fluctuations much larger than those affecting the values computed from the β-model.

These properties of the β-model approach to determining y_o have both positive and negative consequences. On the one hand, reducing the sensitivity of y_o to regions whose structure is not well understood and whose evolution is affected by stochastic effects generated by central AGN should lead to much tighter scaling relations. This is useful for cosmological studies where measures which accurately characterize the total mass of the system are desired. On the other hand, the sensitivity of this measure to the structure of the central 30 kpc could provide useful insights to help us understand the uncertain structure of cluster cores and the processes active within them.

We have also placed thick dashes on Fig. 4.7 to represent the expected mass scaling ($y_{o,2}/y_{o,1} = (M2/M_1)^{\alpha}$, with α determined to be 0.93 from our fiducial models, since adequate empirical measures are not yet available) of y_o from its initial values.

This is performed for the β-model results which include the central core. We can see that the expected mass scaling of y_o is recovered in each case to within 30%, with a systematic tendancy for y_o to fall inreasingly below this value with increasing impact parameter.

Integrated Compton parameters can also be formed from Eqn. 4.9 according to

$$y_{int}(< \theta) = 2\pi \int_0^{\theta} y(\theta')\theta' \, d\theta' \tag{4.10}$$

However, SZ measurements are usually expressed in terms of frequency dependent flux densities which are given by

$$S_\nu = j_\nu(x) y_{int} \tag{4.11}$$

where $x = h\nu/kT$ is a dimensionless frequency and j_ν is a function which describes the spectral shape of the SZ distortion. This function is given by

$$j_\nu(x) = \frac{2(kT_{CMB})^3}{(hc)^2} f_\nu(x) \tag{4.12}$$

where

$$f_\nu(x) = \frac{x^4 e^x}{(e^x - 1)^2} \left(\frac{x}{\tanh(x/2)} - 4 \right) \tag{4.13}$$

To facilitate comparisons to observations, which are performed at many different frequencies and for systems at various redshifts, we remove the frequency and distance

(redshift) dependencies from our computed flux densities by reporting the quantity $S_\nu D_A^2 / f_\nu$.

In Fig. 4.8 we present the evolution of our merging systems' SZ flux integrated within a projected radius of R_{2500}. Once again we illustrate two quantities in each case, the integrated SZ flux computed directly from the simulations and from an isothermal β-model (in the z-projection in both cases). We see that the isothermal β-model successfully tracks the actual value, with a slight and persistent underestimate of $\sim 10-35\%$. In addition, we have placed thick dashed lines to indicate the expected mass scalings of S_ν from its initial values ($S_{\nu,2}/S_{\nu,1} = (M_2/M_1)^\alpha$, with α determined from our fiducial models to be 1.63, once again, because adequate empirical measures are not yet available). We see that this SZ measure recovers the mass scaled values far better than y_o.

In all our simulations the evolution of both S_ν and y_o follows the familiar pattern seen for $L_x(t)$, $T_x(t)$ and $M_t(t)$: a rapid rise that begins shortly before $t_{closest}$, a subsequent drop to values below the initial state, a second (but substantially weaker) peak at $t_{accrete}$, a slow decrease until t_{relax} and then a final rise continuing to the end of the simulation. Radiative and adiabatic cooling (arising from an expansion of the core) results in a significant reduction from the initial value following $t_{accrete}$. As active cooling reestablishes in the remnant cores, the system's integrated SZ signature begins increasing.

For the remainder of this section, we shall examine the scaling relations constructed from these quantities and the X-ray temperature and luminosity. Observations for comparison to our simulations are still very sparse however, and we present these plots for completeness and to establish theoretical expectations for understanding larger data sets, once they become available.

4.4.1 SZ$-T_x$ scaling relations

The scaling behaviours of y_o and S_ν with T_x are presented in Figs. 4.9 and 4.10 following the format of our previous scaling relation plots: blue four and red five point stars mark the system's state at t_o and t_{relax} respectively, while red vectors illustrate the system's evolution from t_o to $t_{closest}$ and blue vectors mark 3 Gyr of evolution following t_{relax}. In this case however, we use the heterogeneous catalogue of massive systems presented by Benson et al. (2004) for our observational comparison (black points).

4.4.2 SZ$-L_x$ scaling relations

In Figs. 4.11 and 4.12 we present the evolution of our simulations in the $y_o - L_x$ and $y_o - T_x$ planes, following the same format as in Section 4.4.1. In the $y_o - L_x$ plane we immediately see the strikingly small variation in the mass scaling relations of our fiducial models, independent of S_o, first predicted by McCarthy et al. (2003). Our simulations also show that in all cases, following t_{relax} (blue five star point) our systems return to this relation and evolve along it. During the initial disturbance from t_o to $t_{closest}$ however (red vector), the system tends to evolve away from this relation towards higher luminosities. Curiously, a significant fraction of the systems in the Benson et al. (2004) catalogue lie to this side of the relation.

In Fig. 4.12 we find that the degeneracy in the SZ$-L_x$ mass scaling relations with K_o is broken, with both our fiducial models and the observations exhibiting significantly more scatter. Once again however, the initial transient tends to take the system away from the mass scaling relations towards higher luminosities, with the system evolving to the low luminosity side of the plane at t_{relax} (blue five point star). Following t_{relax}, the system generally evolves back towards the high luminosity side of the relation (there are three exceptions: the 1:1 and 10:1 $v_t/V_c = 0.4$ cases and 3:1 $v_t/V_c = 0.15$ case, as seen in the $y_o - T_x$ plane).

Without a statistically representative sample of lower mass systems, it is not possible at this point to draw any specific comparisons between our simulations and the observations in these planes however.

4.5 The X-ray Sunyaev-Zeldovich proxy

Lastly, we have examined the evolution of the X-ray proxy for SZ fluxes introduced by Kravtsov et al. (2006). This proxy is given by

$$Y_x(< R) = M_g(< R)T_x \tag{4.14}$$

where M_g is the gas mass within R and T_x is the X-ray temperature measured within R. In Fig. 4.13 we present the evolution of Y_x integrated within R_{500} as measured directly from our simulations (red) and our isothermal β-model fits (blue; in the z-projection in all cases). The evolution of this quantity is (as expected) very similar to that of the integrated SZ flux with a similar underestimate of $\sim 15 - 25\%$ by the isothermal β-model from actual values. We have once again placed thick dashes to indicate the expected mass scalings from initial values.

4.5.1 $M_t - Y_x$ relation

In Fig. 4.14 we present the scaling of the X-ray SZ proxy with total mass. Astonishingly, we find that our system remains well confined within the 8% scatter bounds of the mean relation determined by Kravtsov et al. (2006) at all times. There is a slight tendency for the final remnant to be moved towards the high-Y_x side of the relation with a slow evolution back to the mean relation in the 10:1 cases.

We present results for only the z projection in Fig. 4.14 but have confirmed that the system remains within the 8% scatter bounds at all times in all projections.

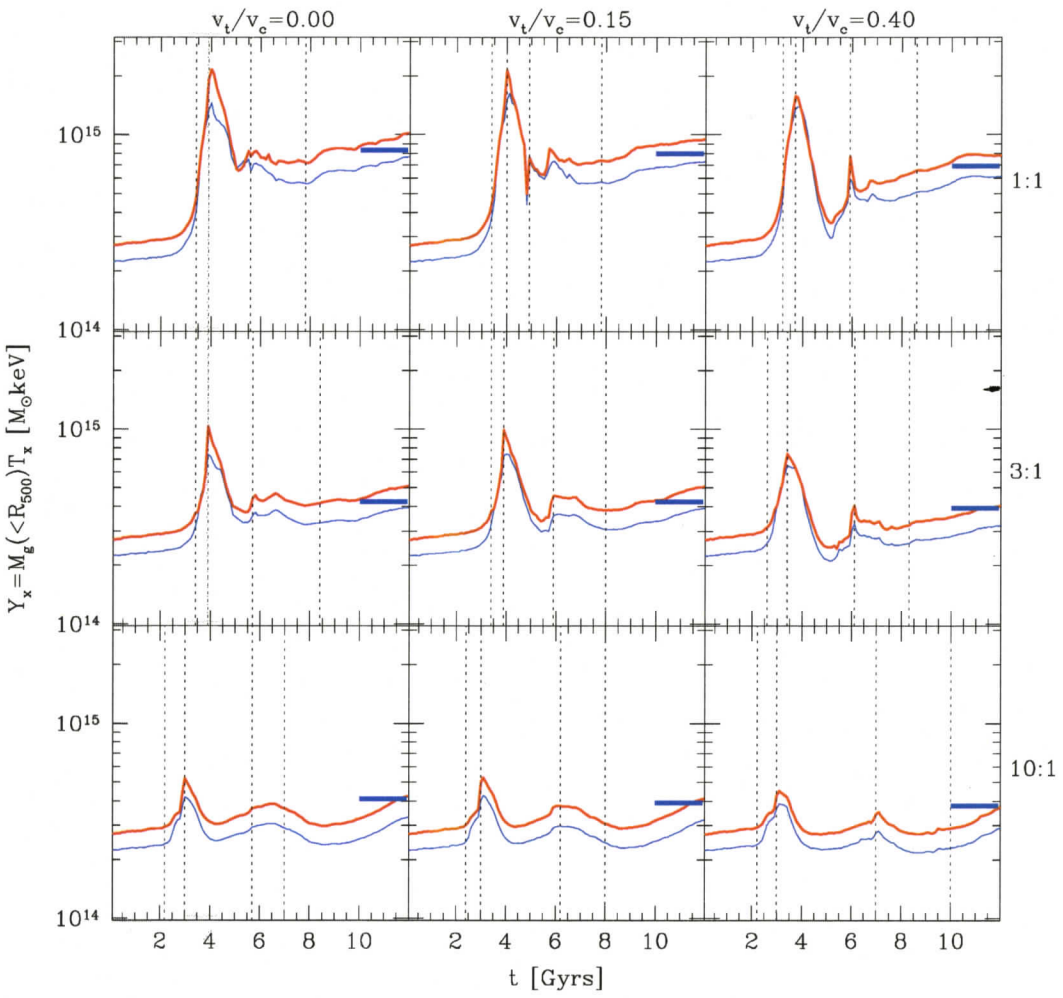

Figure 4.13: The X-ray SZ proxy ($Y_x = M_g T_x$) for our simulations as a function of time. Thick red curves illustrate values integrated directly from our simulations while thin blue lines are computed according to Kravtsov et al. (2006). Horizontal dashes represent the final values expected from the mass scalings derived from our fiducial models (see Section 4.2.1). Vertical dotted lines indicate (from left to right) t_o (the time of virial crossing), $t_{closest}$ (first pericenter), $t_{accrete}$ (second pericenter) and t_{relax} (the moment our remnants would appear relaxed to a 50 ks *Chandra* exposure at $z = 0.1$). Black text around the boundary indicates the mass ratio and v_t/V_c depicted by each panel.

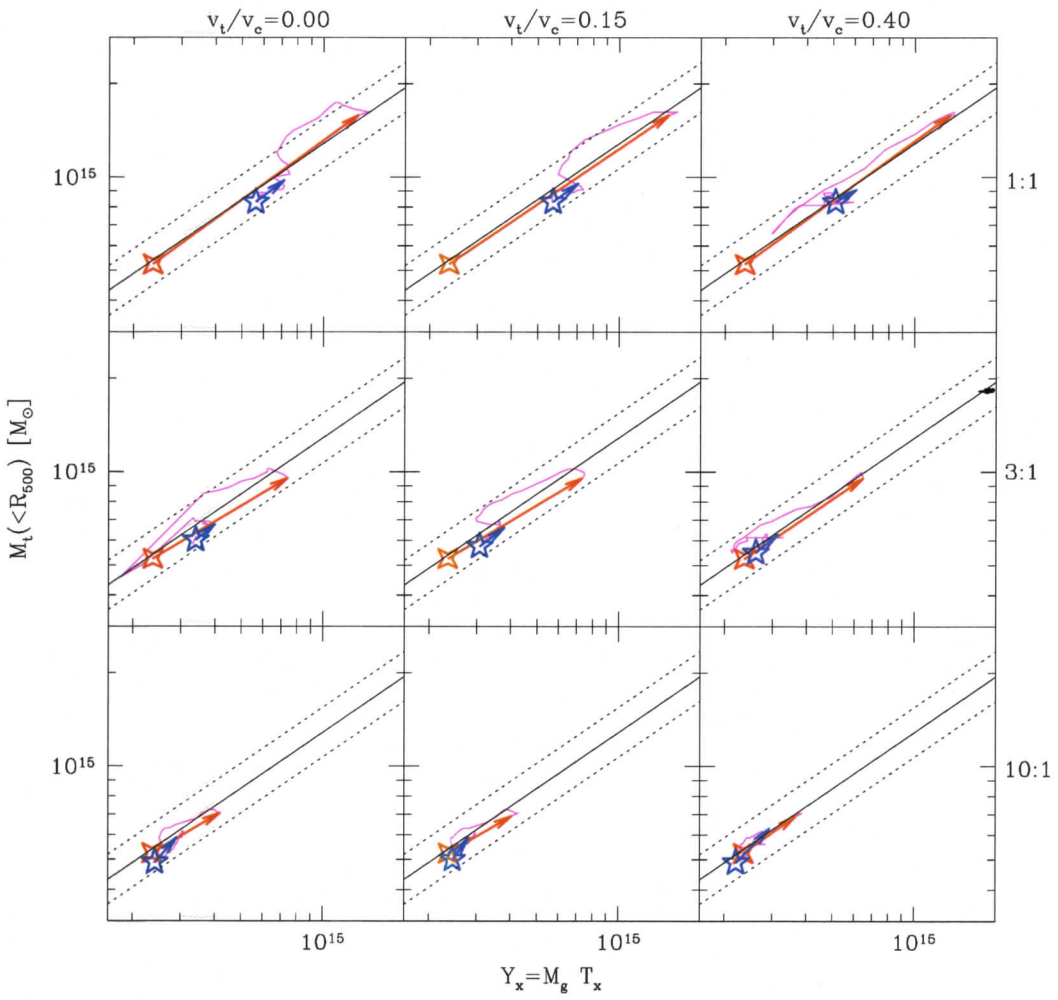

Figure 4.14: Evolution of the X-ray SZ proxy (Y_x) introduced by Kravtsov et al. (2006) plotted against total mass for our simulations (both integrated within R_{500}). Red four and blue five point stars indicate the states of the system at t_o and t_{relax} respectively. The red vector indicates the evolution from t_o to $t_{closest}$ while the blue vector illustrates 3 Gyr of evolution following t_{relax}. The magenta line tracks the evolution from $t_{closest}$ to t_{relax} (generally 4-5 Gyr) during which the system is visibly disturbed. Green crosses indicate the remnant state necessary to preserve the observed mass-scaling relations. Black text around the boundary indicates the mass ratio and v_t/V_c depicted by each panel.

4.6 Chapter summary

Building on the results of previous authors (most notably, Ricker & Sarazin, 2001), we have identified a generic evolutionary sequence for the SZ properties and X-ray luminosity, temperature and mass measures of X-ray cluster mergers. In all the cases we have studied (which we believe represent a significant range of cluster merger initial conditions), these properties exhibit large increases during core-core interactions at $t_{closest}$ and $t_{accrete}$ with an intervening drop from initial values due to the expansion of the primary system in response to the initial core-core interaction. Our systems then experience a subsequent rise in all quantities following t_{relax} due to the reestablishment of efficient radiative cooling in the remnent cores, lasting for the remainder of the simulations.

Because of this common evolution in the global properties we have studied, merger systems tend to evolve in a generic way in scaling relations constructed from them: there is an initial transient which evolves roughly along the mass scaling relations, followed by a drift across the relation until t_{relax}, after which the system quiescently evolves along the mass scaling relation.

Only in the cases of our off-axis equal mass mergers are states produced which can account for the scatter in the observed X-ray scaling relations. We argue that such mergers are extremely rare however and should not have a significant effect on the statistical properties of the population. Our more common 3:1 and 10:1 mergers fail to generate states which can account for the observed scatter in almost all cases. Generally, these mergers can push relaxed clusters to the median position of the observed scaling relations, but not past it (not even transiently).

Several other, more specific findings of our study, include:

- The luminosity integrated within $R_{500}(t)$ recovers the observed mass scaling relations only in the head-on cases. As mergers are moved off-axis, the remnant's luminosity becomes steadily less than expected from the observed mass scaling

(discrepancies are $16-50\%$). This discrepancy is still present but is reduced to levels of $3-28\%$ if the central regions ($r < 0.1R_{200}$) are excised.

- We have studied the evolving temperatures of our mergers using 3 temperature measures: emission weighted temperatures (T_{ew}), the "spectroscopic-like" average presented by Mazzotta et al. (2004) (T_{sl}) and isothermal fits to integrated spectra (T_{spec}). We find that T_{ew} is higher than the other two measures at all times and that T_{spec} produces results which agree with T_{sl} to within 5% at nearly all times. We thus confirm the utility of this method for generating globally averaged temperatures from massive simulated clusters.

- T_{ew} yields remnant temperatures significantly in excess of what is expected from the observed mass scaling relation while the other measures recover the observed mass scaling result in all cases to within 15%. This should lead to significantly less scatter in theoretical $L_x - T_x$ relations computed with T_{sl} or T_{spec}.

- The temperature spikes following first and second pericentric passage (at $t_{closest}$ and $t_{accrete}$ respectively) are $15-40\%$ larger for the T_{ew} measure than the other two methods. This suggests that the estimates of the effect of merger-driven temperaure spikes on mass functions determined from temperature scaling relations utilizing T_{ew} (*e.g.* Randall et al., 2002) have been exagerated.

- As a consequence of the mass scaling behaviours of L_x and T_x, head-on mergers ultimately move systems along the observed $L_x - T_x$ scaling relation while off-axis mergers scatter systems towards lower luminosities.

- Despite the fact that systems do not satisfy the condition of hydrostatic equilibrium to better than 15%, masses determined from assuming that the condition applies are accurate to approximately 5%.

- Isothermal β-models track the evolution of the actual mass of the system before

the interaction and while appearing relaxed afterwards, but with a systematic underestimate of $25 - 40\%$ supporting the findings of several previous studies.

- Adjusting the masses of a set of theoretical models (which account for the observed scatter in the $L_x - T_x$ and SZ scaling relation planes) downwards by 30% sucessfully accounts for normalization of the observations in the $M_t - T_x$ and $M_t - L_x$ planes (which have been compiled using this mass measure). Our mergers remain well within the bounds of these models (except for a few small discrepancies in head-on cases, which last less than 0.5 Gyr) in both planes. In the $M_t - T_x$ plane, this represents a significant fraction of the observed scatter, but not in the $M_t - L_x$ planes. This lends support to the findings of Balogh et al. (2006) who claim that the scatter in the $M_t - L_x$ plane is too large to be accounted for by variations in cosmology, formation time, dark matter concentration or mergers.

- The isothermal β-model effectively reproduces the actual results for the SZ observables y_o and $S_\nu(< R_{2500})$ (with slight underestimates of $X\%$ and $X\%$ respectively). Theoretical mass scaling relations are reproduced in all cases to within $X\%$. There is a slight bias towards being low compared to the mass scalings which increases very weakly with impact parameter.

- Remarkably little scatter is expected in the $y_o - L_x$ plane (McCarthy et al., 2003) and we find that mergers preserve this tight relationship except during periods of exceptional disturbance. During this time, the core's density can be reduced and the system's luminosity increased (due to the enhanced densities and temperatures generated by the event). This has the effect of displacing systems to the right of the relation where many of the systems observed by Benson et al. (2004) are found. This may suggest that many of their systems are significantly disturbed, which might be expected given the high temperatures

of the systems they have examined.

- We have also examined the "SZ proxy" introduced by Kravtsov et al. (2006). It evolves similarly to y_o and S_ν and preserves the expected mass scaling relations as well.

- Regardless of projection effects, the SZ proxy of Kravtsov et al. (2006) obeys their reported mass scaling to within 8% over the entire duration of all our merger events.

We conclude that the full dispersion in none of the scaling relations we have studied (with the exception of the $M_t - T_x$ plane) can be produced from simple two body mergers between common relaxed compact cool core systems. However, some displacement across each plane does occur and this is driven primarily by changes in the structure of our cluster's cores. Thus, the outer (*i.e.* $r > 0.1R_{200}$) structure of clusters which are not experiencing obvious significant mergers are preserved by such events. This is satisfying in light of recent observations suggesting that the outer structure of clusters exhibit a universal structure once scaled appropriately.

We find however that mergers are altering the structure of compact cool cores (although not sufficiently to account for the observed range of system properties) and we shall explore the details of these effects and the processes driving them in the next chapter.

Chapter 5

Effects on compact cool cores

Abstract

We use the simulations presented in Chapter 2 to examine the effects of mergers on compact cool core (CCC) systems. We find that mergers can drive the system into two additional states: extended warm core (EWC) and compact warm core (CWC) states. In off-axis mergers, the initial interaction of the cores does not generally disturb the primary from its initial CCC state. However, in 1:1 and 3:1 off-axis cases, the accretion of a stream of low-entropy material formed from the core of the secondary can significantly disrupt the CCC morphology of the system. In only two cases (1:1 $v_t/V_c = 0.4$ and 3:1 $v_t/V_c = 0.15$) do long lived EWC morphologies result however. More generally, CWC states are generated and in cases where EWC states are produced, the core returns to a compact state much more rapidly than it regains its cool temperatures. Thus, mergers naturally account for the CWC systems seen in recent *Chandra* observations. Furthermore, the morphological segregation identified by McCarthy *et. al.* (2004) in scaling relations and in the $\beta - r_c$ plane are qualitatively produced (although, to reiterate the results of Chapter 4, the full scatter in these planes is not generated). Lastly, we find that mergers have very little impact on central metalicity gradients. Together, these findings pose a significant challenge to the common belief that extended core systems (which generally lack enhanced central metallicities) are a product of cluster mergers.

The latest generation of X-ray telescopes have revolutionized our understanding of the intracluster medium (ICM) of galaxy clusters but yet one of the oldest observations of the field remains poorly understood. As significant sample sizes of X-ray clusters initially became available, it was quickly realized that two distinct

populations could be identified from the shape of a system's X-ray surface brightness profile (Jones & Forman, 1984; Ota & Mitsuda, 2004): one with highly peaked central surface brightnesses (compact cores; $r_c \sim 50\,\mathrm{kpc}$) and one with flat central surface brightnesses (extended cores; $r_c \sim 150$ kpc). It has since become accepted that high and centrally peaked gas densities are primarily responsible for the central surface brightnesses of compact cores while extended cores possess lower and more constant central gas densities.

As a consequence of the ρ^2 dependence of the ICM's emissivity, radiative cooling should be significantly more relevant to the structure of compact cores. This assertion is supported by observations which have indicated that compact cores (classically referred to as "cooling flow" systems) tend to host central positive temperature gradients (De Grandi & Molendi, 2002), low central entropies (McCarthy *et. al.* , 2004) and radiative cooling rates which should release their thermal energy on timescales (the "cooling time"; t_{cool} hereafter) much shorter than a Hubble time (Allen, 1998). Extended cores (classically referred to as "non-cooling flow" systems) on the other hand tend to have flat central temperature profiles, elevated central entropies and cooling times in excess of a Hubble time.

Within the context of specific physical models, cooling-flow systems were once believed to host bulk radial flows of cold gas as a result of the loss of pressure support arising from their short cooling timescales. Great observational progress has been made since the launch of *Chandra* and XMM and cluster cores are now understood to be more complicated than this. As a result, the terminology of this field is in flux. To render the results of our study clearly, we propose the adoption of new nomenclature for describing the morphology of X-ray cluster cores. In Section 5.3.1 we will illustrate that compact core systems can be divided into two classes, yielding three distinct cluster populations: compact cool core (CCC) systems, compact warm core (CWC) systems and extended warm core (EWC) systems. Under this naming convention, classical cooling flows will generally be classified as CCC systems and

non-cooling flows (or extended cores) as EWC systems.

Despite great progress in understanding the structure of cluster cores, the origin and precise nature of the bimodality in surface brightness core radii still lacks a clear and definitive explanation. Several hypotheses have been proposed to account for these populations, with three being particularly persuasive.

First, it has been known for a decade that radiative cooling and shock heating during accretion are not sufficient to account for the observed structure of X-ray clusters. McCarthy *et. al.* (2004) (M04 henceforth) have developed a model in which entropy injection (possibly due to galactic outflows or early AGN activity) during the protocluster phase establishes a spectrum of minimum entropies for clusters leading to variations in cluster core cooling efficiencies. Reasonable amounts of such additional entropy ($\sim$ 200 keVcm^2) and radiative cooling account for the normalization and scatter in the observed $L_x - T_x$ and $M_t - T_x$ relations while obeying observed cold gas constraints. M04 also illustrate how clusters receiving little entropy injection quickly evolve to states resembling CCC systems as a natural consequence of radiative cooling. Systems receiving higher levels remain in long lived NCC states. Although not stated explicitly in their discussion, systems evolving to CCC states in this model would then be stabilized through several possible feedback processes (Voit & Donahue, 2005; Nusser et al., 2006).

Second, the entropy injection required to account for the structure of extended cores may have occurred more recently through interactions of active galactic nuclei (AGN) with the ICM. Such interactions have been observed in the cores of several systems where jets from AGN are seen to be actively inflating large high-entropy cavities (or "bubbles"). Typically, such interactions are localized to the central $\sim$ 50 kpc of a system but in a few instances, much larger outbursts reaching to $\sim$ 200 kpc have been observed (McNamara et al., 2005). Such cases are rare in the local universe and unlikely to transform a compact core into an extended core, but it is possible that repeated events during earlier epochs when AGN activity is observed

to be more active could. There is evidence to support this hypothesis (Nusser et al., 2006). Perhaps the most compelling is the study of ROSAT-observed groups presented by Croston et al. (2005) which strongly suggests that AGN do indeed significantly heat group-scale systems.

Lastly, mergers offer a compelling means by which to transform compact core systems into extended core systems. It has been a tacit belief for some time that extended core systems are a product of merger interactions but the issue has received remarkably little detailed consideration. This hypothesis is primarily based on early anecdotal observations that few compact cores exhibited disturbed morphologies while the limited number of studied extended core systems tended to be disturbed (Edge, Stewart, & Fabian, 1992; Buote & Tsai, 1996). However, with improved instrumentation and larger sample sizes, there are now several examples of disturbed compact core systems (*e.g.* A2204, Sanders et al., 2005), including ones presently undergoing significant mergers (*e.g.* A2142, Markevitch et al., 2000), as well as extended core systems lacking any evidence of having been disturbed at all (*e.g.* RXCJ0043.4-2037 & RXCJ0532.9-3701, Finoguenov et al., 2005).

Despite such concerns, the merger-origin hypothesis for extended core systems is appealing on theoretical grounds. The presently favoured hierarchical clustering paradigm for structure formation predicts that large objects are formed through regular accretion of smaller subclusters with each observed system representing the product of a unique history of many such events. This process is seen to be active to the present epoch with recent *Chandra* and XMM observations routinely detecting evidence of significant recent or ongoing mergers. With as much as 10^{60} ergs of initial kinetic energy, mergers are energetically capable of significantly modifying the structure of a system's ICM through the shocks they produce. Furthermore, the wide variety of individual accretion histories may lead naturally to a range of remnant states like that described by M04.

Recent studies that have investigated cluster mergers in a context capable of

testing the merit of this scenario have yielded inconclusive results. In the influential study of Ricker & Sarazin (2001, RS01 hereafter) for instance, some evidence for the flattening of central density profiles due shock heating from mergers is presented. However, since the focus of their study was on merger induced luminosity and temperature "boosts", they did not include the effects of cooling (which are known to be important to the structure of compact core systems) and they present relatively little detailed analysis of their remnant cores' structures. Gomez et al. (2002) and Ritchie & Thomas (2002) have constructed suites of idealized merging systems but their conclusions regarding the stability of compact core systems to mergers conflict. Gomez et al. (2002) find that systems with initially short cooling times will likely reestablish their structure while Ritchie & Thomas (2002) find that compact core systems are completely disrupted in equal mass and near-axis 8:1 mergers. In both cases however, the initial conditions of their merger systems differ significantly from our contemporary understanding of compact core systems.

In this chapter we establish criterion for quantifying the evolving morphology of merging systems (Section 5.3.1) and present their evolution through three distinct morphological states (Section 5.3.2). We then relate the occurrence of these states to changes in the structure of the system's core (Section 5.3.3). After considering the morphological segregation mergers induce in observed scaling relations (Section 5.3.4) we then consider the mixing effects of mergers on metalicity gradients (Section 5.4). Finally, we summarize the chapter in Section 5.5.

5.1 Consequences of our coarsely sampled initial conditions

In Chapter 4 we performed an extended Press-Schechter analysis of merger rates to argue that our 1:1 mergers are expected to be extremely rare, our 3:1 mergers

uncommon but of statistical significance and our 10:1 mergers extremely common. For these reasons, when considering the effects of mergers in the context of statistical properties of cluster populations, we are primarily concerned with the effects of 3:1 and 10:1 events.

We will find in later sections that the structure of cluster cores following mergers is the result of a delicate balance between shock heating and radiative cooling. In particular, we shall illustrate in Section 5.3.3 the important role stream accretion plays in setting the entropy of our merger remnant's cores. The efficiency of this process depends sensitively on many factors. These include the mass and density of material present in the stream (which depends on the initial mass of the secondary and the initial orbit, which determines in a complicated way, the details of the stream's structure) and the velocity it carries to the remnant core (which also depend on the initial orbit and the secondary mass, which determines the degree of dynamical friction experienced by the secondary).

The impact parameters and mass ratios of our simulations were selected to represent the most interesting range of situations exhibited by dark matter substructure in cosmological simulations. However, these ranges are sampled very sparsely by our simulations. As a result, we can not perform a systematic analysis of many items discussed in this chapter. We shall merely seek to reveal the general processes most relevant to establishing the structure of cluster cores following mergers. Many details will have to be left open to future study.

5.2 A cautionary note regarding central core structure

In SPH cluster simulations, cooling converts hot gas in the centre of the system into dense cold gas which is then (when star formation is included) transformed

into a collisionless stellar medium. As a result of the finite timescales involved in transforming cold gas into stars, a multiphase interface forms between dense cold gas and hot rarefied gas at the center. It is well known that multiphase interfaces of this sort are poorly treated in SPH simulations which incorporate cooling (Ritchie & Thomas, 2001; Marri & White, 2003). The result is a quasi-adiabatic flow which drives compressional heating as hot material collects several kernel radii outside of the multiphase interface. This leads to artificially suppressed densities and enhanced temperatures and entropies in the cores of our systems. These effects appear initially within a couple smoothing kernel sizes of the multiphase interface at $r \sim 3\,\mathrm{kpc}$ but their influence slowly propagates outwards.

To ensure that these effects do not influence the system beyond the 40 kpc radius where we are seeking to accurately model our systems, we have evolved our systems in isolation at both our nominal resolution and with $4\times$ its mass resolution. After 4 Gyr we find that the results of these two resolutions agree to within 10% in density and temperature outside of 30 kpc.

Although our simulations are run for 12 Gyr, such numerical concerns are significant only while a core is dense and its cooling timescales very short. In each of our simulations, the cores of both systems become sufficiently disturbed by the interaction to alleviate this problem and periods of active cooling are restricted to durations shorter than 4 Gyr. Thus, the influence of such numerical effects should remain restricted to radii $< 30\,\mathrm{kpc}$, marginalizing concerns for our study.

There is however one other unwanted effect in our simulations associated with our inclusion of radiative cooling: a steady rise in central temperatures. This rise is a product of deepening central potentials as cooling converts cool gas into stars in the centres of our systems. This builds a dense pressureless stellar core and permits gaseous baryonic material to migrate inward, lowering the system's central potential and raising its temperatures as a result.

Since the effect of these rising central temperatures is to suppress central temper-

ature decrements, timescales of the recovery of warm core to cool core morphologies are likely exaggerated in our simulations, leading to systematic biases in our analysis. It is critical to note however that the direction of this bias is always the same: towards overestimating the longevity of warm core morphologies. It is unlikely that these effects have a significant impact on the accuracy by which we generate extended core systems however.

5.3 Analysis

In this section we present our methods of classifying the evolving morphologies of our simulated mergers. To minimize biases in comparisons to observations, we closely follow the methods of classifying clusters employed in observational studies.

We shall find that as our mergers progress, they exist primarily in one of three states: compact cool core (CCC), compact warm core (CWC) and extended warm core (EWC) morphologies. In the sections which then follow, we shall discuss the temporal evolution of our mergers through these three states and relate their occurrence to the structure of the cores of our merger remnants.

5.3.1 Classification of Morphological States

We seek to determine how our evolving merger systems would appear to an observer: at which points they would manifest as a compact or extended core system, if they would appear to have been significantly affected by radiative cooling based on their entropy and projected temperature profiles, and whether they would exhibit evidence of merger activity under typical observational circumstances. To do so we have developed a classification scheme based on easily observable properties of the system.

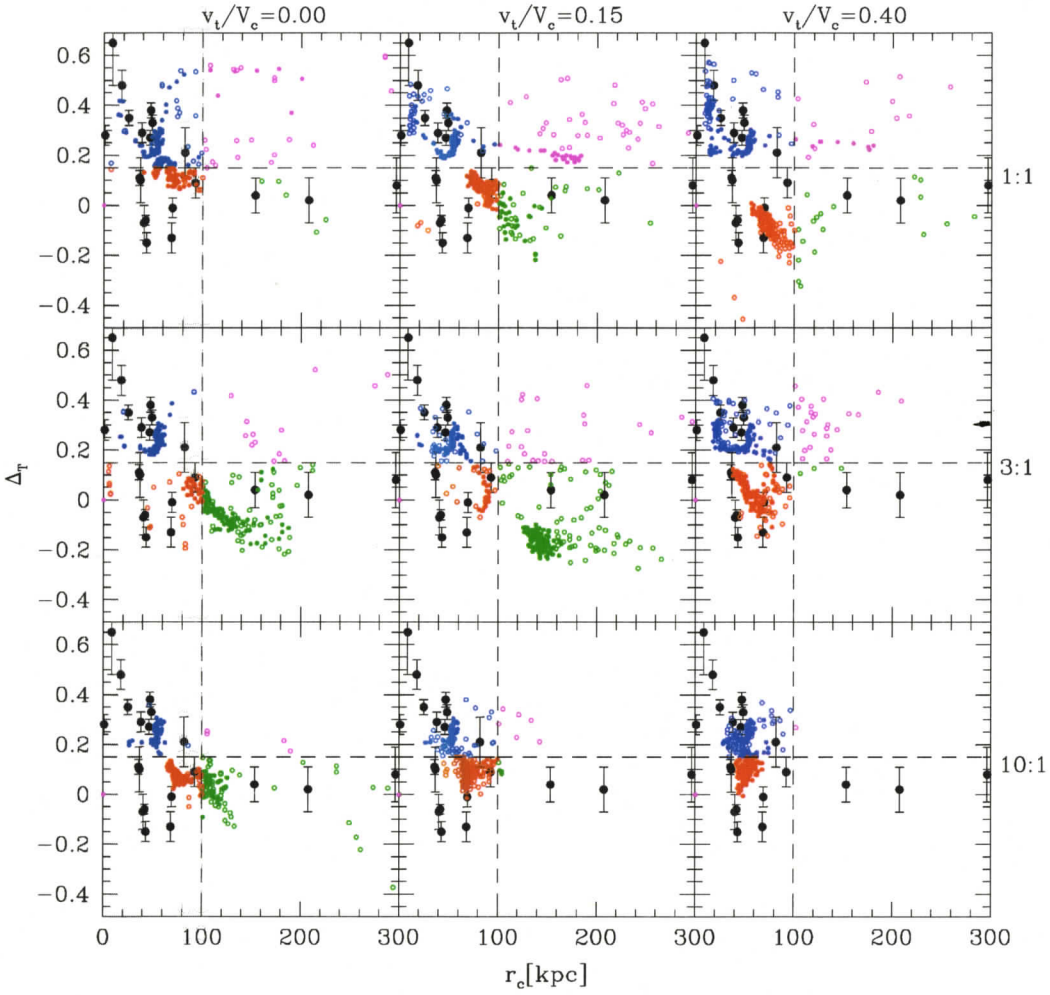

Figure 5.1: Central temperature decrement ($\Delta T/T$) plotted against core radius (r_c) for each output of our nine simulations in three orthogonal projections. Cuts in core radius and $\Delta T/T$ used to classify the morphology of our systems are shown with dashed lines. Systems with/without strong central temperature gradients and compact cores are labelled in blue and red respectively while extended core systems with/without strong central temperature gradients are in magenta and green respectively. Each population is further subdivided into systems showing obvious evidence of substructure (open circles) and systems with none and regular isophots (solid). Systems in states so highly disturbed as to be indescribable by a β model have been omitted. Black text around the boundary indicate the mass ratio and v_t/V_c depicted by each panel.

Surface brightness and projected temperature profiles

We first classify our systems according to the shape of their surface brightness and projected temperature profiles. To classify surface brightness profiles, we utilize the simple 3-parameter β-model commonly employed in analysis of observations. This model characterizes the azimuthally averaged surface brightness profile of a system at a projected radius r_p by the equation

$$\Sigma_x(r_p) = \frac{\Sigma_o}{\left(1 + (r_p/r_c)^2\right)^{3\beta-1/2}} \tag{5.1}$$

where r_c is the profile's core radius, β characterizes its asymptotic logarithmic slope at large radius and Σ_o its normalization. We exclude the central $r_p = R_{excise} \equiv 30\,\mathrm{kpc}$ from this analysis and have verified that varying R_{excise} from 20 to 50 kpc has a minimal effect on our results and does not influence the conclusions of our study. At a redshift of $z = 0.1$, 30 kpc corresponds to 17"; comparable to the size of the ROSAT PSF ($\sim$ 15"). Since this is the instrument used to obtain the data against which we compare our results (and the data's median redshift), removal of this region should not introduce significant biases during our comparisons to observations.

To characterize the apparent temperature structure of the cores of our merging systems, we measure a central temperature decrement (Δ_T) given by

$$\Delta_T = \frac{T_{inner} - T_{peak}}{T_{peak}} \tag{5.2}$$

where T_{inner} is the average spectrally fit temperature measured for material within projected radii $r_p = R_{excise} \rightarrow 0.1R_{200}$ of the cluster's X-ray peak. The radius $0.1R_{200}$ roughly corresponds to the cooling radius for compact core systems and observed

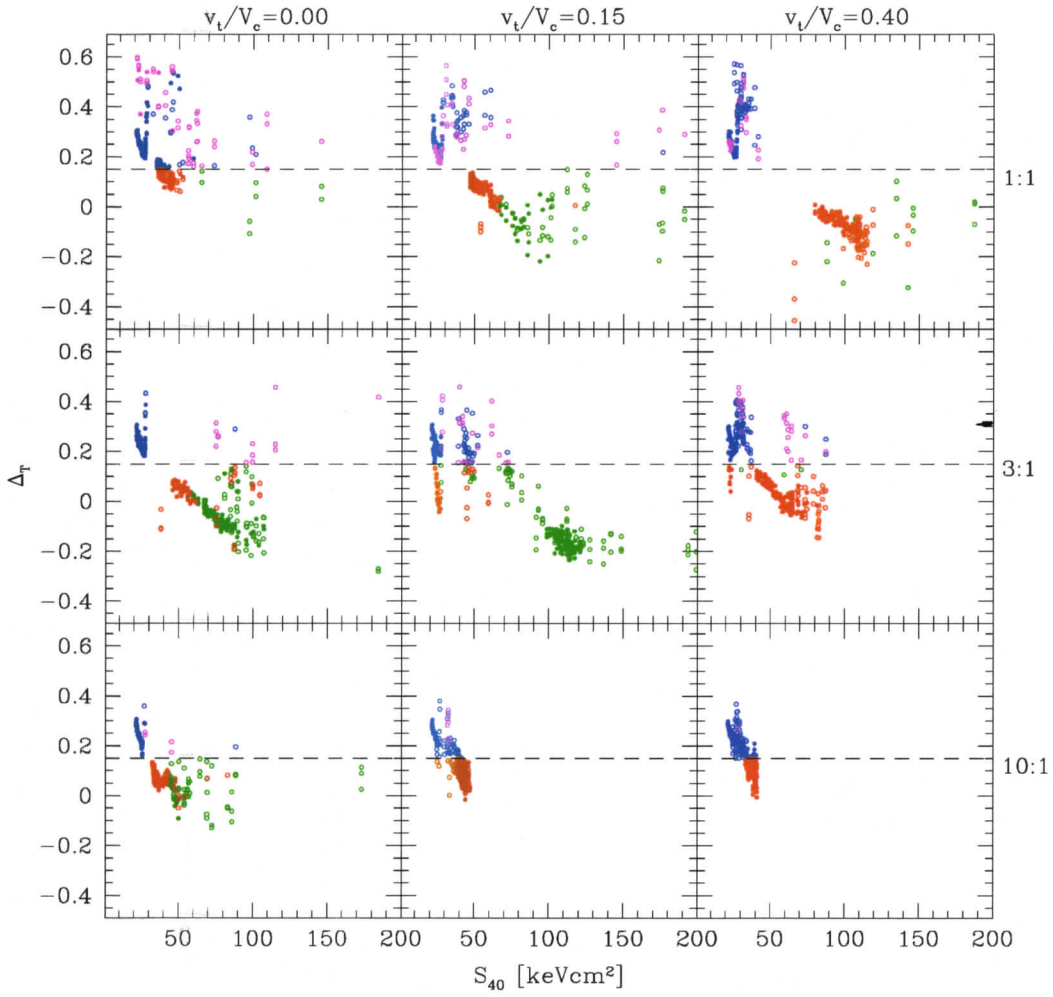

Figure 5.2: Central entropy (S_{40}) plotted against central temperature decrement ($\Delta T/T$) for each output of our nine simulations in three orthogonal projections (following the same format as Fig. 5.1). The cut in $\Delta T/T$ used to classify the morphology of our systems is shown with dashed lines. Systems with/without strong central temperature gradients and compact cores are labelled in blue and red respectively while extended core systems with/without strong central temperature gradients are in magenta and green respectively. Each population is further subdivided into systems showing obvious evidence of substructure (open circles) and systems with none and regular isophots (solid). Systems in states so highly disturbed as to be indescribable by a β model have been omitted. Black text around the boundary indicate the mass ratio and v_t/V_c depicted by each panel.

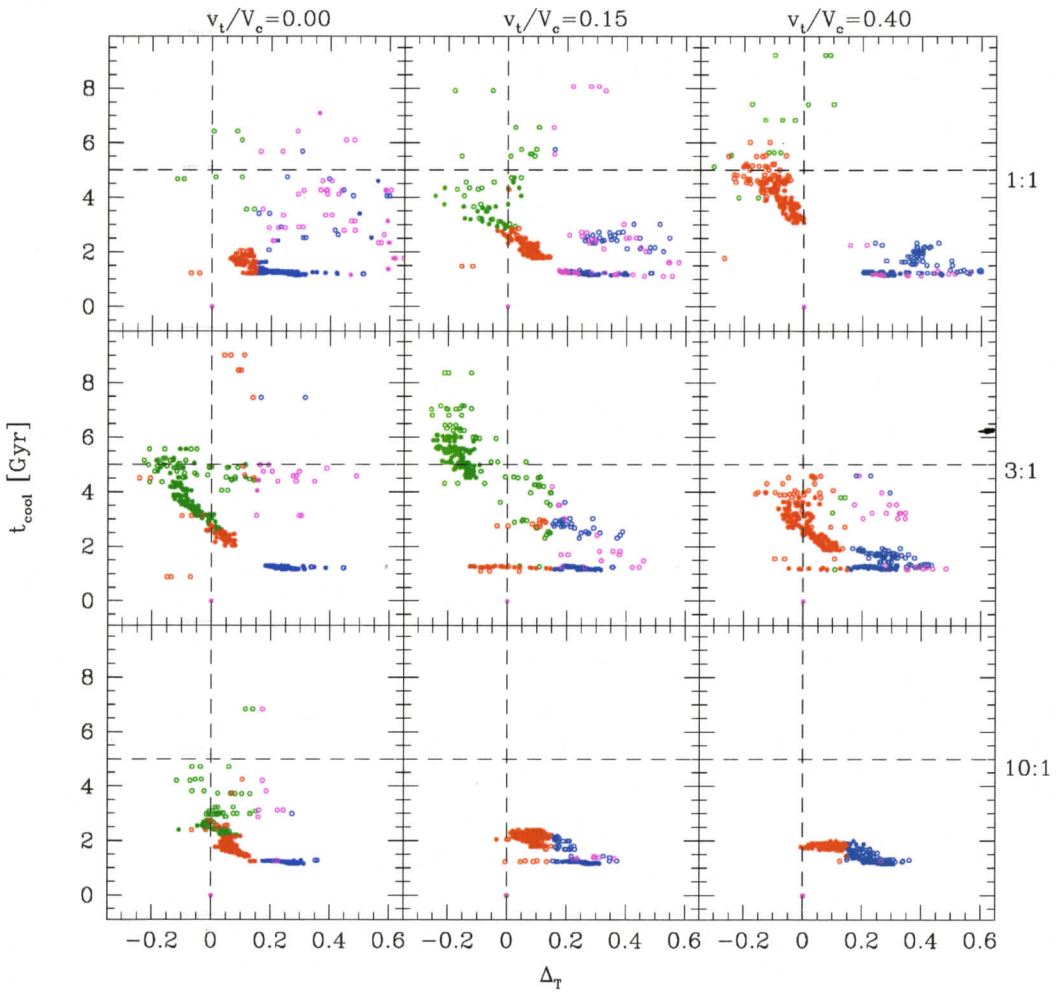

Figure 5.3: Central cooling time ($t_{cool,40}$) plotted against central entropy (S_{40}) for each output of our nine simulations in three orthogonal projections (following the same format as Fig. 5.1). The cut in $\Delta T/T$ used to classify the morphology of our systems and the 5 Gyr cut used by Sanderson et al. (2006) to divide short from long cooling times are shown with dashed lines. Systems with/without strong central temperature gradients and compact cores are labelled in blue and red respectively while extended core systems with/without strong central temperature gradients are in magenta and green respectively. Each population is further subdivided into systems showing obvious evidence of substructure (open circles) and systems with none and regular isophots (solid). Systems in states so highly disturbed as to be indescribable by a β model have been omitted. Black text around the boundary indicate the mass ratio and v_t/V_c depicted by each panel.

projected temperature profiles (Piffaretti et al., 2005; Sanderson et al., 2006; Pratt et al., 2006) which exhibit cool cores generally have suppressed temperatures within this region. T_{peak} is measured for material in the range $0.1R_{200}$ to $0.2R_{200}$. This range corresponds roughly to the region over which observed projected temperature profiles exhibit peak temperatures and universally flat temperature gradients. Hence, Δ_T measures the gradient of the temperature profile within our cluster cores.

It has been noted that projection effects can have a significant influence on the surface brightness structure and projected temperatures of a merging system (Ritchie & Thomas , 2002). For this reason, we consider three orthogonal projections for our computations of r_c and $\Delta T/T$: two in the plane of the orbit along the line initially connecting the systems (x) and in the direction of initial tangential velocity (y) and one normal to the plane of the orbit (z).

Apparent dynamical state

Each projection for each system is also classified into instances where it would exhibit no substructure and regular isophots to an observer, significant substructure, or so much substructure as to render the system indescribable by a β-model (generally due to the close proximity of the secondary or brief but extreme distortions). We refer to these situations as undisturbed, disturbed and strongly disturbed respectively. Classification is performed through visual inspection of simulated 50ks *Chandra* observations for each output, in each projection. This is done following the procedure detailed in Chapter 2.

3 dominant morphological states

In Fig. 5.1 we present a $\Delta T/T - r_c$ plot for our nine simulations. All three projections are displayed for each of the 120 outputs (spanning 12 Gyr in 100 Myr intervals) of our simulations with instances of undisturbed and disturbed morphology indicated

by filled or open circles respectively. Since instances of strongly disturbed morphology can not be assigned meaningful core radii, they are omitted from this morphological discussion. Such instances are generally rare and their exclusion does not represent a significant omission, although it is important to keep in mind that this exceptional class does manifest occasionally at early stages of the interaction.

By making cuts in r_c and $\Delta T/T$ in this plane (indicated by dashed lines) we separate four potential populations: two compact core populations with and without strong central temperature decrements (blue and red points respectively) and two extended core populations with and without strong central temperature decrements (magenta and green points respectively). For our cut in r_c we have selected 100 kpc, which corresponds approximately to the unpopulated region of the observed r_c distribution reported by Ota & Mitsuda (2004) separating compact and extended core systems. For our cut in $\Delta T/T$ we use 15% (the data of Piffaretti et al. (2005) permit the range $\Delta T/T \sim 0.15 - 0.6$). Henceforth, we shall identify systems with $\Delta T/T > 0.15$ as "cool core" systems and systems with $\Delta T/T < 0.15$ as having "warm cores".

With each interval of our simulations classified in this way, we see that few instances of extended core morphologies exhibit central temperature decrements. Looking carefully at those circumstances which do, we find that in all cases it is a result of one of two effects. In some instances, a shock or cold substructure passing through the vicinity of the core can generate localized temperature structures which masquerade as temperature decrements to our algorithm. In other cases, hot material displaced from the regions surrounding the core can return through the low pressure wake of the secondary creating a wave of inwardly flowing warm material, generating the appearance of a temperature decrement. The system is obviously undergoing a merger in nearly all of these cases, although the primary system is sufficiently intact to fit a β-model to its surface brightness.

Exceptional instances such as these aside, we see that throughout the duration of

a merger interaction, an observer would classify the system as existing predominantly in one of three states: as a compact cool core system (CCC) with a temperature decrement, as a compact warm core system (CWC) with a weak or absent central temperature decrement or as an extended warm core (EWC) system without a temperature decrement. In each case, the system may or may not also possess obvious substructure and/or disturbed isophots, meaning that members of each class could be found which appear to be disturbed or undisturbed.

We have also plotted in black on Fig. 5.1 r_c data from the statistically representative observed sample of Sanderson et al. (2006). We find in the observations as well that the cool extended core part of this plane is not occupied. The qualitative agreement between the regions of this plane occupied by this observed sample and our simulations is encouraging.

Cooling, central entropy and morphology

Compact core systems tend to possess central positive temperature decrements and low central entropies while extended systems are observed to be warm with elevated central entropies. To illustrate the extent by which these trends are upheld during and after our simulated mergers, we present in Fig. 5.2 (with the same format as Fig. 5.1) a plot of Δ_T against central entropy (measured at 40 kpc, denoted S_{40}) for our systems. This figure clearly illustrates that, regardless of the dynamical state of the system, cores lacking central positive temperature decrements possess elevated levels of central entropy. With few exceptions, systems with $S_{40} > 50\,\mathrm{keVcm}^2$ have warm cores.

It has recently been noted by Sanderson et al. (2006) that systems lacking cool cores can have short cooling times ($t_{cool} < 5\,\mathrm{Gyr}$). In Fig. 5.3 we can see that very few instances of compact cores (both CCC systems in blue and CWC systems in red) have cooling times greater than this level. Cooling times in excess of 5 Gyr are almost

exclusively expressed in extended core systems, but not all extended core systems express cooling times greater than 5 Gyr. Thus, although the presence of a compact core does not imply the presence of a cool core, it nevertheless implies short cooling times and thus illustrates the importance of radiative cooling in establishing their structure and evolution. The appearance of an extended core morphology generally (but not necessarily) implies a long cooling time.

5.3.2 Temporal Evolution of Morphology

To see how our simulations' morphologies progress through these three states, we present the temporal evolution of r_c and $\Delta T/T$ in Figs. 5.4 and 5.5. In both cases, a black curve traces the system's evolution as seen in the z-projection with coloured points plotted (following the format of Fig. 5.1) to indicate each interval's morphological state. These curves change very little when viewed in y-projections and differ only at early times in the x-projection due to the apparently close proximity of the two cluster cores prior to interaction. To clarify the plot, we show only the z-projection.

Core size

Considering Fig. 5.4 first, we see that in all cases the system starts as a compact core system (by construction) and experiences a period of increased core size following $t_{closest}$. In the on-axis cases, this lasts (with varying amplitude) until roughly $t_{accrete}$. In the off-axis cases there is an interval from $t_{closest}$ to $t_{accrete}$ during which the system returns to a compact core state. This indicates that the initial interaction of the cores fails to disrupt the primary system to an extended core state in any of our off-axis mergers.

Following $t_{accrete}$, most of our merger remnants are in, or nearly in, extended core states. They subsequently evolve back towards their initial core size with only the

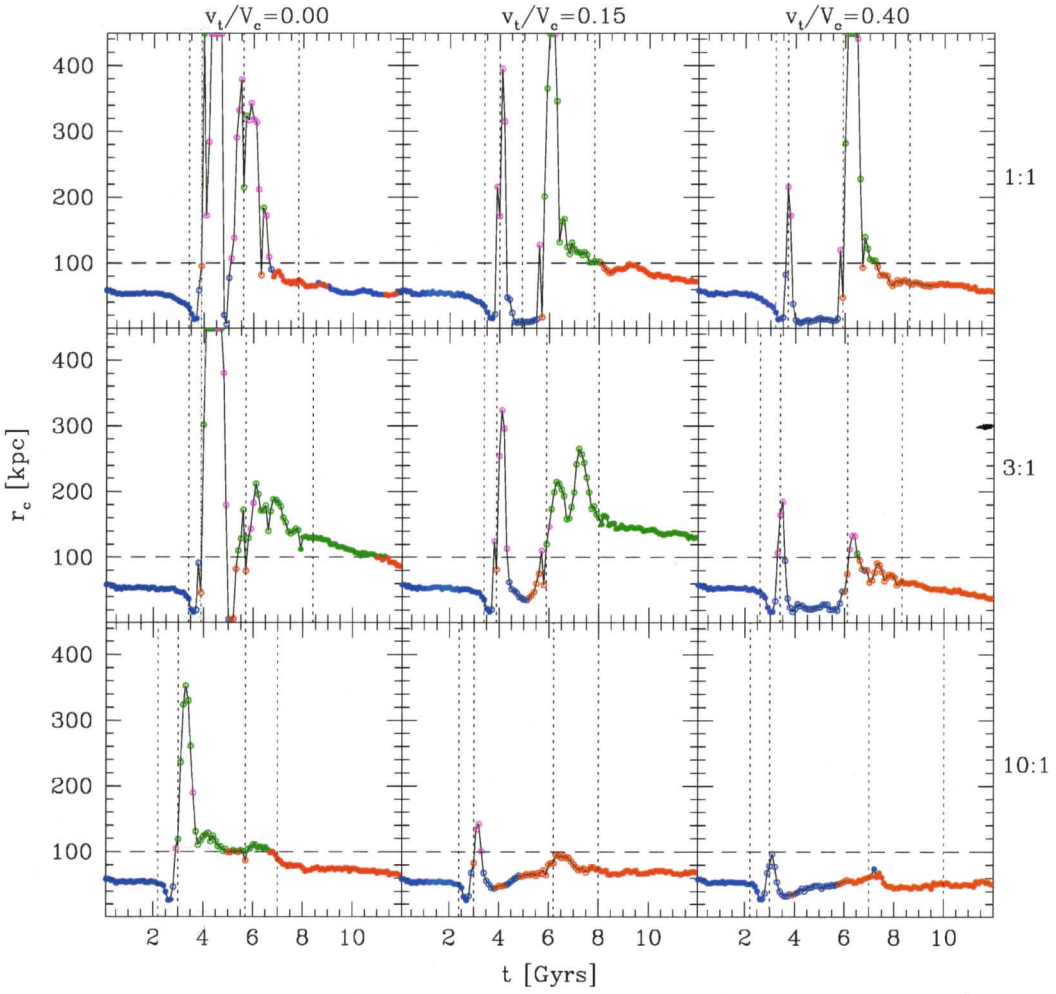

Figure 5.4: The temporal evolution of core radius (r_c) for our simulations. Black curves illustrate $r_c(t)$ and coloured points indicate the morphology (following the format of Fig. 5.1) of the system measured in the z-projection. Systems with/without strong central temperature gradients and compact cores are labelled in blue and red respectively while extended core systems with/without strong central temperature gradients are in magenta and green respectively. Each population is further subdivided into systems showing obvious evidence of substructure (open circles) and systems with none and regular isophots (solid). Systems in states so highly disturbed as to be indescribable by a β model have been omitted. The cut in r_c used to classify the morphology of our systems is shown with dashed lines. Vertical dotted lines indicate (from left to right) t_o, $t_{closest}$, $t_{accrete}$ and t_{relax} for each case. Black text around the boundary indicate the mass ratio and v_t/V_c depicted by each panel.

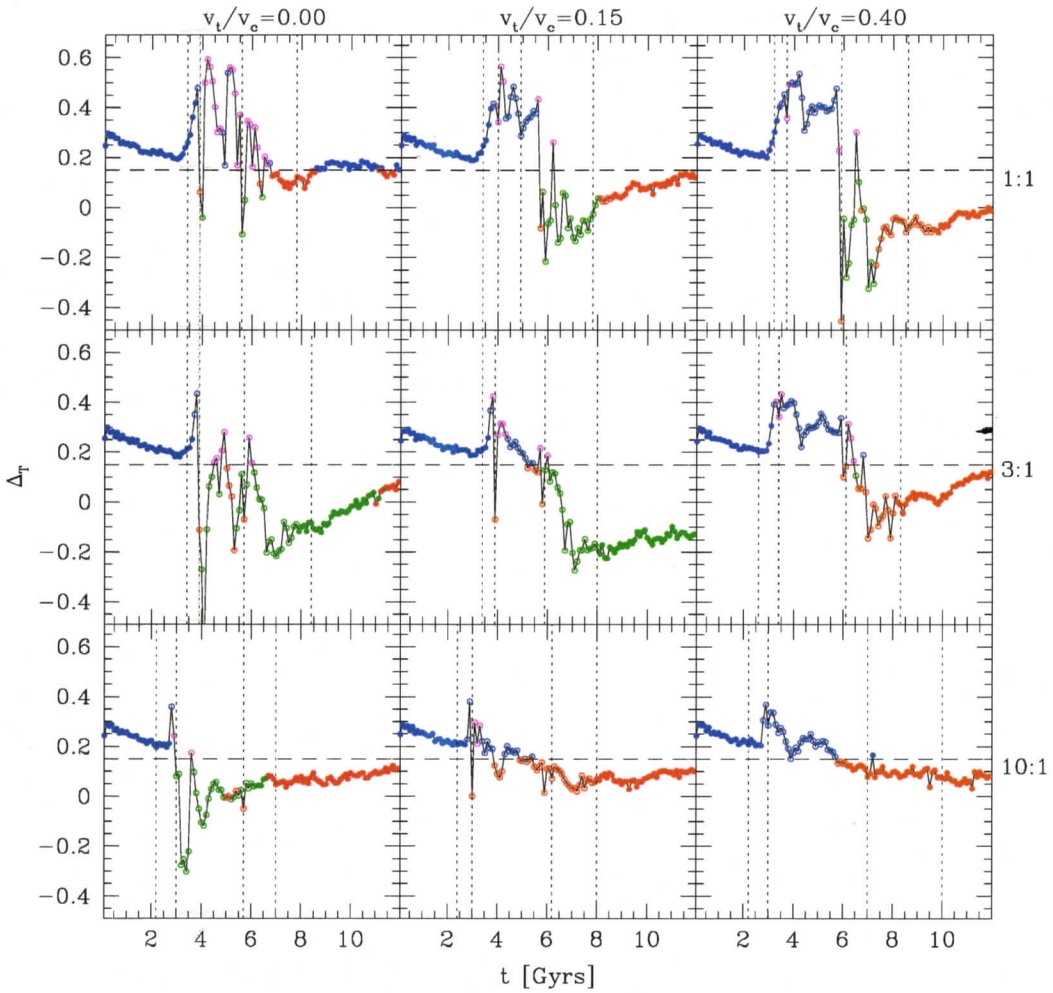

Figure 5.5: The temporal evolution of the central temperature decrement ($\Delta T/T$) (following the same format as Fig. 5.4). Black curves illustrate $\Delta_T(t)$ and coloured points indicate the morphology (following the format of Fig. 5.1) of the system measured in the z-projection. Systems with/without strong central temperature gradients and compact cores are labelled in blue and red respectively while extended core systems with/without strong central temperature gradients are in magenta and green respectively. Each population is further subdivided into systems showing obvious evidence of substructure (open circles) and systems with none and regular isophots (solid). Systems in states so highly disturbed as to be indescribable by a β model have been omitted. The cut in $\Delta T/T$ used to classify the morphology of our systems is shown with dashed lines. Vertical dotted lines indicate (from left to right) t_o, $t_{closest}$, $t_{accrete}$ and t_{relax} for each case. Black text around the boundary indicate the mass ratio and v_t/V_c depicted by each panel.

3:1 head-on and $v_t/V_c = 0.15$ cases spending significant amounts of time in extended core states. The 3:1 head-on case formally recovers a compact core by the end of the simulations while the 3:1 $v_t/V_c = 0.15$ case yields a remnant with $r_c \sim 140\,\mathrm{kpc}$ following $t_{accrete}$ and evolves very little afterwards. In Section 5.3.3 we will discuss why this system evolves so differently.

Temperature decrement

Considering Fig. 5.5, we see that our systems begin with strong central temperature decrements (by construction). In the head-on cases, the temperature decrement is erased in the 3:1 and 10:1 cases but remains above $\Delta_T = 0.10$ at all times in the 1:1 case. In the head-on 10:1 and 3:1 interactions, the system quickly develops a negative central temperature gradient after $t_{closest}$. Examining the dynamical evolution of these cases in surface brightness, temperature and entropy (Figs. 3.1 to 3.9) we see that the secondary core fully penetrates the primary core in these cases, allowing the shocks generated in the event to heat the entire core. In the 1:1 case, the merging cores inelastically collide and remain in very dense structures following $t_{closest}$. This has the dual effect of reducing heating efficiency and increasing cooling efficiency. These effects lead to a counterintuitive result: the 3:1 and 10:1 head-on mergers ultimately heat the primary core more efficiently than the 1:1 head-on merger.

In the off-axis cases, the primary core's temperature decrement is generally present during the period from $t_{closest}$ to $t_{accrete}$. This indicates that the first interaction of the cores in off-axis cases does not heat them to warm states. In all cases except the 10:1 head-on and $v_t/V_c = 0.4$ merger we see a significant decline in $\Delta T/T$ after $t_{accrete}$. In the 1:1 and 3:1 cases, this decline is precipitous. In Chapter 3 we described the formation of long lived streams of material stripped from the secondary cores which accrete onto the core subsequent to $t_{accrete}$. It is during the accretion of these streams that we see $\Delta T/T$ declining. The 3:1 $v_t/V_c = 0.15$ case

produces the stream most disruptive to the primary's core and we see the most severe decline in $\Delta T/T$ after $t_{accrete}$ in this case. In Section 5.3.3 we will examine this process in more detail.

Evolution through 3 distinct states

Our clusters begin (by construction) as CCC systems with small core radii and strong central temperature decrements. We have chosen this initial configuration because it is the natural convergent state for a relaxed cluster in the absence of feedback and representative of the structure of a large fraction of clusters. In the context of hierarchical clustering, such systems are well understood: they are systems which have remained undisturbed long enough for vigorous radiative cooling to have produced a central temperature decrement and high central gas densities.

However, following a merger we find that the system can exist in one of two other states. These states are generally not produced after first pericentric passage. Only in the 3:1 and 10:1 head-on cases, where the secondary core completely penetrates the primary's, is the system immediately transformed from its initial CCC state to a EWC state. In the off-axis 1:1 and 3:1 cases, the core becomes enlarged following second pericentric passage at $t_{accrete}$ and the temperature decrement highly reduced or destroyed. In the cases where the largest and warmest cores are produced, most of this transformation occurs during the accretion of the stream formed from the secondary's core. Following t_{relax}, core radii and temperature decrements generally begin returning towards their initial values. In all cases except this one, the compact core reestablishes itself faster than it returns to a cool state, and recovery thus proceeds with the system in a CWC state. The only exception to this is the 3:1 $v_t/V_c = 0.15$ case which maintains a large warm core following t_{relax}.

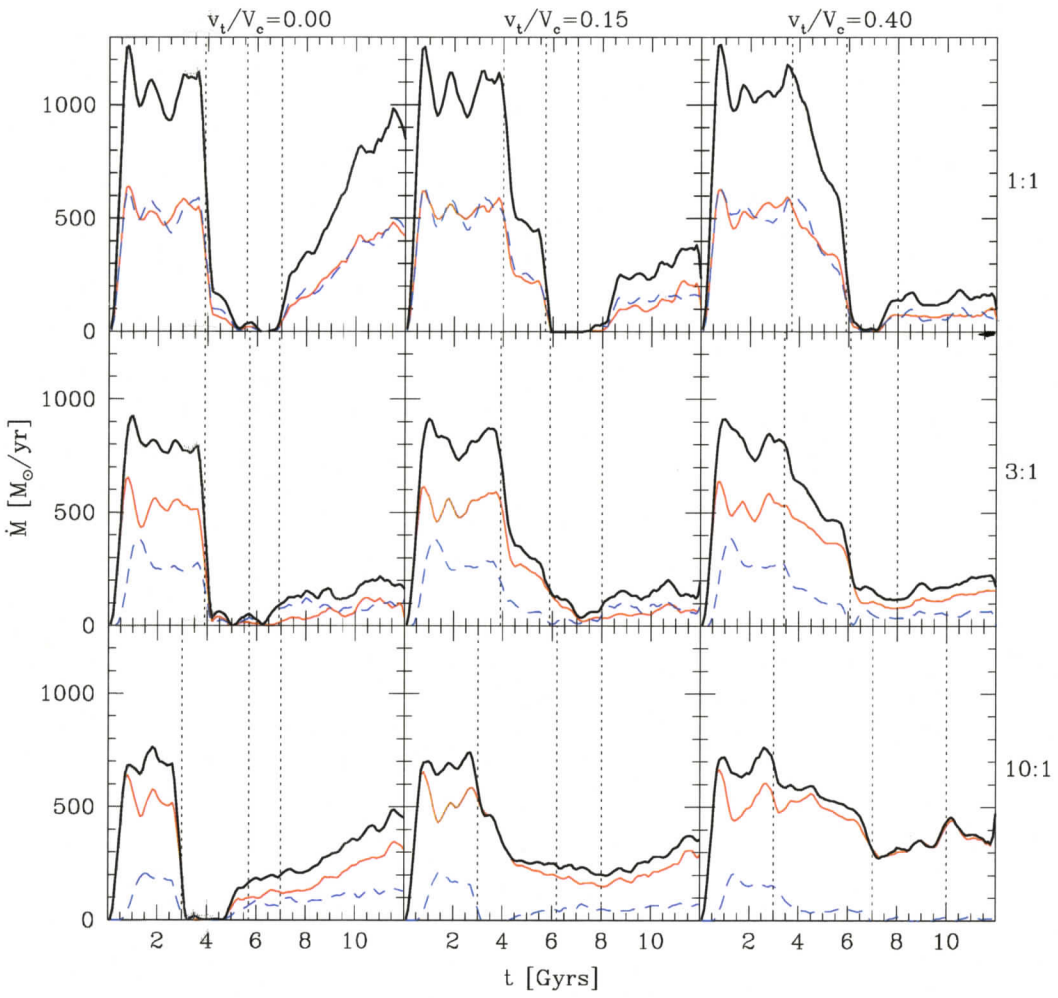

Figure 5.6: Mass deposition rates (stars plus gas colder than $2.5 \times 10^4 K$) as a function of time for each of our simulations. Red lines track material initially in the primary system, blue dashed lines material initially in the secondary, and thick black lines the total. Vertical dotted lines indicate (from left to right) $t_{closest}$, $t_{accrete}$ and t_{relax} for each case. Black text around the boundary indicate the mass ratio and v_t/V_c depicted by each panel.

5.3.3 Effects of entropy and cooling timescales on remnant core structure

Having established the progression of our mergers from CCC to EWC and CWC states, we now seek to understand what properties of a core's structure are principally responsible for establishing the rate at which our clusters evolve back towards CCC states.

The rate of radiative cooling is certainly a principle factor. To provide a physically motivated metric of the cooling status of our merging systems' cores, we have computed the rate at which baryonic material is condensing into cold gas (defined to have $T < 2.5 \times 10^4\,\mathrm{K}$) and stars. In Fig. 5.6 we plot three lines for each of our simulations indicating the mass deposition rates of material originating from the primary (red curve) or secondary (blue dashed curve) as well as the total of both (thick black curve). We quantify these mass deposition rates (denoted as $\dot{M}$) by determining the total mass of condensed baryons in each output and then compute its temporal derivative. In each case we consider all of the material in the interacting system rather than merely isolating material cooling in the core. This is done to reduce noise emerging from the sensitivity of the temporal derivative to small substructures passing in or out of the core. At all times well over 90% of the condenced material lies within the cooling radii of the interacting systems or the final remnant, where all of the condensed material is formed. Furthermore, it is important to note that since we do not include the effects of AGN heating in our simulations, these cooling rates are not meant to represent accurate star formation rates for clusters. Our use of $\dot{M}$ is purly as a diagnostic of the central cooling activity in our simulations.

In each case, the initial behaviour of this plot is the same: our systems are initialized in a static state which, after a quick rise in mass deposition rates for both primary and secondary systems, evolves to a state of steady cooling lasting $1-2\,\mathrm{Gyr}$ before $t_{closest}$. At $t_{closest} \sim 3\,\mathrm{Gyr}$ the cores reach their closest approach and

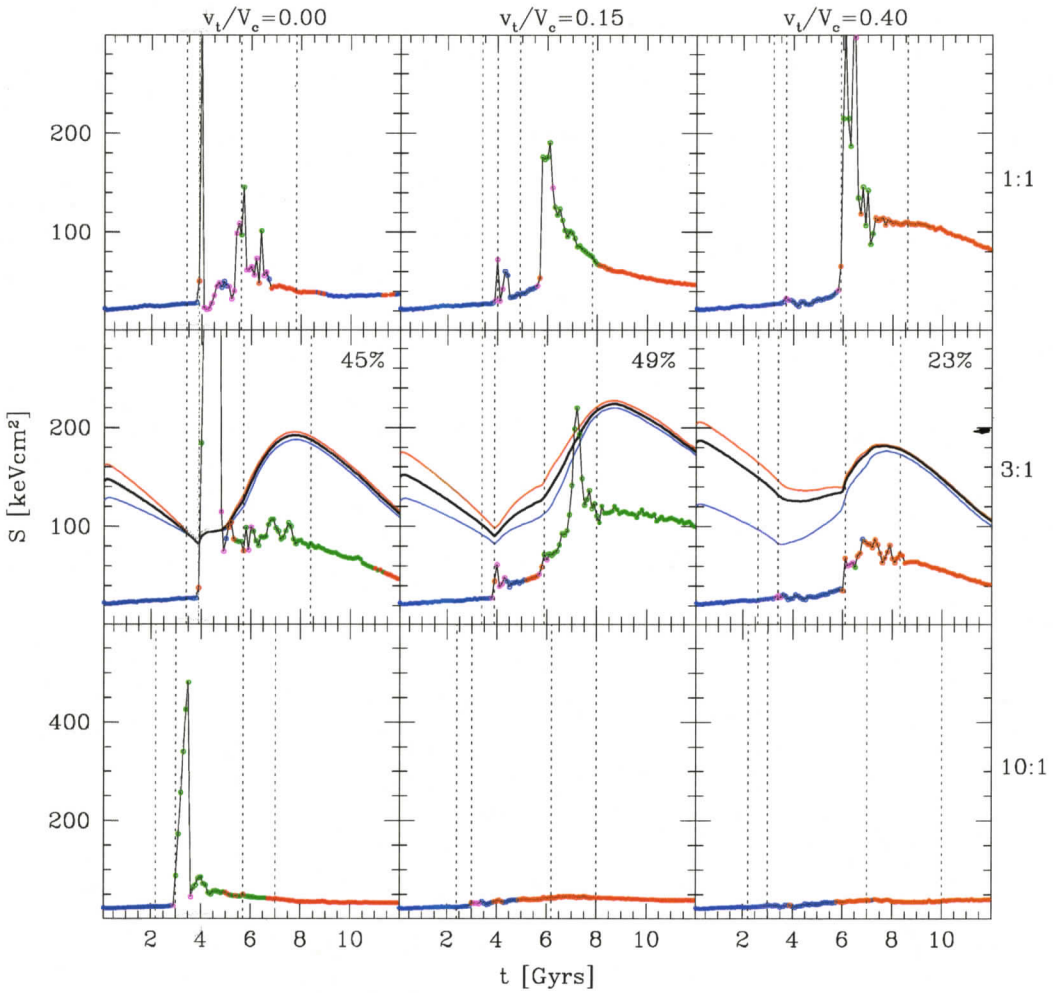

Figure 5.7: The temporal evolution of central entropy (S_{40}). For the 3:1 cases, material identified to end-up within 100 kpc of the remnant center is depicted by the blue, red and black lines with material originating from the primary in red, from the secondary in blue and the mass weighted sum in black. Percentiles in each frame depict the fraction of this material which originates from the secondary. The line with coloured points depict the central entropy of the system (at 40 kpc) as well as the morphological state of the system as seen in the z-projection (following the format of Fig. 5.1). Blue and red points depict compact core states with cool or warm cores respectively and magenta and green points depict extended core states with cool or warm cores respectively. Open points depict systems which are visibly disturbed in our simulated *Chandra* images and solid points systems which appear relaxed. Vertical dotted lines indicate (from left to right) t_o, $t_{closest}$, $t_{accrete}$ and t_{relax} for each case. Black text around the boundary indicate the mass ratio and v_t/V_c depicted by each panel.

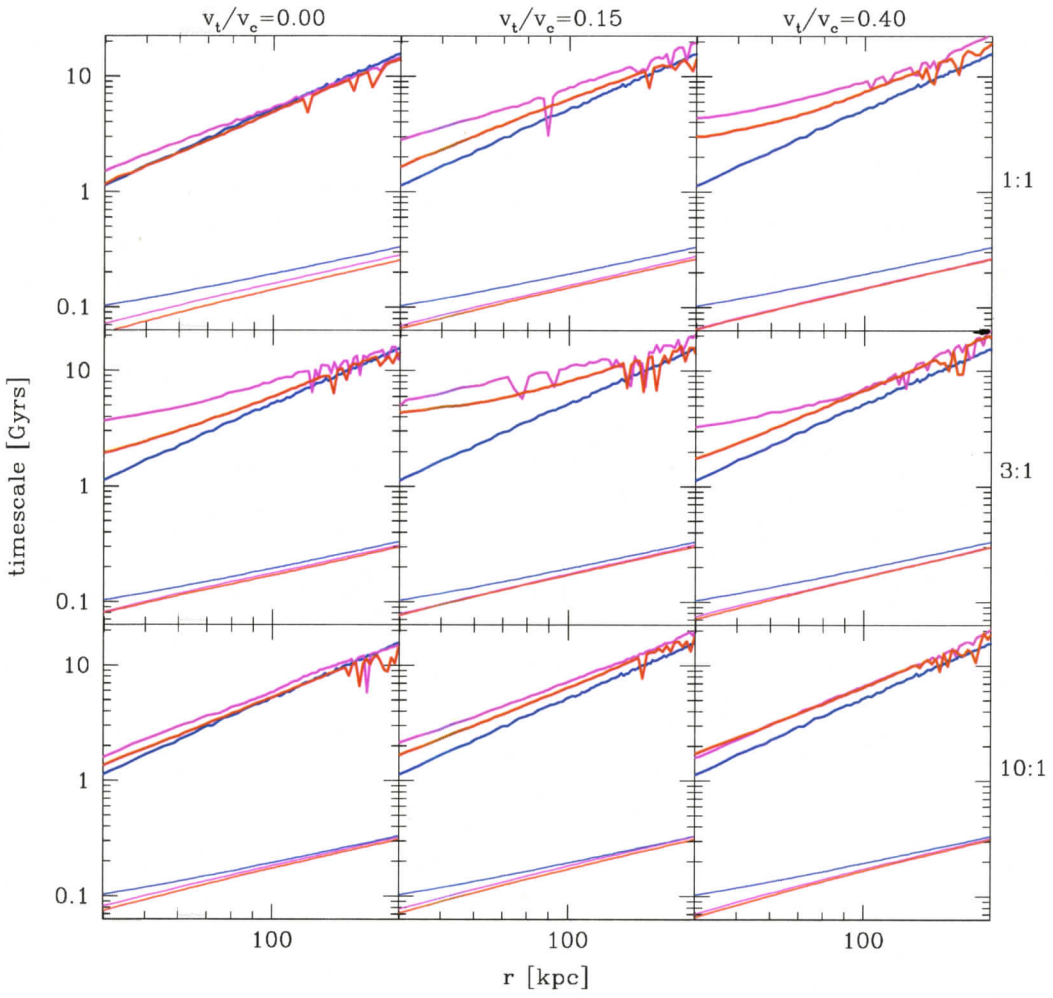

Figure 5.8: Radial profiles of the cooling timescale (t_{cool}; thick lines) and sound crossing timescale (t_{dyn}; thin lines) of our simulations. The initial profiles of the system are in blue, the profiles for the system at t_{relax} (when the system appears undisturbed to 50 ks *Chandra* observations at $z = 0.1$) are in magenta and the final remnant state is in red. Black text around the boundary indicate the mass ratio and v_t/V_c depicted by each panel.

the mass deposition rate is instantly reduced. In all head-on cases, mass deposition is terminated for $\sim 2\,\mathrm{Gyr}$ after which it begins to recover subsequent to $t_{accrete} \sim 5 - 5.6\,\mathrm{Gyr}$. Although mass deposition is similarly reduced in the off-axis cases, there is a $1 - 2$ Gyr delay before it reaches a minimum at $t_{accrete} \sim 6\,\mathrm{Gyr}$. Following this, mass deposition is reduced for $\sim 2\,\mathrm{Gyr}$. It is terminated in the 1:1 cases but merely reduced to 20% or 50% of its pre-interaction value in the 3:1 or 10:1 cases respectively. Subsequent to reaching a minimum rate, it slowly resumes.

Why do some systems recover towards their initial cooling rates while others do not? Surprisingly, the 1:1 head-on merger is the case which most effectively reestablishes it's mass deposition rate, returning to nearly twice the pre-interaction value of the primary, while the most off-axis 10:1 merger (which one might expect to disturb core cooling the least) recovers barely half the primary's pre-interaction rate. Furthermore, all the 3:1 mergers and the 1:1 $v_t/V_c = 0.4$ cases have similar cooling rates at late times, but very different morphologies. Other factors besides the integrated cooling rate of the cores must be involved in setting our merger remnant's morphologies.

Entropy

In the absence of (non-adiabatic) heating, radiative cooling reduces a material's entropy. This can potentially raise its density and/or lower its temperature. In concert, this can move a system towards a CCC state. Hence, entropy plays a central roll in the evolution of our system from EWC or CWC states to CCC states. We present its evolution in Fig. 5.7 where we plot the central entropy of our evolving systems and for the 3:1 cases, the evolution of material destined to constitute the central $100\,\mathrm{kpc}$ of our remnant cores. We do this to illustrate the relative heating of primary and secondary material. Only the 3:1 cases are shown because the secondary systems are too disrupted in the 10:1 cases to illustrate our point, and the symmetry

in the 1:1 cases trivializes such discussions.

Examining the evolution of the central entropy of the system first, we find a slightly different evolution between the on-axis and off-axis cases. In the on-axis cases, the impact of the secondary core is immediately followed by a large peak and in the 1:1 case, a period of erratic oscillations. Large sustained peak values are reached in the 3:1 and 10:1 cases before $t_{accrete}$, with a subsequent decline. This behaviour is more pronounced in these cases than in the 1:1 case due to the higher penetrability of their bow shocks through the primary core. In the equal mass head-on merger the shocks produced are nearly planar which keeps low entropy material confined in dense structures at the center, reducing the efficiency of shock heating and increasing the efficiency of cooling. In the 3:1 head-on case, the bow shock leading the secondary displaces material laterally and can penetrate to the core of the primary, depositing more of its initial kinetic energy in the lowest entropy material of the primary core. This displacement of the primary core's material also reduces its density, strongly reducing its cooling efficiency and increasing the efficiency of entropy production. This occurs in the 10:1 case as well but the reduced kinetic energy of the secondary results in less heating of the core.

In off-axis cases, a slight increase is seen after $t_{closest}$ but generally very little increase in core entropy occurs due to the initial core interaction. It is after $t_{accrete}$, when the stream formed from the disruption of the secondary core begins accreting, that the bulk of the central entropy increase occurs. In Chapter 3 we showed that the 3:1 $v_t/V_c = 0.15$ case produces a high velocity stream which disrupts the primary core. It is because of this stream that this case produces the highest sustained remnant core entropy of all our simulations. In the 10:1 cases, the secondary core is more highly disrupted and fails to accrete as coherently as the 3:1 cases. It is for these reasons that very little core entropy increase is seen in the 10:1 off-axis cases. Subsequent to the peak entropy produced shortly before t_{relax} in the off-axis cases, the entropy slowly declines in the 1:1 and 3:1 cases and stays constant near its initial values in

the 10:1 cases.

Examining the evolution of material which eventually constitutes the final remnant cores in the 3:1 cases, we find a qualitatively similar evolution in the on-axis and off-axis cases. Since most of this material originates in the actively cooling cores of the initial systems, its entropy is initially dropping quickly. At $t_{closest}$, cooling is stopped and both the primary and secondary material becomes slowly heated until $t_{accrete}$ (in the $v_t/V_c = 0.4$ case, the primary material remains at a constant value indicating that cooling in the primary core has been quenched). After a lag following $t_{accrete}$, both the primary and secondary core material experience very dramatic increases in entropy. In the $v_t/V_c = 0.15$ case, we see that the secondary material (which constitutes nearly half of the final remnant core) becomes more significantly heated than the primary material during the stream accretion phase. Even though this material originated in a denser structure, most of its heating was produced while in disturbed, low density structures where entropy generation is more efficient.

Stream accretion is significant in our 1:1 and 3:1 off-axis mergers and in each case, is the mechanism by which most of the final core material's entropy is generated.

Cooling timescales

Cooling can reduce the core temperature, but must it do so? In our 1:1 $v_t/V_c = 0.4$ and 3:1 $v_t/V_c = 0.15$ cases we see that similar peak entropies and cooling rates result after t_{relax}, but Fig. 5.5 illustrates that the recovery of the cool core is proceeding differently.

Imagine a parcel of gas radiatively cooling. As cooling proceeds, it reduces the parcel's entropy on the cooling timescale, $t_{cool} \propto S^{1.5}T^{-1}$. If it is in a dynamically disturbed state, its temperature can drop only if the cooling timescale is sufficiently short with respect to its local dynamical time, $t_{dyn} = \sqrt{3\pi/16G\Delta\rho_c}$ (where Δ is the over density of the system, relative to the critical density, within the parcel's

radius). If $t_{cool} \gg t_{dyn}$, it merely becomes compressed as it falls to the center, leading to increased densities as it loses entropy but not decreased temperatures. Once the system becomes relaxed, the temperature can then fall on timescales governed by the cooling time.

In Fig. 5.8 we present these timescales for each of our systems at its initial state (blue), when it appears undisturbed at t_{relax} (magenta), and in its final state (red). We can see that relatively little change occurs in the dynamical time between these intervals, with t_{dyn} increasing as power laws over the entire region of the core in all cases. The cooling time however, which initially increases as a power law, is significantly higher and flat in the cores of several of our 1:1 and 3:1 cases.

At all times, we see that $t_{cool} \gg t_{dyn}$. As a result, cooling can not lower the temperatures of the cores until it has returned to a stable state of hydrostatic equilibrium. In Chapter 3 we examined how a system returns to hydrostatic equilibrium following a merger. At R_{500} we found that the system returns to within 10% of hydrostatic equilibrium at t_{hydro}, generally $0.5 - 1.0\,\mathrm{Gyr}$ following the system's apparent relaxation at t_{relax}. Examining this behaviour at R_{2500} we find that the system returns to within 10% of hydrostatic equilibrium a little sooner and generally within 0.5 Gyr of t_{relax}. Hence, even though cooling may become reestablished at (or shortly before) t_{relax}, it generally does not begin to lower the core's temperature until afterwards. In Fig. 5.5 we can see that the central temperature decrements of all our remnants are increasing after this point (the 1:1 and 3:1 $v_t/V_c = 0.4$ cases experience slight dips after t_{relax} due to the accretion of unobservable substructure). Prior to this time, cooling can drop the central entropy of the system and lead to increased core densities however. This process contributes to the faster recovery of the core's compact state compared to the recovery of its temperature decrement.

Thus, we expect the temperature decrements of our cores to increase significantly only after $t_{\Delta T} = t_{relax} + t_{cool}(t_{relax})$. In the 1:1 $v_t/V_c = 0.4$ and 3:1 $v_t/V_c = 0.15$ cases, central cooling times have become high and roughly constant following $t_{accrete}$. In the

1:1 $v_t/V_c = 0.4$ case, $t_{\Delta T}$ is roughly at the end of our simulations while in the 3:1 $v_t/V_c = 0.15$ case it is several Gyr after. Thus, despite similar core entropies and mass deposition rates at t_{relax}, we witness different recoveries of $\Delta T/T$ in these cases: slow in the 1:1 $v_t/V_c = 0.4$ case but almost nonexistent in the 3:1 $v_t/V_c = 0.15$ case. Differences in central cooling time are responsible for this difference which, given the similar central entropies of these systems, arise from the discrepant temperature structures of their cores.

5.3.4 Morphological segregation in scaling relations

Scaling relations between mass, X-ray temperature and luminosity are powerful tools for studying the processes that shaped the structure of the ICM. It has been known for some time that a significant fraction of the scatter in these relations is due to variations in the core properties of clusters, with outer cluster regions exhibiting significantly more uniformity. This has been supported by recent observational studies (O'Hara et al., 2006; Sanderson et al., 2006; Pratt et al., 2006). For this reason, and because the generation of mass functions from these scaling relations has been a significant motivator of their study, past studies of scaling relations have generally been conducted with the central cores of systems excised.

It has been shown by M04 however that there is interesting structure in these relations which correlate with the core properties of clusters. In their study, M04 use the ACC catalogue of Horner (2001) to compare their analytic entropy injection model to published *Chandra* and XMM temperature profiles, classifying them by the presence or absence of central temperature decrements. They further separate these systems into classes showing evidence of significant or little substructure. Despite the small number of published *Chandra* and XMM temperature profiles available to them at the time, they found that these classes clearly (but not necessarily distinctly) segregate in both the $L_x - T_x$ and $\beta - r_c$ planes.

In Chapter 4 we have examined the evolving global properties (including X-ray temperature and luminosity) of our simulations, as well as the scaling relations generated from them. Having identified when our systems appear in states without central cool cores (EWC and CWC systems), we now examine how they segregate in these planes. In Chapter 4 we found that the evolution in the $L_x - T_x$, $M_t - L_x$, $M_t - T_x$, $SZ - L_x$ and $SZ - T_x$ planes were quite similar and we find the same for morphological segregation in these planes as well. For this reason we will examine only the $L_x - T_x$ relation here (with the caveat that very similar qualitative statements can be made about the other scaling relations listed above) as well as the $\beta - x_c$ plane examined in M04.

The $L_x - T_x$ plane

In Fig. 5.9 we present the positions of our systems in the $L_x - T_x$ plane, at each time and in all three orthogonal projections, when they appear as EWC (green) or CWC (red) systems. The initial and final states of the systems are indicated with blue four and five point stars respectively. We also identify incidences of apparently disturbed (open symbols) and relaxed (filled circles) morphology as well. These are compared against the observed catalogue of Horner (2001) (in black) for which we similarly differentiate systems with cool cores (squares) from those without (triangles) as well as instances of relaxed morphology (filled symbols) from disturbed morphology (open symbols).

This plot reinforces what was found in Chapter 4: the low-luminosity side of the $L_x - T_x$ scaling relation can not be populated with the mergers we have studied. Furthermore, the off-axis 1:1 and near-axis (head-on and $v_t/V_c = 0.15$) 3:1 mergers produce the greatest displacement across the scaling relation from the initial conditions. We find that systems with warm cores can populate the entire range of the scaling relations between our $S_o = 10\,\mathrm{keVcm}^2$ and $S_o = 300\,\mathrm{keVcm}^2$ fiducial models, but

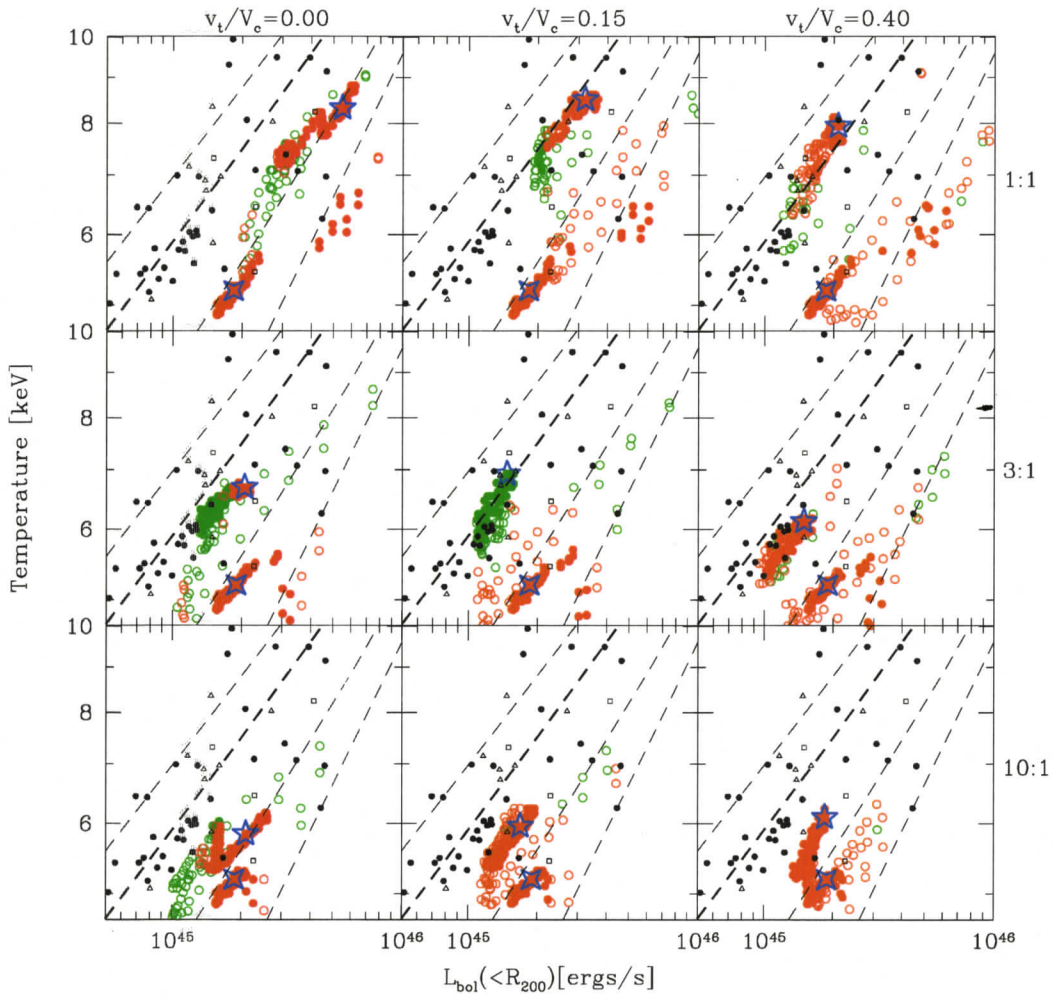

Figure 5.9: A plot of L_x against T_x illustrating the location of warm core systems in this plane. Extended warm core (EWC) systems are in green and compact warm core (CWC) systems are in red, with filled symbols and open symbols denoting systems which appear relaxed or unrelaxed (respectively) to simulated 50 ks *Chandra* observations of the system placed at $z = 0.1$. Three orthogonal projections along x, y, and z are shown (see Section 2.1 for definitions). Black points are the observed catalogue of Horner (2001) with triangles and squares indicating cool core or non-cool core systems following the procedure of McCarthy *et. al.* (2004) (again, open and filled symbols indicate noticeably disturbed or relaxed systems). Black text around the boundary indicate the mass ratio and v_t/V_c depicted by each panel.

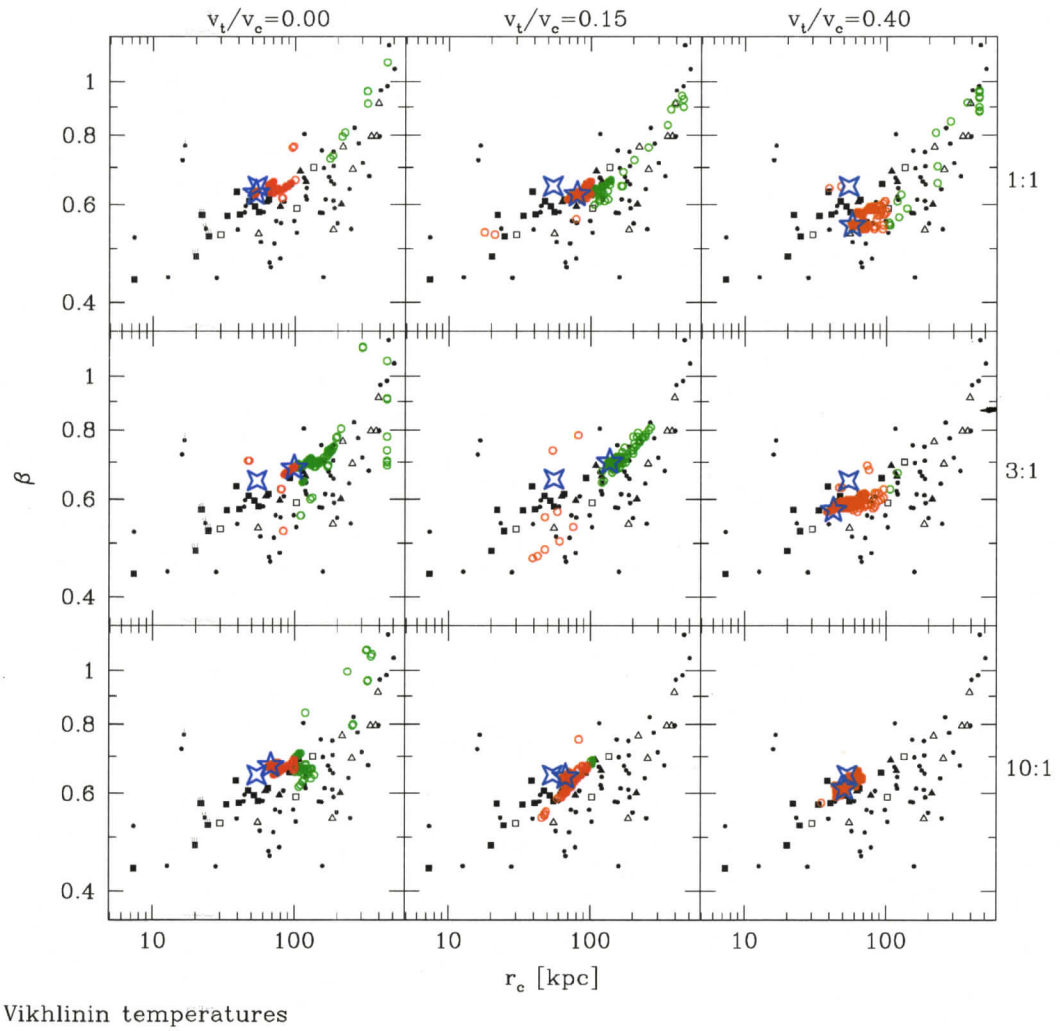

Figure 5.10: A plot of β against r_c illustrating the location of warm core systems in this plane. Extended warm core (EWC) systems are in green and compact warm core (CWC) systems are in red, with filled symbols and open symbols denoting systems which appear relaxed or unrelaxed (respectively) to simulated 50 ks *Chandra* observations of the system placed at $z = 0.1$. Three orthogonal projections along x, y, and z are shown (see Section 2.1 for definitions). Black points are the observed catalogue of Horner (2001) with triangles and squares indicating cool core or non-cool core systems following the procedure of McCarthy *et. al.* (2004) (again, open and filled symbols indicate noticeably disturbed or relaxed systems). Black text around the boundary indicate the mass ratio and v_t/V_c depicted by each panel.

that relaxed EWC systems are not found below a fiducial model of $S_o \sim 200\,\mathrm{keVcm}^2$. We have similarly examined the other scaling relations discussed in Chapter 4 and find the same qualitative behaviour of our systems' morphologies in all cases.

The $\beta - r_c$ plane

In Fig. 5.10 we present the positions of our systems in the $\beta - r_c$ plane, at each time and in all three orthogonal projections, when they appear as EWC (green) or CWC (red) systems. The initial and final states of the systems are indicated with blue four and five point stars respectively. We also identify incidences of apparently disturbed (open symbols) and relaxed (filled circles) morphology as well. These are compared against the observed catalogue of Horner (2001) (in black) for which we similarly differentiate systems with cool cores (squares) from those without (triangles) as well as instances of relaxed morphology (filled symbols) from disturbed morphology (open symbols).

We can see from this plot that β and r_c express a clear correlation in the observations and that our mergers naturally reproduce some of its features. In particular, the observations show a significant increase in the dispersion of β as r_c increases and our simulations remain well confined to the high β side of this scatter. At the largest core radii, the dispersion becomes more narrow and our simulations remain well confined to the region occupied by the observations. Our systems are always obviously disturbed when occupying this region of the plane and several observations in this region are disturbed as well.

The low-β side of the observed dispersion, at large core radii, is not significantly populated by our simulations however.

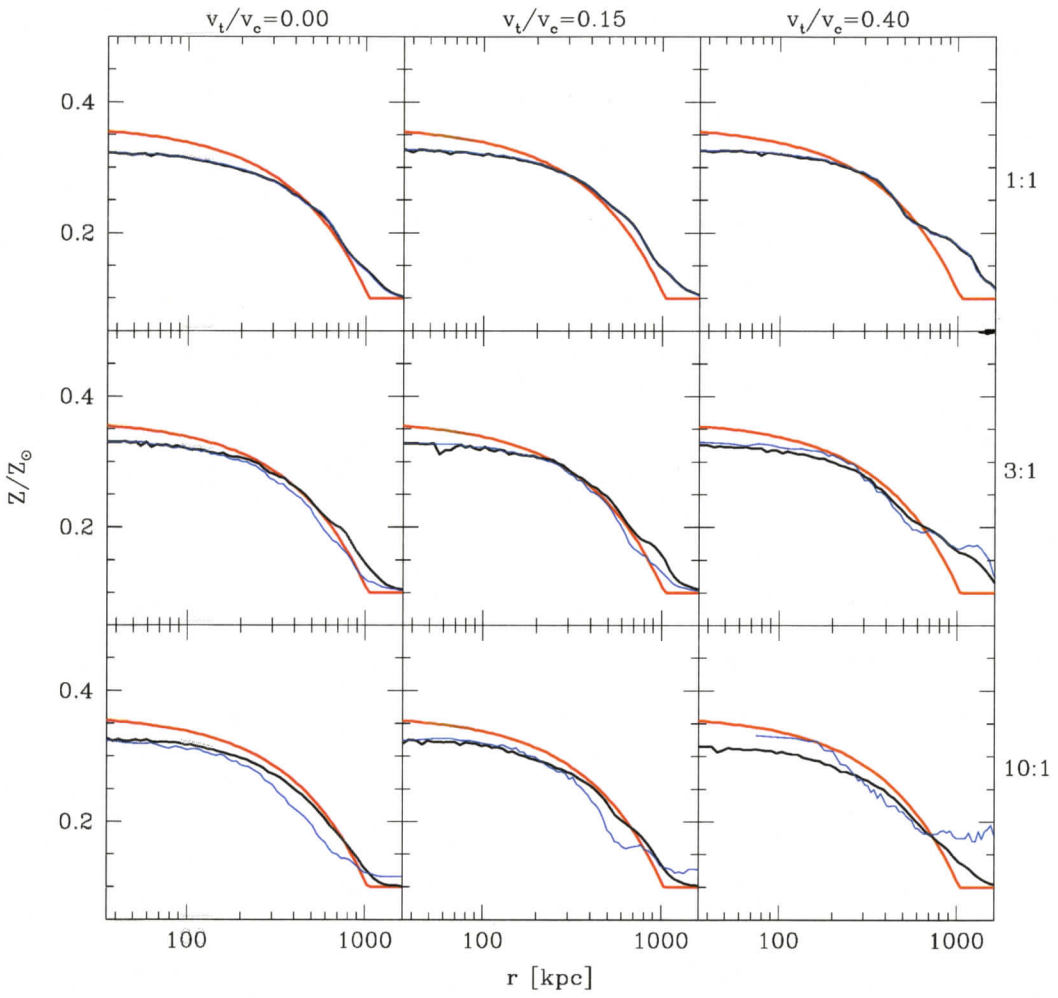

Figure 5.11: A plot comparing the initial and final metalicity gradients of our simulations. Initial profiles of the primary are shown with thick red lines and the final remnant profile is shown with a thick black line. The final distribution of material originating in the secondary is shown with a thin blue line. In all cases, the metalicity profiles of our systems are initialized to have the metalicity profiles observed by De Grandi & Molendi (2002).

5.4 Metalicity gradients

It is a well established fact that extended core systems tend to lack metalicity gradients (with mean amplitudes of $0.1-0.2Z_{\odot}$) while CCC systems routinely exhibit centrally peaked metallicity gradients within $0.2R_{180}$, often reaching central values which approach solar metalicity (De Grandi & Molendi, 2002). Anecdotal evidence suggesting that extended systems tend to be preferentially disturbed has been used to claim, as a result, that mergers effectively mix the ICM.

To examine this hypothesis, we have initialized our systems to have the metallicity profiles presented by De Grandi & Molendi (2002) and examined the resulting metalicity profiles of our merger remnants. We present these results in Fig. 5.11 where the initial metalicity profiles of our primary systems are presented in blue and the final metallicity profiles of our remnants in red.

It is clear from this figure that mergers do not efficiently mix the material of the initial systems. This makes sense given the fact that the enhanced metalicity is initially tied to the lowest entropy material in the clusters. This material is not preferentially heated above the entropy of the surrounding material and thus, remains the low entropy material constituting the remnant. Once the system relaxes, the low-entropy/high-metallicity material sinks to the center of the system due to a lack of buoyant support, reestablishing a central metalicity peak with a slightly lower amplitude and broader distribution.

5.5 Chapter summary

We have proposed a scheme for classifying the morphology of clusters based on the surface brightness and temperature profiles of their cores and illustrated how these states naturally emerge in the context of hierarchical clustering. Specifically, we find:

- Systems exist in three dominant morphologies: those with compact cores and central temperatures which are cool (CCC systems) and warm (CWC systems) and extended warm core (EWC) systems. Each population can appear in both undisturbed and disturbed states.

- In on-axis mergers, the primary's initial CCC state becomes transformed to a EWC state in 3:1 and 10:1 cases soon after the impact of the cores. This is due to the penetration of the secondary core through the primary core in these cases. In the 1:1 head-on merger, the collision of the cores is inelastic and they subsequently evolve in much higher density structure, decreasing the efficiency of heating and increasing the efficiency of cooling. Surprisingly, the 1:1 head-on collision is the case which most rapidly and completely recovers its CCC structure.

- In off-axis mergers, the initial interaction of the cores does not disturb the primary core from it's CCC state. The accretion of a stream of low entropy material formed from the disruption of the secondary's core is the dominant source of heating in these cases and leads to EWC states in the 1:1 $v_t/V_c = 0.4$ cases and 3:1 $v_t/V_c = 0.15$ cases.

- Our 3:1 $v_t/V_c = 0.15$ simulation is the case most effective at producing a sustained EWC state. However, even this case does not produce central entropies or core sizes large enough to account for most observed EWC systems.

- Once disturbed to a EWC state, systems recover their compact cores more rapidly than they recover their cool temperatures. Thus, mergers naturally account for the CWC systems observed in recent *Chandra* and XMM observations.

- The morphological segregation in scaling relations noted by McCarthy *et. al.* (2004) is qualitatively reflected in the results of our mergers: EWC systems preferen-

tially lie towards the low-luminosity/high-temperature side of the scatter in the $L_x - T_x$ plane. As noted in Chapter 4 however, the typical cluster mergers we have studied (3:1 and 10:1 cases) do not produce systems with sufficiently high central entropies to account for the most underluminous EWC systems.

- In the $\beta - r_c$ plane, several trends in the observations can be naturally accounted for by mergers, but some can not. In particular, mergers populate the high-β regions occupied by observations well, but low-β extended core systems are not typically produced.

- Mergers do not efficiently mix the ICM. Mergers between systems which initially host central metalicity gradients produce merger remnants with metalicity gradients only slightly reduced in central amplitude and slope than the initial systems.

Our results thus pose a significant challenge to a long held hypothesis in the study of X-ray clusters: that extended core systems are the product of cluster mergers. They suggest that several rare merger events are required to transform a relaxed CCC system into a EWC system and that even under such circumstances, we would expect EWC systems to host central metalicity gradients. These requirements are at odds with observations of cluster metallicities.

Chapter 6

Concluding remarks

This thesis has been an examination of several aspects of X-ray cluster mergers using idealized two body simulations. This approach has the advantage over cosmological simulations that we can be confident that our systems accurately represent the structure of observed systems, particularly in the central regions. To use this advantage, we have focused particularly on the impact of mergers on the core structure of the parent and remnant systems. Several findings have resulted.

6.1 The dynamical state of clusters

Our simulations do not include the spectrum of substructure present in a realistic clusters. Nevertheless, we find that even our 10:1 merger remnants deviate $10-20\%$ from hydrostatic equilibrium for sustained periods following their apparent relaxation, allowing us to confidently conclude that no cluster should be assumed to satisfy this condition to better than this degree. It is reasonable to conclude that the visible regions of an apparently relaxed cluster are virialized however. Remarkably, total masses computed assuming the validity of this condition should generally be good to 5% when applied to apparently relaxed systems for which accurate temperature and density profiles are available.

6.2 Transient structures

A broad array of transient phenomena are formed from the ICM of merging clusters. With the improved spatial and spectral resolution, energy coverage and collecting area provided by *Chandra* and XMM, these structures are now observed regularly in systems previously thought to be single relaxed systems. We have shown in this thesis that a careful interpretation of these phenomena can provide a great deal of information about the initial state of a merging system. This thesis summarizes only our first most rudimentary steps towards understanding the processes which transform the ICM during mergers. More study involving simulations which include the full cosmological context of merger events and instrumental effects should equip us with many new tools for probing the structure and physical processes active in the ICM of X-ray clusters.

6.3 Scaling relations

Scaling relations are powerful tools for constructing mass functions for cosmological studies. However, it has been known for some time (and we have illustrated in Chapter 4) that variations in core properties induced by mergers (and likely other processes, such as AGN) contribute significantly to the scatter in both X-ray and SZ properties. This is undesirable for cosmological studies (motivating many authors to exclude the central regions of clusters from their analysis) but likely affords an opportunity to understand the processes which shape cluster cores. Such processes include, but are not restricted to, the effects of mergers, AGN and various other processes (such as preheating) which may have contributed to modifying the central entropy (and hence, morphology) of cluster cores.

Keeping the cores in our analysis, we have examined scaling relations between luminosity, temperature, mass and SZ properties. In most cases, we find that relaxed

states which cover the full dispersion in the scaling relations can only be achieved through extremely rare equal-mass, off-axis mergers. Somewhat more common 3:1 mergers are rarely able to generate systems (neither transiently nor as relaxed remnants) which account for the dispersion in the observed scaling relations.

We have initialized our systems to represent common compact cool core systems observed by *Chandra* and to represent a significant range of orbital properties found in cosmological dark matter simulations. As a consequence, our systems should represent a significant range of typical cluster merger events. A natural question to ask however, is whether systems with initially higher central entropies could be driven by mergers to states which account for the dispersion in the scaling relations.

Such a scenario is effectively a multiple heating event scenario in which a system's central entropy becomes elevated (either by a previous merger event or AGN activity) and then additionally heated to states which single mergers between relaxed systems can not generate. This is appealing on the grounds that mergers involving heated cores will generate lower densities and stimulate less radiative cooling, tipping the balance between heating and cooling towards heating. Furthermore, previously heated cores will have lower densities, increasing the efficiency of entropy production.

Although possible, we believe that such a scenario is not plausible. We have found that 3:1 mergers between relaxed systems are merely able to move a system to the best fit median relation in most of the scaling relations we have studied. It would presumably require an additional merger of comparable extent to move the system the rest of the way across the relation. To have a significant effect on the statistics of the population, this would have to occur regularly, but it requires the compounding of two very rare events.

One possibility which requires additional study however, is that merger events may occasionally stimulate subsequent AGN activity. There are several stages during the evolution of our mergers when gaseous material becomes driven towards the cores of our systems. These times generally occur during the interactions of the merging

cores (at $t_{closest}$ or $t_{accrete}$) or during the accretion of the streams generated from the disruption of the secondary's core. During these times, low angular momentum from the primary system which is stationary with respect to the central black hole could be perturbed towards the center of the system. This may provide a natural means of generating multiple heating events in close succession (and thus reproducing the full dispersion of the scaling relations) within the framework of hierarchical clustering.

Impending observational progress should contribute significantly towards resolving these issues. We have shown that isothermal β-model masses, besides being systematically low by as much as 40%, likely also contribute significantly to the scatter in mass scaling relations. These effects are difficult to reliably account for. Improvements in X-ray mass estimates which have been demonstrated to be feasible with *Chandra* (but only on a limited sample so far) will greatly simplify analysis and interpretation of these relations once they have been applied to a large representative sample of clusters.

Furthermore, improvements in available SZ catalogues will be extremely valuable. Our fiducial models predict very little scatter in the $y_o - L_x$ plane and our simulations find that only during periods of significant disruption (particularly in off-axis cases, which affect y_o very little but increase the system's luminosity) should the system deviate significantly from the mass-scaling relation. In the observations reported by Benson et al. (2004) however, there are several systems on the high-luminosity side of the predicted relation. We do not see an obvious way to account for this. If the discrepancy is not due to systematic uncertainties which are not accounted for in the reported uncertainties, then this suggests that these systems may be significantly disturbed. This may not be too surprising given the fact that the observations in this catalogue are all of very hot (and massive) systems, which are particularly prone to merger activity.

6.4 Cluster morphologies

Cooling should naturally drive systems to states with low central entropies, and compact cool cores (CCC systems). However, we have illustrated that merger events can yield two additional morphologies: EWC systems (with warm extended cores and high central entropies) and CWC systems (with compact cores but a range of elevated central temperatures). Mergers of relaxed CCC systems do not generically yield systems with EWC morphologies for extended periods of time. When they do (such as our 3:1 $v_t/V_c = 0.15$ case) it is due to elevated central entropies generated primarily during the accretion of low-density streams of material created from the disruption of the secondary core.

Thus, the notions of compactness, coolness, and active cooling are related but not as simply as once thought. As noted by the observations of Sanderson et al. (2006) (and supported by our simulations) compact cores need not be cool nor actively cooling. Such trends can all be accounted for by merger activity. Once a merger remnant evolves sufficiently to look relaxed to *Chandra*, it typically recovers its compact core more quickly than its core cools. Hence, we must thus be careful when thinking that compact implies cool, although cool should generically imply compact.

The central entropy of a system correlates well with each of these properties however. CCC systems have low central entropies, EWC core systems high central entropies and CWC systems a distribution of central entropies which generally lie in an overlapping range in between. This naturally explains the observed morphological segregation in the scaling relations noted by McCarthy *et. al.* (2004). The present work adds to their findings the fact that even for a recently disturbed system, it's position in the $L_x - T_x$ plane (and it's core morphology) is primarily a product of its central entropy. The fact that our mergers do not efficiently produce EWC states is thus a result of the fact that they do not sufficiently heat, and thus raise the central entropy, of cluster cores.

How then are systems with high central entropies ($S_{40} > 150\,\mathrm{keVcm}^2$) and large surface brightness cores ($r_c > 150\,\mathrm{kpc}$) produced? Merger induced AGN heating such as that suggested above? Significant outburst such as those observed by McNamara et al. (2005) could potentially heat the cores of a disturbed system to EWC states but even MS0735.6+7421, the largest AGN outburst yet observed, still has a significant metalicity gradient. It would appear that neither AGN outbursts nor mergers are able to sufficiently erase a metalicity gradient once it is established. How then do we reconcile the lack of metalicity gradients in observed EWC systems with our results?

It may be that mergers yield more mixing than our simulations suggest. SPH is an inherently non-diffusive algorithm and handles turbulence poorly. Alternatively, it may be that the observed spectrum of cluster morphologies are a product of processes active early in the system's evolution. We find that near equal mass mergers are more efficient at producing heated cores and at early epochs, such events (between much lower mass systems than we study) are expected to be more common. Systems having experienced a greater proportion of such events may have altered star formation histories as a result, yielding the observed differences in metalicity profiles observed between compact and extended core systems. Clearly, further investigation is required to enable us to select between competing possibilities.

Bibliography

Abramopoulos, F. & Ku, W. H.-M. 1983, ApJ, 271, 446

Allen, S. W. 1998, MNRAS, 296, 392

Allen, S. W. & Fabian, A. C. 1998, MNRAS, 297, L63

Babul A., Balogh M.L., Babul A., Lewis G., Poole G., 2002, MNRAS 330, 329

Balogh, M. L., Babul, A., Voit, G. M., McCarthy, I. G., Jones, L. R., Lewis, G. F., & Ebeling, H. 2006, MNRAS, 78

Barnes, J., & Efstathiou, G. 1987, ApJ, 319, 575

Belsole, E., Sauvageot, J.-L., Pratt, G. W., & Bourdin, H. 2005, Advances in Space Research, 36, 630

Benson, B. A., Church, S. E., Ade, P. A. R., Bock, J. J., Ganga, K. M., Henson, C. N., & Thompson, K. L. 2004, ApJ, 617, 829

Benson, A. J. 2005, MNRAS, 358, 551

Bertschinger, E. 1989, ApJ, 340, 666

Bialek, J. J., Evrard, A. E., & Mohr, J. J. 2002, ApJ, 578, L9

Binney, J., & Tremaine, S. 1987, Princeton, NJ, Princeton University Press, 1987, p. 237

Böhringer, H., Matsushita, K., Churazov, E., Finoguenov, A., & Ikebe, Y. 2004, A&A, 416, L21

Bregman, J. N. 2004, The Riddle of Cooling Flows in Galaxies and Clusters of galaxies,

Briel, U. G., Finoguenov, A., & Henry, J. P. 2004, A&A, 426, 1

Buote, D. A., & Tsai, J. C. 1995, ApJ, 452, 522

Buote, D. A. & Tsai, J. C., 1996, ApJ, 458, 27

Byram, E. T., Chubb, T. A., & Friedman, H. 1966, Science, 152, 66

Cavaliere, A., Gursky, H., & Tucker, W. 1971, Nature, 231, 437

Chatzikos, M., Sarazin, C. L., & Kempner, J. C. 2006, ArXiv Astrophysics e-prints, arXiv:astro-ph/0602199

Chen, L.-W., Fabian, A. C., & Gendreau, K. C. 1997, MNRAS, 285, 449

Cohn, J. D., & White, M. 2005, Astroparticle Physics, 24, 316

Collins, G. W. 1978, Tucson, Ariz., Pachart Publishing House (Astronomy and Astrophysics Series. Volume 7), 1978. 143 p.,

Cowie, L. L. & Binney, J. 1977, ApJ, 215, 723

Croston, J. H., Hardcastle, M. J., & Birkinshaw, M. 2005, MNRAS, 357, 279

Davé, R., Katz, N., & Weinberg, D. H. 2002, ApJ, 579, 23

David, L. P., & Kempner, J. 2004, ApJ, 613, 831

De Grandi, S. & Molendi, S. 2001, ApJ, 551, 153

De Grandi, S., & Molendi, S. 2002, ApJ, 567, 163

Edge, A. C., Stewart, G. C., & Fabian, A. C. 1992, MNRAS, 258, 177

Donahue, M., Horner, D. J., Cavagnolo, K. W., & Voit, G. M. 2005, ArXiv Astrophysics e-prints, arXiv:astro-ph/0511401

Dubinski, J., & Carlberg, R. G. 1991, ApJ, 378, 496

Dupke, R., & White, R. E. 2003, ApJ, 583, L13

Durret, F., Lima Neto, G. B., & Forman, W. 2005, A&A, 432, 809

Edge, A. C., Stewart, G. C., & Fabian, A. C. 1992, MNRAS, 258, 177

Egami, E., et al. 2006, ArXiv Astrophysics e-prints, arXiv:astro-ph/0603656

Eke, V. R., Navarro, J. F., & Steinmetz, M. 2001, ApJ, 554, 114

Fabian, A. C. 1994, ARA&A, 32, 277

Fabian, A. C., Sanders, J. S., Crawford, C. S., Conselice, C. J., Gallagher, J. S., & Wyse, R. F. G. 2003, MNRAS, 344, L48

Fabian, A. C., Sanders, J. S., Taylor, G. B., & Allen, S. W. 2005, MNRAS, 360, L20

Feretti, L. 2003, ArXiv Astrophysics e-prints, astro-ph/0309221

Finoguenov, A., Böhringer, H., & Zhang, Y.-Y. 2005, A&A, 442, 827

Forman, W., Jones, C., Markevitch, M., Vikhlinin, A., & Churazov, E. 2002, Lighthouses of the Universe: The Most Luminous Celestial Objects and Their Use for Cosmology Proceedings of the MPA/ESO/, p. 51, 51

Fritz, G., Davidsen, A., Meekins, J. F., & Friedman, H. 1971, ApJ, 164, L81

Gardini, A., Rasia, E., Mazzotta, P., Tormen, G., De Grandi, S., & Moscardini, L. 2004, MNRAS, 351, 505

Gnedin, O. Y., Kravtsov, A. V., Klypin, A. A., & Nagai, D. 2004, ApJ, 616, 16

Gomez P.L., Loken C., Roettiger K., Burns J.O. 2002, ApJ 569, 122

Govoni, F., Markevitch, M., Vikhlinin, A., VanSpeybroeck, L., Feretti, L., & Giovannini, G. 2004, ApJ, 605, 695

Gursky, H., Kellogg, E. M., Leong, C., Tananbaum, H., & Giacconi, R. 1971, ApJ, 165, L43

Gursky, H., Kellogg, E., Murray, S., Leong, C., Tananbaum, H., & Giacconi, R. 1971, ApJ, 167, L81

Guth, A. H. 1981, Phys. Rev. D, 23, 347

Gutierrez, K., & Krawczynski, H. 2005, ApJ, 619, 161

Hallman, E. J., Motl, P. M., Burns, J. O., & Norman, M. L. 2006, ApJ, 648, 852

Hallman, E. J. & Markevitch, M. 2004, ApJ, 610, L81

Heinz, S., Churazov, E., Forman, W., Jones, C., & Briel, U. G. 2003, MNRAS, 346, 13

Henry, J. P., Branduardi, G., Fabricant, D., Feigelson, E., Murray, S., Tananbaum, H., Briel, U., & Soltan, A. 1979, ApJ, 234, L15

Henry, J. P., Finoguenov, A., & Briel, U. G. 2004, ApJ, 615, 181

Horner, D. J. 2001, Ph.D. thesis, Univ. Maryland

Irwin, J. A. & Bregman, J. N., 2001, ApJ, 546, 150

Jaffe, W., Bremer, M. N., & Baker, K. 2005, MNRAS, 360, 748

Jeans, J. 1902, Phil. Trans, 199A, 49

Jeltema, T. E., Canizares, C. R., Bautz, M. W., & Buote, D. A. 2005, ApJ, 624, 606

Jing, Y. P., & Suto, Y. 2002, ApJ, 574, 538

Jones, C. & Forman, W. 1984, ApJ, 276, 38

Kaiser, N. 1986, MNRAS, 222, 323

Kaiser, C. R. & Binney, J. 2003, MNRAS, 338, 837

Edge, A. C., Stewart, G. C., & Fabian, A. C., 1992, MNRAS, 258, 177

Kapteyn, J. C. 1922, ApJ, 55, 302

Katz, N., Weinberg, D. H., & Hernquist, L. 1996, ApJS, 105, 19

Kay, S. T., da Silva, A. C., Aghanim, N., Blanchard, A., Liddle, A. R., Puget, J.-L., Sadat, R., & Thomas, P. A. 2006, ArXiv Astrophysics e-prints, arXiv:astro-ph/0611017

Kazantzidis, S., Kravtsov, A. V., Zentner, A. R., Allgood, B., Nagai, D., & Moore, B. 2004, ApJ, 611, L73

Kazantzidis, S., Magorrian, J., & Moore, B. 2004, ApJ, 601, 37

Kempner, J. C., & David, L. P. 2004, MNRAS, 349, 385

Kempner et al. 2003, ArXiv Astrophysics e-prints, astro-ph/0310263

Kempner, J. C., Sarazin, C. L., & Markevitch, M. 2003, ApJ, 593, 291

Kim, W. & Narayan, R.2003, ApJ, 596, L139

Knox, L., Holder, G. P., & Church, S. E. 2004, ApJ, 612, 96

Kolokotronis, V., Basilakos, S., Plionis, M., & Georgantopoulos, I. 2001, MNRAS, 320, 49

Kravtsov, A. V., Vikhlinin, A., & Nagai, D. 2006, ArXiv Astrophysics e-prints, arXiv:astro-ph/0603205

Lewis, G. F., Babul, A., Katz, N., Quinn, T., Hernquist, L., & Weinberg, D. H. 2000, ApJ, 536, 623

Loken, C., Melott, A. L., & Miller, C. J., 1999, ApJL, 520, L5

Loken, C., Norman, M. L., Nelson, E., Burns, J., Bryan, G. L., & Motl, P. 2002, ApJ, 579, 571

Majumdar, S., & Mohr, J. J. 2003, ApJ, 585, 603

Markevitch, M. 1998, ApJ, 504, 27

Markevitch, M., et al. 2000, ApJ, 541, 542

Markevitch, M., Gonzalez, A. H., David, L., Vikhlinin, A., Murray, S., Forman, W., Jones, C., & Tucker, W. 2002, ApJ, 567, L27

Markevitch, M., et al. 2003, ApJ, 586, L19

Markevitch, M., & Vikhlinin, A. 2001, ApJ, 563, 95

Markevitch, M. & Vikhlinin, A. 2001, ApJ, 563, 95

Markevitch, M., Vikhlinin, A., & Mazzotta, P. 2001, ApJ, 562, L153

Marri, S. & White, S. D. M. 2003, MNRAS, 345, 561

Mathews, W. G., Faltenbacher, A., & Brighenti, F. 2006, ApJ, 638, 659

Mathiesen, B. F. & Evrard, A. E. 2001, ApJ, 546, 100

Mathis, H., Lavaux, G., Diego, J. M., & Silk, J. 2005, MNRAS, 357, 801

Mazzotta, P., Markevitch, M., Vikhlinin, A., Forman, W. R., David, L. P., & VanSpeybroeck, L. 2001, ApJ, 555, 205

Mazzotta, P., Rasia, E., Moscardini, L., & Tormen, G. 2004, MNRAS, 354, 10

McCarthy, I. G., Babul, A., Holder, G. P., & Balogh, M. L. 2003, ApJ, 591, 515

McCarthy I.G., Balogh M.L., Babul A., Poole G.B., Horner D.J., 2004 ApJ ??, ??

McCarthy, I. G., Fardal, M. A., & Babul, A. 2005, ArXiv Astrophysics e-prints, astro-ph/0501137

McNamara, B. R., Nulsen, P. E. J., Wise, M. W., Rafferty, D. A., Carilli, C., Sarazin, C. L., & Blanton, E. L. 2005, Nature, 433, 45

Meekins, J. F., Gilbert, F., Chubb, T. A., Friedman, H., & Henry, R. C. 1971, Nature, 231, 107

Mohr, J. J., Fabricant, D. G., & Geller, M. J. 1993, ApJ, 413, 492

Moore, B., Governato, F., Quinn, T., Stadel, J., & Lake, G. 1998, ApJ, 499, L5

Motl P.M., Burns J.O., Loken C., Norman M., Bryan G., 2004, ApJ 606, 635

Mulchaey, J. S., Dressler, A., & Oemler, A. 2004, Clusters of Galaxies: Probes of Cosmological Structure and Galaxy Evolution. Carnegie Observatories Astrophysics Series, Volume 3. Edited by John S. Mulchaey, Alan Dressler and Augustus Oemler. ISBN 0 521 75576 X. Published by Cambridge University Press, Cambridge, UK, 2004.

Nagai, D., Vikhlinin, A., & Kravtsov, A. V. 2006, ArXiv Astrophysics e-prints, arXiv:astro-ph/0609247

Navarro, J. F., Frenk, C. S., & White, S. D. M. 1996, ApJ, 462, 563

Nusser, A., Silk, J., & Babul, A. 2006, ArXiv Astrophysics e-prints, arXiv:astro-ph/0602566

O'Hara, T. B., Mohr, J. J., Bialek, J. J., & Evrard, A. E. 2006, ApJ, 639, 64

Ota, N. & Mitsuda, K. 2004, Astronomy & Astrophysics, 428, 757

Pearce, F. R., Thomas, P. A., & Couchman, H. M. P. 1994, MNRAS, 268, 953

Peres, C. B., Fabian, A. C., Edge, A. C., Allen, S. W., Johnstone, R. M., & White, D. A. 1998, MNRAS, 298, 416

Peterson, J. R., Kahn, S. M., Paerels, F. B. S., Kaastra, J. S., Tamura, T., Bleeker, J. A. M., Ferrigno, C., & Jernigan, J. G. 2003, ApJ, 590, 207

Piffaretti, R., Jetzer, P., Kaastra, J., & Tamura, T. 2004, Astronomy & Astrophysics, 433, 101

Poole, G. *et. al.* , 2006

Poole, G. *et. al.* , 2006

Poole, G. *et. al.* , 2006

Pratt, G. W., Boehringer, H., Croston, J. H., Arnaud, M., Borgani, S., Finoguenov, A., & Temple, R. F. 2006, ArXiv Astrophysics e-prints, arXiv:astro-ph/0609480

Randall, S. W., Sarazin, C. L., & Ricker, P. M. 2002, ApJ, 577, 579

Rasia, E., et al. 2006, MNRAS, 369, 2013

Raymond, J. C. & Smith, B. W. 1977, ApJS, 35, 419

Reiprich, T. H., & Böhringer, H. 2002, ApJ, 567, 716

Reiprich, T. H., Sarazin, C. L., Kempner, J. C., & Tittley, E. 2004, ApJ, 608, 179

Ricker, P. M. 1998, ApJ, 496, 670

Ricker, P. M. & Sarazin, C. L. 2001, ApJ, 561, 621

Ritchie, B. W. & Thomas, P. A. 2001, MNRAS, 323, 743

Ritchie B.W. and Thomas P.A., 2002, MNRAS, 329, 675

Roettiger, K., Burns, J., & Loken, C. 1993, ApJ, 407, L53

Roettiger, K., Loken, C., & Burns, J. O. 1997, ApJS, 109, 307

Rowley, D. R., Thomas, P. A., & Kay, S. T. 2004, MNRAS, 352, 508

Silk, J. 1976, ApJ, 208, 646

Sakelliou, I., & Ponman, T. J. 2004, MNRAS, 351, 1439

Sakelliou, I., & Ponman, T. J. 2006, ArXiv Astrophysics e-prints, arXiv:astro-ph/0601382

Sanders, J. S., Fabian, A. C., & Taylor, G. B. 2005, MNRAS, 356, 1022

Sanderson, A. J. R., Ponman, T. J., Finoguenov, A., Lloyd-Davies, E. J., & Markevitch, M. 2003, MNRAS, 340, 989

Sanderson, A. J. R., Ponman, T. J., & O'Sullivan, E. 2006, ArXiv Astrophysics e-prints, arXiv:astro-ph/0608423

Sarazin, C. L. 1988, Cambridge Astrophysics Series, Cambridge: Cambridge University Press, 1988

Schindler, S., & Mueller, E. 1993, A&A, 272, 137

Silk, J. 1976, ApJ, 208, 646

Smith, G. P., Kneib, J.-P., Smail, I., Mazzotta, P., Ebeling, H., & Czoske, O. 2005, MNRAS, 359, 417

Smoot, G. F., et al. 1992, ApJ, 396, L1

Springel, V., et al. 2005, Nature, 435, 629

Spitzer, L. 1978, New York Wiley-Interscience, 1978. 333 p.,

Stinson, G., Seth, A., Katz, N., Wadsley, J., Governato, F., Quinn, T. 2006. ArXiv Astrophysics e-prints arXiv:astro-ph/0602350

Sun, M., Murray, S. S., Markevitch, M., & Vikhlinin, A. 2002, ApJ, 565, 867

Sunyaev, R. A., & Zeldovich, Y. B. 1970, Comments on Astrophysics and Space Physics, 2, 66

Sunyaev, R. A., & Zeldovich, Y. B. 1972, Comments on Astrophysics and Space Physics, 4, 173

Taylor, J. E., & Babul, A. 2004, MNRAS, 348, 811

Thomas, P. A., et al. 1998, MNRAS, 296, 1061

Tittley, E. R. & Henriksen, M. 2005, ApJ, 618, 227

Toomre, A., & Toomre, J. 1972, ApJ, 178, 623

Tormen, G. 1997, MNRAS, 290,411

Tormen, G., Moscardini, L., & Yoshida, N. 2004, MNRAS, 350, 1397

Vikhlinin, A. 2006, ApJ, 640, 710

Vikhlinin, A., Kravtsov, A., Forman, W., Jones, C., Markevitch, M., Murray, S. S., & Van Speybroeck, L. 2006, ApJ, 640, 691

Vikhlinin, A., Markevitch, M., & Murray, S. S. 2001, ApJ, 551, 160

Vitvitska, M., Klypin, A. A., Kravtsov, A. V., Wechsler, R. H., Primack, J. R., & Bullock, J. S. 2002, ApJ, 581, 799

Voigt, L. M. & Fabian, A. C. 2004, MNRAS, 347, 1130

Voit, G. M. 2005, Reviews of Modern Physics, 77, 207

Voit, G. M., & Donahue, M. 2005, ApJ, 634, 955

Voit, G. M., Balogh, M. L., Bower, R. G., Lacey, C. G., & Bryan, G. L. 2003, ApJ, 593, 272

Voit, G. M., Kay, S. T., & Bryan, G. L. 2005, MNRAS, 364, 909

Voit, G. M., & Ponman, T. J. 2003, ApJ, 594, L75

Wadsley, J. W., Stadel, J., & Quinn, T. 2004, New Astronomy, 9, 137

White, D. A., Jones, C., & Forman, W. 1997, MNRAS, 292, 419

Zwicky, F. 1933, Helvetica Physica Acta, 6, 110